SOLUTION REACTIVITY STUDIES OF GROUP 14 ZINTL CLUSTERS TOWARDS ORGANOMETALLIC REAGENTS

A thesis submitted in partial fulfilment of the requirements for the degree of Doctor of Philosophy at the University of Oxford

Binbin Zhou

Linacre College, Oxford

March 2012

DOCTOR OF PHILOSOPHY SCHOOL OF CHEMISTRY

DECLARATION OF AUTHORSHIP

Name: BINBIN ZHOU	**Candidate number: 390050**
College: LINACRE COLLEGE	**Supervisor: DR. JOSE GOICOECHEA**
Title of thesis: SOLUTION REACTIVITY STUDIES OF GROUP 14 ZINTL CLUSTERS TOWARDS ORGANOMETALLIC REAGENTS	
Word Count: 45,000	

Please tick to confirm the following:

I have read and understood the University's disciplinary regulations concerning conduct in examinations and, in particular, the regulations on plagiarism (Available at www.admin.ox.ac.uk/proctors/info/pam/section9.shtml).	✓
I have read and understood the Education Committee's information and guidance on academic good practice and plagiarism at www.admin.ox.ac.uk/edc/goodpractice.	✓
The thesis I am submitting is entirely my own work except where otherwise indicated.	✓
It has not been submitted, either partially or in full, for another Honour School or qualification of this University (except where the Special Regulations for the subject permit this), or for a qualification at any other institution.	✓
I have clearly indicated the presence of all material I have quoted from other sources, including any diagrams, charts, tables or graphs.	✓
I have clearly indicated the presence of all paraphrased material with appropriate references.	✓
I have acknowledged appropriately any assistance I have received in addition to that provided by my supervisor.	✓
I have not copied from the work of any other candidate.	✓
I have not used the services of any agency providing specimen, model or ghostwritten work in the preparation of this thesis. (See http://www.admin.ox.ac.uk/statutes/352-051a.shtml#_Toc28142348.)	✓
I agree to retain an electronic copy of this work until the publication of my final examination result, except where submission in hand-written format is permitted.	✓
I agree to make any such electronic copy available to the examiners should it be necessary to confirm my word count or to check for plagiarism.	✓

Candidate's signature:	Date:

Abstract

The group 14 Zintl clusters $[E_9]^{4-}$ (E = Ge, Sn, Pb) have been reacted with organometallic reagents in solution in the presence of alkali metal cation sequestering agents. The synthesis, characterisation and reactivity studies of the resultant complexes are reported herein.

These negatively charged clusters reductively cleave one of the M–C bonds in the group 12 homoleptic organometallic reagents MR_2 (M = Zn, Cd; R = Ph, mes, ^{i}Pr) to yield η^4-coordinated functionalised clusters *closo*-$[E_9MR]^{3-}$. They can also activate both of the M–C bonds in $Cd(mes)_2$ to form metal-bridged dimers $[Ge_9CdGe_9]^{6-}$ and $[Pb_9CdCdPb_9]^{6-}$. Investigating the reactivity of the functionalised cluster $[E_9CdPh]^{3-}$ (E = Sn, Pb) towards $HSn(^n Bu)_3$ results in the synthesis of the novel *closo*-clusters $[E_9CdSn(^n Bu)_3]^{3-}$.

The reaction of K_4Ge_9 with the heteroleptic organometallic reagent $Fe(COT)(CO)_3$ yields the metalated cluster anion $[Ge_8Fe(CO)_3]^{3-}$, in which the nuclearity of the Zintl anion is altered upon coordination of the $[Fe(CO)_3]$ moiety. Two side products have also been isolated as $[K(2,2,2\text{-crypt})]^+$ salts of $[Fe(\eta^3\text{-}C_8H_8)(CO)_3]^-$ and $[Fe_2(\eta^3, \eta'^3\text{-}C_{16}H_{16})(CO)_6]^{2-}$.

In the presence of highly reduced Zintl anions, all the M–C bonds in homoleptic mid-row transition metal organometallic reagents can also be cleaved. These ‘naked’ metal atoms have templated the formation of the endohedral clusters $[Fe@Ge_{10}]^{3-}$, $[Fe@Sn_{10}]^{3-}$ and $[Mn@Pb_{12}]^{3-}$. These clusters adopt very different geometries and the electronic origin of their structures has been investigated in-depth by DFT calculations. Structural characterisation of some side products is also reported for: $[E_9(mes)]^{3-}$ (E = Ge, Sn) and $[Ge_9Mn(mes)]^{3-}$.

Acknowledgements

Firstly, I would like to express my deepest appreciation to my supervisor Dr. Jose Goicoechea for giving me the opportunity to study at Oxford, particularly for all his guidance, advice, inspiration and encouragement over the past few years. It truly has been a wonderful experience.

I would like to acknowledge the contributions made by the following people: Dr. Tobias Krämer and Prof. John E. McGrady (University of Oxford) for performing the DFT calculations. Dr. Amber Thompson (University of Oxford) for help with crystallography. Diamond Light Source for beam-time on I19, and additionally Dr. Kirsten E. Christensen and Dr. David R. Allan (Diamond Light Source) for their assistance with data collection and refinement. Dr. Jeffrey Harmer and Mark Irwin (University of Oxford) for their assistance with EPR spectroscopy. Steve Boyer (London Metropolitan University) for carrying out the elemental analyses. Dr. Mark Denning for the synthesis of the Zintl phase precursors and helpful advice. My Part II students Tom Chapman, Carl Jones and David Hansen for contributions to some of the work discussed herein.

A huge thank you must go to Mark Irwin and Rob Turbervill for their help in providing indispensable advice and the proofreading of this thesis. Thanks also to the past and present members of lab/S11 for their help and encouragement over the years and, most importantly, the laughs that made my D.Phil. some of the best years of my life – Caroline, Gaby, Lawrence, Amy, Pete, Belinda, Joe, Charlotte, Dave, Ed, Rhiannon and Charlie.

To Mum, Dad, the rest of my family and friends for their constant and unconditional support, encouragement and love.

Abbreviations

(2,2)diaza-18-crown-6	1,4,10,13- tetraoxa-7,16-diazacyclooctadecane
18-crown-6	1,4,7,10,13,16-hexaoxacyclooctadecane
2,1,1-crypt	4,7,13,18-tetraoxa-1,10-diazabicyclo[8,5,5]eicosane
2,2,2-crypt	4,7,13,16,21,24-hexaoxa-1,10diazabicyclo[8,8,8]hexacosane
Ar	2,6-$mes_2C_6H_3$
benzo-18-crown-6	2,3-benzo-1,4,7,10,13,16-hexaoxacycloocta-deca-2-ene
COD	1,5-cyclooctadiene
COSY	correlation spectroscopy
COT	1,3,5,7-cyclooctatetraene
Cp	cyclopentadienyl
Cp*	pentamethylcyclopentadienyl
CW EPR	continuous wave electron paramagnetic resonance
Cy	cyclohexyl
δ	chemical shift
d	doublet
dd	doublet of doublets
DFT	density functional theory
DMF	*N*,*N*-dimethylformamide
DMSO	dimethyl sulfoxide
dppe	1,2-bis(diphenylphosphino)ethane
E^{IV}	group 15 elements
en	ethylenediamine
ES-MS	electrospray mass spectrometry
E^{V}	group 14 elements
Fc	ferrocenyl
HMQC	heteronuclear multiple quantum coherence
HOMO	highest occupied molecular orbital
I	nuclear spin quantum number
i	*ipso*

^{i}Pr	isopropyl
IR	infrared
J	coupling constant
LUMO	lowest unoccupied molecular orbital
m	multiplet
m	*meta*
m/z	mass to charge ratio
Me	methyl
mes	mesityl
v	stretching frequency
^{n}Bu	*n*-butyl
NMR	nuclear magnetic resonance
norbornene	bicyclo[2.2.1]hept-2-ene
o	*ortho*
p	*para*
Ph	phenyl
ppm	parts per million
py	pyridine
S	total spin angular momentum
s	singlet
^{s}Bu	*sec*-butyl
sep	septet
SOMO	singly occupied molecular orbital
t	triplet
^{t}Am	*t*-amyl
^{t}Bu	*t*-butyl
THF	tetrahydrofuran
tol	toluene
tq	triplet of quartets
UV-Vis	ultraviolet/visible

Contents

Chapter 1 – Introduction

1.1 A brief history of Zintl clusters

The chemistry of Zintl ions is a fascinating yet often overlooked area of inorganic chemistry. The earliest reports of this class of molecular anions date back to 1891, when Joannis noticed that liquid ammonia solutions of sodium could dissolve elemental lead to give deeply coloured green solutions.[1-3] Following this observation, Kraus carried out similar experiments dissolving elemental tin in liquid ammonia solutions of alkali metals, which were found to yield deep red solutions.[4] At the time the composition of such binary systems was not clear and estimated to have an approximate 1:2 alkali metal to p-block element ratio. It was not until the 1930s when a German chemist named Eduard Zintl carried out a series of potentiometric titration experiments that the exact ratios of the different elements in these intensely coloured liquid ammonia solutions were determined.[5-9] As a result these negatively charged polyatomic clusters are named after him for his contribution to this field of chemistry. A binary Zintl compound has the general formula A_xE_y, where A is a very electropositive element such as an alkali or alkali earth metal, and E is a more electronegative p-block element. It is assumed that there is a complete electron transfer from A to E, resulting in a cluster $[E_y]$ with a formal charge of x–.

The difficulty of using liquid ammonia as a reaction solvent initially slowed the development of Zintl chemistry. For many years, research mainly focused on improving the synthesis of known Zintl clusters. It was subsequently realised that there is a relationship between Zintl cluster anions in solution and the solid-state salt-like intermetallic Zintl phases. For example

the neat Zintl phases Cs_4Ge_9 and Rb_4Ge_9 are isostructural and contain the same $[Ge_9]^{4-}$ clusters as those isolated from solution in systems such as Rb_4Ge_9·en (en = ethylenediamine).[10] Hence the modern synthesis of Zintl clusters generally involves making the alloys by high temperature solid-state reactions from a mixture of the elements in the appropriate stoichiometric ratios. Many of these alloys can then be dissolved or exacted into aprotic solvents with high dielectric constants such as ethylenediamine, pyridine and *N*,*N*-dimethylformamide (DMF).

Cation sequestering agents such as the three-dimensional cryptand 2,2,2-crypt (4,7,13,16,21,24-hexaoxa-1,10-diazabicyclo[8.8.8]-hexacosane) and the two-dimensional crown ether 18-crown-6 (1,4,7,10,13,16-hexaoxacyclooctadecane) play an important role in the chemistry of Zintl ions. They have a great affinity towards alkali metal cations and form strong complexes with them. This binding also helps to prevent the electrons being transferred back to the alkali metal cation and increases the overall stability of the Zintl phases in polar organic solvents. When 2,2,2-crypt forms a complex with a metal cation the resulting almost spherical cryptate has a size that is comparable to the negatively charged Zintl clusters, which aids the crystallisation of these highly reduced Zintl clusters.

By introducing alkali metal cation sequestering agents, a large number of homoatomic cluster anions with remarkably different structural and electronic features have been crystallised and characterised. Examples of group 14 homoatomic Zintl clusters include $[E_4]^{4-}$, $[E_5]^{2-}$ and $[E_9]^{4-}$ (E = Si, Ge, Sn, Pb).[11-14] The largest crystallographically characterised empty

homoatomic group 14 Zintl anion is the 10-vertex cluster $[Pb_{10}]^{2-}$ reported by Fässler and co-workers, which exhibits near perfect D_{4d} symmetry.[15]

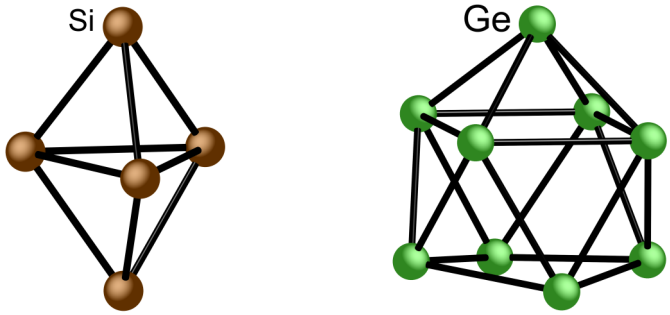

Figure 1.1 Molecular structures of some of the group 14 Zintl cluster anions isolated from solution: $[Si_5]^{2-}$ (left) and $[Ge_9]^{3-}$ (right). The sequestered alkali-metal cations have been omitted for clarity.

1.2 Nine-atom group 14 Zintl clusters

1.2.1 Synthesis of nine-atom group 14 Zintl clusters

Nine-atom group 14 Zintl clusters with the general formula $[E_9]^{n-}$ (n = 2 – 4) are the most extensively studied type of Zintl clusters and are known for E = Si, Ge, Sn and Pb. They can be routinely obtained from the dissolution of intermetallic solid state Zintl alloys and have been characterised both in the solid state by single crystal X-ray diffraction experiments and also in solution by multielement NMR experiments and/or electrospray mass spectrometry. In 1975 Corbett reported the single crystal structure of deltahedral polyatomic anion $[Sn_9]^{4-}$,[16] after which several other nine-atom group 14 Zintl clusters have been crystallographically characterised including $[Sn_9]^{3-}$, $[Ge_9]^{2-}$ and $[Ge_9]^{4-}$.[17-19] The first naked cluster anions $[Si_9]^{3-}$ and $[Si_5]^{2-}$ were structurally characterised from liquid ammonia solutions of $K_{12}Si_7$ and $Rb_{12}Si_7$, respectively.[20] These studies reveal that these nine-atom species have an overall geometry of a distorted tricapped trigonal prism or monocapped square antiprism.

1.2.2 Electron counting of nine-atom group 14 Zintl clusters

The number of valence electrons available for the known nonatetrelide cluster anions is not sufficient for localised two-centre two-electron bonding. The interactions between the group 14 elements in Zintl clusters are therefore achieved by delocalising electrons over the whole framework. This is analogous to the well-known cage-like deltahedral boranes, and as a result such Zintl ions follow the Wade-Mingos rules for electron counting and bonding.[21-23] Each group 14 element is considered to be sp^3 hybridised contributing three orbitals and two electrons to cluster bonding, and making it isolobal with the B–H unit in boranes. The other two electrons form a lone pair in an orbital which points radially away from the cluster. Wade's rules state that *closo*- (closed deltahedral clusters), *nido*- (missing one vertex), and *arachno*-clusters (missing two vertices) require 2n + 2, 2n + 4 and 2n + 6 electrons for cluster bonding, respectively. Therefore an $[E_9]^{2-}$ cluster is predicted to have *closo* geometry: a tricapped trigonal prism with D_{3h} point symmetry; and an $[E_9]^{4-}$ cluster should have *nido* geometry: a monocapped square antiprism with C_{4v} point symmetry. An $[E_9]^{3-}$ cluster anion has 2n + 3 skeletal electrons and should have a geometry halfway between *closo* and *nido*. Most of the $[E_9]^{3-}$ cluster anions exhibit a distorted tricapped trigonal prismatic structure with one or two elongated prismatic heights parallel to the three-fold axis, which gives them C_{2v} point symmetry. The only exception is the $[Sn_9]^{3-}$ anion, which has three elongated prismatic heights and displays D_{3h} point symmetry.

1.2.3 Structural features of nine-atom group 14 Zintl clusters

The cluster frameworks of nine-atom group 14 Zintl anions are rather flexible and can interconvert between different geometries without the need for extensive structural distortions.

A tricapped trigonal prism can easily transform to a monocapped square antiprism by elongating one of its trigonal prismatic edges parallel to the three-fold axis. These geometrical transformations have low energy barriers and affect the relative energies of the cluster frontier orbitals, allowing these nine-atom clusters to accommodate different numbers of valence electrons without dramatic geometric changes.

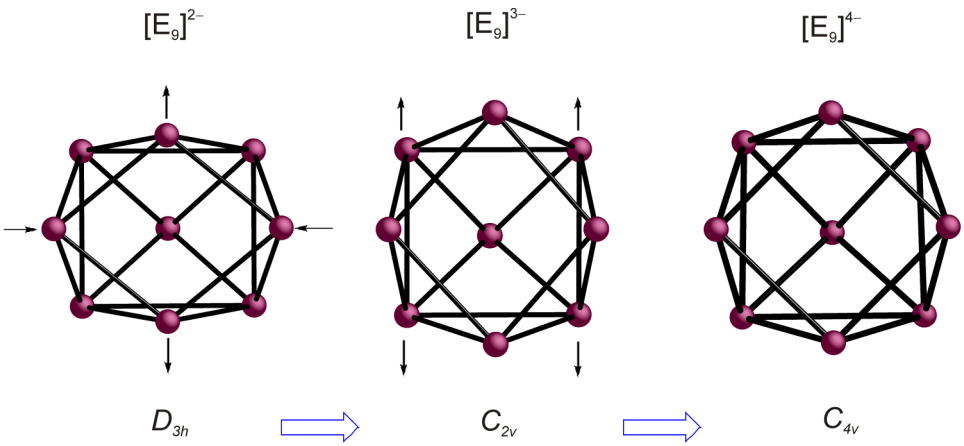

Scheme 1.1 A schematic drawing to illustrate the geometric transformation between $[E_9]^{n-}$ clusters with different overall charges.

1.2.4 Equilibria of $[E_9]^{n-}$ (n = 2 – 4) group 14 Zintl clusters in solution

As a consequence of such a flexible cluster framework, in solution the $[E_9]^{n-}$ clusters are in equilibria between different cluster charges and free solvated electrons: $[E_9]^{4-} \rightleftharpoons [E_9]^{3-} + e^- \rightleftharpoons [E_9]^{2-} + 2e^-$. A similar charge equilibrium can be observed when dissolving elemental alkali metals in either ethylenediamine or liquid ammonia: $A \rightleftharpoons A^+ + e^-$. In both cases, the free solvated electrons are capable of reacting with the solvent to produce an amide and hydrogen gas, however this is a kinetically slow process. This provides a window of opportunity and makes it viable to use amine based solvents to carry out a variety of different reactions for the nine-atom group 14 Zintl clusters.

Clusters in different oxidation states can be selectively crystallised from solution. This has been extensively studied in the case of the nonagermanide cluster-cages. This is achieved either by varying the amount of metal cation sequestering agents in solution or using metal cations that do not fit in the sequestering agent cavities in the case of mixed-cation Zintl phases. The size of the cryptated $[K(2,2,2\text{-crypt})]^+$ cation is much bigger than the naked metal cation K^+. If the potassium cations are all complexed by 2,2,2-crypt then there is not sufficient space to efficiently pack four $[K(2,2,2\text{-crypt})]^+$ around a $[Ge_9]^{4-}$ cluster, which favours the crystallisation of $[Ge_9]^{3-}$.[17, 24] If three equivalents of 2,2,2-crypt are instead used, it is possible to pack three $[K(2,2,2\text{-crypt})]^+$ cations and a naked K^+ cation around the cluster allowing for the crystallisation of $[Ge_9]^{4-}$.[25]

Another consequence of the flexible polyhedral skeleton is that the nine-atom clusters are fluxional in solution. Solution NMR experiments at –40 ºC in liquid ammonia and at 30 ºC in ethylenediamine were carried out by Rudolph and co-workers, and showed only a single resonance for the $[Sn_9]^{4-}$ cluster anion.[26] This implies that all nine vertices of the tricapped trigonal prism are equivalent on the time scale of NMR experiments, and are in rapid exchange *via* a proposed diamond-square-diamond process.

1.2.5 MO studies of nine-atom group 14 Zintl clusters

The flexible cluster geometry of the nonatetrelide cages can be accounted for by studying the electronic structure of the nine-atom Zintl clusters.[27] A frontier molecular orbital analysis of a $[Ge_9]^{4-}$ cluster with a tricapped trigonal prismatic structure, in which one of the prismatic edges has been elongated is discussed herein. The top three molecular orbitals (see Figure 1.2)

consist mainly of p_z orbitals of the germanium atoms, where the z axis coincides with the three-fold axis of the cluster. The highest energy molecular orbital (a in Figure 1.2) is the HOMO of $[E_9]^{4-}$, SOMO of $[E_9]^{3-}$ or LUMO of $[E_9]^{2-}$. This orbital is π-bonding within the triangular bases of the tricapped trigonal prism, but σ-antibonding between the two bases. Conversely the next two lower energy molecular orbitals (semi-degenerate, b and c in Figure 1.2) are π-antibonding within the triangular bases but σ-bonding between the two bases. These three top molecular orbitals are most strongly affected by any structural distortions along the three-fold symmetric axis. If the two triangular bases are pulled apart from each other along the prismatic heights, the σ-antibonding character of the LUMO of $[E_9]^{2-}$ is reduced and hence the orbital is lowered in energy. This allows electrons to populate this orbital and explains why $[E_9]^{4-}$ clusters exhibit monocapped square antiprismatic structures with C_{4v} point symmetry. This also explains the presence of an equilibrium between different charges of the cluster and free solvated electrons in solution. Such systems are well suited to accommodate different number of electrons without excessive structural distortions.

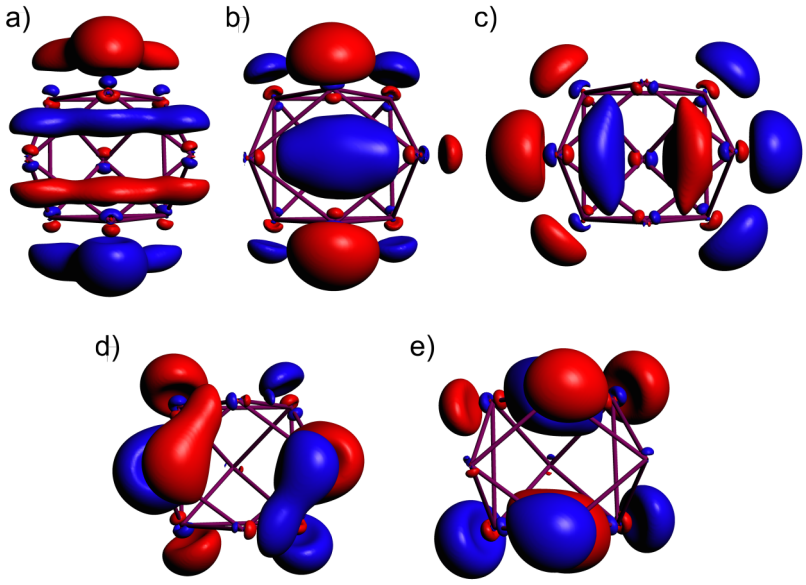

Figure 1.2 The top five MOs of a $[Ge_9]^{4-}$ cluster with an elongated prismatic edge.

1.2.6 Synthesis and characterisation of group 14 heteroatomic Zintl clusters

The synthesis of heteroatomic group 14 Zintl clusters was recently reported by the Sevov group.[28, 29] They can be formed by the direct high temperature solid state synthesis of precursors with nominal compositions $K_4Ge_{9-x}Sn_x$ (x = integer from 0 to 9), although their crystal structures have not been determined successfully due to the mixed occupancy of Ge/Sn atoms on the nine sites of the clusters in the crystal lattice. The tertiary precursors can then be extracted into solution by solvents such as ethylenediamine, pyridine, dimethyl sulfoxide (DMSO), DMF and acetonitrile, and the electrospray mass spectra of the resulting solutions show the presence of heteroatomic clusters. Alternatively they can be synthesised by dissolving mixtures of binary precursors K_4Ge_9 and K_4Sn_9 in DMSO, DMF or acetonitrile, with the presence of the heteroatomic clusters in solution again confirmed by electrospray mass spectrometry. It is interesting to note that in ethylenediamine or pyridine, mixtures of K_4Ge_9 and K_4Sn_9 only show evidence of homoatomic clusters of germanium and tin by mass spectrometry. This can be attributed to the much lower dielectric constants of these two solvents compared with those of DMSO, DMF and acetonitrile. The dielectric constant is a rough measure of the polarity of the solvent and an indication of its ability to reduce the local electric field surrounding the solute. Solvents with high dielectric constants allow charged clusters to interact more readily and directly with each other. In addition, ethylenediamine and pyridine show chelating and coordinating character, respectively, which may prevent the atom exchange required to form heteroatomic clusters.

1.3 Reactivity studies of group 14 Zintl clusters

Highly reduced nine-atom group 14 Zintl clusters have fascinating geometric and electronic properties. As mentioned earlier, in solution there exists an equilibrium between different charged clusters and free solvated electrons. A frontier molecular orbital analysis of $[E_9]^{n-}$ (n = 2 – 4) clusters suggests that they are capable of various types of bonding interactions with electrophilic reagents. The use of alkali metal cation sequestering agents can aid crystallisation of the Zintl clusters, allowing the salts to be characterised in the solid state by single crystal X-ray diffraction. These clusters are stable in solution and can be analysed by NMR spectroscopy and electrospray mass spectrometry. Si, Sn and Pb all have NMR active isotopes, which adds another spectroscopic handle to characterise the cluster compounds via multielement NMR experiments. All of the above features have prompted several research groups to study their reactivity towards a variety of different chemical reagents. The reactions can be broadly divided into four categories: 1) oxidative coupling reactions; 2) *exo*-functionalisation with main group organometallics; 3) functionalisation with transition metal organometallic fragments or naked transition metals; and 4) encapsulation of transition metals in cluster cages.

1.3.1 Oxidative coupling reactions of group 14 Zintl clusters

1.3.1.1 Interconnected $[Ge_9–Ge_9]^{6–}$ dimers

Nonagermanide cluster anions can be oxidatively coupled to form dimeric species. The mild oxidation of $LiRb_3Ge_9$ in the presence of benzo-18-crown-6 yielded the dimeric species $[Ge_9–Ge_9]^{6–}$, accompanied by two $[Rb(benzo\text{-}18\text{-}crown\text{-}6)]^+$ complexes and four naked Rb^+ metal

cations. The dimeric cluster $[Ge_9–Ge_9]^{6–}$ can also be formed from the crystallisation of a solution of $K_2Cs_2Ge_9$ with a stoichiometric deficiency of 18-crown-6.[29-31]

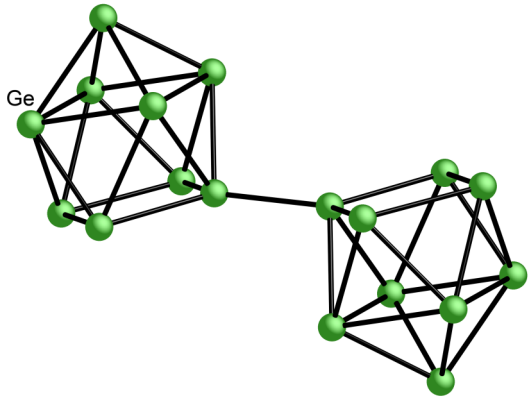

Figure 1.3 Ball and stick diagram of the anionic moiety $[Ge_9–Ge_9]^{6–}$ in the crystal structure of $[Rb(benzo\text{-}18\text{-}crown\text{-}6)]_2Rb_4[Ge_9–Ge_9]$.

These dimers consist of two nonagermanide clusters that are connected via an *exo*-bond between vertices of the open flat bases of the monocapped square antiprisms. X-ray structure determination reveals that the *exo*-bonds (2.517(2) Å) are orientated along the shorter diagonal of the square base of the antiprism. They are shorter than the delocalised bonds within the nine-atom clusters but slightly longer than the inter-atomic distance in elemental germanium, suggesting they are conventional two-centre, two-electron single bonds.

The number of skeletal electrons available for cluster bonding in each nonagermanide can be calculated as follows: the germanium atoms without *exo*-bonds each contribute 2 electrons, the site with an *exo*-bond contributes 3 electrons, and there are 3 addition electrons from half of the overall charge of the dimer. According to the Wade-Mingos rules, a nine-atom cluster with $(8 \times 2) + 3 + 3 = 22 = 2n + 4$ cluster bonding electrons should have a *nido*-structure.

Single crystal X-ray diffraction confirms that each half of the dimer has a geometry close to that of a monocapped square antiprism, the expected shape of a *nido* nine-atom cluster.

In 2006 Fässler and co-workers reported a new structure of the $[Ge_9–Ge_9]^{6–}$ dimer by extracting the solid Zintl phases A_4Ge_9 (A = K, Rb) into *N*,*N*-dimethylformamide (DMF) and then cooling the solution to a low temperature (–36 °C).[31] This results in the crystallisation of a $[Ge_9–Ge_9]^{6–}$ dimeric anion with the *exo*-bond pointing radially towards the cluster centre, alongside dimers with the structure that has been previously discussed (Figure 1.3).

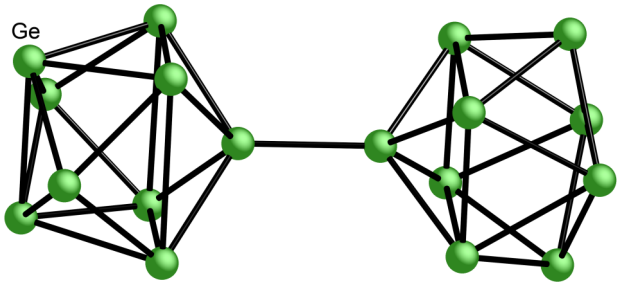

Figure 1.4 Ball and stick diagram of a second polymorph of the $[Ge_9–Ge_9]^{6–}$ dimer.

The synthesis of the dimeric species $[Ge_9–Ge_9]^{6–}$ confirms the presence of the equilibrium between group 14 Zintl clusters in different oxidation states and free solvated electrons in solution. It is believed to proceed via an oxidative coupling of two $[Ge_9]^{4–}$ clusters, where a second Ge_9 cluster is linked to the first one through a conventional two-centre two-electron single bond. The chemical bonding within each cluster still follows Wade-Mingos rules for electron counting.

1.3.1.2 A one-dimensional $_{1\infty}[Ge_9^{2-}]$ polymer

In the previously discussed $[Ge_9–Ge_9]^{6-}$ dimeric anion each nonagermanide cluster can be considered to carry a 3– charge. Upon further oxidation the nine-atom cluster can carry a 2– charge, and two different ways of inter-connecting these clusters have been observed. Firstly, they can be linked together through one *exo*-bond on each side of the cage to give a one-dimensional infinite chain of nonagermanide clusters. The two-centre two-electron bonding is analogous to that in the discrete unit $[Ge_9–Ge_9]^{6-}$, and can be viewed as a simple extension of the dimeric species. Secondly, the nine-atom clusters can also be linked together through two *exo*-bonds, yielding the trimer $[Ge_9=Ge_9=Ge_9]^{6-}$ and tetramer $[Ge_9=Ge_9=Ge_9=Ge_9]^{8-}$, which will be discussed in detail in the next section.

Reaction between K_4Ge_9 and 18-crown-6 in solvent mixtures of ethylenediamine and toluene yielded polymeric Zintl clusters of $[K(18\text{-crown-6})]_2[Ge_9]\bullet en$.[32] Single crystal X-ray diffraction studies show that the nine-atom clusters form a one-dimensional chain of vertex-linked cages with an alternating up/down arrangement. Each of the cluster units has a geometry close to that of a monocapped square antiprism, which are inter-connected through *exo*-bonds, analogous to those in the discrete dimer $[Ge_9–Ge_9]^{6-}$ anion.[29-31] These *exo*-bonds are collinear with the shorter diagonal of the open square basal plane of each antiprism. The bond lengths of the *exo*-bonds (2.486(1) Å) are very close to those of the dimer $[Ge_9–Ge_9]^{6-}$, indicating that they are all localised single Ge–Ge bonds.

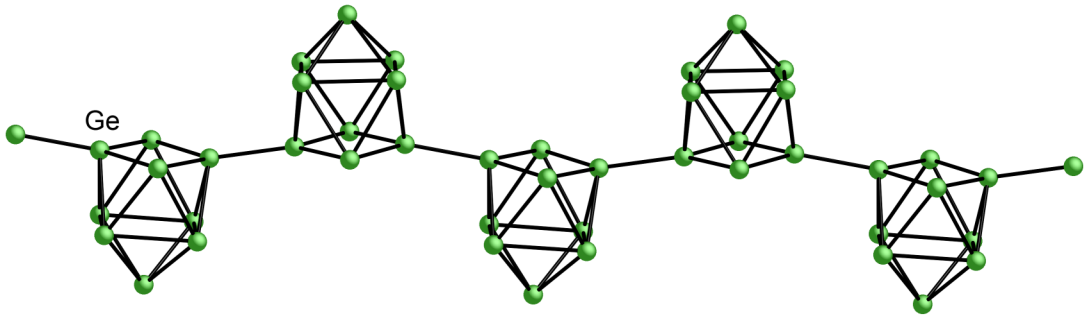

Figure 1.5 Molecular structure of the one dimensional polymeric chain $_{1\infty}[Ge_9^{2-}]$.

The number of skeletal electrons available for each cluster can be calculated as follows: the germanium atoms without *exo*-bonds contribute two electrons, those with *exo*-bonds contribute three electrons and each cluster unit carries a 2– charge. According to Wade-Mingos rules, a nine-atom cluster with (7 × 2) + (3 × 2) + 2 = 22 = 2n + 4 cluster bonding electrons should have a *nido*-structure. Single crystal X-ray diffraction experiments confirm that each of the cluster units has a monocapped square antiprismatic geometry; the expected shape of a *nido* nine-atom cluster. Overall the reaction can be described as a two-electron oxidative polymerisation of the parent *nido*-$[Ge_9]^{4-}$ Zintl cluster anion.

A similar one-dimensional polymeric chain of $_{1\infty}[Ge_9^{2-}]$ has also been reported from reactions between other solid Zintl phases and metal cation sequestering agents. Reaction of K_4Ge_9 and (2,2)diaza-18-crown-6 in solvent mixtures of ethylenediamine and toluene yielded the crystalline polymer [K((2,2)diaza-18-crown-6)][KGe_9]•3en.[33, 34] Diaza-crown ethers do not coordinate to alkali metal cations as strongly as the corresponding crown ethers. This allows direct interaction between naked K^+ cations and nonagermanide units, resulting in the formation of a polymeric chain of $_{1\infty}[(KGe_9)^-]$.

Reaction between a precursor of nominal composition Li_2RbGe_{17} and 2,1,1-crypt in solution yielded the polymer $[Rb_2(4,2,1,1\text{-crypt})][Ge_9]$•en. It consists of parallel one-dimensional chains of $_{1\infty}[Ge_9^{2-}]$ and the complexed dications $[Rb_2(4,2,1,1\text{-crypt})]^{2+}$.[34] The geometry and bonding in the chain is analogous to that of other polymeric nonagermanides. It is interesting to note that the cation sequestering agent 2,1,1-crypt undergoes a dimerisation reaction to produce a larger ring 4,2,1,1-crypt that coordinates to two Rb^+ cations at the same time. The binding is analogous to that of crown ethers, hence a significant portion of the coordination sphere of Rb^+ is exposed for additional interactions with the polymeric $[Ge_9^{2-}]$ chain.

1.3.1.3 A $[Ge_9=Ge_9=Ge_9]^{6-}$ trimer exhibiting delocalised bonding between subunits

Controlled oxidative coupling of $[Ge_9]^{4-}$ can be carried out by the addition of mild oxidising agents from group 15 such as PPh_3, $AsPh_3$ or elemental As or Sb. The reaction between Rb_4Ge_9 and $AsPh_3$ or PPh_3 in the presence of 2,2,2-crypt in ethylenediamine at 70 °C yields crystals of $[Rb(2,2,2\text{-crypt})]_6[Ge_9=Ge_9=Ge_9]$•2en.[35] When elemental As or Sb is used instead of the group 15 organometallics, the same trimeric species is synthesised, accompanied by the well known group 15 Zintl anions $[As_7]^{3-}$ and $[Sb_7]^{3-}$, respectively.

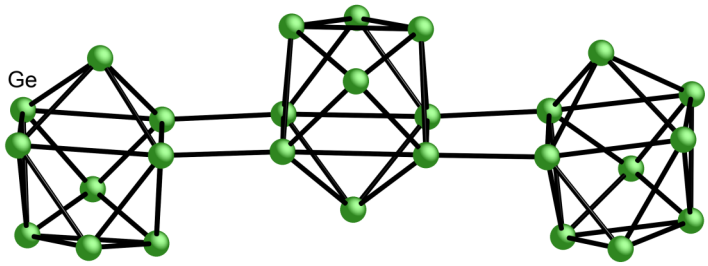

Figure 1.6 Ball and stick diagram of the trimer $[Ge_9=Ge_9=Ge_9]^{6-}$.

Single crystal X-ray structural analysis reveals that the $[Ge_9=Ge_9=Ge_9]^{6-}$ anion contains a linear row of three nonagermanide units, linked together through two *exo*-bonds between neighbouring clusters. Each cluster has tricapped trigonal prismatic geometry with two elongated prismatic heights. All four *exo*-bonds in the trimer are extensions of the elongated prismatic edges and are almost parallel to each other. These *exo*-bond lengths (approx. 2.59 Å) are significantly longer than the intercluster two-centre, two-electron single bonds in the dimers $[Ge_9–Ge_9]^{6-}$ and the polymers $_{1\infty}[Ge_9^{2-}]$ (approx. 2.49 Å).[29-34] The nine-atom clusters in the dimers and polymers are monocapped square antiprisms, and the intercluster bonds are collinear with the shorter diagonal of the open rectangular basal plane of each of the antiprism.

The differences in the bond lengths and orientation between the intercluster bonds in the trimer $[Ge_9=Ge_9=Ge_9]^{6-}$ compared to the previously discussed dimer and polymer are an important consequence of the different bonding in these systems. Fenske–Hall and extended–Hückel calculations were carried out for $[Ge_9=Ge_9=Ge_9]^{6-}$ and these showed that the 6-fold negative charge is evenly distributed among three cluster units. The intercluster bonds are not conventional two-centre, two-electron bonds, but are delocalised over the whole trimeric system. Unlike the dimer and the polymer, the trimer $[Ge_9=Ge_9=Ge_9]^{6-}$ is best described as one monolithic structure where the delocalised bonding occurs over the whole molecule.

UV-Vis spectra were recorded for an ethylenediamine solution of $[Ge_9]^{4-}$ before and after the addition of the oxidizing agents, as well as that of the crystalline product. The spectrum of the crystalline product shows three bands that are almost identical to those in the spectrum of the reaction mixture after adding the oxidizing agents. This implies that the final trimeric species

are not assembled during crystallisation, but already exist in solution after stirring the reaction mixture for a few hours.

1.3.1.4 A $[Ge_9=Ge_9=Ge_9=Ge_9]^{8-}$ tetramer exhibiting delocalised bonding between subunits

Another nine-atom germanium cluster can be added to the end of the $[Ge_9=Ge_9=Ge_9]^{6-}$ trimer with analogous chemical bonding to yield a $[Ge_9=Ge_9=Ge_9=Ge_9]^{8-}$ tetramer. 18-crown-6 was added to a saturated ethylenediamine solution of Rb_4Ge_9 at 50 °C and stirred, before being filtered, split in two test tubes, and layered with THF and toluene, respectively. This resulted in the isolation of two different crystalline products of $[Rb(18\text{-crown-6})]_8[Ge_9=Ge_9=Ge_9=Ge_9]$ packed with different numbers of solvent molecules in the crystal lattice.[36] The tetrameric cluster anions are discrete oligomers of nonagermanide clusters with a length of ~2 nm and diameter of ~0.4 nm. The K analogue $[K(18\text{-crown-6})]_8[Ge_9=Ge_9=Ge_9=Ge_9]\bullet 8en$ was synthesised under slightly different reaction conditions.[37]

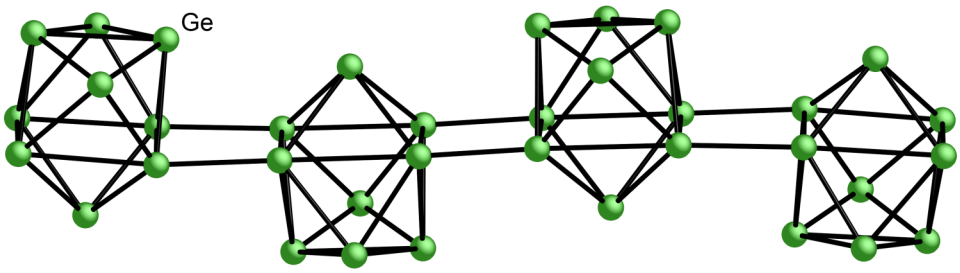

Figure 1.7 Molecular structure of the tetramer $[Ge_9=Ge_9=Ge_9=Ge_9]^{8-}$.

Analogous to the $[Ge_9=Ge_9=Ge_9]^{6-}$ trimer, all the cluster units are tricapped trigonal prisms with two elongated prismatic heights, which are linked together by pairs of *exo*-bonds. These intercluster bonds are parallel to each other and collinear with the elongated prismatic edges

of the trigonal prisms. The bond lengths of the *exo*-bonds are all longer than those of the localised Ge–Ge single *exo*-bonds in the dimers and polymers discussed previously, indicating that the bonding between cluster units is delocalised in nature.

There are eight complexed cations surrounding this linear row of four nonagermanide clusters. In each of the complexed cations, a portion of the coordination sphere of the metal centre is occupied by the 2-dimensional crown ether molecule. This leaves a significant amount of the coordination sphere of the Rb^+ cations exposed for interaction with the faces and edges of the negatively charged tetramer. Overall the packing in the crystal lattice can be described as a linear negatively charged nanorod surrounded by a sphere of charge balancing crown ether complexed alkali metal cations and solvent molecules.

DFT calculations have been carried out for a tricapped trigonal prism with two elongated prismatic heights.[38] The HOMO is made up predominantly of the p_z (z is parallel to the three-fold axis of the prism) atomic orbitals with larger contributions from the atoms of the elongated edges and one of the atoms capping a rectangular face of the prism. This molecular orbital is π-bonding within the triangular faces of the tricapped trigonal prism, and σ-antibonding between the two (see Figure 1.2). It extends along the two elongated edges outwards from the nine-atom cluster, which explains why the intercluster *exo*-bonds are all collinear with the elongated prismatic edges of the trigonal prisms. Analogously to the trimer, $[Ge_9{=}Ge_9{=}Ge_9]^{6-}$, the negative charge is evenly distributed over the entire tetramer. Both the intracluster and intercluster bonds participate in the delocalised bonding of the oligomers.

The four subunits in the tetramer have an alternating up-down-up-down confirmation. If all the clusters were to point in the same direction, they could be joined together through three *exo*-bonds along three elongated prismatic edges of the tricapped trigonal prisms. Calculations show that for oligomers with the same number of clusters, as the number of *exo*-bonds between the clusters is increased by one the overall negative charge is decreased by two.[27, 39] Therefore the proposed triply inter-connected species [Ge_9≡Ge_9≡Ge_9≡Ge_9] is expected to have a negative charge of 6−. So far there has been no report of this species in the literature, which may be attributed to the relatively low charge-to-size ratio.

1.3.2 Reactions between group 14 Zintl clusters and main group reagents

1.3.2.1 Reactions with homoleptic organometallic reagents of group 15

The discovery of the dimers, trimers, tetramers and one-dimensional polymer chains of nonagermanide clusters had important consequences for Zintl chemistry. They confirmed the unique geometric and electronic properties of Zintl cluster anions in solution. By analogy, one would expect a similar behaviour for other group 14 nine-atom Zintl clusters anions. The formation of the oligomers of [Ge_9] shows that these highly reduced clusters can undergo mild oxidation to give oligomerised *exo*-bonded species. This has prompted several research groups to explore the possibility of forming similar covalent bonds to the nonatetrelide clusters with other functional groups.

The solution reactivity of $[Ge_9]^{4-}$ cluster anions towards the group 15 homoleptic organometallics $SbPh_3$ and $BiPh_3$ was studied by the Sevov group.[40, 41] The reactions were performed by addition of the organometallic reagent to ethylenediamine solutions of the

precursor and 2,2,2-crypt. In the case of $SbPh_3$, subsequent crystallisation resulted in the isolation of a range of *exo*-functionalised Zintl clusters. Depending on the specific reaction conditions, the disubstituted clusters $[Ph–Ge_9–SbPh_2]^{2–}$, $[Ph_2Sb–Ge_9–SbPh_2]^{2–}$, and the disubstituted dimer $[Ph_2Sb–Ge_9–Ge_9–SbPh_2]^{4–}$ could be obtained, alongside crystals of $[K(2,2,2\text{-crypt})]_2[Ge_9]$ and $[K(2,2,2\text{-crypt})]_6[Ge_9–Ge_9]\bullet 0.5en$. The analogous reaction with $BiPh_3$ yields a disubstituted cluster $[Ph_2Bi–Ge_9–BiPh_2]^{2–}$, which is isostructural with the antimony analogue. The ^1H NMR spectrum of the reaction products of K_4Ge_9 and $SbPh_3$ show the presence of phenyl groups in all three functionalised clusters, as well as resonances arising from $SbPh_3$ and $[SbPh_2]^–$. This implies all these species coexist in solution and that which one of the complexes is crystallised depends on the specific reaction conditions.

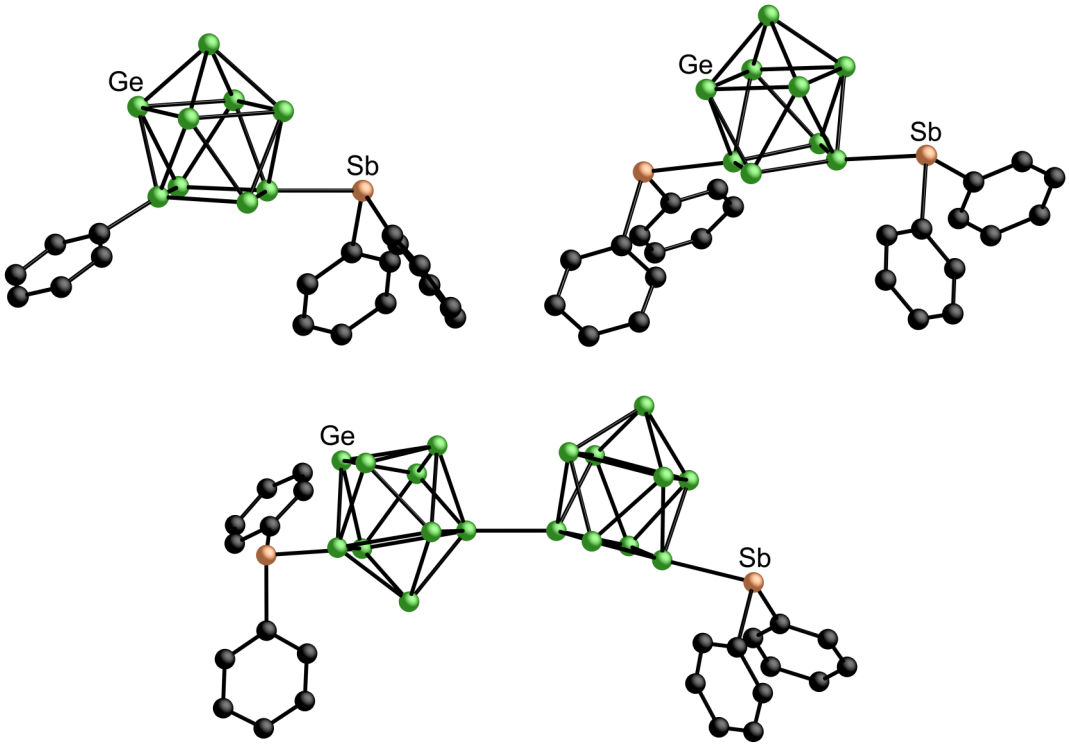

Figure 1.8 Molecular structures of the different *exo*-functionalised cluster anions obtained from the reaction of $[Ge_9]^{4–}$ with $SbPh_3$. The anions have been omitted for clarity.

All the nine-atom frameworks in the above disubstituted dimeric clusters can be described as tricapped trigonal prisms with one elongated prismatic height. The covalent *exo*-bonds to the organometallic substituents are all extensions of the elongated edges of the clusters. For the disubstituted dimer $[Ph_2Sb–Ge_9–Ge_9–SbPh_2]^{4–}$, each nine-atom cluster acts as a ligand to the other cluster through an *exo*-bond along the elongated prismatic edge. This makes the *exo*-bonds in the disubstituted dimer collinear with two elongated Ge–Ge bonds resulting in a linear row of six atoms.

A closer look at the bond lengths of all the *exo*-bonds reveals that they are all conventional two-centre, two-electron single bonds. The distances of Ge–C (1.94(1) Å) and Ge–Sb (average value 2.66 Å) both compare nicely to similar single bonds in the literature, such as those observed in $GePh_4$ and $[(CH_3)_3Ge]_2Sb–Sb[Ge(CH_3)_3]_2$.[42, 43] The Ge–Ge *exo*-bonds in the disubstituted dimer are comparable to the intercluster distances in the dimer $[Ge_9–Ge_9]^{6–}$ and the polymer $_{1\infty}[Ge_9^{2–}]$, confirming that they are localised single bonds. In summary, for these functionalised clusters, the substituents are added along the elongated prismatic heights through conventional single bonds. The bonding within the nine-atom clusters remains unchanged upon *exo*-functionalisation and the skeletal electrons are delocalised over all nine atoms of the cluster cage.

DFT calculations on a tricapped trigonal prismatic naked cluster $[Ge_9]^{2–}$ with D_{3h} symmetry have been carried out, with the z axis defined in the direction parallel to the 3-fold prismatic axis. The top three frontier molecular orbitals (LUMO, HOMO and HOMO–1) are predominantly composed of p_z atomic orbitals of atoms in the triangular bases with little

contribution from the atomic orbitals of the capping positions. Both HOMO and LUMO extend outside the cluster and are able to interact with the molecular orbitals of the substituent. They are mostly concentrated at the vertices of the elongated prismatic edges, which defines the position and orientation of the *exo* bonds in the subsequently formed functionalised Zintl cluster anions.

This bonding model was confirmed by DFT calculations on a proposed monosubstituted cluster anion $[Ge_9–Ph]^{3–}$. The monosubstituted cluster anion was chosen for its simplicity and the results can be easily applied to other *exo*-functionalised Zintl clusters. The HOMO of $[Ge_9–Ph]^{3–}$ (a in Figure 1.9) mostly resembles the LUMO of naked cluster $[Ge_9]^{2–}$ and is slightly perturbed as a result of the addition of the phenyl group. The HOMO of the naked cluster is strongly stabilised upon functionalisation and is similar to the HOMO–9 of $[Ge_9–Ph]^{3–}$ (d in Figure 1.9). The HOMO–2 molecular orbital of $[Ge_9–Ph]^{3–}$ (c in Figure 1.9) predominantly originates from the HOMO–1 molecular orbital of the naked cluster $[Ge_9]^{2–}$. The energy difference between these frontier orbitals is small, which suggests the possibility of a similar charge equilibrium between functionalised clusters at different oxidation states and free solvated electrons, such as $[Ge_9–Ph]^{3–} \rightleftharpoons [Ge_9–Ph]^{2–} + e^{–} \rightleftharpoons [Ge_9–Ph]^{–} + 2e^{–}$.

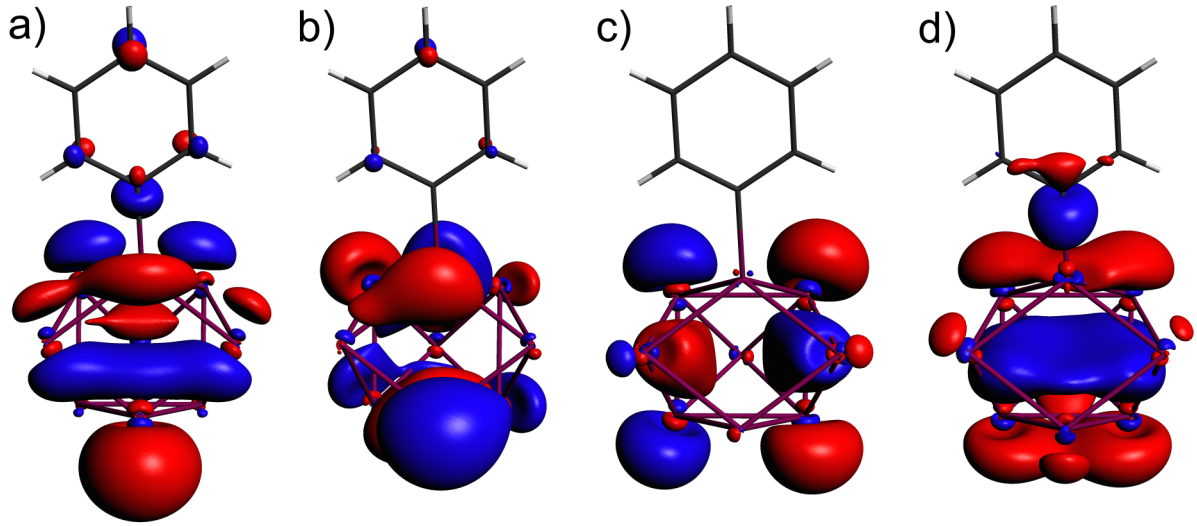

Figure 1.9 Selected molecular orbitals for the hypothetical species $[Ge_9\text{-}Ph]^{3-}$: a) HOMO, b) HOMO–1, c) HOMO–2 and d) HOMO–9.

As mentioned above, all three functionalised clusters, unreacted $SbPh_3$ and $[SbPh_2]^-$ anions coexist in the solution of reaction mixture, and the complex crystallised depends on the specific reaction conditions. This observation can be explained by studying the reaction mechanism in detail. The free solvated electrons can react with the organometallic reagent $SbPh_3$ to give Ph^- and a radical species $^{\bullet}SbPh_2$. The Ph^- anion is very basic and rapidly abstracts a proton from the solvent to form benzene. The radical $^{\bullet}SbPh_2$ picks up a free electron and subsequently becomes an anionic species $[SbPh_2]^-$, however its presence is difficult to confirm by NMR spectroscopy due to the presence of many other phenyl group containing species in solution. Despite this ambiguity, a similar anion $[SnPh_3]^-$ has been observed by ^{119}Sn NMR experiment in a related reaction between $[Ge_9]^{4-}$ and $SnPh_4$, which indirectly implies the presence of such nucleophilic anions in the reaction mixture. The nucleophile $[SbPh_2]^-$ can either donate an electron to the LUMO of $[Ge_9]^{2-}$ or to the half occupied HOMO of the radical cluster $[^{\bullet}Ge_9]^{3-}$ to yield $[Ph_2Sb\text{–}Ge_9]^{3-}$ or $[Ph_2Sb\text{–}^{\bullet}Ge_9]^{4-}$,

which can subsequently release an electron to give $[Ph_2Sb–Ge_9]^{3–}$. This monosubstituted cluster most likely has the same charge equilibrium in solution, as illustrated by $[Ph_2Sb–Ge_9]^{3–} \rightleftharpoons [Ph_2Sb–^{\bullet}Ge_9]^{2–} + e^– \rightleftharpoons [Ph_2Sb–Ge_9]^– + 2e^–$. They can either react further in a similar fashion with a second nucleophile $[SbPh_2]^–$ to form the disubstituted cluster $[Ph_2Sb–Ge_9–SbPh_2]^{2–}$, or alternatively they can couple with themselves to produce the disubstituted dimer $[Ph_2Sb–Ge_9–Ge_9–SbPh_2]^{4–}$.

In summary, the reactions between K_4Ge_9 and the group 15 organometallic reagents $SbPh_3$ and $BiPh_3$ can be described as a nucleophilic addition of $[SbPh_2]^–$ or $[BiPh_2]^–$ to a vertex of the elongated prismatic edge of the nine-atom cluster. Effectively, a lone pair of electrons on the Ge vertex is replaced with a conventional single bond between Ge and the substituent, yielding the *exo*-functionalised group 14 Zintl clusters. It is interesting to note that the analogous reactions between K_4Ge_9 and lighter group 15 organometallic reagents PPh_3 and $AsPh_3$ do not result in the formation of the *exo*-functionalised clusters. Instead oxidative coupling of the parent nine-atom clusters take place to give a trimeric species $[Ge_9=Ge_9=Ge_9]^{6–}$. This perhaps is because in solution the heavier diphenylpnictides are less stable as anions and prefer to attach covalently to the clusters as ligands.

Recently the reaction between K_4Ge_9 and $SbPh_3$ has been reinvestigated by systematic variation of the reaction conditions.[44] If the reaction mixture in ethylenediamine is heated to 75 °C for 3 days it yields a dimeric species $[(SbGe_8)–(Ge_8Sb)]^{4–}$, which is isostructural and isoelectronic with the previously discussed dimeric cluster anion $[Ge_9–Ge_9]^{6–}$. The incorporation of two group 15 atoms contributes two extra electrons to cluster bonding, and

hence, reduces the overall charge by two in comparison to the group 14 homoatomic analogues. Each [$SbGe_8$] unit can be described as a monocapped square antiprism with the Sb atom occupying a vertex in the open square face. The intercluster bond in the dimer is between the two Ge atoms that are diagonally opposite the Sb atom in the square bases of both [$SbGe_8$] units. The reaction mechanism is proposed to be an exchange of cluster atoms and partial cluster decomposition of $[Ph_2Sb–Ge_9–Ge_9–SbPh_2]^{4–}$ at elevated temperatures. Analogous reactions with $BiPh_3$ under similar reaction conditions result in the formation of a similar dimeric species $[(BiGe_8)–(Ge_8Bi)]^{4–}$.

To increase the degree of exchange of the cluster atoms, a similar reaction was carried out at 100 °C for 3 days, which produced the heteroatomic Zintl cluster anion $[Sb_2Ge_7]^{2–}$. It is isostructural and isoelectronic with the homoatomic cluster $[Ge_9]^{4–}$ and the structure can be described as a tricapped trigonal prism with both of the Sb atoms at the capping positions. Again the reaction mechanism is proposed as exchange of cluster atoms and partial cluster decomposition of $[Ph_2Sb–Ge_9–SbPh_2]^{2–}$ at elevated temperatures.

Sonication of the reaction mixture between K_4Ge_9 and $SbPh_3$ in ethylenediamine for 3 days formed the functionalised heteroatomic cluster anion $[(SbGe_8)–SbPh_2]^{2–}$. This can be viewed as the intermediate species between the disubstituted cluster $[Ph_2Sb–Ge_9–SbPh_2]^{2–}$ and doubly exchanged cluster $[Sb_2Ge_7]^{2–}$. The $SbPh_2$ fragment in this new species is bonded to the Ge atom that is diagonally opposite the Sb atom in the open square face of the monocapped square antiprism, which is the same site as the second Sb atom in $[Sb_2Ge_7]^{2–}$.

This recent development in the reaction between K_4Ge_9 and $SbPh_3$ can be described as stepwise substitution of the atoms in group 14 homoatomic clusters. The dimeric species $[(SbGe_8)–(Ge_8Sb)]^{4–}$ can undergo an alkenylation reaction with $Me_3SiC{\equiv}CSiMe_3$ to produce the organically functionalised cluster $[(SbGe_8)–CH{=}CH_2]^{2–}$. Alkenylation reactions of group 14 Zintl clusters will be discussed in more detail in later sections.

1.3.2.2 Reactions with homoleptic organometallic reagents of group 14

The reactions between group 14 Zintl clusters and the group 15 homoleptic organometallic reagents $SbPh_3$ or $BiPh_3$ resulted in the synthesis and isolation of the first *exo*-functionalised clusters.[40, 41] The reaction mechanism proposed was a nucleophilic addition of $[SbPh_2]^–$ or $[BiPh_2]^–$ to the nine-atom cluster. Analogous reactions between K_4E_9 (E = Ge, Sn) and group 14 homoleptic organometallic reagents in the presence of alkali metal cation sequestering agents have also been studied in ethylenediamine solutions. They show similar reactivity towards the Zintl clusters yielding a range of *exo*-functionalised cluster anions.[45]

Reactions between K_4Ge_9 and $SnPh_4$ in ethylenediamine produced the disubstituted cluster $[Ph_3Sn–Ge_9–SnPh_3]^{2–}$. However, analogous reactions with $GePh_4$ do not give the $–GePh_3$ functionalised clusters and only result in the oxidative coupling of $[^{\bullet}Ge_9]^{3–}$. The difference in reactivity is probably due to the difference in bond dissociation enthalpy between the Sn–Ph and Ge–Ph fragments. In the case of $GePh_4$, the Ge–Ph bond is harder to break and hence it is more difficult to make the nucleophile $[GePh_3]^–$. To test this hypothesis a related compound, Ph_3GeCl, was used as an alternative reagent, which can be easily reduced to give $Cl^–$ and the nucleophile $[GePh_3]^–$. When reacted with K_4Ge_9 extensive decomposition was observed

because some of the clusters are oxidised in providing the electrons necessary for reduction of Ph_3GeCl. An excess of the Zintl clusters was therefore used and this reaction successfully formed a disubstituted dimer $[Ph_3Ge–Ge_9–Ge_9–GePh_3]^{4–}$. The reaction can be represented by the equation: $2\ Ph_3GeCl + K_4Ge_9 \rightarrow 2\ KCl + 2\ K^+ + 2\ [Ph_3Ge]^- + 9\ Ge^0$.

It is difficult to control the exact amount of cluster decomposition, and so alkali metals such as potassium have been employed as alternative reducing agents. R_3ECl (R = Ph, Me; E = Sn, Ge) and K are dissolved in ethylenediamine to generate the nucleophile $[ER_3]^-$, which is then added to an ethylenediamine solution of K_4Ge_9 and a metal cation sequestering agent. By generating the nucleophile separately, these reactions yielded a range of disubstituted clusters $[R_3E–Ge_9–ER_3]^{2–}$ as well as two monosubstituted clusters $[Ge_9–SnR_3]^{3–}$ (R = Ph, Me). Compared with the previous method of sacrificing some clusters to generate the nucleophile, this new method provides much better control of the reaction and helps to confirm the proposed nucleophilic addition reaction pathway. The monosubstituted cluster $[Ge_9–SnR_3]^{3–}$ results from addition of one nucleophile to the cluster and represents a stable intermediate of this nucleophilic addition to group 14 Zintl clusters.

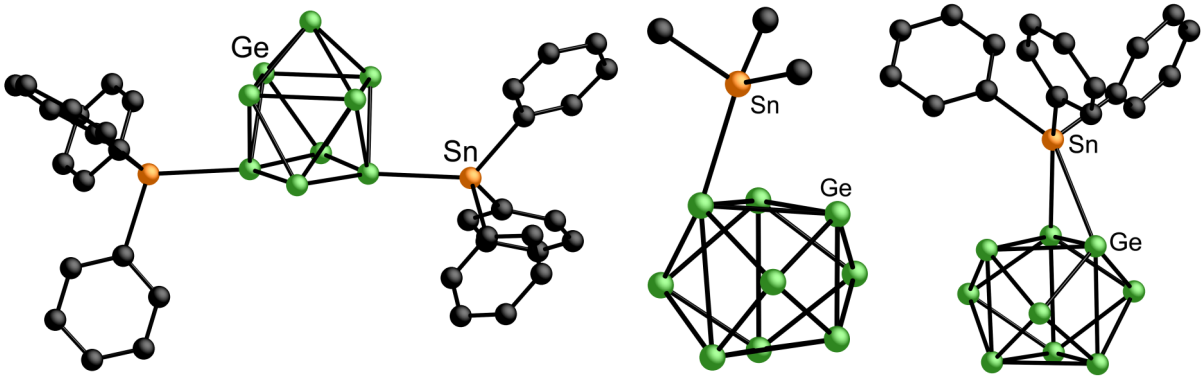

Figure 1.10 Molecular structures of $[Ph_3Sn–Ge_9–SnPh_3]^{2–}$, $[Ge_9–SnMe_3]^{3–}$ and $[Ge_9–SnPh_3]^{3–}$.

These *exo*-functionalised Zintl clusters have similar structures to the analogous $SbPh_2$ and $BiPh_2$ functionalised clusters discussed previously. All the nine-atom clusters in the products are tricapped trigonal prisms with one or two elongated prismatic edges parallel to the 3-fold axis. The covalent *exo*-bonds are extensions of the elongated prismatic edges of the clusters. The structures of the two monosubstituted clusters $[Ge_9–SnR_3]^{3–}$ (R = Ph, Me) are slightly different to the disubstituted clusters. In the anion $[Ge_9–SnPh_3]^{3–}$, the tin atom bridges between two germanium atoms at two elongated prismatic edges of the nine-atom cluster. When the phenyl group is replaced by a methyl group in the anionic species $[Ge_9–SnMe_3]^{3–}$ the tin atom is bonded to only one germanium atom at one elongated prismatic edge of the cluster. The Ge–Sn bond bends slightly towards the 3-fold rotation axis of the tricapped trigonal prism.

Almost all the *exo*– and the intercluster bonds in these functionalised clusters are comparable with the reported literature values of single Ge–Sn and Ge–Ge bonds.[46, 47] The only exceptions are the two *exo* bonds in the monosubstituted cluster $[Ge_9–SnPh_3]^{3–}$, which are three-centre, two-electron delocalised bonds and therefore significantly longer than the single Ge–Sn bond distances. The electronic structures of these functionalised Zintl clusters are analogous to those of the $SbPh_2$ or $BiPh_2$ functionalised clusters that have been discussed in section **1.3.2.1**.

In summary, the reactions between group 14 Zintl clusters and group 14 and 15 homoleptic organometallic reagents proceed *via* nucleophilic addition to vertices at elongated edges of the distorted tricapped trigonal prisms. The resulting *exo*– and intercluster bonds are mostly

conventional single bonds, with the exception of $[Ge_9–SnPh_3]^{3–}$, and there is little change in geometry and chemical bonding within the nine-atom deltahedral clusters.

1.3.2.3 Alkylation and alkenylation of group 14 Zintl clusters

The *exo*-functionalisation of clusters described in the previous sections opened up a new area of Zintl chemistry and suggested that these highly reduced clusters could be functionalised by purely organic substituents. The success in functionalising nine-atom Zintl clusters with group 14 organohalides such as Ph_3GeCl prompted research investigating analogous reactions with carbon-based functional groups. This resulted in the isolation and characterisation of a range of functionalised Zintl clusters with various organic group substituents through alkylation and alkenylation reactions.

1.3.2.3.1 Alkylation of group 14 Zintl clusters

The reaction between K_4Ge_9 and RCl (R = ^{t}Bu (t-butyl), ^{s}Bu (sec-butyl), ^{n}Bu (n-butyl), ^{t}Am (t-amyl)) in the presence of alkali metal cation sequestering agents in ethylenediamine yields the disubstituted dimers $[R–Ge_9–Ge_9–R]^{4–}$.[48] All the dialkylated dimers of the nonagermanide cages have had their presence in solution confirmed using electrospray mass spectrometry, and for R = ^{t}Bu the *exo*-functionalised cluster has also been characterised by ^{1}H and $^{13}C\{^1H\}$ NMR spectroscopy and as the $[K(2,2,2\text{-crypt})]^+$ salt by single crystal X-ray diffraction.

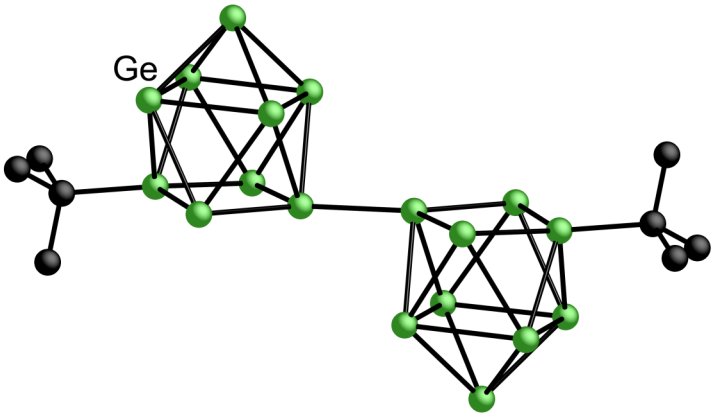

Figure 1.11 Ball and stick diagram of the disubstituted dimer [^{t}Bu–Ge$_9$–Ge$_9$–^{t}Bu]$^{4-}$.

The crystal structure of [^{t}Bu–Ge$_9$–Ge$_9$–^{t}Bu]$^{4-}$ is analogous to the previously discussed cluster anion [Ph$_3$Sn–Ge$_9$–Ge$_9$–SnPh$_3$]$^{4-}$ and similar to the –SbPh$_2$ disubstituted dimer.[40, 45] The nine-atom clusters are tricapped trigonal prisms with one elongated prismatic edge. The substitution happens at the vertices of the elongated edge and both the Ge–C and intercluster Ge–Ge bonds are collinear with this elongated edge. A detailed analysis of interatomic distances shows that the *exo* Ge–C and intercluster Ge–Ge bonds are all single bonds.

As with the other disubstituted dimers the clusters in [^{t}Bu–Ge$_9$–Ge$_9$–^{t}Bu]$^{4-}$ follow Wade-Mingos rules and have 22 = 2*n* + 4 skeletal electrons for cluster bonding, confirming a *nido*-structure. This is consistent with the structure obtained from single crystal X-ray diffraction. Starting from a nine-atom cluster with a 4– charge, every time a lone pair of electrons of a vertex is replaced with a single *exo*-bond, the overall charge of the cluster is reduced by one. In the case of the disubstituted dimers, each of clusters has two substituents, leading to an overall negative charge of two.

Electrospray mass spectrometry has proven to be a very useful tool to characterise Zintl clusters in solution. The elements present in the clusters have a multitude of naturally occurring isotopes which results in mass envelopes with distinct distribution patterns, allowing a given cluster anion to be identified and assigned unequivocally. However, the relatively high cone voltage in the ionising process can lead to electrochemical fragmentation as well as reduction of the overall charge of these highly reduced species. For example, in the case of $[^{t}Bu–Ge_9–Ge_9–^{t}Bu]^{4–}$ the monoanion of the monoalkylated monomer $[Ge_9–^{t}Bu]^{–}$ is observed in the negative ion mode mass spectrum. This cluster anion results from a single substitution of the nine-atom cluster and is analogous to the intermediate $[Ge_9–SnR_3]^{3–}$ (R = Ph, Me) in the nucleophilic addition reaction between K_4Ge_9 and SnR_3Cl. The negative ion mode electrospray mass spectra of other $[R–Ge_9–Ge_9–R]^{4–}$ clusters all show mass envelopes for both $[Ge_9–R]^{–}$ (major product) and $[R–Ge_9–R]^{–}$.

The ^{1}H and $^{13}C\{^{1}H\}$ NMR spectra of the disubstituted cluster $[^{t}Bu–Ge_9–Ge_9–^{t}Bu]^{4–}$ were recorded for both the pure, crystalline phase and the reaction mixture before crystallisation. They reveal sharp resonances corresponding to the ^{t}Bu groups in both $[^{t}Bu–Ge_9–Ge_9–^{t}Bu]^{4–}$ (major product) and $[^{t}Bu–Ge_9–^{t}Bu]^{2–}$. The single set of predominant peaks for $[^{t}Bu–Ge_9–Ge_9–^{t}Bu]^{4–}$ indicates the disubstituted dimer stays largely intact in solution.

The reaction mechanism presumably involves reduction of the alkyl halides by the free solvated electrons in solution to form organic radicals and halide anions. The radicals can then interact with the low-lying LUMO of $[Ge_9]^{2–}$ and the singly occupied HOMO of $[Ge_9]^{3–}$ clusters to form conventional two-centre, two-electron single bonds. The interaction with the

frontier molecular orbitals of the cluster is similar to that of the nucleophilic addition to the Zintl clusters by group 14 and 15 organometallic reagents.[40, 41, 45] The appearance and distribution of the cluster based molecular orbitals defines the position and orientation of the resulting *exo*-bonds.

The reactivity of group 14 Zintl polyatomic anions towards organic halides is not limited to germanium clusters, but is also feasible for the heavier analogues. K_4Sn_9 reacts with tertiary alkyl halides such as ^{t}BuCl in the presence of 2,2,2-crypt in ethylenediamine to yield the monosubstituted cluster anion $[Sn_9–^tBu]^{3-}$.[49] Recrystallisation of the product from pyridine afforded single crystals of the monoalkylated clusters, which show a similar geometry to that of the germanium analogue. The negative ion mode electrospray mass spectrum of the reaction mixtures before crystallisation reveals the presence of monoanions of both the mono- and di-alkylated species. The mass spectra of analogous reactions between K_4Sn_9 and primary and secondary alkyl halides (^{n}BuCl and ^{s}BuCl) are almost identical to that obtained for ^{t}BuCl, suggesting that analogous alkylated clusters have been synthesised.

1.3.2.3.2 Alkenylation of group 14 Zintl clusters

In addition to the reactions with organic halides, nine-atom group 14 germanium clusters have also been found to show reactivity towards a range of alkynes such as FcC≡CH (Fc = ferrocenyl) and PhC≡CPh.[50] These bond to the clusters as alkenes, following a partial hydrogenation of the unsaturated bond in ethylenediamine. All the resultant products have been characterised in solution by electrospray mass spectrometry. Additionally one of the functionalised clusters: $[Fc–CH=CH–Ge_9–CH=CH–Fc]^{2-}$ has been characterised by single

crystal X-ray diffraction experiments and ^{1}H NMR spectroscopy. This represents a new route to attaching organic functionalities to the highly reduced Zintl clusters and expands the area of organo-Zintl chemistry.

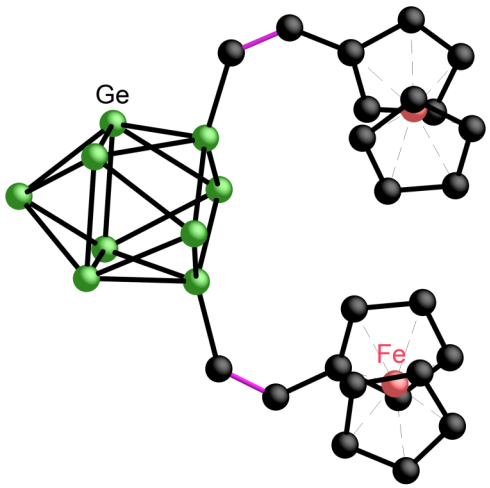

Figure 1.12 Structure of the functionalised cluster $[Fc–CH=CH–Ge_9–CH=CH–Fc]^{2–}$.

Crystallographic studies of the disubstituted cluster anion $[Fc–CH=CH–Ge_9–CH=CH–Fc]^{2–}$ show that the nine-atom framework has the geometry of a tricapped trigonal prism with one elongated prismatic edge. The substituents attach to the vertices of the elongated prismatic heights and the *exo* Ge–C bond lengths (1.967(4) and 1.927(8) Å) are comparable to that in $[Ph–Ge_9–SbPh_2]^{2–}$.[40] This indicates that the bonding is analogous to that of the previously discussed *exo*-functionalised Zintl clusters: the interaction within the nine-atom cluster is delocalised and the *exo*-bond is a conventional two-centre, two-electron covalent bond.

It is interesting to note that the cluster and the ferrocenyl substituents are in *cis* geometry at the double bond, which puts the two substituents very close to each other. The solution ^{1}H NMR spectrum of the disubstituted cluster $[Fc–CH=CH–Ge_9–CH=CH–Fc]^{2–}$ shows a small

coupling constant of 13 Hz between the two protons in the –CH=CH– fragment, confirming the *cis* geometry of the two substituents. The confirmation is retained even in solution and there is no *trans* isomer observed in the proton NMR spectrum.

The negative ion-mode electrospray mass spectrum of crystals of $[Fc–CH=CH–Ge_9–CH=CH–Fc]^{2–}$ with $[K(18\text{-crown-6})]^+$ countercations in DMF solutions shows mass envelopes corresponding to the disubstituted cluster, the disubstituted cluster / K^+ ion pair and also the cluster / $[K(18\text{-crown-6})]^+$ ion pair. All these species are observed as monoanions due to the ionisation process occurring in the mass spectrometer. If the reaction mixture is introduced to the mass spectrometer before crystallisation without the presence of any cation sequestering agent, the monosubstituted cluster $[Fc–CH=CH–Ge_9]^{3–}$ is also observed with a charge of –1.

Analogous reactions between K_4Ge_9 and similar alkynes have yielded a range of monosubstituted and disubstituted clusters, which have been characterised in solution by electrospray mass spectrometry. The reaction mixtures are introduced to the mass spectrometer before crystallisation without the presence of any cation sequestering agent. Both the monosubstituted and disubstituted cluster anions have been observed.

Analogous alkenylation of nonastannide clusters with $Me_3Si–C\equiv C–SiMe_3$ and $Ph–C\equiv CH$ have yielded the monosubstituted cluster anions $[Sn_9–CH=CH_2]^{3–}$ and $[Sn_9–CH=CHPh]^{3–}$, respectively.[49] In the $[Sn_9–CH=CHPh]^{3–}$ anion, the cluster and the phenyl group are *cis* to each other with respect to the double bond. Structurally, they adopt similar geometries to

those of the functionalised nonagermanide clusters with main group organometallic or organic groups attached through conventional two-centre two-electron bonds.

Heteroatomic Zintl clusters such as $[Ge_{9-x}Sn_x]^{4-}$ show similar reactivity towards alkynes with both terminal and internal triple bonds, yielding the first structurally characterised alkenylated heteroatomic Zintl clusters.[28] The structures of the cluster anions are similar to those of previously reported alkenylated homoatomic Zintl clusters. In addition to characterisation by single crystal X-ray diffraction, the mono- and di-substituted heteroatomic organo-Zintl clusters have also been characterised in solution by electrospray mass spectrometry.

The mechanism of the alkenylation of Zintl clusters has been proposed to be a nucleophilic addition to the triple bonds followed by hydrogenation in the presence of protic solvents. A nine-atom cluster anion $[E_9]^{4-}$ (E = group 14 element) acts as a nucleophile, attacking the empty π^* orbital of a triple bond at the more electropositive site to form an organic radical anion and $[E_9]^{3-}$. The two anions then rapidly combine to form an anionic species with a carbanionic centre, which is very basic and can readily abstract a proton from ethylenediamine. In most of the structurally characterised alkenylated cluster anions, the cluster and proton are predominantly added in an anti conformation across the triple bond. The first example of the minor, trans isomer $\{[Ge_2Sn_7]HC{=}CHPh\}^{3-}$ was isolated and structurally characterised by the Sevov group, in which the cluster and proton are in a syn geometry across the triple bond.[28] This supports the nucleophilic addition mechanism and indicates that both conformations are possible. In summary, the alkenylation of group 14 Zintl clusters follows a stereoselective and regioselective reaction pathway.

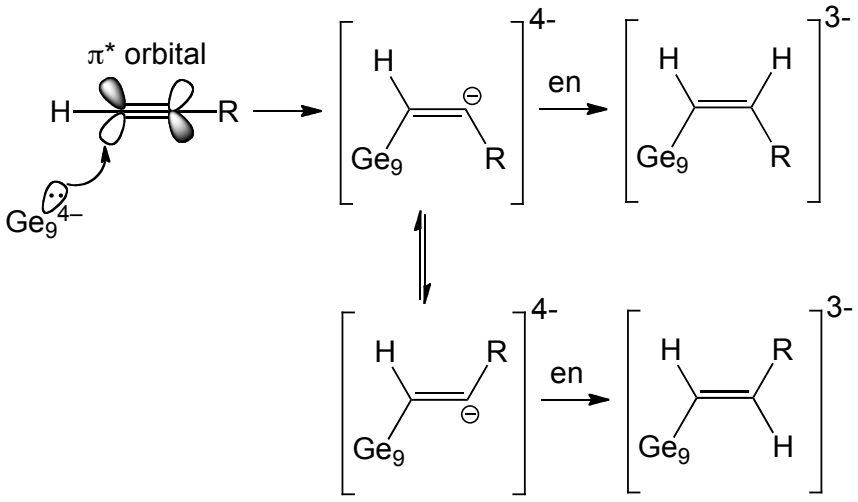

Scheme 1.2 Reaction pathway of the formation of two different isomers.

1.3.2.4 Remarks

Redox reactions of nine-atom Zintl clusters with various main group organometallic reagents, organic halides and alkynes have yielded a range of *exo*-functionalised clusters through two-centre, two-electron bonds. In solution these highly reduced Zintl clusters exist in equilibrium between different oxidation states and free electrons. One electron is required to reductively cleave the weak chemical bond in organometallic reagents, hence each addition to the cluster is accompanied with unit reduction of the overall charge. However, there is no change in the total number of skeletal electrons because when one vertex is bonded to the substituent via a single bond, one extra valence electron is contributed to cluster bonding, which compensates for the decrease in the overall charge. As a result there is no change in nuclearity, the geometry or chemical bonding in the nine-atom clusters of the functionalised species.

1.3.3 Group 14 Zintl ions as ligands in transition metal complexes

1.3.3.1 Reactions with mid transition metal organometallic reagents $LM(CO)_3$

The first structurally characterised transition metal functionalised group 14 Zintl cluster was $[Sn_9Cr(CO)_3]^{4-}$ reported by Pennington et al.[51] The product $[K(2,2,2\text{-crypt})]_4[Sn_9Cr(CO)_3]$ could be obtained by reacting a toluene solution of $Cr(CO)_3$(mesitylene) with an ethylenediamine solution of the K_4Sn_9 precursor in the presence of 2,2,2-crypt. Single crystal X-ray diffraction experiment showed that the anionic cluster is a bicapped square antiprism with the Cr atom occupying one of the capping positions.

Electronically, the negatively charged cluster is made up of a $[Sn_9]^{4-}$ cluster and a neutral organometallic fragment, $Cr(CO)_3$, which contributes no electrons to cluster bonding. According to Wade-Mingos rules, a ten-vertex cluster with a total of 22 skeletal electrons is expected to have a *closo*-structure, which is the observed geometry of the product. From the point of view of the Cr containing organometallic fragment, it achieves an 18-electron configuration by combining the six valence electrons from the Cr centre, six electrons from three carbonyl groups and six electrons from the η^4 coordinated cluster. The compound contains carbonyl groups and was also characterised by IR spectroscopy. The low frequency of the CO bands in the IR spectrum and long C≡O bond distances suggest extensive metal to CO π back-donation.

Several other examples of the *closo*-$[Sn_9M(CO)_3]^{4-}$ (M = Cr, Mo, W) Zintl cluster anions have also been reported by the Eichhorn group using similar reaction conditions.[52-54]

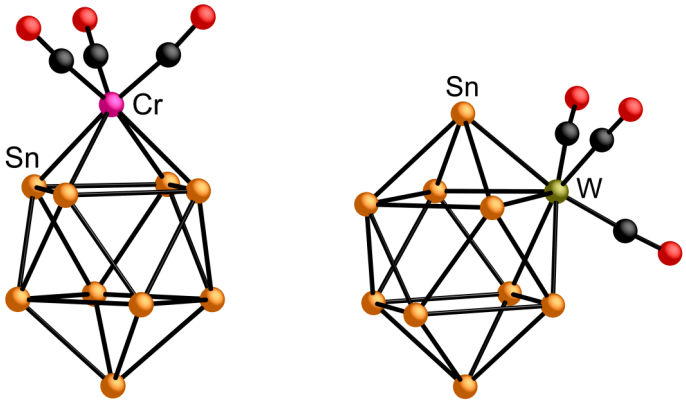

Figure 1.13 Ball and stick diagram of the cluster anions $[(\eta^4\text{-}Sn_9)Cr(CO)_3]^{4-}$ and $[(\eta^5\text{-}Sn_9)W(CO)_3]^{4-}$.

Single crystal X-ray structural analysis showed that $[(\eta^4\text{-}Sn_9)Cr(CO)_3]^{4-}$ and $[(\eta^4\text{-}Sn_9)Mo(CO)_3]^{4-}$ are isomorphic and best described as bicapped square antiprisms with the $M(CO)_3$ fragments occupying the capping position.[51-54] Conversely, in the cluster anion $[(\eta^5\text{-}Sn_9)W(CO)_3]^{4-}$ the tungsten atom coordinates to five tin atoms, occupying a waist position of the bicapped square antiprismatic structure.[53] In a subsequent publication the Schrobilgen group reported the isolation and characterisation of the η^4-coordinated species $[K(2,2,2\text{-crypt})]_4[(\eta^4\text{-}Sn_9)W(CO)_3]\bullet en$ under slightly different reaction conditions.[54] As discussed above all these cluster anions have 22 cluster bonding electrons and follow the Wade-Mingos electron counting rules for a *closo*-structure.

Solid state IR spectroscopic studies of these compounds have been carried out, and display characteristic bands corresponding to the C–O stretching mode of carbonyl groups. The absorption frequencies of the CO stretching vibrations (1681 – 1830 cm^{-1} for $[(\eta^4\text{-}E_9)M(CO)_3]^{4-}$, where E = Sn, Pb; M = Mo, W) indicate there is strong metal to ligand back

donation. The spectra of several crystalline samples of $[Sn_9W(CO)_3]^{4-}$ salts by the Eichhorn group showed the presence of CO bands corresponding to both η^4 and η^5 configuration in ratios that vary from 1:2 to 2:1. The two isomers are in equilibrium in solution and the ratios in the crystalline products depend on their relative rates of nucleation.

The *closo*-$[(\eta^4\text{-}Sn_9)M(CO)_3]^{4-}$ (M = Cr, Mo, W) anions were studied comprehensively in liquid ammonia solutions by ^{119}Sn and ^{117}Sn NMR spectroscopy by the Schrobilgen group.[54] Both of the high resolution spectra showed three resonances in a 1:4:4 intensity ratio, indicating the functionalised clusters are rigid and retain their η^4 coordination mode in solution. This is in contrast with the parent *nido*-$[Sn_9]^{4-}$ anion, which shows only a single resonance in the ^{119}Sn NMR spectra, implying a rapid fluxionality of all nine vertices.[26] All ^{119}Sn resonances of the $[(\eta^4\text{-}Sn_9)M(CO)_3]^{4-}$ anions are deshielded relative to that of the $[Sn_9]^{4-}$ precursor, suggesting electron transfer from the negatively charged nonastannide cage to the transition metal fragment. The most deshielded ^{119}Sn and ^{117}Sn NMR resonances correspond to the apical Sn atom, whereas the least deshielded ones correspond to the vertices in the square plane capped by the apical tin atom. This observation can be explained by the atomic charges and valences and the bond orders in the cluster, which are calculated by computational methods. All the experimental ^{119}Sn and ^{117}Sn NMR resonances have been simulated using the program ISOTOPOMER.

In 2005 Fässler and co-workers reported the first example of pure $[K(2,2,2\text{-crypt})]_4[(\eta^5\text{-}Pb_9)Mo(CO)_3]$ by reacting the precursor K_4Pb_9 with $[Mo(CO)_3(MeCN)_3]$ in the presence of 2,2,2-crypt in a mixture of ethylenediamine and toluene.[55] If the Zintl precursor is reacted with

$[Mo(CO)_3(mesitylene)]$ instead, a mixture of both η^4 and η^5 isomers is obtained under exactly the same reaction conditions. The coordination number of Mo atom to the cluster affects the degree of metal to CO back bonding, which subsequently shifts the stretching frequencies of the carbonyl bands. This makes the solid state IR studies of these clusters a diagnostic method of checking the purity of the product and of identifying the isomeric form (η^4 or η^5) present.

1.3.3.2 Reactions with the late transition metal organometallic reagent $[Ir(COD)Cl]_2$

Ethylenediamine solutions of K_4E_9 (E = Sn, Pb) react with toluene solutions of $[Ir(COD)Cl]_2$ (COD = 1,5-cyclooctadiene) in the presence of 2,2,2-crypt to yield the *closo*-$[E_9Ir(COD)]^{3-}$ cluster.[56] The reaction proceeds via the formation of Cl^- and the electrophilic $[Ir(COD)]^+$ fragment, which subsequently attacks the electron-rich $[E_9]^{4-}$ clusters at the open square base of the monocapped square antiprism. The $[K(2,2,2\text{-crypt})]^+$ salts of the functionalised clusters have been characterised by single crystal X-ray diffraction and ^1H and ^{13}C NMR spectroscopy.

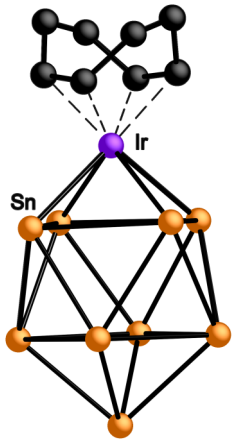

Figure 1.14 Molecular structure of the cluster anion $[Sn_9Ir(COD)]^{3-}$, in which the iridium atom is coordinated to the COD ligand in a η^4 fashion.

Single crystal X-ray structural analysis of the *closo*-$[E_9Ir(COD)]^{3-}$ (E = Sn, Pb) clusters shows that they both adopt bicapped square antiprismatic geometries, with the Ir atom occupying one of the capping positions. The transition metal fragment is coordinated to the group 14 nine-atom cluster in a η^4 fashion and overall the framework has pseudo C_{4v} symmetry. Electronically, they follow the Wade-Mingos rules and are best described as 10-vertex *closo*-structures with 22 skeletal electrons, because the $[Ir(COD)]^+$ unit does not donate any electrons to cluster bonding. This makes the clusters isostructural and isoelectronic with the previously discussed $[E_9M(CO)_3]^{4-}$ (E = Sn, Pb; M = Cr, Mo, W) species.

Due to the organic group attached to the functionalised clusters, they have also been characterised in solution by ^1H and ^{13}C NMR spectroscopy. The ^1H NMR spectra display three resonances due to three distinct proton environments in the COD ligand, in addition to the resonances for $[K(2,2,2\text{-crypt})]^+$. The proton coupled ^{13}C NMR spectra show a doublet and a triplet due to two distinct carbon environments in the COD ligand and also resonances for $[K(2,2,2\text{-crypt})]^+$. Relative to the starting reagent $[Ir(COD)Cl]_2$, the carbon resonances for the COD ligand in the functionalised clusters are more deshielded. This is attributed to the strong metal to ligand back donation between the filled Ir *d* atomic orbitals and the empty π^* antibonding molecular orbitals of the COD ligand. The lengthening of C=C bonds compared to those in other Ir^I-COD complexes has also confirmed the weakening of the bonds and indicates that there is significant charge transfer to the ligand.

1.3.3.3 Reactions with the post transition metal organometallic reagent $ZnPh_2$

Group 14 Zintl precursors K_4E_9 (E = Si, Ge, Sn, Pb) react with $ZnPh_2$ in the presence of 2,2,2-crypt in ethylenediamine to yield *closo*-$[E_9ZnPh]^{3-}$ cluster anions. The reactions proceed via the reductive cleavage of the Zn–Ph bond to form a $[ZnPh]^{\bullet}$ fragment and phenyl anion.[57] The $[ZnPh]^{\bullet}$ fragment is electrophilic and attacks the electron-rich $[E_9]^{3-}$ clusters to produce the functionalised $[E_9ZnPh]^{3-}$ clusters. The phenyl anion rapidly abstracts a proton from the solvent to form benzene. The $[K(2,2,2\text{-crypt})]^{+}$ salts of the homologous series of functionalised clusters have been characterised by single crystal X-ray diffraction, $^{13}C\{^{1}H\}$ NMR spectroscopy and electrospray mass spectrometry.

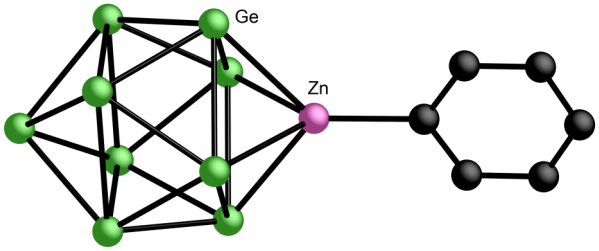

Figure 1.15 Ball and stick diagram of the anionic moiety $[Ge_9ZnPh]^{3-}$.

Single crystal X-ray structural analysis of the *closo*-$[E_9ZnPh]^{3-}$ clusters shows that the [ZnPh] fragment occupies one of the capping positions of the bicapped square antiprism. The η^4 coordination mode of the transition metal moiety to the cluster is analogous to that in the previously discussed cluster anions $[E_9M(CO)_3]^{4-}$ (E = Sn, Pb; M = Cr, Co, W) and $[E_9Ir(COD)]^{3-}$ (E = Sn, Pb).

The electronic structure of $[E_9ZnPh]^{3-}$ is analogous to deltahedral borane clusters and follows Wade-Mingos rules for a 10-vertex *closo*-cluster. Each group 14 atom is sp^3 hybridised and

donates three orbitals and two electrons to cluster bonding. The other two valence electrons of the group 14 atom form a lone pair and occupy an orbital that points radially outward from the cluster. The Zn atom uses one valence electron for *exo*-bonding with the phenyl group and donates the other valence electron for cluster bonding. Taking into account of the 3– charge of the cluster, overall there are 22 skeletal electrons and it is predicted to have a *closo* structure, which is consistent with what is observed experimentally. From the point of view of the Zn fragment, it achieves an 18-electron configuration by combining the eleven valence electrons from the Zn centre with one from the organic substituent and six electrons from the η^4 coordinated cluster.

A frontier orbital analysis shows that the Zn atom is *sp* hybridised with one of its *sp* orbitals utilized for *exo*-bonding with the phenyl group. This leaves one *sp* hybrid and two degenerate p_x and p_y orbitals of the Zn atom available for interaction with the cluster orbitals. There are three filled molecular orbitals of the cluster that have the appropriate symmetry and energy to overlap with the three Zn orbitals. One cluster orbital is predominantly made up of atomic orbitals at the four corners of the open base, which lie in the plane pointing towards the centre of the square face. It is totally bonding within the open square base and matches the symmetry of the *sp* hybrid orbital of Zn. There are two degenerate cluster orbitals that predominantly contain two out of phase p_z orbitals at the diagonally opposite ends of the open square base of the monocapped square antiprism. They overlap with the degenerate p_x and p_y orbitals of the $[ZnPh]^+$ fragment. As a result, the $[E_9]^{4-}$ cluster acts as a six-electron donor ligand when the open square base interacts with electrophiles. The same bonding model can be applied to other group 14 functionalised Zintl clusters that have an η^4-bound electrophilic moiety.

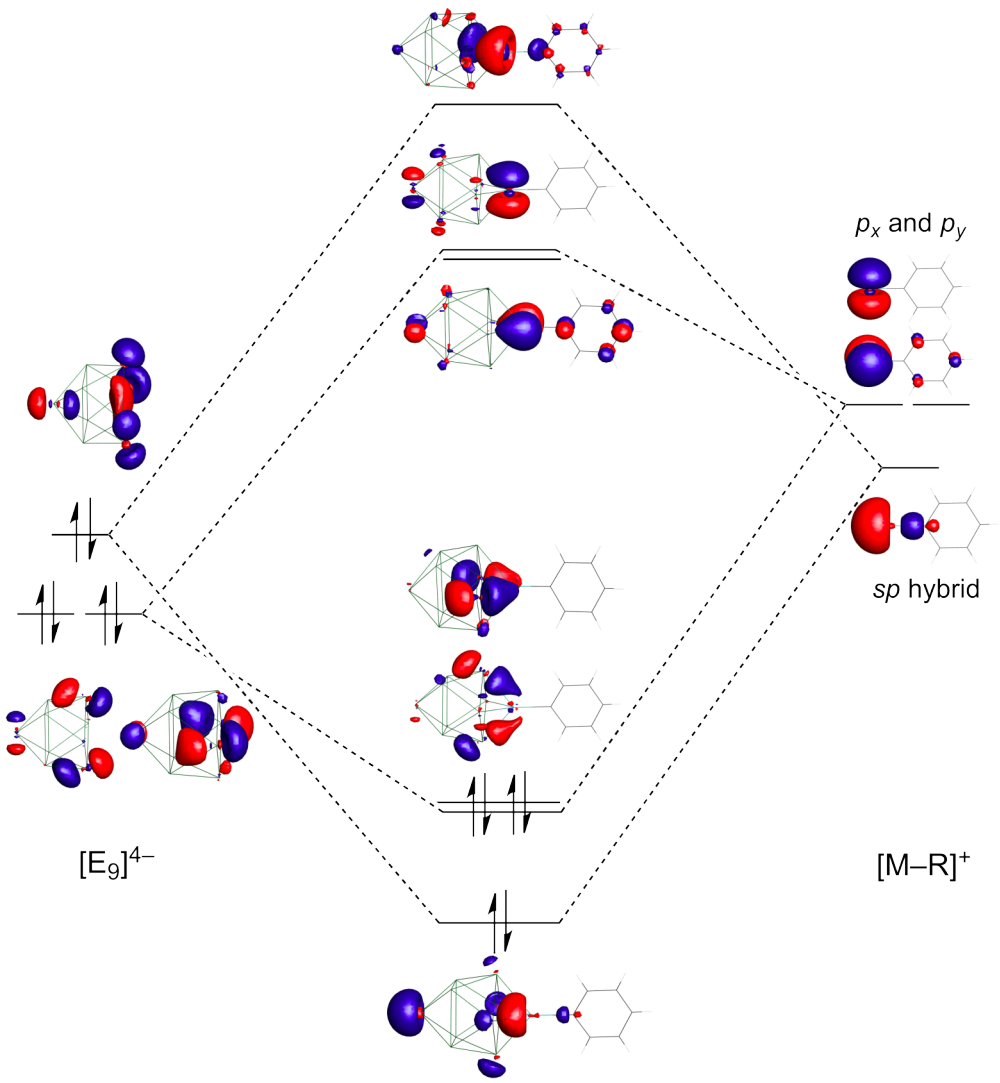

Figure 1.16 Schematic diagram showing the frontier molecular orbitals involved in the formation of $[E_9ZnPh]^{3-}$.

In addition to structural characterisation by single crystal X-ray diffraction, all the compounds were studied by electrospray mass spectrometry and ^{13}C NMR spectroscopy. They confirm the presence and stability of the functionalised clusters in solution. Furthermore, the ^{13}C NMR spectra indicate either no fluxionality at the [ZnPh] site or very fast fluxionality between η^4 and η^5 conformations compared with the NMR time scale at room temperature.

1.3.3.4 Reactions with Hg and $HgPh_2$

Ethylenediamine solutions of K_4Ge_9 react with elemental mercury in the presence of 2,2,2-crypt to produce the polymeric species $[K(2,2,2\text{-crypt})]_2[HgGe_9]\bullet 2en$.[58] The same reaction can be carried out in DMF resulting in the formation of $[K(2,2,2\text{-crypt})]_2[HgGe_9]\bullet DMF$.[59] Both of the compounds have been characterised in the solid state by single crystal X-ray diffraction and elemental analysis. The nine-atom clusters are linked together by Hg atoms to form linear polymeric strands of composition $^{1}_{\infty}[HgGe_9]^{2-}$.

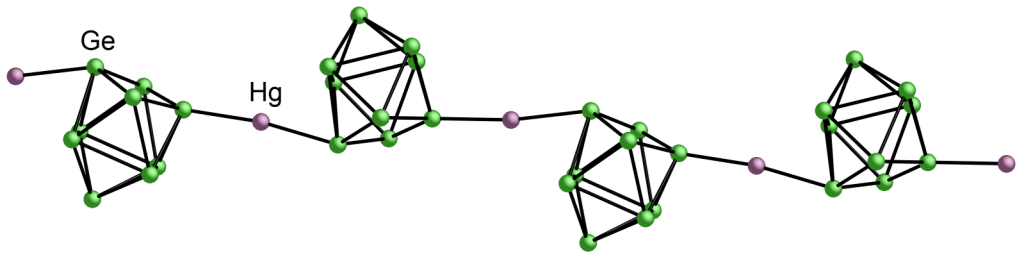

Figure 1.17 Molecular structure of a section of $^{1}_{\infty}[HgGe_9]^{2-}$ in $[K(2,2,2\text{-crypt})]_2[HgGe_9]\bullet 2en$.

The two structures are very similar with the Hg atoms bridging the nonagermanide clusters in the linear polymer. The nine-atom clusters can be roughly described as monocapped square antiprisms and each Hg atom is bonded to two Ge atoms of the open square bases of two adjacent clusters. In the en analogue, the Hg atom is bonded to one cluster through the extension of the diagonal of open square base, while it is almost symmetrically coordinated to a triangular side face of a second cluster. In the DMF analogue the Hg–Ge bonds are all collinear with the diagonal of the open square bases. The two Hg–Ge bond lengths in the en analogue are not quite the same, however in the DMF analogue the Hg atoms are equidistant from two neighbouring clusters. The bond lengths of the Hg–Ge bonds in both structures indicate they are conventional covalent bonds. The subtle differences in the coordination

between Hg atoms and the clusters in the two analogues also suggest that the Hg–Ge interaction is not very directional and may have significant ionic character. Electronically, the linear polymers can be viewed as either covalently bonded species –([Ge_9]$^{2-}$)–Hg–([Ge_9]$^{2-}$)–Hg– or with formal charges of ([Ge_9]$^{4-}$)(Hg^{2+})([Ge_9]$^{4-}$)(Hg^{2+}). The nine-atom clusters have 22 cluster bonding electrons whether considered as [Ge_9]$^{4-}$; or as [Ge_9]$^{2-}$ with two *exo*-bonds.

Recently, the reaction between K_4Ge_9 and $HgPh_2$ in ethylenediamine in the presence of 2,2,2-crypt was reported to yield a nanometric cluster rod [$Hg_3(Ge_9)_4$]$^{10-}$.[60] Similar to the reaction pathway in the synthesis of [E_9ZnPh]$^{3-}$ (E = Si, Ge, Sn, Pb) the first step is believed to involve reductive cleavage of the Hg–Ph bonds to produce isolated Hg atoms and phenyl anions. The phenyl anion is strongly basic and rapidly abstracts a proton from the solvent to yield benzene. Three Hg atoms and four [Ge_9]$^{4-}$ clusters are then assembled together to form the Hg linked molecular rod with an overall length of 3 nm. The structure of the anionic molecular rod was determined by single crystal X-ray diffraction. The bulk purity of the crystalline product was confirmed in the solid state by elemental analysis and powder X-ray diffraction.

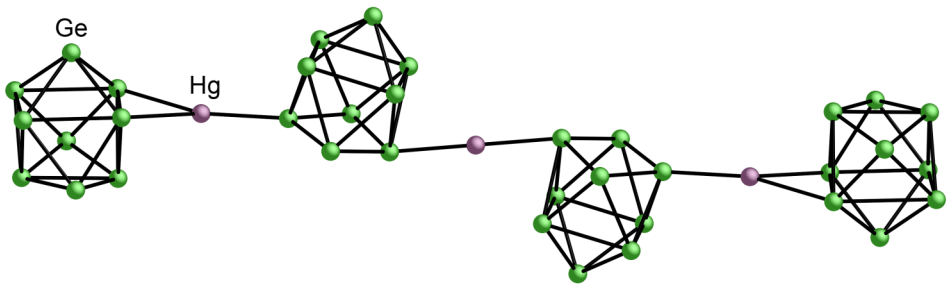

Figure 1.18 Molecular structure of the anionic cluster rod [$Hg_3(Ge_9)_4$]$^{10-}$.

Single crystal X-ray diffraction shows that the cluster coordination and arrangement in [$Hg_3(Ge_9)_4$]$^{10-}$ is slightly different to that observed in the previously discussed polymeric

species $^{1}_{\infty}[HgGe_9]^{2-}$. The central mercury atom of $[Hg_3(Ge_9)_4]^{10-}$ sits on the inversion centre of the molecular rod, meaning the anion is made up of two crystallographically non-equivalent germanium clusters, and two distinct Hg atoms. The nonagermanide clusters at both ends of the rod are best described as distorted tricapped trigonal prisms with two elongated prismatic heights, whereas the other two clusters in the middle of the rod are monocapped square antiprisms. One mercury atom is bonded to two germanium atoms of the cluster at the end of the rod, and simultaneously singly coordinated to a Ge atom in the second germanium cluster. The central mercury atom is bridging to two neighbouring central clusters through single *exo* bonds. All the Hg–Ge bond lengths suggest the interaction between Hg and the clusters is covalent in nature.

Stoichiometrically, four $[Ge_9]^{4-}$ clusters and three $HgPh_2$ molecules are required to make one molecule of $[Hg_3(Ge_9)_4]^{10-}$. In solution the nine-atom clusters are in equilibrium between the different possible charges of the cluster and can provide the six electrons required to cleave all the Hg–Ph bonds. As a result, the overall charge of the molecule should be 10– due to the loss of six electrons. Alternatively the four clusters in $[Hg_3(Ge_9)_4]^{10-}$ can be viewed as two monosubstituted 3– clusters and two disubstituted 2– clusters, which also confirms the overall 10– charge of the molecule.

Recrystallisation of the $[K(2,2,2\text{-crypt})]^{+}$ salt of $[Hg_3(Ge_9)_4]^{10-}$ in pyridine results in the formation of the polymeric species $\{[K(2,2,2\text{-crypt})][Hg(Ge_9)]\bullet 2py\}_{\infty}$. This suggests that the cluster anion $[Hg_3(Ge_9)_4]^{10-}$ can be viewed as a stable intermediate between the parent $[Ge_9]^{4-}$ cluster and the linear polymer $^{1}_{\infty}[HgGe_9]^{2-}$. The difference in reactivity of group 14 Zintl

clusters towards the group 12 homoleptic organometallic reagents $HgPh_2$ and $ZnPh_2$ can be attributed to the difference in the bond dissociation energy of the M–Ph fragments. The metal-carbon bond dissociation energy decreases as going down the group, which makes easier to cleave both bonds, providing a source of 'naked' transition metal atom.[61, 62]

A similar reaction between an ethylenediamine solution of K_4Sn_9 and 2,2,2-crypt and elemental mercury yielded $[K(2,2,2\text{-crypt})]_{12}[Sn_9]_2[Sn_9HgSn_9]$.[63] Single crystal X-ray analysis shows that the crystal lattice contains two isolated $[Sn_9]^{3-}$ clusters and the mercury atom bridged dimeric $[Sn_9HgSn_9]^{6-}$ anion. In $[Sn_9HgSn_9]^{6-}$ the Hg atom sits at the inversion centre of two tricapped trigonal prisms and coordinates to two Sn atoms of each nine-atom cluster at the ends of the elongated prismatic heights. The electron counting is analogous to that in the previously discussed $^{1}_{\infty}[HgGe_9]^{2-}$.

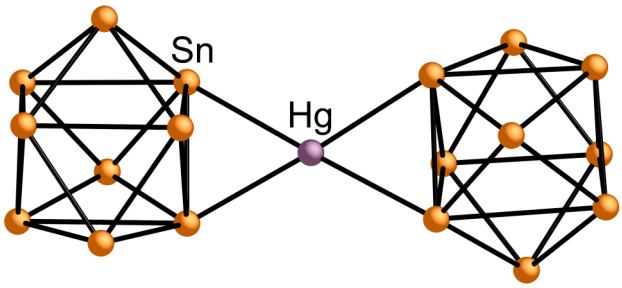

Figure 1.19 Ball and stick diagram of the cluster anion $[Sn_9HgSn_9]^{6-}$.

1.3.3.5 Reactions with transition metal reagents of Cu, Ag and Au

The reactions of K_4Ge_9 with $Cu^{I}Cl(PR_3)$ (R = isopropyl, cyclohexyl) in various solvents and under different reaction conditions have resulted in the formation of three functionalised cluster anions including $[Cu(\eta^4\text{-}Ge_9)(PR_3)]^{3-}$ (R = ^{i}Pr, Cy) and $[Cu(\eta^4\text{-}Ge_9)(\eta^1\text{-}Ge_9)]^{7-}$.[64] The η^4 coordinated $Cu(PR_3)$ functionalised clusters are bicapped square antiprisms with the

transition metal moiety occupying one of the capping positions. The ligand-free metalated cluster anion $[Cu(\eta^4\text{-}Ge_9)(\eta^1\text{-}Ge_9)]^{7-}$ is the first example in which the homoatomic polyanions are bonded to a transition metal in two different coordination modes. The $[Cu(\eta^4\text{-}Ge_9)]$ moiety can be described as a bicapped square antiprism with the copper atom occupying one of the capping vertices, whilst one lone pair of a Ge atom is bonded to the Cu atom via a conventional two-centre two-electron *exo*-bond in the $[(\eta^1\text{-}Ge_9)]$ unit.

Electronically, the bridged dimer can be viewed as a d^{10} Cu^+ cation and two $[Ge_9]^{4-}$ cluster anions. From the viewpoint of the copper atom, it achieves a stable 18-electron configuration by combining its 10 valence electrons, 6 electrons from the $[\eta^4\text{-}Ge_9]$ unit and 2 electrons from the $[\eta^1\text{-}Ge_9]$ cluster. The isolation of these functionalised cluster anions indicates that the first step of the reaction pathway involves ligand substitution of the labile Cl^- ligand by a $[\eta^4\text{-}Ge_9]^{4-}$ cluster. Under different reaction conditions, the remaining Cu^I–phosphine bond is cleaved to give the ligand-free intermetalloid cluster $[Cu(\eta^4\text{-}Ge_9)(\eta^1\text{-}Ge_9)]^{7-}$.

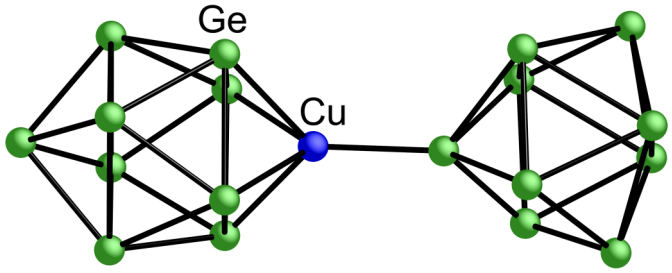

Figure 1.20 Molecular structure of the functionalised cluster $[Cu(\eta^4\text{-}Ge_9)(\eta^1\text{-}Ge_9)]^{7-}$.

Another example of a transition metal bridged Zintl cluster dimer is $[Ag(Sn_9\text{–}Sn_9)]^{5-}$, which can be obtained from the reaction of K_4Sn_9 with $[Ag(mes)]_4$ (mes = 2,4,6-$Me_3C_6H_2$) in the presence of 2,2,2-crypt in ethylenediamine.[65] The two nonastannide clusters are bonded

through a two-centre, two-electron Sn–Sn single bond, analogous to the intercluster *exo*-bond in $[Ge_9–Ge_9]^{6–}$. In addition, the two clusters are further supported by coordination to a silver cation. Both nine-atom clusters are tricapped trigonal prisms with three elongated 3-fold prismatic heights. The silver atom is bonded to three Sn atoms at the ends of the elongated heights of each cluster.

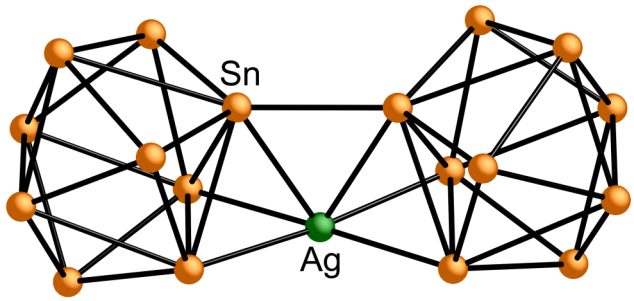

Figure 1.21 Ball and stick diagram of the anionic moiety $[Ag(Sn_9–Sn_9)]^{5–}$.

The first isolated ligand-free germanium-gold intermetalloid cluster anion was $[Au_3Ge_{18}]^{5–}$, obtained by reaction of K_4Ge_9 with $[Au^I(PPh_3)Cl]$ in ethylenediamine in the presence of 2,2,2-crypt.[66] Single crystal X-ray diffraction experiments showed that two triangular faces of two nonagermanide clusters are each bonded to either side of a central Au_3 triangle. Analysis of bond lengths shows that the Au–Au and Au–Ge distances compare well to other molecular species containing similar bonds.[67-69] Preliminary density functional theoretical calculations showed that there are covalent bonding interactions between the gold and germanium atoms, but only very weak gold–gold interactions. It is another example of transition metal atoms serving as linkers between negatively charged nine-atom group 14 Zintl clusters. Slight changes in the reaction conditions result in the formation of a binary cluster anion $[Au_3Ge_{45}]^{9–}$, containing four deltahedral nonagermanide units covalently bonded to nine germanium atoms and three gold atoms.[70]

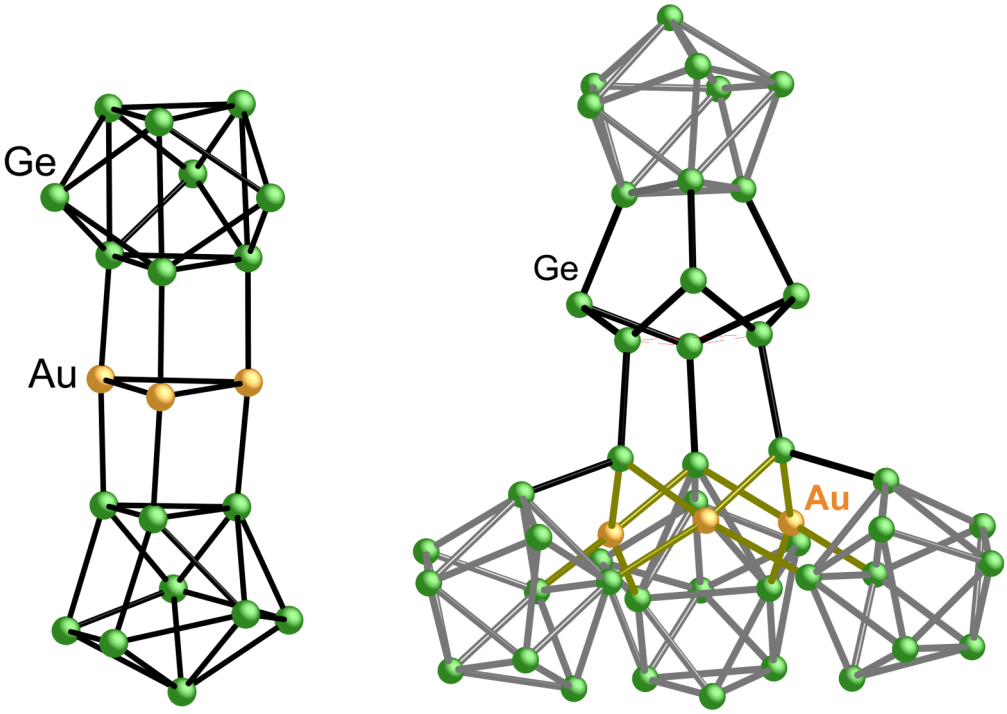

Figure 1.22 Molecular structures of the cluster anions $[Au_3Ge_{18}]^{5-}$ and $[Au_3Ge_{45}]^{5-}$.

1.3.3.6 Reactions with the mid transition metal organometallic reagent $Mn_2(CO)_{10}$

In the reactions between group 14 Zintl clusters and transition metals or organometallic reagents that have been discussed above, the nuclearity of the clusters in the products remains unchanged. However, the reaction between K_4Ge_9 and $Mn_2(CO)_{10}$ in ethylenediamine in the presence of 2,2,2-crypt results in the soft oxidation of the cluster, and yields a manganese tetracarbonyl complex $[Ge_{10}Mn(CO)_4]^{3-}$.[71] The deltahedral $[Ge_{10}]$ anion acts as a normal two-electron ligand and coordinates to the Mn centre via the lone pair of a Ge atom at the capping position of the 10-atom cluster. $[K(2,2,2\text{-crypt})]_3[Ge_{10}Mn(CO)_4]$•tol was characterised by single crystal X-ray diffraction, negative ion mode electrospray mass spectrometry and infrared spectroscopy.

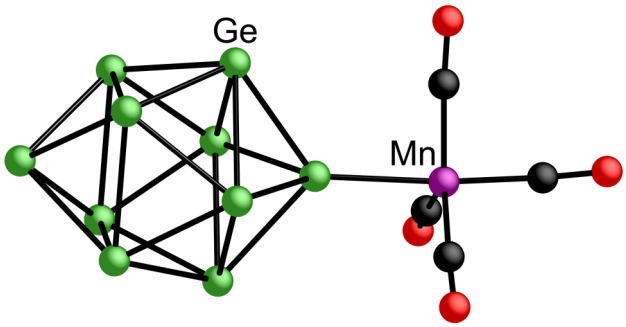

Figure 1.23 Ball and stick diagram of $[Ge_{10}Mn(CO)_4]^{3-}$, which contains a $[Ge_{10}]$ moiety.

Single crystal structural analysis shows that the 10-atom cluster adopts a bicapped square antiprismatic geometry with pseudo-D_{4d} symmetry. Electronically, the polyatomic anion $[Ge_{10}Mn(CO)_4]^{3-}$ can be divided into two parts: the deltahedral cluster $[Ge_{10}]^{2-}$ and the transition metal fragment $[Mn(CO)_4]^-$. The *closo*-$[Ge_{10}]^{2-}$ follows the Wade-Mingos rules for electron counting and has 22 skeletal electrons for cluster bonding. The Mn centre in the transition metal fragment $[Mn(CO)_4]^-$ achieves an 18-electron configuration by combining its seven valence electrons, eight electrons from four CO groups, two electrons from the lone pair of the cluster and the negative charge of 1–.

In addition to characterisation by single crystal X-ray diffraction, the electrospray mass spectrum and infrared vibrational spectrum of the compound have been recorded. The negative ion mode mass spectrum shows the presence of $[Ge_{10}Mn(CO)_4]^-$ and its derivatives after the loss of one or more carbonyl groups due to fragmentation in the ionisation process. The infrared spectrum reveals three CO group stretching bands at very low frequencies (1892, 1789, 1775 cm^{-1}) indicating very strong metal to ligand back donation. Formally the Mn centre in the fragment $[Mn(CO)_4]^-$ carries a 1– charge and so the electron density can be

transferred from the transition metal to the antibonding π^* orbitals of the carbonyl group. This significantly weakens the C≡O bond and hence results in a reduction of stretching frequency in the infrared spectrum. The single crystal structure of $[Ge_{10}Mn(CO)_4]^-$ also shows short Mn–C and long C–O bond distances.

1.3.3.7 Remarks

Group 14 Zintl clusters can react with a range of transition metal organometallic reagents to yield functionalised cluster anions with multiple coordination modes (η^1, η^3, η^4 and η^5). The clusters generally act as nucleophiles towards transition metals when their empty *d* orbitals match the symmetry of the frontier molecular orbitals of the cluster. In most examples, the nuclearity of the clusters remains unchanged, and electrophilic attack occurs at the open square base of the monocapped square antiprism. When the organometallic moiety is bonded to the cluster in an η^4 fashion, the cluster acts as 6-electron donor ligand and the transition metal centre generally achieves a stable 18-electron configuration.

1.3.4 Endohedral Zintl clusters

1.3.4.1 Nine-atom endohedral Zintl clusters

Reaction between K_4E_9 (E = Sn, Pb) and $[Cu(mes)]_5$ in DMF in the presence of 2,2,2-crypt result in the isolation of the intermetalloid clusters $[Cu@E_9]^{3-}$.[72] Single crystal X-ray diffraction shows that the nine-atom clusters can be described as distorted tricapped trigonal prisms with the Cu–E distances lying in a very narrow range.

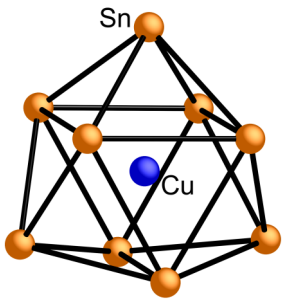

Figure 1.24 Molecular structure of the deltahedral endohedral cluster anion $[Cu@Sn_9]^{3-}$.

Electronically the $[Cu@E_9]^{3-}$ anions can be viewed as made up of a Cu^{+} cation with a stable d^{10} configuration and a *nido*-$[E_9]^{4-}$ cluster. The diamagnetic nature of crystalline salts of $[Cu@Sn_9]^{3-}$ was confirmed by magnetic measurements.

Crystalline samples of $[K(2,2,2\text{-crypt})]_3[Cu@Sn_9]\bullet 2DMF$ dissolved in acetonitrile have been additionally characterised by solution state multielement NMR spectroscopy. The ^{119}Sn NMR spectrum shows one quartet with a 1:1:1:1 intensity ratio, which indicates all the Sn atoms are equivalent on the NMR time scale creating a spherical coordination environment. The highly symmetrical framework couples to the interstitial Cu atom (69% ^{63}Cu and 31% ^{65}Cu, $I = 3/2$) to give the observed splitting pattern. Coupling to ^{117}Sn ($I = 1/2$, 7.61% natural abundance) results in the appearance of satellites in the spectrum.

The room temperature ^{63}Cu NMR spectrum of the same sample reveals one sharp resonance that has satellites consistent with coupling to the $^{119/117}Sn$ atoms ($I = ½$, ~16% total natural abundance for ^{119}Sn and ^{117}Sn). The chemical shift of the resonance is comparable to those of other Cu^{I} compounds, confirming the charge distribution discussed previously.[73, 74] The observed ^{63}Cu NMR resonance is a result of the highly symmetrical geometry of the

surrounding Sn atoms. Both the ^{119}Sn and ^{63}Cu NMR spectra remain the same even recorded at low temperatures, suggesting a very rapid fluxionality of all nine Sn sites in the cluster.

Another example of a metal-centred nine-atom clusters is $[Ni@E_9]^{3-}$ (E = Ge, Sn) obtained by reacting ethylenediamine solutions of K_4E_9 and 2,2,2-crypt with $Ni(COD)_2$.[75, 76] Single crystal X-ray diffraction analysis of $[Ni@Ge_9]^{3-}$ shows that the endohedral cluster is best described as a tricapped trigonal prism with three elongated prismatic heights parallel to the 3-fold rotation axis. The analogous $[Ni@Sn_9]^{3-}$ cluster is a distorted tricapped trigonal prism with two elongated prismatic heights. Overall, upon insertion of a Ni atom the nine-atom cluster expands and distorts to an almost spherical structure compared to the structure of empty $[E_9]^{n-}$ clusters. The Ni–E distances fall within a narrow range as a result of optimising the interactions between the interstitial atom and the surrounding nine atoms. The Ni atom has a d^{10} configuration and does not contribute any electrons to cluster bonding. There are therefore 21 skeletal electrons for the endohedral cluster $[Ni@E_9]^{3-}$, making it isoelectronic with the paramagnetic radical anion $[E_9]^{3-}$.

The reactivity of the centred clusters $[Ni@E_9]^{3-}$ (E = Ge, Sn) towards TlCp (Cp = cyclopentadienyl anion) has recently been explored, yielding the ten-atom *closo*-$[Ni@E_9Tl]^{3-}$ cluster anion.[77] The shape of $[Ni@Sn_9Tl]^{3-}$ determined by single crystal X-ray diffraction is that of a bicapped square antiprism with the Tl atom occupying one of the capping positions. The interstitial Ni atom is not positioned at the centre of the ten-atom cluster, but remains at the centre of the nonastannide unit. The electron counting for $[Ni@E_9Tl]^{3-}$ follows the Wade-Mingos rules and has 22 skeletal electrons, since the Tl atom contributes one electron to

cluster bonding. A ten-atom cluster with 22 electrons is expected to have a *closo* structure, which is consistent with the observed geometry.

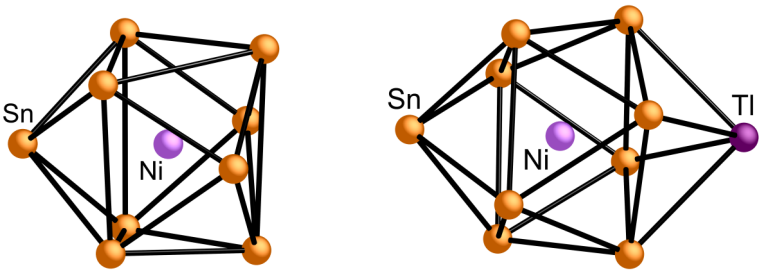

Figure 1.25 Structures of the endohedral cluster anions $[Ni@Sn_9]^{3-}$ and $[Ni@Sn_9Tl]^{3-}$.

Interestingly, the reaction between the $[E_9]^{4-}$ (E = Ge, Sn) cluster and TlCp results in the formation of *closo*-$[E_9Tl]^{3-}$. The Tl atom is attached to the cluster as a tenth vertex of a bicapped square antiprism at the capping positions for both the empty and Ni-centred clusters. The interstitial atom seems to have no effect on the reactivity of the cluster.

1.3.4.2 Ten-atom endohedral Zintl clusters

The reaction of K_4Pb_9 and $Ni(COD)_2$ in the presence of 2,2,2-crypt in a mixture of ethylenediamine and toluene yielded the endohedral cluster anion $[Ni@Pb_{10}]^{2-}$, accompanied by a small amount of $[Ni@Pb_{12}]^{2-}$ (to be discussed in the section **1.3.4.3**).[78] The structure, as determined by single crystal X-ray diffraction, shows that the $[Ni@Pb_{10}]^{2-}$ anion has a bicapped square antiprismatic $[Pb_{10}]^{2-}$ cluster encapsulating a Ni atom. The central atom, with a closed-shell d^{10} configuration, does not contribute any electrons to cluster bonding and as a result there are 22 skeletal electrons. According to the Wade-Mingos electron-counting rules, such a cluster is expected to have a *closo* geometry, which is consistent with the

experimentally observed structure. The distances between Ni and the apical Pb atoms are slightly longer than the other eight Ni–Pb lengths.

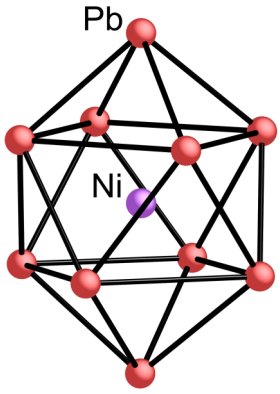

Figure 1.26 Ball and stick diagram of the anionic moiety $[Ni@Pb_{10}]^{2-}$.

The $[K(2,2,2\text{-crypt})]^{+}$ salt of $[Ni@Pb_{10}]^{2-}$ has been studied by solution ^{207}Pb NMR spectroscopy. The spectrum shows a single resonance, which gets broader as the temperature is lowered, suggesting a rapid, dynamic intramolecular exchange of all ten Pb atoms on the NMR time scale. The expected limiting low temperature spectrum should consist of two discrete, mutually coupled resonances corresponding to the two axial and eight equatorial Pb atoms, however this has yet to be observed.

The reaction of $[Ni(PPh_3)_2(CO)_2]$, K_4Ge_9 and 2,2,2-crypt in ethylenediamine yields the $[K(2,2,2\text{-crypt})]^{+}$ salt of $[Ni@(Ge_9Ni)PPh_3]^{2-}$, which was originally wrongly assigned as $[Ge@(Ge_9Ni)PPh_3]^{2-}$ by Eichhorn.[76, 79] This is because Ni and Ge atoms have similar electron count, and hence are indistinguishable by X-ray diffraction. In the endohedral anion, the transition metal moiety is incorporated into the cluster-bonding framework as a tenth vertex.

Electronically, both of the Ni atoms achieve a stable d^{10} configuration and do not contribute any electrons for cluster bonding, giving a total of 20 skeletal electrons.

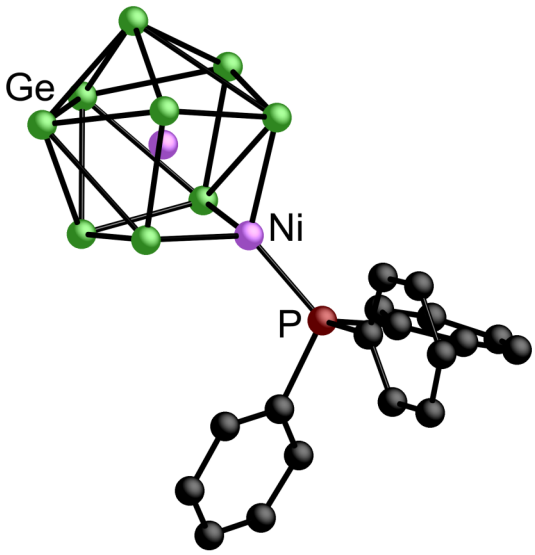

Figure 1.27 Molecular structure of the cluster anion $[Ni@(Ge_9Ni)PPh_3]^{2-}$.

Analogous reactions between $[Ni(PPh_3)_2(CO)_2]$, K_4Sn_9 and 2,2,2-crypt in ethylenediamine results in the formation of the $[K(2,2,2\text{-crypt})]^+$ salt of $[Ni@(Sn_9Ni)CO]^{3-}$.[80] Single crystal X-ray diffraction reveals that the endohedral cluster anion contains a bicapped square antiprismatic moiety $[Sn_9Ni]$ with the Ni atom occupying the capping position. The carbonyl group, the capping and interstitial Ni atoms and the capping Sn atom are collinear. Electronically, both the central and capping Ni atoms contribute no electrons for cluster bonding, giving rise to an overall electron count of 21 skeletal electrons. This endohedral cluster has been characterised in solution by EPR studies.

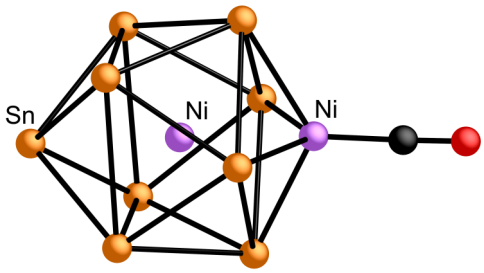

Figure 1.28 Molecular structure of the endohedral cluster ion $[Ni@(Sn_9Ni)CO]^{3-}$.

1.3.4.3 Twelve-atom endohedral Zintl clusters

Reactions between K_4Pb_9 and the organometallic reagents $M(PPh_3)_4$ (M = Pt, Pd) in the presence of 2,2,2-crypt yielded the $[K(2,2,2\text{-crypt})]^+$ salts of $[M@Pb_{12}]^{2-}$.[81] These endohedral cluster anions are rare examples of naked metal icosahedra and presumably result from extensive fragmentation and rearrangement of the parent $[Pb_9]^{4-}$ clusters. The crystalline products were characterised by a number of methods including single crystal X-ray diffraction, ^{207}Pb NMR and ^{195}Pt solution NMR spectroscopy.

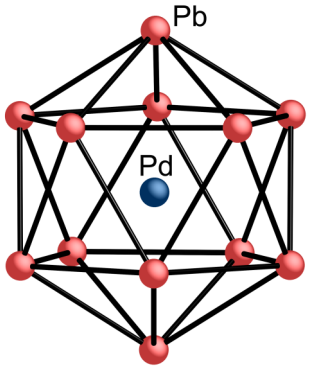

Figure 1.29 Ball and stick diagram of the icosahedral cluster anion $[Pd@Pb_{12}]^{2-}$.

The framework of the $[M@Pb_{12}]^{2-}$ cluster anions consists of a 12-atom icosahedral cage possessing almost perfect I_h point symmetry containing an interstitial transition metal atom. As the interstitial atom gets smaller, all the bond lengths decrease but the size of the

distribution and variance of bond distances increase. This suggests the icosahedral framework becomes more distorted as the size of the central atom decreases, with Pt being the best fit for the cage cavity. This is confirmed by the fact that when Ni is inserted a smaller $[Ni@Pb_{10}]^{2-}$ cage (section **1.3.4.2**) is more stable and favoured relative to the icosahedral $[Ni@Pb_{12}]^{2-}$.

Electronically, the central transition metal retains a stable d^{10} configuration and does not contribute any electrons to cluster bonding. Overall there are 26 skeletal electrons and according to the Wade-Mingos rules it is predicted to have a *closo* structure. This is consistent with the experimentally observed highly symmetric icosahedral geometry.

In addition, all the endohedral clusters $[M@Pb_{12}]^{2-}$ were characterised in solution by multielement NMR spectroscopy. The ^{207}Pb NMR spectrum for $[Pt@Pb_{12}]^{2-}$ reveals a singlet accompanied by satellites, indicating all 12 Pb atoms are equivalent and there is a strong coupling with the central Pt atom (^{195}Pt, I = ½, 34% natural abundance). The corresponding ^{195}Pt NMR spectrum shows one resonance with a splitting pattern due to coupling with 12 equivalent Pb atoms (^{207}Pb, I = ½, 23% natural abundance). The coupling constants between ^{207}Pb and ^{195}Pt nuclei obtained from both spectra are comparable. It is also interesting to note that the ^{207}Pb resonances of the cluster anions $[M@Pb_{12}]^{2-}$ are significantly more deshielded in comparison to other known lead-containing compounds.[54, 78, 82] This may be explained by the σ-aromatic character resulting from the highly symmetric icosahedral geometry. This is further supported by the observation that the ^{207}Pb resonance of icosahedral $[Ni@Pb_{12}]^{2-}$ is shifted deshielded by more than 2000 ppm relative to that of $[Ni@Pb_{10}]^{2-}$.

To probe the possible reaction mechanisms for the formation of these endohedral Zintl cluster anions, the reactivity of $[Sn_9Ir(COD)]^{3-}$ with mild oxidising agents such as PPh_3 and dppe ($Ph_2PCH_2CH_2PPh_2$) has been studied in ethylenediamine at 80 °C.[83] As discussed above, the functionalised deltahedral cluster $[Sn_9Ir(COD)]^{3-}$ is synthesised by reacting the solid state precursor with $[Ir(COD)Cl]_2$ (see section **1.3.3.2**). Mild oxidation of $[Sn_9Ir(COD)]^{3-}$ at elevated temperature has yielded the $[K(2,2,2\text{-crypt})]^+$ salt of the endohedral cluster anion $[Ir@Sn_{12}]^{3-}$ that possesses near perfect I_h point group symmetry. This result is an important piece of evidence for the step-by-step synthesis of endohedral cluster anions. The parent Zintl cluster and intermediate product both contain nine-atom frameworks, whereas the nuclearity of the cluster in the final product is increased to twelve.

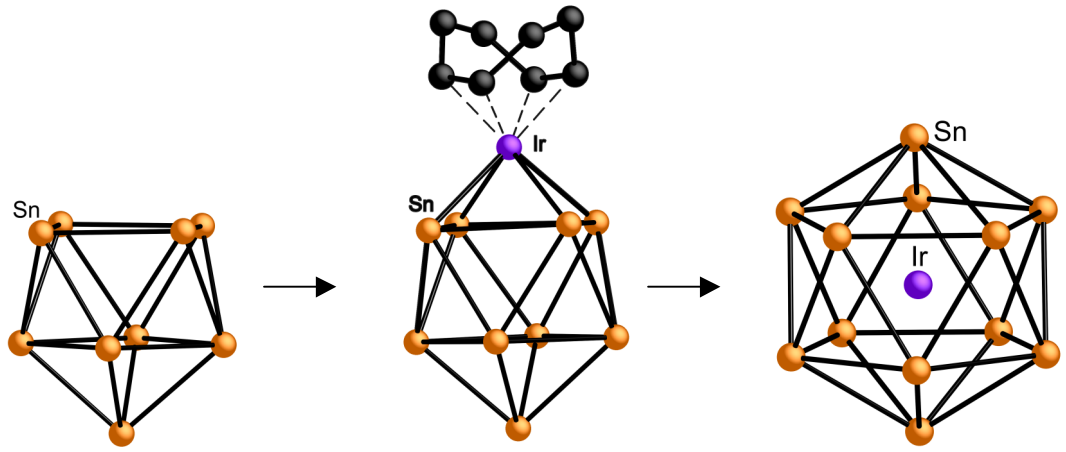

Scheme 1.3 Step-by-step synthesis of $[Sn_9Ir(COD)]^{3-}$ and $[Ir@Sn_{12}]^{3-}$.

Single crystal X-ray diffraction studies of $[Ir@Sn_{12}]^{3-}$ reveal that the endohedral cluster is icosahedral, and thus isostructural with the previously discussed $[M@Pb_{12}]^{2-}$ (M = Ni, Pd, Pt). All the Ir–Sn distances lie within a very narrow range and are considerably longer than conventional Ir–Sn single bonds, indicating weak interactions between them.[84, 85]

Electronically, the cluster anion can be viewed as $[Ir^{-}][Sn_{12}]^{2-}$ with the central transition metal achieving a closed-shell d^{10} configuration. The encapsulated atom does not donate any electrons to cluster bonding and so there are 26 skeletal electrons, resulting in a *closo* structure. As such the cluster is isoelectronic with the previously discussed clusters $[M@Pb_{12}]^{2-}$ (M = Ni, Pd, Pt).[81] All these cluster anions have a total valence electron count of 4 × 12 + 10 + 2 = 60.

1.3.4.4 Larger endohedral Zintl clusters with non-traditional structures

Ethylenediamine solutions of K_4Sn_9 and toluene solutions of $Ni(COD)_2$ have been reacted in a 1:1 molar ratio in the presence of 2,2,2-crypt to yield the $[K(2,2,2\text{-crypt})]^{+}$ salt of endohedral cluster $[Ni_2Sn_{17}]^{4-}$.[86] Single crystal X-ray diffraction experiments show that the anion can be viewed as two endohedral $[Ni@Sn_9]^{2-}$ clusters fused together at a common ninth vertex.

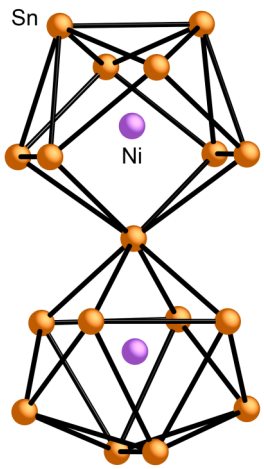

Figure 1.30 Ball and stick diagram of the cluster anion $[Ni_2Sn_{17}]^{4-}$.

The dynamic properties of $[Ni_2Sn_{17}]^{4-}$ have been explored by variable temperature ^{119}Sn NMR spectroscopy. At –64 °C the spectrum contains four resonances in the intensity ratio, 4:8:4:1, corresponding to the four distinct Sn environments of the cluster with D_{2d} point symmetry. No

dynamic exchange of the vertices is observed at low temperatures. As the solution is heated (from –50 to 44 °C) three of the resonances in the intensity ratio, 4:8:4, broaden and eventually disappear into the baseline, whilst the fourth resonance is still present. At 60 °C all four initial peaks have disappeared and the spectrum reveals a shifted single time averaged exchange peak. This suggests that at intermediate temperatures the Sn atoms can exchange intramolecularly apart from the common vertex of the two $[Ni@Sn_9]^{2-}$ clusters. At higher temperatures all the intramolecular Sn atoms rapidly exchange including the common vertex.

An analogous reaction between K_4Ge_9 and $Ni(COD)_2$ in a 1:3 molar ratio in ethylenediamine has afforded crystals of $[K(2,2,2\text{-crypt})]_4[(Ni@Ge_9)Ni(Ni@Ge_9)]\bullet 2tol$.[75] The cluster anion can be similarly described as two endohedral $[Ni@Ge_9Ni]$ species coupled at a common tenth vertex. Alternatively the ligand-free intermetalloid cluster can be viewed as a linear trimer of Ni atoms encapsulated inside two nonagermanide clusters.

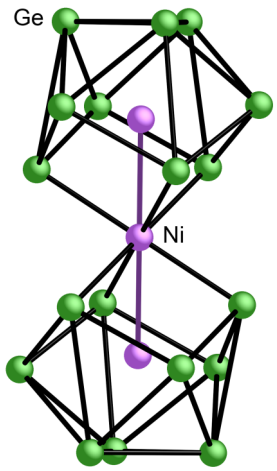

Figure 1.31 Ball and stick diagram of the anionic cage $[(Ni@Ge_9)Ni(Ni@Ge_9)]^{4-}$.

The reaction of K_4Sn_9 with $Pt(norbornene)_3$ (norbornene = bicycle[2,2,1]heptene) in the presence of 2,2,2-crypt in solvent mixtures of ethylenediamine and toluene yielded exclusively one crystalline product: the $[K(2,2,2\text{-crypt})]^+$ salt of $[Pt_2@Sn_{17}]^{4-}$.[87] A similar reaction between K_4Sn_9 and $Pt(PPh_3)_4$ in ethylenediamine gives a mixture of four different products, including the same endohedral cluster $[Pt_2@Sn_{17}]^{4-}$. Single crystal X-ray diffraction studies show that this cluster cage has a capsule-like structure, which can be described as two $[PtSn_6]$ bicapped pentagonal prisms fused by a central planar five-membered $[Sn_5]$ ring. The Pt–Pt distance in the complex suggests there is no bonding interaction between the two central atoms. It is isoelectronic to the previously discussed cluster anion $[Ni_2Sn_{17}]^{4-}$, however they adopt very different geometries.

Variable temperature ^{195}Pt and ^{119}Sn solution NMR spectroscopic experiments have been conducted to study the solution behaviour of the $[Pt_2@Sn_{17}]^{4-}$ cluster anion. The ^{119}Sn spectrum at both room temperature and –60 °C show a single resonance, indicating a rapid dynamic exchange process of all tin sites on the NMR timescale. The single resonance is also flanked by ^{195}Pt and ^{117}Sn satellites corresponding to couplings to two equivalent interstitial Pt atoms and ^{117}Sn atoms of the cluster. The ^{195}Pt NMR spectrum displays a single resonance with satellites corresponding to coupling to all 17 tin atoms. In solution the clusters are therefore best described as having a liquid-like shell of tin atoms encapsulating two Pt atoms at the core. The highly dynamic behaviour of the $[Pt_2@Sn_{17}]^{4-}$ complex is similar to that of the previously discussed $[Ni_2Sn_{17}]^{4-}$ cluster anion.

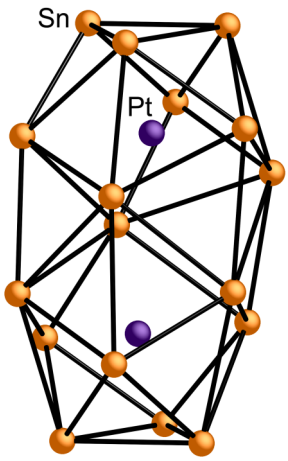

Figure 1.32 Molecular structure of the cluster anion $[Pt_2@Sn_{17}]^{4-}$.

One of the largest single-cage deltahedral Zintl anions is $[Pd_2@Ge_{18}]^{4-}$, synthesised by reaction of K_4Ge_9 with an excess of $Pd(PPh_3)_4$ in ethylenediamine in the presence of 2,2,2-crypt.[88] An analogous reaction between K_4Sn_9 and $Pd(PPh_3)_4$ in a mixture of en and toluene yielded the isoelectronic cluster anion $[Pd_2@Sn_{18}]^{4-}$ as the $[K(2,2,2\text{-crypt})]^+$ salt.[89, 90]

The $[Pd_2@E_{18}]^{4-}$ cage is prolate, with the two Pd atoms occupying the foci of the capsule-like $[E_{18}]^{4-}$ (E = Ge, Sn) deltahedron. The geometry is quite similar to that of $[Pt_2@Sn_{17}]^{4-}$ and can be described as two $[PdE_6]$ (E = Ge, Sn) bicapped pentagonal prisms fused by a central planar six-membered ring. Neither Pd atom contributes any electrons to cluster bonding and both retain a closed-shell d^{10} configuration. This leaves 40 skeletal electrons for an 18-vertex cluster, which is thus predicted to have a *nido* geometry. The endohedral $[Pd_2@Sn_{18}]^{4-}$ cluster anion was studied in solution by variable temperature ^{119}Sn NMR experiments. The observation of one, temperature dependent resonance in the NMR spectrum indicates that all 18 tin atoms are in rapid global exchange and are chemically equivalent on the NMR time scale between –50 and +10 °C. These measurements suggest the endohedral anion

$[Pd_2@Sn_{18}]^{4-}$ is highly dynamic in solution, much like the $[Pt_2Sn_{17}]^{4-}$ anion described previously. The Pd–Pd distances in the $[Pd_2@E_{18}]^{4-}$ (E = Ge, Sn) cluster anions are all significantly longer than the reported single bond distance, implying no bonding interaction between the two central atoms.

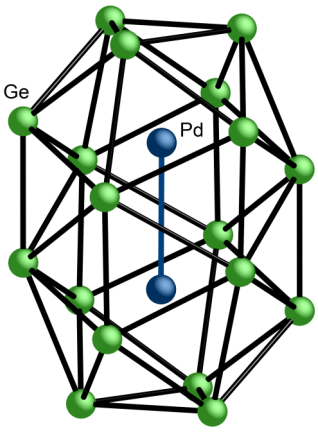

Figure 1.33 Molecular structure of the cluster anion $[Pd_2@Ge_{18}]^{4-}$.

It is worth noting that the $[Pb_9]^{4-}$ clusters show remarkably different reactivity towards group 10 organometallics. As discussed in the previous sections, the zero valent transition metals Ni, Pd and Pt template cluster redistribution to give $[M@Pb_{10}]^{2-}$ and $[M@Pb_{12}]^{2-}$ clusters (sections **1.3.4.2** and **1.3.4.3**). This may suggest that $[Sn_{17}]^{4-}$, $[Ge_{18}]^{4-}$, $[Sn_{18}]^{4-}$, $[Pb_{10}]^{2-}$ and $[Pb_{12}]^{2-}$ are the more stable geometries relative to structures of any other nuclearity, and require d^{10} central atoms for their stabilisation. However, it is also possible that the optimised reaction conditions for yielding other endohedral clusters have not yet been discovered.

1.3.4.5 Remarks

Currently the interstitial transition metals in the endohedral homoatomic Zintl clusters all have a closed-shell, d^{10} configuration and contribute no electrons to cluster bonding. However, they

can provide empty *s* and *p* orbitals to interact with the cluster orbitals and hence template and stabilise large cluster frameworks. While these large, endohedral, polyanionic clusters are stable discrete entities in the solid state, many of them exhibit highly dynamic behaviour in solution. Some gas-phase experiments and theoretical calculations have been employed by a number of research groups to study these ligand-free intermetalloid species.[91-93]

1.4 Aims and objectives

Group 14 Zintl clusters have shown remarkable reactivity towards a range of main-group and transition metal reagents in solution. They normally retain their nuclearity and act as nucleophiles when reacted with main-group organometallic reagents. However with transition metal organometallics, the anionic cluster products show a greater structural diversity, and interesting electronic properties emerge from this.

Highlighted below in the periodic table are the elements of the transition metal organometallic reagents with which the solution reactivity of group 14 Zintl ions has been studied thus far. The scope of this research is to study some of the unexplored areas by reacting the $[E_9]^{4-}$ (E = Ge, Sn and Pb) clusters with various organometallic reagents of Zn, Cd, Fe and Mn. This may result in functionalised clusters with unprecedented coordination modes or nuclearities, which can be used as building blocks for nanometric materials. The solution reactivity of these cluster compounds will also be investigated, giving us a better understanding of their structural and electronic properties. The outcomes of this research will help us to form a more complete picture of the reactivity of group 14 Zintl clusters towards mid to late transition metal organometallics, which is important for the development of Zintl chemistry.

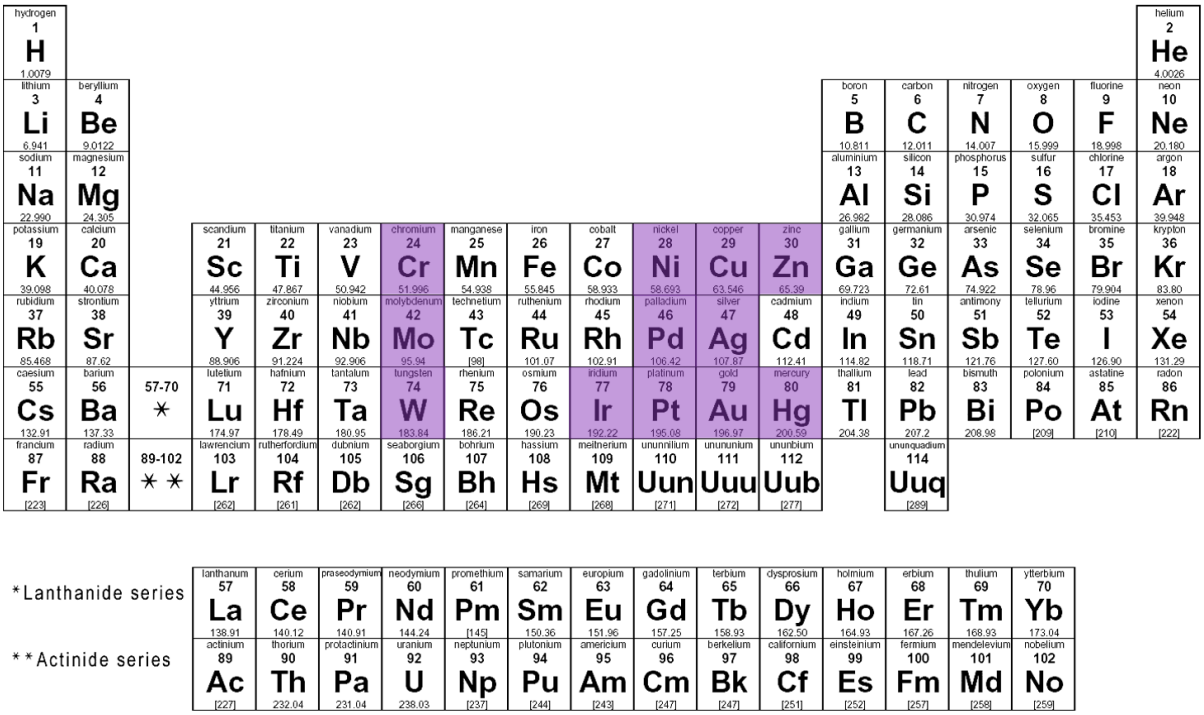

Figure 1.34 The periodic table (URL for the image: http://www.wpclipart.com/science/atoms_molecules/periodic_tables/periodic_table_of_elements_BW.png.html) with the areas that have been previously explored highlighted in purple.

1.5 References

1. Joannis, A., *Ann. Chim. Phys* **1906**, *7*.
2. Joannis, A., *Hebd. Seances Acad. Sci.* **1891**, *113*.
3. Joannis, A., *Hebd. Seances Acad. Sci.* **1892**, *113*.
4. Kraus, C. A.; Kurtz, H. F., *J. Am. Chem. Soc.* **1925**, *47*.
5. Zintl, E.; Kaiser, H., *Z. Anorg. Allg. Chem.* **1933**, *211*.
6. Zintl, E.; Dullenkopf, W., *Z. Phys. Chem. Abt. B* **1932**, *16*.
7. Zintl, E.; Goubeau, J.; Dullenkopf, W., *Z. Phys. Chem. Abt. A* **1931**, *154*.
8. Zintl, E.; Harder, A. Z., *Z. Phys. Chem. Abt. A* **1931**, *154*.

9. Zintl, E.; Harder, A.; Neumayr, S., *Z. Phys. Chem. Abt. A* **1931**, *154*.

10. Queneau, V.; Sevov, S. C., *Angew. Chem. Int. Ed.* **1997**, *36*, 1754.

11. Scharfe, S.; Kraus, F.; Stegmaier, S.; Schier, A.; Fassler, T. F., *Angew. Chem. Int. Ed.* **2011**, *50*, 3630.

12. Fassler, T. F., *Angew. Chem. Int. Ed.* **2001**, *40*, 4161.

13. Corbett, J. D., *Chem. Rev.* **1985**, *85*, 383.

14. Corbett, J. D., *Angew. Chem. Int. Ed.* **2000**, *39*, 670.

15. Spiekermann, A.; Hoffinann, S. D.; Fassler, T. F., *Angew. Chem. Int. Ed.* **2006**, *45*, 3459.

16. Corbett, J. D.; Edwards, P. A., *J. Am. Chem. Soc.* **1977**, *99*, 3313.

17. Critchlow, S. C.; Corbett, J. D., *J. Am. Chem. Soc.* **1983**, *105*, 5715.

18. Fassler, T. F.; Schutz, U., *Inorg. Chem.* **1999**, *38*, 1866.

19. Somer, M.; Carrillo-Cabrera, W.; Peters, E. M.; Peters, K.; von Schnering, H. G., *Z. Anorg. Allg. Chem.* **1998**, *624*, 1915.

20. Goicoechea, J. M.; Sevov, S. C., *J. Am. Chem. Soc.* **2004**, *126*, 6860.

21. Wade, K., *J. Chem. Soc. D* **1971**, 792.

22. Mingos, D. M. P., *Nat. Phys. Sci.* **1972**, *236*, 99.

23. Mingos, D. M. P., *Acc. Chem. Res.* **1984**, *17*, 311.

24. Belin, C. H. E.; Corbett, J. D.; Cisar, A., *J. Am. Chem. Soc.* **1977**, *99*, 7163.

25. Campbell, J.; Dixon, D. A.; Mercier, H. P. A.; Schrobilgen, G. J., *Inorg. Chem.* **1995**, *34*, 5798.

26. Rudolph, R. W.; Wilson, W. L.; Parker, F.; Taylor, R. C.; Young, D. C., *J. Am. Chem. Soc.* **1978**, *100*, 4629.

27. Sevov, S. C.; Goicoechea, J. M., *Organometallics* **2006**, *25*, 5678.

28. Gillett-Kunnath, M. M.; Petrov, I.; Sevov, S. C., *Inorg. Chem.* **2010**, *49*, 721.

29. Xu, L.; Sevov, S. C., *J. Am. Chem. Soc.* **1999**, *121*, 9245.

30. Hauptmann, R.; Fassler, T. F., *Z. Anorg. Allg. Chem.* **2003**, *629*, 2266.

31. Nienhaus, A.; Hoffmann, S. D.; Fassler, T. F., *Z. Anorg. Allg. Chem.* **2006**, *632*, 1752.

32. Downie, C.; Tang, Z. J.; Guloy, A. M., *Angew. Chem. Int. Ed.* **2000**, *39*, 338.

33. Downie, C.; Mao, J. G.; Parmar, H.; Guloy, A. M., *Inorg. Chem.* **2004**, *43*, 1992.

34. Ugrinov, A.; Sevov, S. C., *C. R. Chim.* **2005**, *8*, 1878.

35. Ugrinov, A.; Sevov, S. C., *J. Am. Chem. Soc.* **2002**, *124*, 10990.

36. Ugrinov, A.; Sevov, S. C., *Inorg. Chem.* **2003**, *42*, 5789.

37. Yong, L.; Hoffmann, S. D.; Fassler, T. F., *Z. Anorg. Allg. Chem.* **2004**, *630*, 1977.

38. Corbett, J. D.; Rundle, R. E., *Inorg. Chem.* **1964**, *3*, 1408.

39. Pancharatna, P. D.; Hoffmann, R., *Inorg. Chim. Acta* **2006**, *359*, 3776.

40. Ugrinov, A.; Sevov, S. C., *J. Am. Chem. Soc.* **2003**, *125*, 14059.

41. Ugrinov, A.; Sevov, S. C., *J. Am. Chem. Soc.* **2002**, *124*, 2442.

42. Karipide.A; Haller, D. A., *Acta Crystallogr. Sec. B* **1972**, *B 28*, 2889.

43. Roller, S.; Drager, M.; Breunig, H. J.; Ates, M.; Gulec, S., *J. Organomet. Chem.* **1989**, *378*, 327.

44. Gillett-Kunnath, M. M.; Oliver, A. G.; Sevov, S. C., *J. Am. Chem. Soc.* **2011**, *133*, 6560.

45. Ugrinov, A.; Sevov, S. C., *Chem. Eur. J.* **2004**, *10*, 3727.

46. Pannell, K. H.; Parkanyi, L.; Sharma, H.; Cervanteslee, F., *Inorg. Chem.* **1992**, *31*, 522.

47. Roller, S.; Simon, D.; Drager, M., *J. Organomet. Chem.* **1986**, *301*, 27.

48. Hull, M. W.; Ugrinov, A.; Petrov, I.; Sevov, S. C., *Inorg. Chem.* **2007**, *46*, 2704.

49. Chapman, D. J.; Sevov, S. C., *Inorg. Chem.* **2008**, *47*, 6009.

50. Hull, M. W.; Sevov, S. C., *Angew. Chem. Int. Ed.* **2007**, *46*, 6695.

51. Eichhorn, B. W.; Haushalter, R. C.; Pennington, W. T., *J. Am. Chem. Soc.* **1988**, *110*, 8704.

52. Yong, L.; Hoffmann, S. D.; Fassler, T. F., *Z. Krist. New Cryst. St.* **2005**, *220*, 53.

53. Kesanli, B.; Fettinger, J.; Eichhorn, B., *Chem. Eur. J.* **2001**, *7*, 5277.

54. Campbell, J.; Mercier, H. P. A.; Franke, H.; Santry, D. P.; Dixon, D. A.; Schrobilgen, G. J., *Inorg. Chem.* **2002**, *41*, 86.

55. Yong, L.; Hoffmann, S. D.; Fassler, T. F., *Eur. J. Inorg. Chem.* **2005**, 3663.

56. Downing, D. O.; Zavalij, P.; Eichhorn, B. W., *Eur. J. Inorg. Chem.* **2010**, 890.

57. Goicoechea, J. M.; Sevov, S. C., *Organometallics* **2006**, *25*, 4530.

58. Nienhaus, A.; Hauptmann, R.; Fassler, T. F., *Angew. Chem. Int. Ed.* **2002**, *41*, 3213.

59. Boeddinghaus, M. B.; Hoffmann, S. D.; Faessler, T. F., *Z. Anorg. Allg. Chem.* **2007**, *633*, 2338.

60. Denning, M. S.; Goicoechea, J. M., *Dalton Trans.* **2008**, 5882.

61. Antes, I.; Frenking, G., *Organometallics* **1995**, *14*, 4263.

62. Simoes, J. A. M.; Beauchamp, J. L., *Chem. Rev.* **1990**, *90*, 629.

63. Yong, L.; Boeddinghaus, M. B.; Faessler, T. F., *Z. Anorg. Allg. Chem.* **2010**, *636*, 1293.

64. Scharfe, S.; Faessler, T. F., *Eur. J. Inorg. Chem.* **2010**, 1207.

65. Wang, J.-Q.; Wahl, B.; Faessler, T. F., *Angew. Chem. Int. Ed.* **2010**, *49*, 6592.

66. Spiekermann, A.; Hoffmann, S. D.; Kraus, F.; Fassler, T. F., *Angew. Chem. Int. Ed.* **2007**, *46*, 1638.

67. Schmidbaur, H., *Chem. Soc. Rev.* **1995**, *24*, 391.

68. Bauer, A.; Schmidbaur, H., *J. Am. Chem. Soc.* **1996**, *118*, 5324.

69. Schmidbaur, H., *Gold Bull.* **2000**, *33*, 3.

70. Spiekermann, A.; Hoffmann, S. D.; Fassler, T. F.; Krossing, I.; Preiss, U., *Angew. Chem. Int. Ed.* **2007**, *46*, 5310.

71. Rios, D.; Sevov, S. C., *Inorg. Chem.* **2010**, *49*, 6396.

72. Scharfe, S.; Fassler, T. F.; Stegmaier, S.; Hoffmann, S. D.; Ruhland, K., *Chem. Eur. J.* **2008**, *14*, 4479.

73. Tang, J. A.; Ellis, B. D.; Warren, T. H.; Hanna, J. V.; Macdonald, C. L. B.; Schurko, R. W., *J. Am. Chem. Soc.* **2007**, *129*, 13049.

74. Doyle, G.; Heaton, B. T.; Occhiello, E., *Organometallics* **1985**, *4*, 1224.

75. Goicoechea, J. M.; Sevov, S. C., *Angew. Chem. Int. Ed.* **2005**, *44*, 4026.

76. Goicoechea, J. M.; Sevov, S. C., *J. Am. Chem. Soc.* **2006**, *128*, 4155.

77. Rios, D.; Gillett-Kunnath, M. M.; Taylor, J. D.; Oliver, A. G.; Sevov, S. C., *Inorg. Chem.* **2011**, *50*, 2373.

78. Esenturk, E. N.; Fettinger, J.; Eichhorn, B., *Chem. Commun.* **2005**, 247.

79. Gardner, D. R.; Fettinger, J. C.; Eichhorn, B. W., *Angew. Chem. Int. Ed.* **1996**, *35*, 2852.

80. Kesanli, B.; Fettinger, J.; Gardner, D. R.; Eichhorn, B., *J. Am. Chem. Soc.* **2002**, *124*, 4779.

81. Esenturk, E. N.; Fettinger, J.; Eichhorn, B., *J. Am. Chem. Soc.* **2006**, *128*, 9178.

82. Wilson, W. L.; Rudolph, R. W.; Lohr, L. L.; Taylor, R. C.; Pyykko, P., *Inorg. Chem.* **1986**, *25*, 1535.

83. Wang, J.-Q.; Stegmaier, S.; Wahl, B.; Faessler, T. F., *Chem. Eur. J.* **2010**, *16*, 1793.

84. Allen, J. M.; Brennessel, W. W.; Buss, C. E.; Ellis, J. E.; Minyaev, M. E.; Pink, M.; Warnock, G. F.; Winzenburg, M. L.; Young, V. G., *Inorg. Chem.* **2001**, *40*, 5279.

85. Kilian, M.; Wadepohl, H.; Gade, L. H., *Organometallics* **2008**, *27*, 524.

86. Esenturk, E. N.; Fettinger, J. C.; Eichhorn, B. W., *J. Am. Chem. Soc.* **2006**, *128*, 12.

87. Kesanli, B.; Halsig, J. E.; Zavalij, P.; Fettinger, J. C.; Lam, Y. F.; Eichhorn, B. W., *J. Am. Chem. Soc.* **2007**, *129*, 4567.

88. Goicoechea, J. M.; Sevov, S. C., *J. Am. Chem. Soc.* **2005**, *127*, 7676.

89. Kocak, F. S.; Zavalij, P.; Lam, Y.-F.; Eichhorn, B. W., *Inorg. Chem.* **2008**, *47*, 3515.

90. Sun, Z.-M.; Xiao, H.; Li, J.; Wang, L.-S., *J. Am. Chem. Soc.* **2007**, *129*, 9560.

91. Zhang, X.; Li, G. L.; Xing, X. P.; Zhao, X.; Tang, Z. C.; Gao, Z., *Rapid Commun. Mass Spectrom.* **2001**, *15*, 2399.

92. Neukermans, S.; Wang, X.; Veldeman, N.; Janssens, E.; Silverans, R. E.; Lievens, P., *Int. J. Mass Spectrom.* **2006**, *252*, 145.

93. Chen, X.; Deng, K. M.; Liu, Y. Z.; Tang, C. M.; Yuan, Y. B.; Hu, F. L.; Wu, H. P.; Huang, D. C.; Tan, W. S.; Wang, X., *Chem. Phys. Lett.* **2008**, *462*, 275.

Chapter 2 – Reactivity of group 14 Zintl ions towards homoleptic group 12 organometallic reagents

2.1 Introduction

The reactivity of group 14 Zintl clusters towards main group homoleptic organometallic reagents has been studied by a handful of research groups. This has resulted in the isolation and characterisation of a range of *exo*-functionalised cluster anions exhibiting two-centre two-electron bonds to the *exo*-substituents. In the case of the group 15 reagents ER_3 (E = Sb, Bi; R = C_6H_5), examples of the outcome of such reactions are illustrated in the scheme below and will be discussed in detail in the following sections.[1, 2]

$$[Ge_9]^{4-} + ER_3 \longrightarrow [R{-}Ge_9{-}ER_2]^{2-} + 2e^-$$

$$[Ge_9]^{4-} + 2ER_3 \longrightarrow [R_2E{-}Ge_9{-}ER_2]^{2-} + 2R^-$$

$$2[Ge_9]^{4-} + 2ER_3 \longrightarrow [R_2E{-}Ge_9{-}Ge_9{-}ER_2]^{4-} + 2R^- + 2e^-$$

Scheme 2.1 Reactions between $[Ge_9]^{4-}$ and group 15 homoleptic reagents ER_3 have yielded a range of *exo*-functionalised cluster anions.

This reactivity can be explained by the fact that in solution the Zintl cluster $[Ge_9]^{4-}$ exists in equilibrium between $[Ge_9]^{2-}$, $[Ge_9]^{3-}$ and free solvated electrons. The free solvated electrons can be used to reductively cleave the E–R bonds in group 14 and 15 homoleptic organometallic reagents such as $E^{V}R_3$ and $E^{IV}R_4$, respectively.[1-3] The resulting negatively charged fragments $[E^{V}R_2]^-$ and $[E^{IV}R_3]^-$ have very nucleophilic lone pairs of electrons, which can interact with the low-lying empty LUMO orbital of $[Ge_9]^{2-}$ and/or the half filled HOMO of $[Ge_9]^{3-}$.

As mentioned in the Introduction, reactions of Rb_4Ge_9 with group 15 organometallics such as PPh_3 and $AsPh_3$ in the presence of 2,2,2-crypt were found to yield a linear trimer $[Ge_9{=}Ge_9{=}Ge_9]^{6-}$.[4] When moving to the heavier group 15 analogues such as $SbPh_3$ and $BiPh_3$, the reactivity of these main group homoleptic organometallics towards group 14 Zintl clusters is very different. Instead of the oxidative coupling of the $[Ge_9]^{4-}$ clusters, one of the E^V–C bonds (E^V = Sb, Bi) in the organometallic reagent is reductively cleaved and the remaining $E^V(C_6H_5)_2$ fragment coordinates to the cluster through a two-centre two-electron *exo* bond.[1, 2]

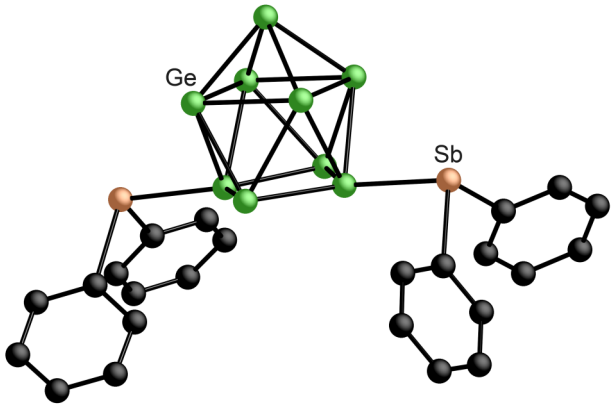

Figure 2.1 Structure of $[Ph_2Sb–Ge_9–SbPh_2]^{2-}$ determined by single crystal X-ray diffraction. The bonds between Sb and the nonagermanide cluster are conventional two-centre two-electron single bonds.

Recently the reaction between K_4Ge_9 and $SbPh_3$ has been reinvestigated by systematically varying the reaction conditions. This has resulted in the isolation and characterisation of a range of heteroatomic clusters including a dimeric species $[(SbGe_8)–(Ge_8Sb)]^{4-}$, $[Sb_2Ge_7]^{2-}$ and $[(SbGe_8)–SbPh_2]^{2-}$.[5]

The reactivity of $[Ge_9]^{4-}$ towards group 14 organometallic reagents such as $E^{IV}R_4$, $E^{IV}R_3Cl$ and $E^{IV}R_3^-$ (E^{IV} = Ge, Sn; R = Me, Ph) is similar to that of the group 15 analogues.[3] This has also yielded a series of different *exo*-functionalised Zintl cluster anions.

	Monosubstituted $[Ge_9–ER_3]^{3-}$	Disubstituted $[R_3E–Ge_9–ER_3]^{2-}$	Disubstituted dimer $[R_3E–Ge_9–Ge_9–ER_3]^{4-}$
$[Ge_9]^{4-}$ + $SnPh_4$		✓	
$[Ge_9]^{4-}$ + Ph_3SnCl			✓
$[Ge_9]^{4-}$ + SnR_3^-	✓	✓	
$[Ge_9]^{4-}$ + GeR_3^-		✓	

Table 2.1 A summary of *exo*-functionalised Zintl cluster anions obtained from reactions between $[Ge_9]^{4-}$ and group 14 organometallic reagents.

Sevov and co-workers reported that such reactions proceed via the anionic nucleophilic addition of R_3E^- to the nine-atom Zintl cluster. It is interesting to note that the clusters with one *exo* single bond have a 3– charge, whereas systems with two *exo* single bonds have an overall charge of 2– associated with each nine-atom cluster.

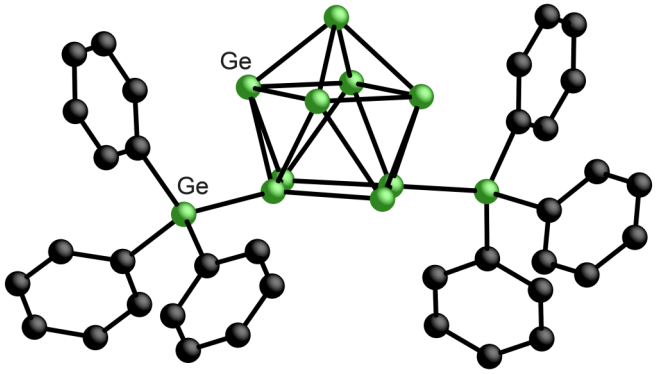

Figure 2.2 Structure of the disubstituted $[Ph_3Ge–Ge_9–GePh_3]^{2-}$ determined by single crystal X-ray diffraction.

Group 12 elements are at the borderline between the main group elements and transition metals. The reactivity of group 14 Zintl ions towards $ZnPh_2$ was explored by Sevov and Goicoechea.[6] The reactions between K_4E_9 (E = Si, Ge, Sn, Pb), 2,2,2-crypt and $ZnPh_2$ in ethylenediamine yielded the functionalised *closo*-clusters $[E_9ZnPh]^{3-}$. They were characterised as the $[K(2,2,2\text{-crypt})]^+$ salts in the solid state by single crystal X-ray diffraction, which revealed that these clusters were all bicapped square antiprisms with the ZnPh fragment occupying one of the capping positions. Similar to the reactions with group 14 and 15 homoleptic organometallic reagents, it also proceeds *via* a reductive cleavage of one of the M–C bonds. The coordination mode is, however, very different to that observed for the group 14 and 15 organometallics, because the ZnPh fragment is electrophilic and interacts with the open square face of the cluster. The same coordination mode is observed for the electrophilic $[M(CO)_3]$ (M = Cr, Mo, W) functionalised Zintl clusters $[E_9M(CO)_3]^{4-}$ (E = Sn, Pb).[7-11]

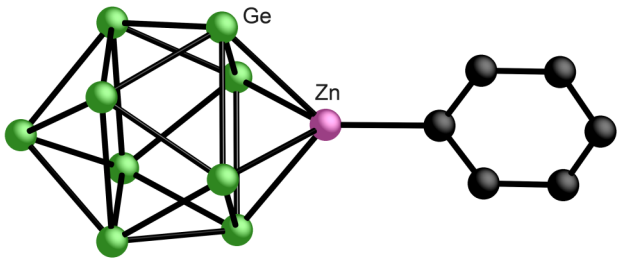

Figure 2.3 Structure of $[Ge_9ZnPh]^{3-}$ determined by single crystal X-ray diffraction. The organometallic moiety ZnPh coordinates to the cluster at the open square face in an η^4 mode.

Moving down group 12, the reaction of group 14 Zintl ions $[Ge_9]^{4-}$ with $HgPh_2$ was studied in ethylenediamine.[12] This was found to yield crystals of $[Hg_3(Ge_9)_4]^{10-}$, which consists of four nonagermanide clusters linked by three Hg atoms. The Fässler group have also reported the synthesis and characterisation of crystalline linear polymeric $^1_\infty[HgGe_9]^{2-}$ by reacting K_4Ge_9

with elemental mercury.[13, 14] The discrete unit of $[Hg_3(Ge_9)_4]^{10-}$ can be converted to the infinite polymeric chain of $^1_\infty[HgGe_9]^{2-}$ by dissolving the crystals of the former in pyridine and layering with toluene.

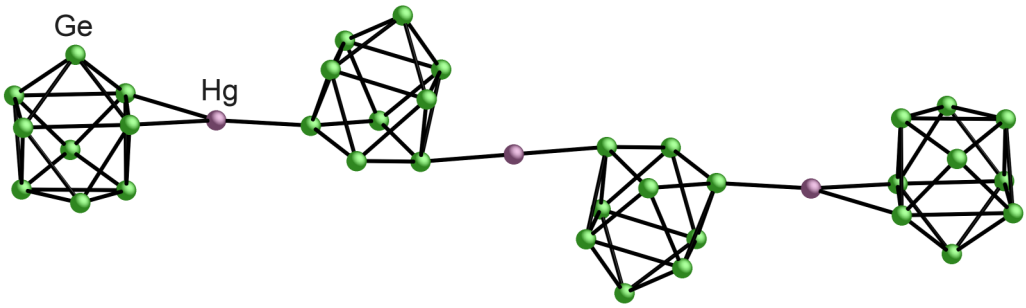

Figure 2.4 Structure of $[Hg_3(Ge_9)_4]^{10-}$ determined by single crystal X-ray diffraction. This links the discrete parent clusters $[Ge_9]^{4-}$ and the polymeric species $^1_\infty[HgGe_9]^{2-}$.

A frontier orbital analysis of a $[Ge_9]^{4-}$ cluster predicts that anionic main group nucleophiles will attack one of the vertices in the triangular faces of the tricapped trigonal prism to give *exo*-functionalised Zintl clusters. Conversely electrophiles such as the organometallic ZnPh fragment have three empty orbitals that can interact with three filled orbitals of $[E_9]^{4-}$, and therefore the electrophilic attack occurs at the open square face of the cluster.

As discussed above, the reaction of group 14 Zintl clusters with diphenylzinc proceed *via* reductive cleavage of one of the Zn–Ph bonds to yield the novel functionalised clusters $[E_9ZnPh]^{3-}$. We decided to study how the size and electronic properties of the R group affect the outcome of reactions between other homoleptic organozinc reagents ZnR_2 (R = mesityl, isopropyl) and K_4E_9 (E = Ge, Sn, Pb). Following the success of the M–C bond activation reactions between group 14 Zintl clusters and diphenylzinc and diphenylmercury, the next

logical step was to explore the reactivity of $[E_9]^{4-}$ with homoleptic diorganocadmium reagents such as diphenylcadmium and dimesitylcadmium. This chapter describes the synthesis and characterisation of a series of functionalised Zintl clusters $[E_9MR]^{3-}$ (E = Ge, Sn, Pb; M = Zn, Cd; R = Ph, mes, ^{i}Pr), and the dimeric species $[Ge_9CdGe_9]^{6-}$ and $[Pb_9CdCdPb_9]^{6-}$. Solution reactivity studies of the cluster anions $[E_9CdPh]^{3-}$ (E = Sn, Pb) towards $HSn(^{n}Bu)_3$ were also studied and resulted in the isolation of *closo*-$[E_9CdSn(^{n}Bu)_3]^{3-}$.

2.2 Results and discussion

2.2.1 Synthesis and characterisation of *closo*-$[E_9MR]^{3-}$ clusters

2.2.1.1 General synthetic methods

In a typical reaction an intermetallic precursor K_4E_9 (E = Ge, Sn, Pb), 2,2,2-crypt and a group 12 organometallic MR_2 (M = Zn, Cd; R = Ph, mes) were weighed out in a 1 : 3½ : 1 molar ratio and mixed in a small Schlenk tube in a glovebox. The reaction vessel was then transferred onto a Schlenk line. Dry ethylenediamine (~ 2 mL) was added to the solid mixture via a metal cannula under argon and the reaction mixture stirred for 1 h. The resulting solution was then filtered into a crystallisation ampoule and layered with ~ 20 mL toluene. After a few days, crystals suitable for single crystal X-ray diffraction were obtained at the interface of the two solvents on the walls of the ampoule.

Due to the light sensitivity of the organocadmium compounds, all Schlenk tubes and crystallisation ampoules employed for those reactions were wrapped with aluminium foil. For the reactions between K_4E_9 (E = Ge, Sn, Pb), 2,2,2-crypt and $Zn(^{i}Pr)_2$, diisopropylzinc was added *via* a microsyringe to an ethylenediamine solution of the Zintl precursor and 2,2,2-crypt.

$Zn(^{i}Pr)_2$ was stored in a Schlenk tube under argon at –20 °C. The majority of these reactions yielded the novel M–R functionalised clusters *closo*-$[E_9MR]^{3-}$ (E = Ge, Sn, Pb; M = Zn, Cd; R = ^{i}Pr, Ph, mes), which were characterised both in solution and the solid-state.

2.2.1.2 Electronic structure of the $[E_9MR]^{3-}$ cluster anions

These reactions are analogous to those between $ZnPh_2$ and group 14 Zintl ions, and proceed *via* the loss of one of the R groups of the MR_2 reagent by a single electron reduction to give an M–R moiety and a strong base R^- (which can readily deprotonate ethylenediamine *via* a solvolysis reaction to give RH and an amide). M–R fragments are electrophilic and can attack the open square face of the monocapped square antiprismatic $[E_9]^{3-}$ to give the resulting *closo*-$[E_9MR]^{3-}$. The shape of these clusters is that of a bicapped antiprism with the metal atom of the M–R fragment occupying one of the capping positions.

As discussed in the Introduction, the coordinated metal atom can be considered to be *sp* hybridised, with one of the hybrid orbitals used for bonding to the phenyl group. The other *sp* hybrid orbital and the degenerate p_x and p_y orbitals are empty and match the symmetry of highest energy filled frontier orbitals of the cluster. Interaction between the empty *sp* hybrid orbital and a cluster orbital that is totally bonding within the open square face results in σ bonding and antibonding orbitals. There are two degenerate cluster orbitals that consist of mainly out of phase p_π orbitals at opposite corners of the open square base. These interact with empty degenerate p_x and p_y orbitals of the metal atom resulting in π bonding and antibonding orbitals. Thus the open square face of the nine-atom cluster acts as a six-electron donor similar to cyclopentadienyl anion. This discussion of the electronic structure is completely analogous

to that of the previously reported *closo*-$[E_9ZnPh]^{3-}$. The cluster anion can be considered to be isoelectronic with the (η^5-Cp*)Zn(η^1-Cp*) complex reported by Budzelaar and co-workers.[15]

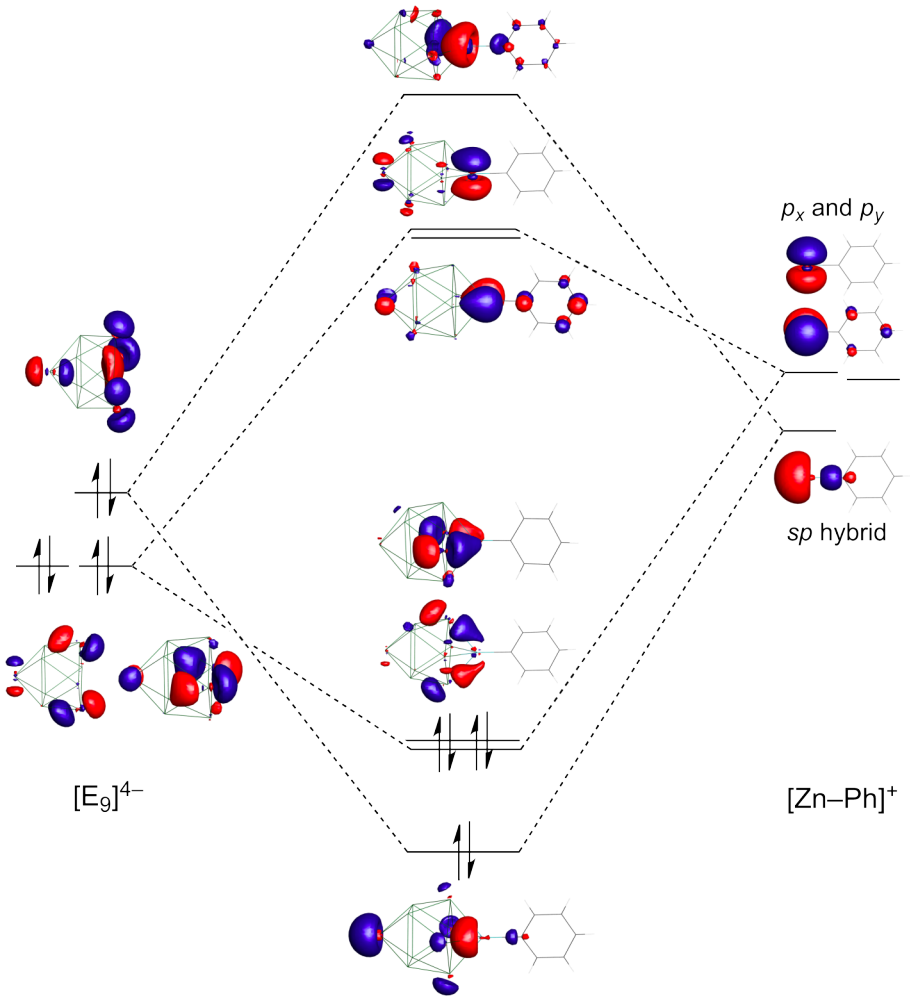

Figure 2.5 Analysis of the interactions between frontier orbitals of $[E_9]$ and the Zn–Ph fragment in the formation of $[E_9ZnPh]^{3-}$.

The reaction scheme can be represented as follows:

$$[E_9]^{4-} \rightleftharpoons [E_9]^{3-} + e^- \xrightarrow{MR_2} [E_9MR]^{3-} + R^- \xrightarrow{en} RH + H_2NCH_2CH_2NH^-$$

Scheme 2.2 Loss of one of the R groups by single electron reduction to give the *closo*-$[E_9MR]^{3-}$ anion and a strong base R^- that can readily deprotonate ethylenediamine.

All the clusters have the overall geometry of a bicapped square antiprism. Each group 14 atom has 4 valence electrons. Two of them are used for cluster bonding, which is analogous to the B–H unit of deltahedral borane clusters. The other 2 electrons form a lone pair and occupy an orbital pointing radially outwards from the cluster. For the M–R fragment, both Zn and Cd have 2 valence electrons: one of them is used for M–C bonding and the other one contributes to cluster bonding. Taking into account the overall 3– charge, there are (2 × 9) + 1 + 3 = 22 = 2*n* + 2 cluster bonding electrons. According to the Wade-Mingos rules, such a cluster should have a *closo*-structure, which is indeed the observed geometry from X-ray crystallographic studies. From an organometallic point of view, the group 12 atom achieves a stable 18-electron configuration by combining the eleven valence electrons from the metal centre, one from the organic substituent and six electrons from the η^4 coordinated cluster.

2.2.1.3 Characterisation of $[E_9Zn(mes)]^{3-}$ (E = Ge, Sn, Pb)

2.2.1.3.1 Single crystal X-ray structural analysis

$[E_9Zn(mes)]^{3-}$ (E = Ge (**1**), Sn (**2**), Pb (**3**))

The E–E distances for $[K(2,2,2\text{-crypt})]_3[Ge_9Zn(mes)]$ range from 2.5327(1) to 2.8852(1) Å, which compare nicely with previously reported distances for the functionalised clusters $[Ge_9ZnPh]^{3-}$: 2.5427(7)–2.8377(8) Å.[6] The Zn–E distances to the four atoms of the capped square lie within the very narrow range of 2.5644(11) to 2.6230(12) Å, which are very similar to the values of those in $[Ge_9ZnPh]^{3-}$: 2.5720(8)–2.5944(9) Å. Finally, the Zn–C distance in the Zn(mes) fragment is 2.001(7) Å (1.994(5) Å for $[Ge_9ZnPh]^{3-}$). Crystals of $[K(2,2,2\text{-crypt})]_3[\mathbf{2}]$•tol and $[K(2,2,2\text{-crypt})]_3[\mathbf{3}]$ show crystallographic disorder and therefore are not suitable for detailed discussion of bond metric data. The data are, however, of sufficient

quality to determine cluster connectivity and charge, and it is evident that reactions of $Zn(mes)_2$ with the tin and lead clusters yield the functionalised *closo*-clusters $[E_9Zn(mes)]^{3-}$ (E = Sn, Pb). All these clusters are bicapped square antiprisms with the Zn(mes) fragment occupying one of the capping positions. The bond metric values are in reasonable agreement with the previously reported Zintl clusters $[E_9ZnPh]^{3-}$.

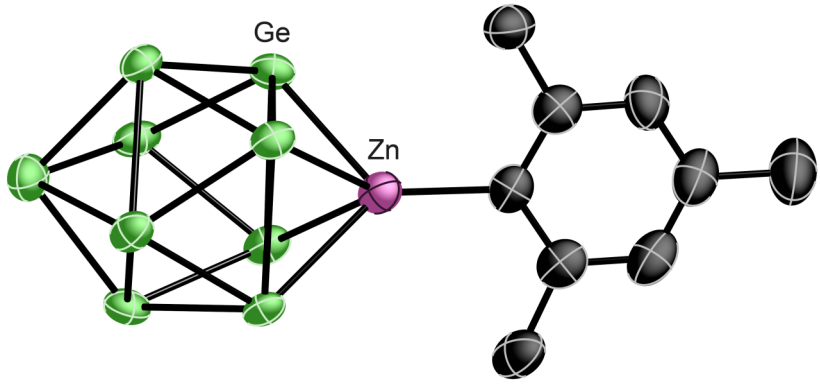

Figure 2.6 Thermal ellipsoid plot of $[Ge_9Zn(mes)]^{3-}$ (**1**) as determined by single crystal X-ray diffraction. Anisotropic displacement ellipsoids pictured at the 50% probability level. Hydrogen atoms have been omitted for clarity.

2.2.1.3.2 Electrospray mass spectrometry

All the compounds were found to be soluble in DMF, and their electrospray mass spectra were recorded in both negative and positive ion modes. Due to the multiple isotopes of Zn, Ge, Sn and Pb, all mass envelopes in the observed mass spectra exhibit characteristic isotopic distributions, which allow them to be assigned unambiguously. As observed from the mass spectra of previously reported anionic Zintl clusters, negative ion mode electrospray mass spectrometry has the tendency to oxidise these highly reduced clusters, lowering their overall negative charges, so only the singly charged anion is detected.[6] It is also often possible to

observe mass envelopes that correspond to the clusters ion-paired with the complexed $[K(2,2,2\text{-crypt})]^+$ cation. The negative ion mode spectra of all the clusters thus display mass envelopes corresponding to $[E_9Zn(mes)]^-$ (e.g. *m/z* 838.5 for $[Ge_9Zn(mes)]^-$) with a single negative charge. Similarly, the spectra also showed mass envelopes corresponding to the ion-paired species $\{[K(2,2,2\text{-crypt})][E_9Zn(mes)]\}^-$ and $\{[K(2,2,2\text{-crypt})]_2[E_9Zn(mes)]\}^-$ (e.g. *m/z* 1253.8 for $\{[K(2,2,2\text{-crypt})][Ge_9Zn(mes)]\}^-$, and 1669.0 for $\{[K(2,2,2\text{-crypt})]_2[Ge_9Zn(mes)]\}^-$). The positive ion mode mass spectra show mass envelopes for the extensively ion-paired species $\{[K(2,2,2\text{-crypt})]_4[E_9Zn(mes)]\}^+$ for E = Ge and Sn (e.g. *m/z* 2500.0 for $\{[K(2,2,2\text{-crypt})]_4[Ge_9Zn(mes)]\}^+$). This peak was not observed for the lead analogue. The experimental data fit well with the calculated isotopic distributions. This confirms the presence and stability of these functionalised Zintl clusters in solution.

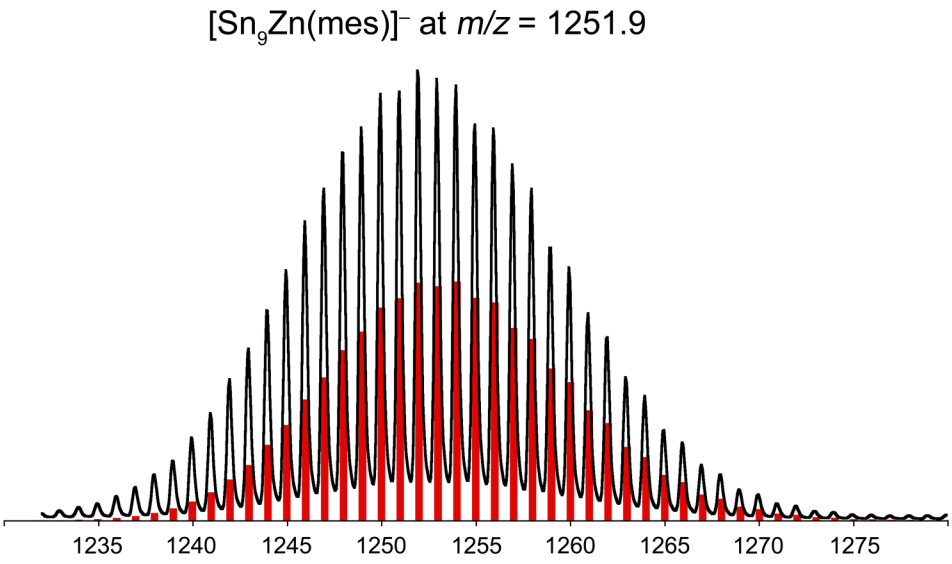

Figure 2.7a Selected mass envelope from the negative ion-mode electrospray mass spectrum of $[Sn_9Zn(mes)]^{3-}$. Experimental data are drawn in black with calculated isotopic distributions in red. The horizontal axis shows the mass-to-charge ratio, *m/z*.

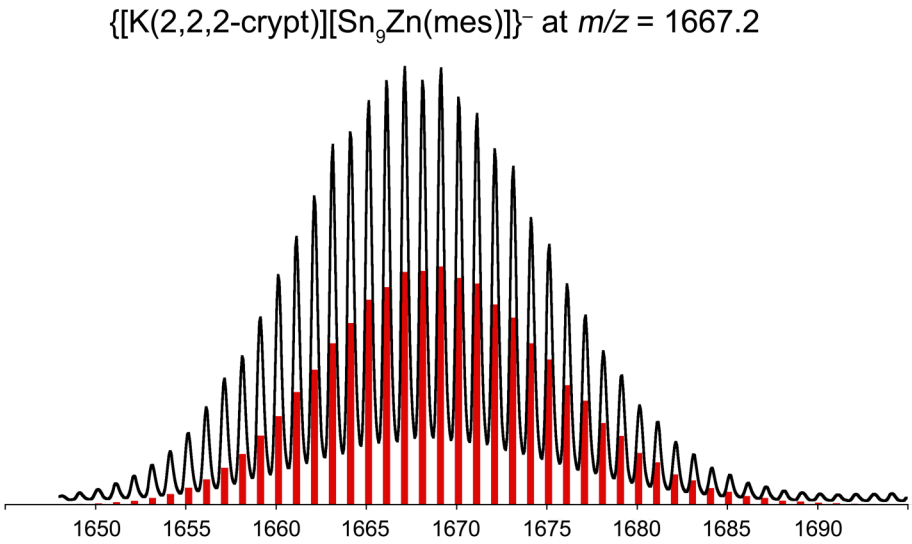

Figure 2.7b Selected mass envelope from the negative ion-mode electrospray mass spectrum of $[Sn_9Zn(mes)]^{3-}$. Experimental data are drawn in black with calculated isotopic distributions in red. The horizontal axis shows the mass-to-charge ratio, *m/z*.

2.2.1.3.3 ^{1}H and ^{13}C{^{1}H} NMR data

Crystals of $[K(2,2,2\text{-crypt})]_3$[**1**], $[K(2,2,2\text{-crypt})]_3$[**2**]•tol and $[K(2,2,2\text{-crypt})]_3$[**3**] were dissolved in d_5-pyridine and characterised by ^{1}H and ^{13}C{^{1}H} NMR spectroscopy. All three ^{1}H NMR spectra show three resonances corresponding to the three distinct proton environments of the mesityl groups. The ^{13}C{^{1}H} spectra of $[K(2,2,2\text{-crypt})]_3$[**1**] and $[K(2,2,2\text{-crypt})]_3$[**3**] show six resonances corresponding to six distinct carbon environments of the mesityl group. The ^{13}C{^{1}H} spectrum of $[K(2,2,2\text{-crypt})]_3$[**2**]•tol showed evidence of only five resonances with that corresponding to the *ipso*-carbon missing. This is not unusual because of the inherent weakness of quaternary carbon signals. In addition, the signal sensitivity is limited by the solubility of the sample in pyridine. The spectra of these clusters do not differ greatly from one to another, as would be expected for such chemically similar systems. The

most significant change in chemical shift is that of the *ipso*-carbon in the $^{13}C\{^{1}H\}$ spectra. This is as expected due to the fact that the *ipso*-carbon is the atom closest to the group 14 cluster and hence will be affected the most by the highly reduced nonatetrelide cage.

The ^{1}H NMR spectrum of the starting material $Zn(mes)_2$ in d_8-THF shows resonances at 6.71 (m), 2.45 (s) and 2.20 (s) ppm in the intensity ratio 2:6:3 and the $^{13}C\{^{1}H\}$ NMR spectrum has peaks at 152.0, 145.4, 136.7, 126.5, 27.3 and 21.6 ppm. Comparing the ^{1}H spectra of $[E_9Zn(mes)]^{3-}$ with that of $Zn(mes)_2$, the *meta*-proton and *ortho*-substituted methyl protons are the most significantly shifted resonances, since they are close to the nine-atom cluster. Comparing the $^{13}C\{^{1}H\}$ spectra of the functionalised clusters and the starting material, the *ipso*-carbon is the most strongly affected one due to its proximity to the Zintl clusters.

	^{1}H δ (ppm)			**$^{13}C\{^{1}H\}$ δ (ppm)**					
Cluster	*m*-C_9H_{11}	*o*-CH_3	*p*-CH_3	*i*-C_9H_{11}	*o*-C_9H_{11}	*m*-C_9H_{11}	*p*-C_9H_{11}	*o*-CH_3	*p*-CH_3
$[Ge_9Zn(mes)]^{3-}$	6.95	3.78	2.19	172.3	144.9	132.1	126.6	31.0	22.2
$[Sn_9Zn(mes)]^{3-}$	6.99	3.85	2.19	n/o	142.1	130.8	126.2	31.4	21.0
$[Pb_9Zn(mes)]^{3-}$	7.28	3.86	2.18	177.4	142.5	134.2	131.4	29.9	23.3

Table 2.2 Summary of ^{1}H and $^{13}C\{^{1}H\}$ NMR chemical shifts for –Zn(mes) functionalised group 14 Zintl clusters. Data were recorded at 298K at 300.17 MHz for ^{1}H and 75.49 MHz for $^{13}C\{^{1}H\}$ NMR experiments, respectively.

In addition, despite numerous attempts to record ^{119}Sn and ^{207}Pb NMR spectra of $[E_9Zn(mes)]^{3-}$ (E = Sn, Pb) in d_5-pyridine at various temperatures, it was not possible to

observe resonances corresponding to these clusters. This again can probably be attributed to the low solubility of the sample in pyridine. In addition, the ^{119}Sn and ^{207}Pb nuclei have very wide chemical shift ranges, hence the spectra of these clusters had to be recorded over long acquisition times, during which the samples decomposed extensively due to their long-term instability in pyridine.

2.2.1.4 Characterisation of $[E_9Zn(^iPr)]^{3-}$ (E = Ge, Sn, Pb)

2.2.1.4.1 Single crystal X-ray structural analysis

$[E_9Zn(^iPr)]^{3-}$ (E = Ge (**4**), Sn (**5**), Pb (**6**))

The E–E distances for $[K(2,2,2\text{-crypt})]_3[\mathbf{4}]\bullet 2tol\bullet en$, $[K(2,2,2\text{-crypt})]_3[\mathbf{5}]\bullet 0.5en$ and $[K(2,2,2\text{-crypt})]_6[\mathbf{6}]_2\bullet en$ lie in the ranges of 2.5519(4)–2.8638(4) Å, 2.8955(8)–3.2641(8) Å and 3.0244(5)–3.4250(5) Å, respectively. These distances are comparable to the previously reported distances for $[E_9ZnPh]^{3-}$: 2.5427(7)–2.8377(8) Å (E = Ge), 2.9156(3)–3.2275(3) Å (E = Sn) and 3.0447(6)–3.4078(5) Å (E = Pb), respectively.[6] The Zn–E distances to the four atoms of the capped square lie within a very narrow range 2.5915(5)–2.6225(5) Å, 2.7702(1)–2.8095(1) Å, and 2.8013(12)–2.8574(12) Å for the cluster anions **4**, **5** and **6**, respectively. In the previously reported $[E_9ZnPh]^{3-}$ clusters, the values are 2.5720(8)–2.5944(9) Å, 2.7397(4)–2.7867(4) Å and 2.7883(13)–2.8411(12) Å for E = Ge, Sn and Pb, respectively. Variation of the organic groups of the homoleptic organometallic reagents does not seem to affect the coordination mode or the geometric features of the resulting functionalised clusters. Finally, the Zn–^{i}Pr bonds are 2.023(3) Å, 2.014(11) Å, and 2.033 Å (average) for **4**, **5** and **6**. The Zn–C bond distances are very similar to one another.

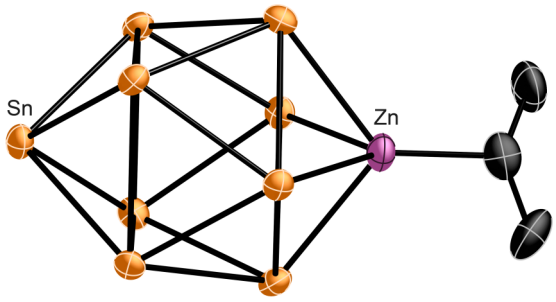

Figure 2.8 Thermal ellipsoid plot of $[Sn_9Zn(^iPr)]^{3-}$ (**5**) determined by single crystal X-ray diffraction. Anisotropic displacement ellipsoids pictured at 50% probability level. Hydrogen atoms have been omitted for clarity.

2.2.1.4.2 Electrospray mass spectrometry

Crystals of $[K(2,2,2\text{-crypt})]_3$[**4**]•2tol•en, $[K(2,2,2\text{-crypt})]_3$[**5**]•0.5en and $[K(2,2,2\text{-crypt})]_6$[**6**]$_2$•en were found to be soluble in DMF, and their electrospray mass spectra were recorded from such solutions in both negative and positive ion modes. The negative ion mode spectra of all the clusters revealed mass envelopes corresponding to $[E_9Zn(^iPr)]^{3-}$ with a single negative charge (e.g. *m/z* 1175.7 for $[Sn_9Zn(^iPr)]^-$). Similarly the spectra also showed isotopic distributions corresponding to the ion-paired species $\{[K(2,2,2\text{-crypt})][E_9Zn(^iPr)]\}^-$ (e.g. *m/z* 1590.8 for $\{[K(2,2,2\text{-crypt})][Sn_9Zn(^iPr)]\}^-$). In addition the electrospray mass spectra of E = Ge and Sn show mass envelopes corresponding to the ion-paired species $\{[K(2,2,2\text{-crypt})]_2[E_9Zn(^iPr)]\}^-$ (e.g. *m/z* 2006.8 for $\{[K(2,2,2\text{-crypt})]_2[Sn_9Zn(^iPr)]\}^-$). The positive ion mode mass spectra show mass envelopes for the extensively ion-paired species $\{[K(2,2,2\text{-crypt})]_4[E_9Zn(^iPr)]\}^+$ for E = Ge and Sn (e.g. *m/z* 2839.0 for $\{[K(2,2,2\text{-crypt})]_4[Sn_9Zn(^iPr)]\}^+$). Isotopic distributions corresponding to $\{[K(2,2,2\text{-crypt})]_2[Pb_9Zn(^iPr)]\}^-$ and $\{[K(2,2,2\text{-crypt})]_4[Pb_9Zn(^iPr)]\}^+$ were not observed due to the low long-term stability of the cluster in

DMF. All the experimental data fit well with the calculated isotopic distributions. This confirms the presence of these functionalised clusters in solution.

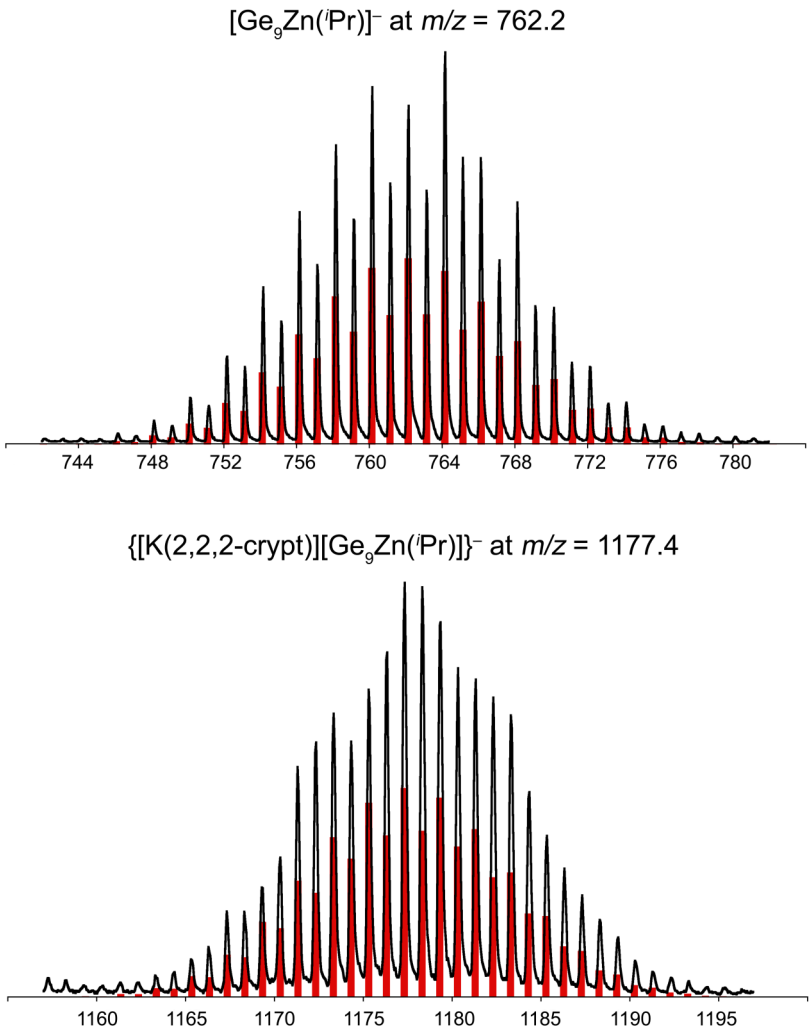

Figure 2.9 Selected mass envelopes from the negative ion-mode electrospray mass spectrum of $[Ge_9Zn(^iPr)]^{3-}$. Experimental data are drawn in black with calculated isotopic distributions in red. The horizontal axis shows the mass-to-charge ratio, *m/z*.

2.2.1.4.3 ^{1}H and ^{13}C{^{1}H} NMR data

Crystals of [K(2,2,2-crypt)]$_3$[**4**]•en·2tol, [K(2,2,2-crypt)]$_3$[**5**]•0.5en and [K(2,2,2-crypt)]$_6$[**6**]$_2$•en were dissolved in d$_5$-pyridine and characterised in solution by ^{1}H and ^{13}C{^{1}H}

NMR spectroscopy. The ^{1}H NMR spectra for all three compounds show two distinct peaks corresponding to the two different proton environments of the isopropyl group. The furthest upfield peak is a septet and corresponds to the methine proton. It couples to six equivalent neighbouring methyl protons to generate the observed multiplet ($^{3}J_{H-H}$ = 8 Hz). The more downfield peak (more deshielded) corresponds to six protons of the two equivalent methyl groups. They couple to a single methine proton giving rise to a doublet. The relative intensities are in the ratio 6:1 (doublet: septet). The $^{13}C\{^{1}H\}$ spectrum shows two distinct peaks corresponding to two different carbon environments of the isopropyl group.

The ^{1}H NMR spectrum of the starting material $Zn(^{i}Pr)_2$ in d_8-THF shows resonances at δ ppm 0.99 (d) and 0.25 (sep) in the ratio of 6:1 and the $^{13}C\{^{1}H\}$ NMR spectrum has peaks at δ ppm 23.6 and 16.4. Comparing the spectra of $[E_9Zn(^{i}Pr)]^{3-}$ with those of $Zn(^{i}Pr)_2$ one can see the chemical shifts of all the resonances have become more deshielded due to the highly negatively charged Zintl clusters. The most affected sites are the carbon alpha to the zinc and the proton bound to it, because they are in closest proximity to the clusters.

	^{1}H δ (ppm)		**$^{13}C\{^{1}H\}$ δ (ppm)**	
Cluster	$CH(CH_3)_2$	$CH(CH_3)_2$	$CH(CH_3)_2$	$CH(CH_3)_2$
$[Ge_9Zn(^{i}Pr)]^{3-}$	2.35	1.36	36.8	27.5
$[Sn_9Zn(^{i}Pr)]^{3-}$	2.51	1.09	60.1	25.3
$[Pb_9Zn(^{i}Pr)]^{3-}$	2.83	0.03	70.4	17.5

Table 2.3 Summary of ^{1}H and $^{13}C\{^{1}H\}$ NMR chemical shifts for $-Zn(^{i}Pr)$ functionalised Zintl clusters. Data were recorded at 298K at 300.17 MHz for ^{1}H and 75.49 MHz for $^{13}C\{^{1}H\}$ NMR experiments respectively.

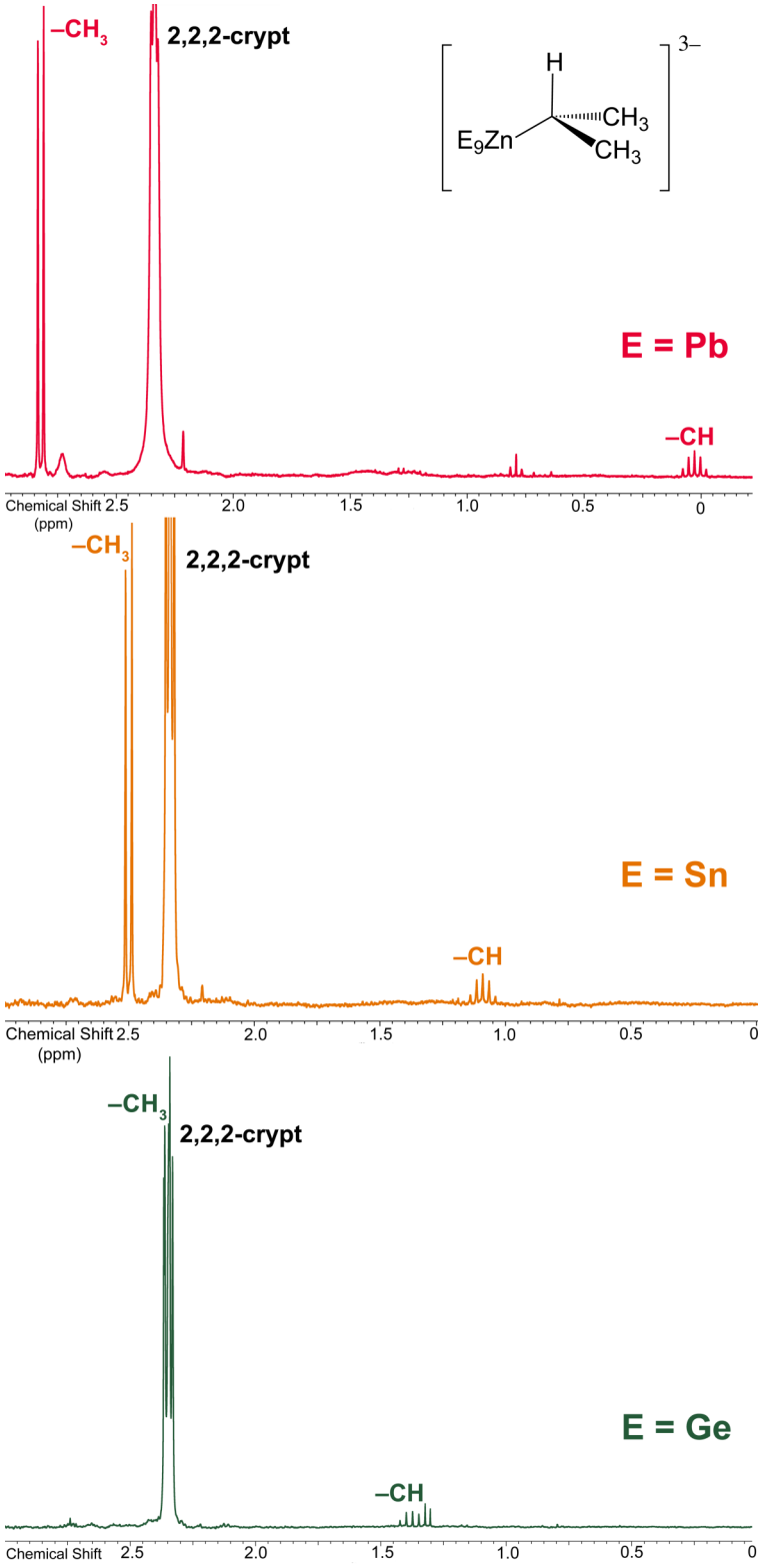

Figure 2.10 Aliphatic region of the ^{1}H NMR spectrum of $[E_9Zn(^{i}Pr)]^{3-}$ (E = Ge, Sn, Pb) in d_5-pyridine. Data were recorded at 298 K at 300.17 MHz.

2.2.1.5 Characterisation of $[E_9CdPh]^{3-}$ (E = Sn, Pb)

2.2.1.5.1 Single crystal X-ray structural analysis

$[E_9CdPh]^{3-}$ (E = Sn (**7**), Pb (**8**))

Crystals of $[K(2,2,2\text{-crypt})]_3[\mathbf{7}]_{0.8}[Sn_9]_{0.2}\bullet en$ and $[K(2,2,2\text{-crypt})]_6[\mathbf{8}]_2\bullet 2en\bullet tol$ were characterised in the solid state by single crystal X-ray diffraction. The crystal structure of **8** contains two crystallographically distinct $[Pb_9CdPh]^{3-}$ (**8**) clusters in the unit cell. The tin analogue contains two clusters, $[Sn_9CdPh]^{3-}$ (**7**) and $[Sn_9]^{3-}$, which occupy the same position in the crystal lattice in a 4:1 ratio. The E–E distances are in the range 2.9082(2)–3.2413(2) Å for **7** and 3.0479(1)–3.4410(1) Å for **8**. They are comparable to the previously reported distances for $[E_9ZnPh]^{3-}$ clusters: 2.9156(3)–3.2275(3) Å for E = Sn, and 3.0447(6)–3.4078(5) Å for E = Pb.[6] The Cd–E distances to the four atoms of the capped square range between: 2.8697(2)–2.9721(2) Å for **7**, and 2.9337(2)–3.0045(1) Å for **8**. These bonds are slightly longer than the previously reported Zn analogues due to the greater atomic radius of Cd.[16] Finally, the Cd–Ph distances are 2.215(1) Å for **7** and 2.188 Å (average) for **8**, which are very similar to one another, as expected.

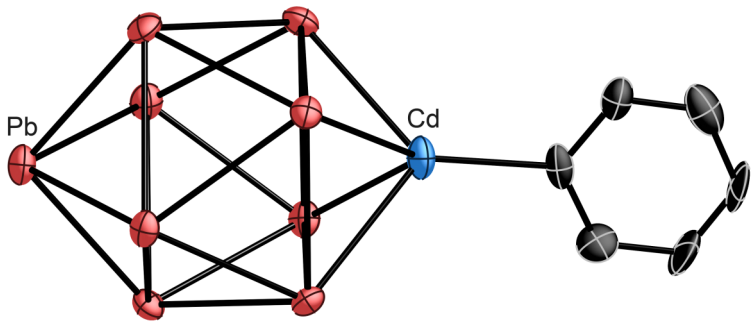

Figure 2.11 Thermal ellipsoid plot of $[Pb_9CdPh]^{3-}$ (**8**) determined by single crystal X-ray diffraction. Anisotropic displacement ellipsoids pictured at 50% probability level. Hydrogen atoms have been omitted for clarity.

2.2.1.5.2 Electrospray mass spectrometry

Both $[K(2,2,2\text{-crypt})]_3[\mathbf{7}]_{0.8}[Sn_9]_{0.2}\bullet en$ and $[K(2,2,2\text{-crypt})]_6[\mathbf{8}]_2\bullet 2en\bullet tol$ were found to be soluble in DMF, and their electrospray mass spectra were recorded from such solutions in negative ion mode. The spectra of both the clusters revealed mass envelopes corresponding to the $[E_9CdPh]^-$ anion (e.g. *m/z* 1258.0 for $[Sn_9CdPh]^-$). Similarly the spectra also showed mass envelopes corresponding to the ion-paired species $\{[K(2,2,2\text{-crypt})][E_9CdPh]\}^-$ (e.g. *m/z* 1673.2 for $\{[K(2,2,2\text{-crypt})][Sn_9CdPh]\}^-$). In addition the electrospray mass spectra of E = Sn show mass envelopes corresponding to the ion-paired species $\{[K(2,2,2\text{-crypt})]_2[Sn_9CdPh]\}^-$ at *m/z* 2089.4. Due to the high molecular mass, the positive ion mode spectra did not show mass envelopes corresponding to extensively ion-paired functionalised clusters such as $\{[K(2,2,2\text{-crypt})]_4[E_9CdPh]\}^+$. All the experimental data fit well with the calculated isotopic distributions patterns, indicating the presence of these highly reduced CdPh functionalised Zintl clusters in solution.

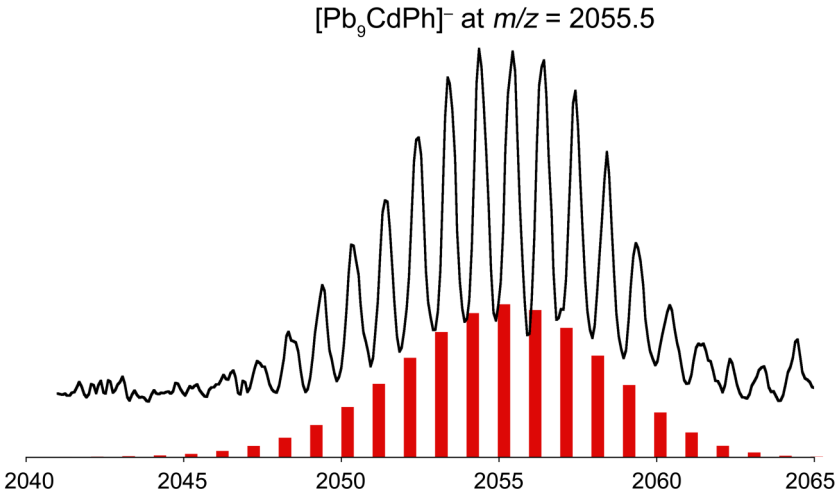

Figure 2.12a Isotopic distribution from the negative ion-mode electrospray mass spectrum of $[Pb_9CdPh]^{3-}$. Experimental data are drawn in black with calculated isotopic distributions in red. The horizontal axis shows the mass-to-charge ratio, *m/z*.

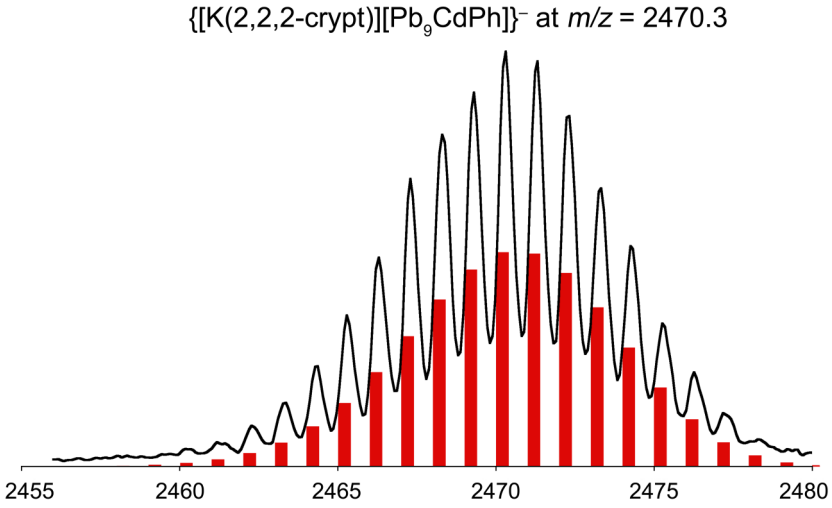

Figure 2.12b Mass envelope from the negative ion-mode electrospray mass spectrum of $[Pb_9CdPh]^{3-}$. Experimental data are drawn in black with calculated isotopic distributions in red. The horizontal axis shows the mass-to-charge ratio, *m/z*.

2.2.1.5.3 ^{1}H and ^{13}C{^{1}H} NMR data

In addition to characterisation by mass spectrometry, crystals of both $[K(2,2,2\text{-crypt})]_3[\mathbf{7}]_{0.8}[Sn_9]_{0.2}$•en and $[K(2,2,2\text{-crypt})]_6[\mathbf{8}]_2$•2en•tol were dissolved in d_5-pyridine and characterised in solution by ^{1}H and ^{13}C{^{1}H} NMR spectroscopy. In the ^{1}H NMR spectra, there are three resonances corresponding to the three distinct proton environments of the phenyl rings in $[E_9CdPh]^{3-}$. The *ortho*-proton of the phenyl ring couples to the *meta* and the *para*-protons with different coupling constants to give a doublet of doublets. The *para*-proton couples to two equivalent *meta* and two equivalent *ortho*-protons with different coupling constants to give a triplet of triplets. The *meta*-proton couples to the *ortho* and *para*-protons with similar coupling constants giving rise to an apparent triplet. As well as the coupling between different protons, $^{113/111}$Cd satellites were also observed for the *ortho* ($^{3}J_{Cd\text{-}H}$ = 33 Hz) and the *meta*-protons ($^{4}J_{Cd\text{-}H}$ = 6 Hz). The coupling constants were confirmed by running the

^{1}H NMR experiment on 300 MHz and 500 MHz spectrometers and found to be independent of magnetic field strength. The $^{13}C\{^{1}H\}$ spectra show three resonances in the aromatic region corresponding to *ortho*, *meta* and *para*-carbon of the phenyl rings in $[E_9CdPh]^{3-}$. All attempts to observe the *ipso*-carbon resonances proved unsuccessful due to the inherent weakness of such resonances and limitations on sample solubility in pyridine. The spectra of these two clusters do not differ greatly from one another, as expected for such chemically similar systems. The most notable difference is in the resonance shift of the *ortho*-protons, which are strongly affected by the different cluster atoms.

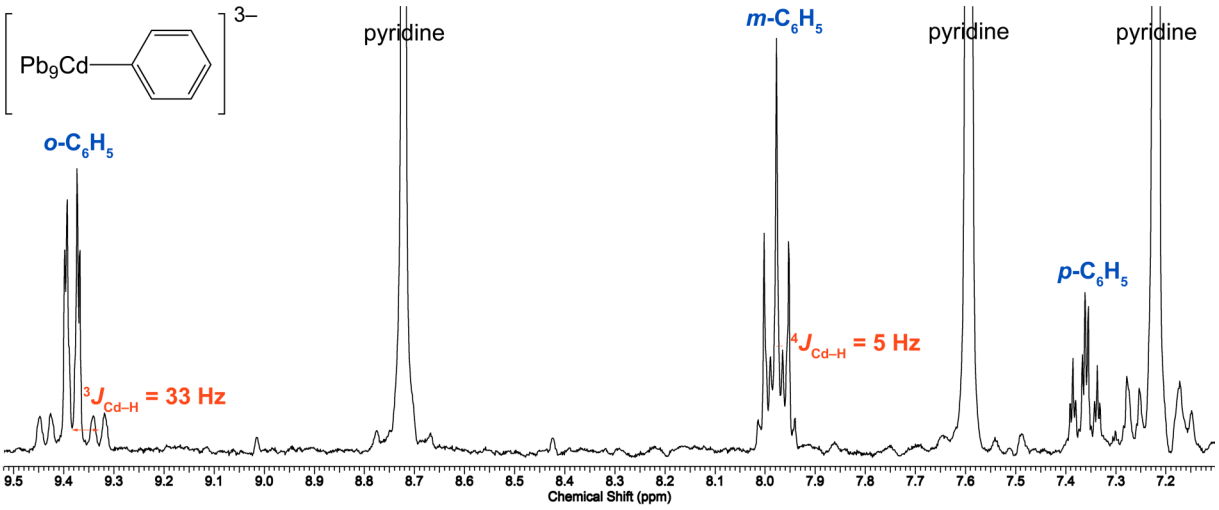

Figure 2.13 Aromatic region of the ^{1}H NMR spectrum of $[Pb_9CdPh]^{3-}$ (**8**) in d_5-pyridine. Data were recorded at 298 K at 300.17 MHz.

The ^{1}H NMR spectrum of $CdPh_2$ in d_8-THF shows resonances at 7.48 (m), 7.07 (m) and 6.98 (m) ppm in a 2:2:1 ratio and the $^{13}C\{^{1}H\}$ NMR spectrum exhibits resonances at 159.9, 140.5, 127.7 and 126.6 ppm. All the proton resonances of $[E_9CdPh]^{3-}$ (E = Sn, Pb) are deshielded relative to the $CdPh_2$ starting material due to the highly reduced Zintl clusters that are attached to the CdPh fragment. The *ortho* aromatic proton experiences the greatest downfield shift due

to the fact that it is the proton closest to the cluster. The resonances in the $^{13}C\{^{1}H\}$ NMR spectrum are very close to related chemical shifts in $CdPh_2$.

2.2.1.5.4 Synthesis and characterisation of $[Ge_9CdGe_9]^{6-}$ (9)

During the course of these studies it was found that the analogous reaction of K_4Ge_9, $CdPh_2$ and 2,2,2-crypt in ethylenediamine resulted in the formation of free benzene; revealed by preliminary ^{1}H NMR studies of the crude reaction mixture. Difficulties in producing crystalline products prompted the use of 18-crown-6 as an alternative alkali metal sequestering agent. Layering the ethylenediamine solution with toluene occasionally produced a highly disordered crystalline phase of $[K(18\text{-crown-6})]^{+}$ salt of $[Ge_9CdGe_9]^{6-}$ (**9**), which was also identified by negative ion mode electrospray mass spectrometry.

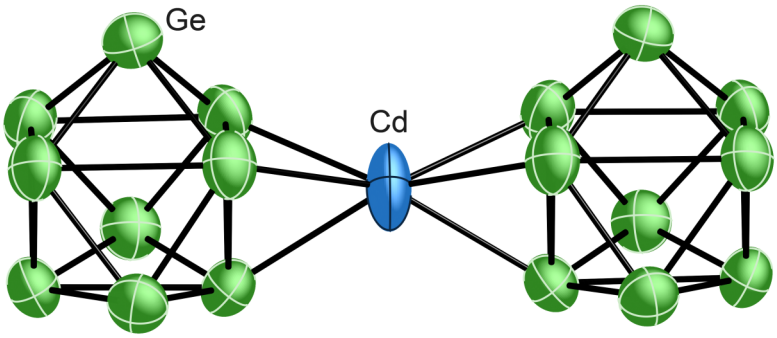

Figure 2.14 Thermal ellipsoid plot of $[Ge_9CdGe_9]^{6-}$ (**9**) determined by single crystal X-ray diffraction. Anisotropic displacement ellipsoids pictured at 50% probability level. The Cd atom coordinates to each of the clusters at one of the triangular faces through a η^3 mode.

The Cd bridged dimeric anion $[Ge_9CdGe_9]^{6-}$ exhibits D_{3h} point symmetry with the two clusters eclipsed to each other and a three-fold rotation axis passing through the central Cd atom. The *s* orbital and the triply degenerate p_x, p_y and p_z orbitals of the Cd(II) atom transform

as a_1', a_2'' and e′, respectively. The two nine-atom clusters transform as the symmetric a_1' and antisymmetric a_2'' irreducible representations. Bonding in $[Cd(Ge_9)_2]^{6-}$ can be thought of as that in a related $[EH_2]^{2-}$ type system. This result gives rise to a molecular orbital diagram like that pictured in Figure 2.14. From an organometallic point of view, the group 12 Cd atom achieves a 14-electron configuration by combining the ten valence electrons from the metal centre and four electrons from two η^3-coordinated clusters.

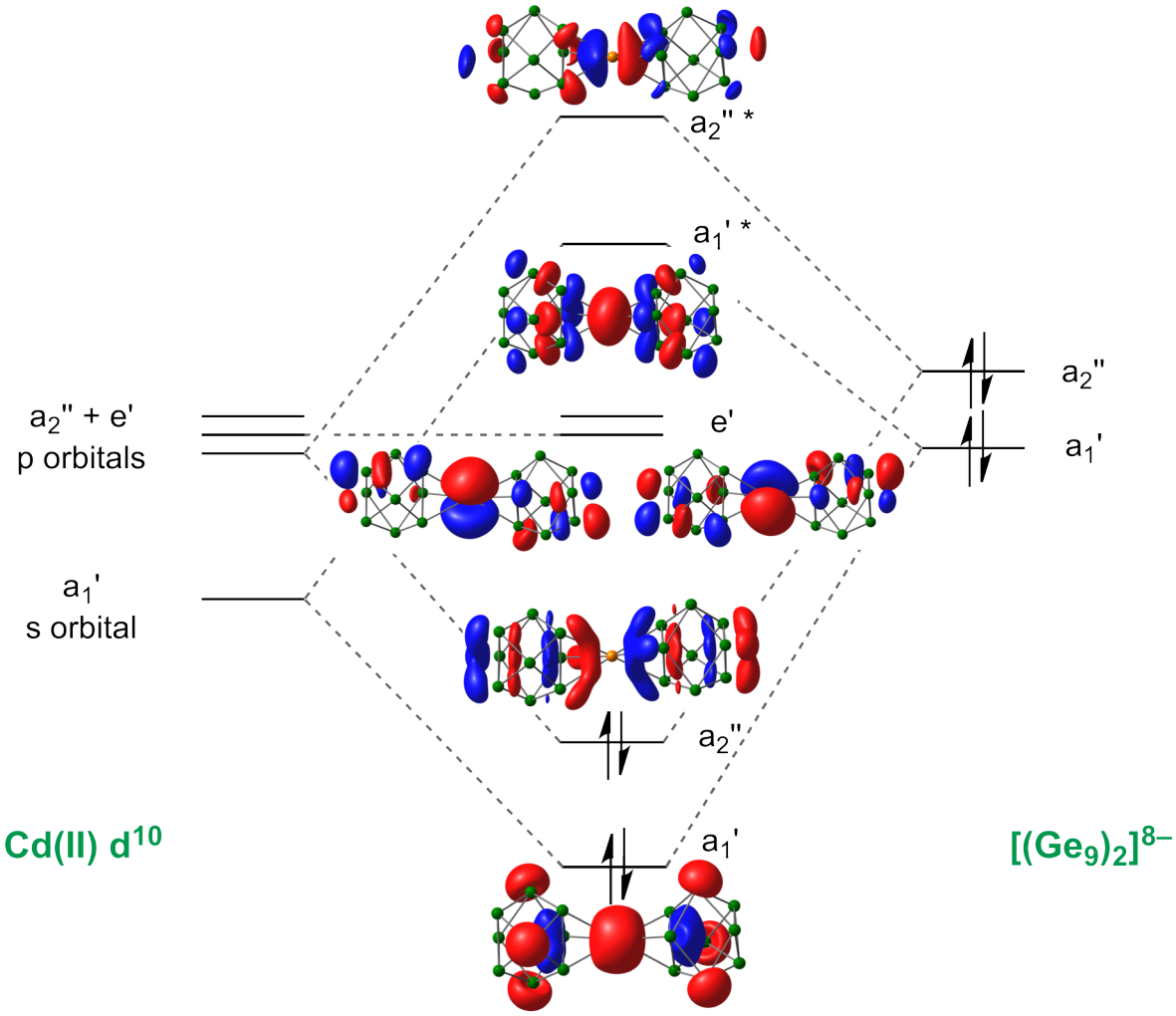

Figure 2.15 Analysis of the interactions between frontier orbitals of $[(Ge_9)_2]^{8-}$ and the central transition metal Cd^{2+} (d^{10}) in the formation of $[Ge_9CdGe_9]^{6-}$.

The electrospray mass spectrometry of the $[K(18\text{-crown-}6)]^+$ salt of $[Ge_9CdGe_9]^{6-}$ (**9**) in solution shows a mass envelope at *m/z* 1802.3 for the extensively ion-paired species $\{K_2[K(18\text{-crown-}6)][Ge_9CdGe_9]\}^-$, and one at 2066.4 corresponding to $\{K[K(18\text{-crown-}6)]_2[Ge_9CdGe_9]\}^-$. It demonstrates the presence of the cadmium-bridged dimer $[Ge_9CdGe_9]^{6-}$ in solution. The low yield of this reaction has prevented further characterisation of the product.

As discussed above, in solution the $[Ge_9]^{4-}$ clusters exist in equilibrium between different charges and free solvated electrons. This first step of the reaction mechanism is presumably similar to that of the functionalised Zintl clusters $[E_9MR]^{3-}$, which involves the single electron reductive cleavage of the Cd–C bond. At present is not clear what subsequently happens. The resulting CdPh fragment may coordinate to the nonagermanide cluster to give the presumably unstable functionalised cluster $[Ge_9CdPh]^{3-}$, before the remaining Cd–Ph bond is reductively cleaved to give the final product $[Ge_9CdGe_9]^{6-}$. More studies are needed to fully understand the reaction mechanism.

2.2.1.6 Characterisation of $[E_9Cd(mes)]^{3-}$ (E = Sn, Pb)

2.2.1.6.1 Single crystal X-ray structural analysis

$[E_9Cd(mes)]^{3-}$ (E = Sn (**10**), Pb (**11**))

The –Cd(mes) functionalised group 14 Zintl clusters have been synthesised and characterised for both tin and lead. Potassium salts of $[E_9Cd(mes)]^{3-}$ (E = Sn, Pb) synthesised from multiple solvent systems and sequestering agents all show crystallographic disorder, and only partially solved structures are obtained from single crystal X-ray diffraction experiments. While the data quality is not good enough to provide bond metric values, it does, however, show that the

clusters have the same coordination mode as the previously discussed phenyl analogues $[E_9CdPh]^{3-}$ (E = Sn, Pb). The reaction proceeds via reductive cleavage of one of the Cd–mes bonds to give free mesitylene (see ^{1}H NMR data below) and the *closo*-functionalised Zintl clusters $[E_9Cd(mes)]^{3-}$.

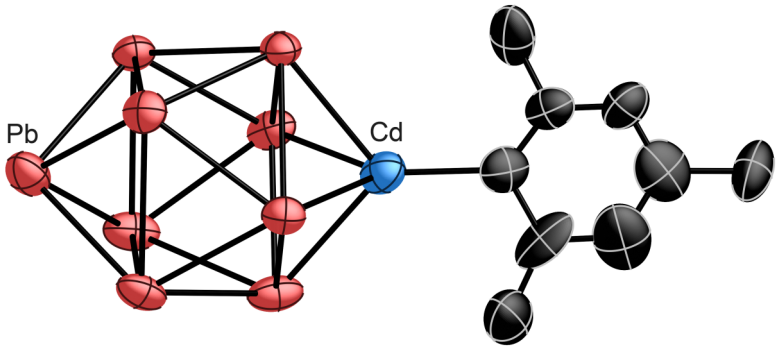

Figure 2.16 Thermal ellipsoid plot of $[Pb_9Cd(mes)]^{3-}$ (**11**) determined by single crystal X-ray diffraction. Anisotropic displacement ellipsoids pictured at 50% probability level. Hydrogen atoms have been omitted for clarity.

2.2.1.6.2 Electrospray mass spectrometry

Crystalline cryptated potassium salts of $[E_9Cd(mes)]^{3-}$ (E = Sn(**10**), Pb(**11**)) were found to be soluble in DMF, and their electrospray mass spectra were recorded from such solutions in negative ion mode. The negative ion mode spectra of E = Sn revealed mass envelopes corresponding to $[Sn_9Cd(mes)]^-$ at *m/z* 1300.2. Similarly the spectra also showed mass envelopes corresponding to the ion-paired species $\{[K(2,2,2\text{-crypt})][Sn_9Cd(mes)]\}^-$ (*m/z* 1715.5) as well as the extensively ion-paired species $\{[K(2,2,2\text{-crypt})]_2[Sn_9Cd(mes)]\}^-$ (*m/z* 2131.6). Due to the low crystalline yield, low stability of the cluster in DMF solution and high molecular mass, the positive ion mode spectra did not show any mass envelopes

corresponding to these functionalised Zintl clusters. Attempts to record both positive and negative ion mode electrospray mass spectra of $[Pb_9Cd(mes)]^{3-}$ were not successful.

2.2.1.6.3 ^{1}H and $^{13}C\{^{1}H\}$ NMR data

The reactions that produced $[E_9Cd(mes)]^{3-}$ had very low yields and the products were highly sensitive to even trace amounts of air or moisture. Therefore the reaction between K_4Sn_9 and $Cd(mes)_2$ was monitored by ^{1}H and $^{13}C\{^{1}H\}$ NMR spectroscopic measurements of the crude reaction mixture in ethylenediamine with a C_6D_6 capillary. The ^{1}H NMR spectrum shows a singlet at 6.98 ppm corresponding to the aromatic protons of free mesitylene. The resonance that corresponds to the methyl protons of free mesitylene is obscured by an ethylenediamine resonance. The $^{13}C\{^{1}H\}$ spectrum shows a singlet at 138.00 ppm corresponding to the aromatic carbon bound to a methyl group, a singlet at 110.62 ppm corresponding to the aromatic carbon that has a proton attached and a singlet at 21.39 ppm corresponding to the carbon of the methyl group. Both spectra show the formation of free mesitylene in the crude reaction mixture. Considering the very low yield of the reaction and the fact that the product decomposes readily in solution, it is not surprising that the resonances due to the η^1 bound mesityl group in **10** are not easily detected.

For the lead analogue, the reaction mixture was filtered and dried to remove any volatiles present. The ^{1}H NMR spectrum of the solid residue redissolved in d_5-pyridine shows resonances at 7.24 (s), 3.55 (m) and 2.70 (s) ppm due to three different proton environments in the η^1 bound mesityl group in the cluster anion **11**. The $^{13}C\{^{1}H\}$ spectrum shows resonances at 144.4, 134.3, 131.3, 46.0 and 25.7 ppm, corresponding to the five different carbon

environments in the mesityl group, with the resonance corresponding to the *ipso*-carbon missing. Both the ^{1}H and $^{13}C\{^{1}H\}$ NMR spectra also show resonances corresponding to a small amount of free mesitylene present in solution. This suggests that the product is not very stable in solution and readily decomposes to elemental lead and free mesitylene.

The ^{1}H NMR spectrum of the starting material $Cd(mes)_2$ in d_8-THF shows resonances at δ (ppm) 6.76 (m), 2.45 (s) and 2.21 (s) in a 2:6:3 ratio and the $^{13}C\{^{1}H\}$ NMR spectrum exhibits resonances at δ (ppm) 145.3, 138.2, 136.7, 28.2 and 21.5. The resonance corresponding to the *ipso*-carbon of $Cd(mes)_2$ was not observed. Comparing the ^{1}H NMR spectrum of $[Pb_9Cd(mes)]^{3-}$ with that of $Cd(mes)_2$ one can see the chemical shifts of all the resonances have become more deshielded due to the highly negatively charged Zintl clusters. The $^{13}C\{^{1}H\}$ NMR spectrum of the cluster $[Pb_9Cd(mes)]^{3-}$ seems to closely resemble to that of $Cd(mes)_2$.

2.2.2 Synthesis and characterisation of $[Pb_9CdCdPb_9]^{6-}$ (12)

2.2.2.1 Synthetic method

While carrying out these studies, we observed that the reaction of K_4Pb_9 and 2,2,2-crypt with $Cd(mes)_2$ in a 1:1 stoichiometric ratio (K_4Pb_9:$Cd(mes)_2$) formed a crystalline phase of $[K(2,2,2\text{-crypt})]_6[Pb_9CdCdPb_9]\bullet 2en$, accompanied by considerable amounts of metallic precipitate. This is a rare example of a molecular complex with an unsupported sterically accessible Cd–Cd bond. This bond is predominantly stabilised by the electronic properties of the clusters. The only other crystallographically characterised molecular species exhibiting a Cd–Cd bond in the literature is Ar'CdCdAr' (Ar' = C_6H_3-2,6-(C_6H_3-2,6-Pr^{i}_2)$_2$), where the bond is sterically blocked by the use of bulky organic substituents.[17] Other structurally characterised

molecular homonuclear metal-metal bonded species of the group 12 elements include Cp*ZnZnCp* (Cp* = C_5Me_5) and Ar'ZnZnAr' (Ar' = C_6H_3-2,6-(C_6H_3-2,6-Pr^i_2)$_2$).[18-22]

The reaction mechanism is presumably similar to that of the cadmium bridged dimer $[Ge_9CdGe_9]^{6-}$. The free solvated electrons resulting from the equilibrium between differently charged $[Pb_9]^{n-}$ (n = 2 – 4) clusters can reductively cleave one of the Cd–C bonds to initially give the functionalised cluster anion $[Pb_9Cd(mes)]^{3-}$. During the course of this reaction there was substantial decomposition leaving elemental lead, which would release more solvated electrons. These electrons break the remaining Cd–C bond to give the $[Pb_9Cd]^{3-}$ fragment, which then couple together to give the Cd–Cd bridged dimer $[Pb_9CdCdPb_9]^{6-}$. At the moment it is not clear why the reactions between K_4Pb_9 and CdR_2 (R = Ph, mes) give rise to different products. It might be attributed to the subtle difference in bond enthalpy between Cd–Ph and Cd–mes bonds in the two otherwise very similar homoleptic organometallics.

2.2.2.2 Single crystal X-ray structural analysis

Analysis by single crystal X-ray diffraction shows that there are one and a half crystallographically distinct $[Pb_9CdCdPb_9]^{6-}$ clusters in the unit cell of $[K(2,2,2\text{-crypt})]_6$[**12**]•2en. The half moiety contains an inversion centre at the mid-point of the Cd–Cd bond. The distances between two central Cd atoms are 2.697(1) and 2.715(2) Å, which are *ca.* 0.08 Å longer than the value for Ar'CdCdAr' and comparable to the computed single-bond length (2.70 Å) in HCdCdH.[16] The distances between Cd and Pb range between 2.996(1) and 3.113(1) Å and 3.043(1) and 3.102(1) Å for the two distinct clusters in the unit cell. They are similar to the values of those in $[Pb_9CdPh]^{3-}$ (**8**). The Pb–Pb bond lengths in the cluster are

also comparable with those found in the other functionalised lead cluster anions $[Pb_9MR]^{3-}$ (M = Cd, Zn; R = Ph, mes, ^{i}Pr).[6]

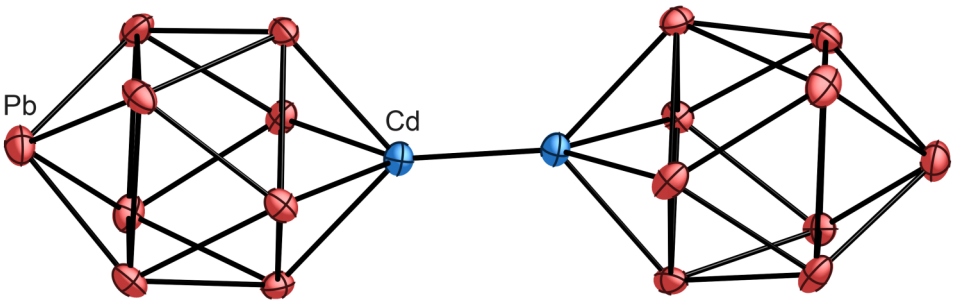

Figure 2.17 Thermal ellipsoid plot of one of the two crystallographically unique cluster anions present in $[Pb_9CdCdPb_9]^{6-}$ (**12**) as determined by single crystal X-ray diffraction. Anisotropic displacement ellipsoids pictured at 50% probability level.

The geometry of the Cd–Cd bridged dimer $[Pb_9CdCdPb_9]^{6-}$ can be described as a *conjuncto* (from Latin, meaning "joined together") species. Each half of the dimer is a 10-vertex bicapped square antiprism with the cadmium atom occupying one of the capping positions. The halves of the dimer are eclipsed, making the overall geometry D_{4h}. The electron counting of $[Pb_9CdCdPb_9]^{6-}$ can be explained as follows: Cd has two valence electrons, of which one is used to form a single bond with the other Cd atom, and the other one is used for cluster bonding. Each half of the dimer has 2 electrons from each Pb atom, 1 electron from Cd and 3 electrons from half of the overall negative charge for cluster bonding. In total there are $2 \times 9 + 1 + 3 = 22 = 2n + 2$ electrons for each half conferring the electron count of a *closo*-cluster according to the Wade-Mingos rules.

2.2.2.3 Computational studies

The DFT calculated optimised structure also has D_{4h} point symmetry, which is consistent with the crystallographically determined geometry. The calculated Cd–Cd bond length is 2.77 Å, which is slightly longer than the experimental value. This is probably due to the fact that the cations surrounding the clusters are modelled using a continuum dielectric model, which is a simplistic picture. DFT calculations show that the HOMO–4 has electron density mostly resembling a Cd–Cd σ bond; LUMO and LUMO+1 are degenerate orbitals with the character of Cd–Cd π bonding; and LUMO+4 is the molecular orbital which shows Cd–Cd σ* bonding character. All these molecular orbitals also have contribution from cluster-based orbitals. The HOMO to HOMO–3 mainly contain contributions from $[Pb_9]^{4-}$ orbitals. The interactions between Cd and Pb_9 in the 10-vertex bicapped square antiprism are similar to those in the previously discussed cluster $[Pb_9ZnPh]^{3-}$ and $[Pb_9CdR]^{3-}$ (R = Ph, mes).

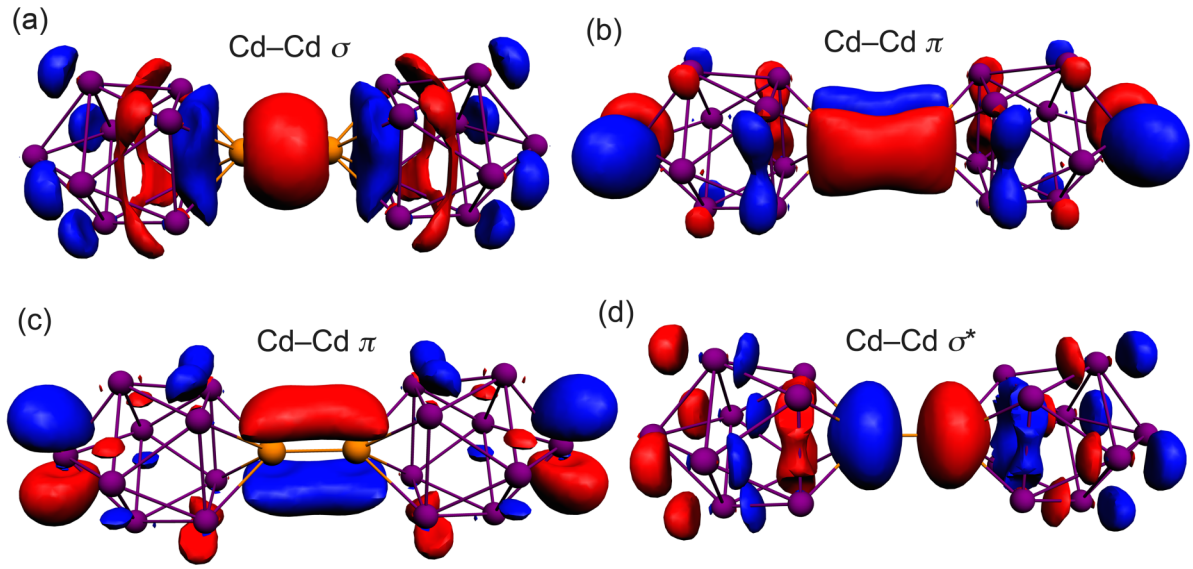

Figure 2.18 Representation of selected frontier molecular orbitals of the cluster anion in **12**: (a) HOMO–4, (b) LUMO, (c) LUMO+1 and (d) LUMO+4.

This reaction has a very low crystalline yield and it proved difficult to make a bulk quantity of the pure sample. This prevented further analysis and characterisation of this unusual Zintl cluster species, such as solution state ^{207}Pb and ^{113}Cd NMR spectroscopy. ^{207}Pb NMR spectroscopy could provide information about whether the dimer is fluxional in solution. ^{113}Cd NMR spectroscopy could be used to establish the existence of a Cd–Cd bond as the resulting resonance would exhibit satellites due to coupling to ^{111}Cd (I = 1/2, 12.80% natural abundance). The low stability of the product in solution and the high molecular mass also makes characterisation by electrospray mass spectrometry difficult.

As proposed earlier the reaction mechanism for formation of the cadmium–cadmium bridged dimer presumably involves forming the intermediate $[Pb_9Cd(mes)]^{3-}$ first. Then further reduction by the free solvated electrons breaks the remaining Cd–mes bond to give $[Pb_9Cd]^{3-}$, which self couples to give the final product $[Pb_9CdCdPb_9]^{6-}$. The reaction between K_4Pb_9 and $CdPh_2$ produces the functionalised cluster $[Pb_9CdPh]^{3-}$ reliably and in good crystalline yield. Therefore, we were prompted to try to actively target the Cd–Cd bridged dimer by synthesizing the $[Pb_9CdPh]^{3-}$ cluster as an intermediate first, and then attempting to reductively cleave the remaining Cd–Ph bond using a reducing agent. If successful, this could be a synthetic way to target other metal–metal bonded species. Attempts to reduce $[Pb_9CdPh]^{3-}$ using potassium metal or the potassium–graphite intercalate KC_8 resulted in reduction of the starting material $[Pb_9CdPh]^{3-}$ to $[Pb_9]^{4-}$, instead of giving the metal–metal bonded product. Subsequent attempts using the radical reducing agent tributyltin hydride still did not yield the desired Cd–Cd bonded species, but instead formed the functionalised *closo*-cluster $[E_9CdSn(^nBu)_3]^{3-}$ (E = Sn (**13**), Pb).

2.2.3 Reactivity studies of $[E_9CdPh]^{3-}$ (E = Sn (7), Pb (8)) with $HSn(^nBu)_3$

2.2.3.1 Synthetic method

Organotin hydrides are good radical reducing agents due to the relatively weak, non-ionic bond between tin and hydrogen that can cleave homolytically, generating two free radicals.[23, 24] Reactions with functionalised clusters were carried out to study whether it could potentially be a systematic way to access compounds like $[Pb_9CdCdPb_9]^{6-}$.

Crystals of $[K(2,2,2\text{-crypt})]_3$[**7**]•en and $[K(2,2,2\text{-crypt})]_6$[**8**]$_2$•2en•tol were dissolved in d_5-pyridine and 1 equivalent of $HSn(^nBu)_3$ was added to the solutions. The NMR tube scale reactions were monitored by ^{1}H NMR spectroscopy. After the reaction had gone to completion, as judged by the disappearance of the hydride resonance at 4.95 ppm, the reaction mixtures were dried in *vacuo* to remove any volatiles present. The solids were then redissolved in pyridine, the solutions filtered and the filtrates layered with toluene for crystallisation. Crystals of $[K(2,2,2\text{-crypt})]_6[Sn_9CdSn(^nBu)_3]_2$•6tol•py (**13**) were obtained in high yield. However, the Pb analogue was not crystallised successfully. The reaction scheme can be represented as follows:

$$[E_9]^{4-}\ (E = Sn, Pb) \xrightarrow[en]{CdPh_2} [E_9CdPh]^{3-} + C_6H_6 + NH_2(CH_2)_2NH^- \xrightarrow[d_5\text{-pyridine}]{HSn(^nBu)_3} [E_9CdSn(^nBu_3)]^{3-} + C_6H_6$$

Scheme 2.3 A two-step reaction to synthesise the *closo*-cluster $[E_9CdSn(^nBu)_3]^{3-}$.

2.2.3.2 Single crystal X-ray structural analysis

The radical reducing agent tributyltin hydride was found to cleave the remaining Cd–Ph bond. However, instead of coupling two $[Sn_9Cd]$ fragments together to give the Cd–Cd bridged

dimeric cluster, the tributyltin group forms a Cd–Sn bond to yield the tributyltin functionalised $[Sn_9CdSn(^nBu)_3]^{3-}$ cluster. As of yet the reaction mechanism leading to the formation of the *closo*-cluster $[E_9CdSn(^nBu)_3]^{3-}$ is not clear. Tributyltin hydride is a radical reducing agent so the reaction could proceed via a radical coupling mechanism.[23, 24] It is also possible the hydrogen of tributyltin hydride is transferred to the phenyl ligand in $[Sn_9CdPh]^{3-}$ via a concerted hydrogen transfer mechanism.[25, 26]

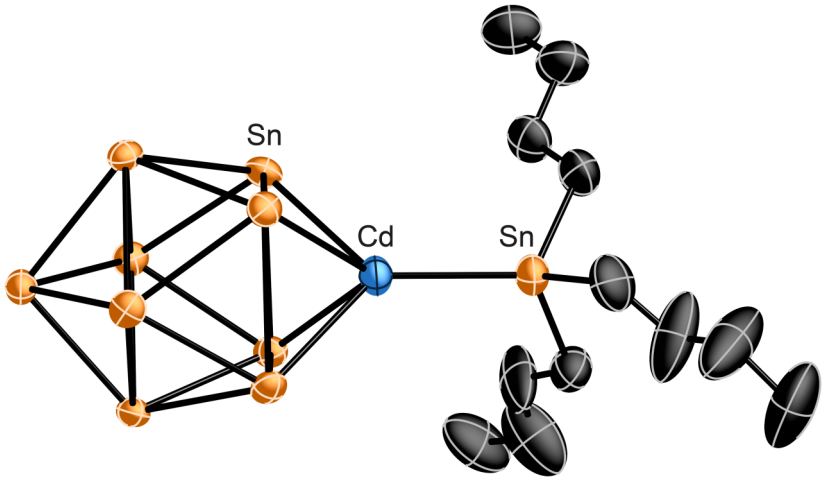

Figure 2.19 Thermal ellipsoid plot of one of the two crystallographically unique cluster anions of $[Sn_9CdSn(^nBu)_3]^{3-}$ (**13**) determined by single crystal X-ray diffraction. Anisotropic displacement ellipsoids pictured at 50% probability level. Hydrogen atoms have been omitted.

Single crystal X-ray diffraction experiments performed on $[K(2,2,2\text{-crypt})]_6[\mathbf{13}]_2$•6tol•py revealed that there are two crystallographically distinct clusters in the asymmetric unit cell. The $[Sn_9Cd]$ fragment is a bicapped square antiprism that has the same geometry as observed in **7**. The Sn–Sn distances in the Sn_9 unit are in good agreement with the values found in **7**, ranging from 2.9206(6) to 3.2695(6) Å for the two clusters in the unit cell. The distances between Cd and the four Sn atoms in the open square face of the cluster are in the range of

2.9074(7) and 2.9504(7) Å. The average Cd–Sn(^{n}Bu)$_3$ bond length is 2.7277 Å, which is shorter than those between Cd and the square face of the cluster, but only slightly longer than the only other previously reported Sn–Cd distance of 2.6758(2) Å in {MeSi[SiMe$_2$N(*p*-Tol)]$_3$Sn}$_2$Cd.[27] The electron counting for the [Sn$_9$Cd] fragment follows the Wade-Mingos rules for a *closo* 10-vertex structure, analogous to other 10-vertex cluster [E$_9$MR]$^{3-}$.

2.2.3.3 Electrospray mass spectrometry

Crystals of [K(2,2,2-crypt)]$_6$[**13**]$_2$•6tol•py were found to be soluble in DMF, and the electrospray mass spectrum was recorded from such solutions in both positive and negative ion modes. The positive ion mode spectrum of [K(2,2,2-crypt)]$_6$[**13**]$_2$•6tol•py revealed mass envelopes corresponding to the extensively ion-paired cluster with a single positive charge, i.e., {[K(2,2,2-crypt)]$_4$[**13**]}$^+$ at *m/z* 3131.0. The negative ion mode mass spectrum of the crystals only shows mass envelopes corresponding to [Sn$_9$CdSn(^{n}Bu)]$^-$ and {[K(2,2,2-crypt)][Sn$_9$CdSn(^{n}Bu)]}$^-$ at *m/z* 1354.5 and 1768.3, respectively, due to extensive fragmentation in the ionisation process. The molecular ion was not observed in the negative ion mode mass spectrum.

2.2.3.4 NMR data

Crystals of [K(2,2,2-crypt)]$_6$[**13**]$_2$•6tol•py were redissolved in d$_5$-pyridine for ^{1}H and ^{13}C{^{1}H} NMR studies. The ^{1}H NMR spectrum shows resonances at δ (ppm) 2.37 (m), 1.74 (tq), 1.44 (m) and 1.08 (t) (m = multiplet, tq = triplet of quartets, t = triplet) corresponding to H$_\beta$, H$_\gamma$, H$_\alpha$ and H$_\delta$ in the butyl group. They have very similar coupling constants and their assignment was confirmed by a ^{1}H COSY experiment. The ^{13}C{^{1}H} NMR spectrum shows four

resonances at δ (ppm) 32.9, 29.5, 17.7 and 15.1 corresponding to four different carbon environments in three magnetically equivalent ^{n}Bu groups. The Pb analogue shows similar NMR spectra and hence it is evident that these two reactions give similar products despite the fact that crystallisation of **14** was unsuccessful.

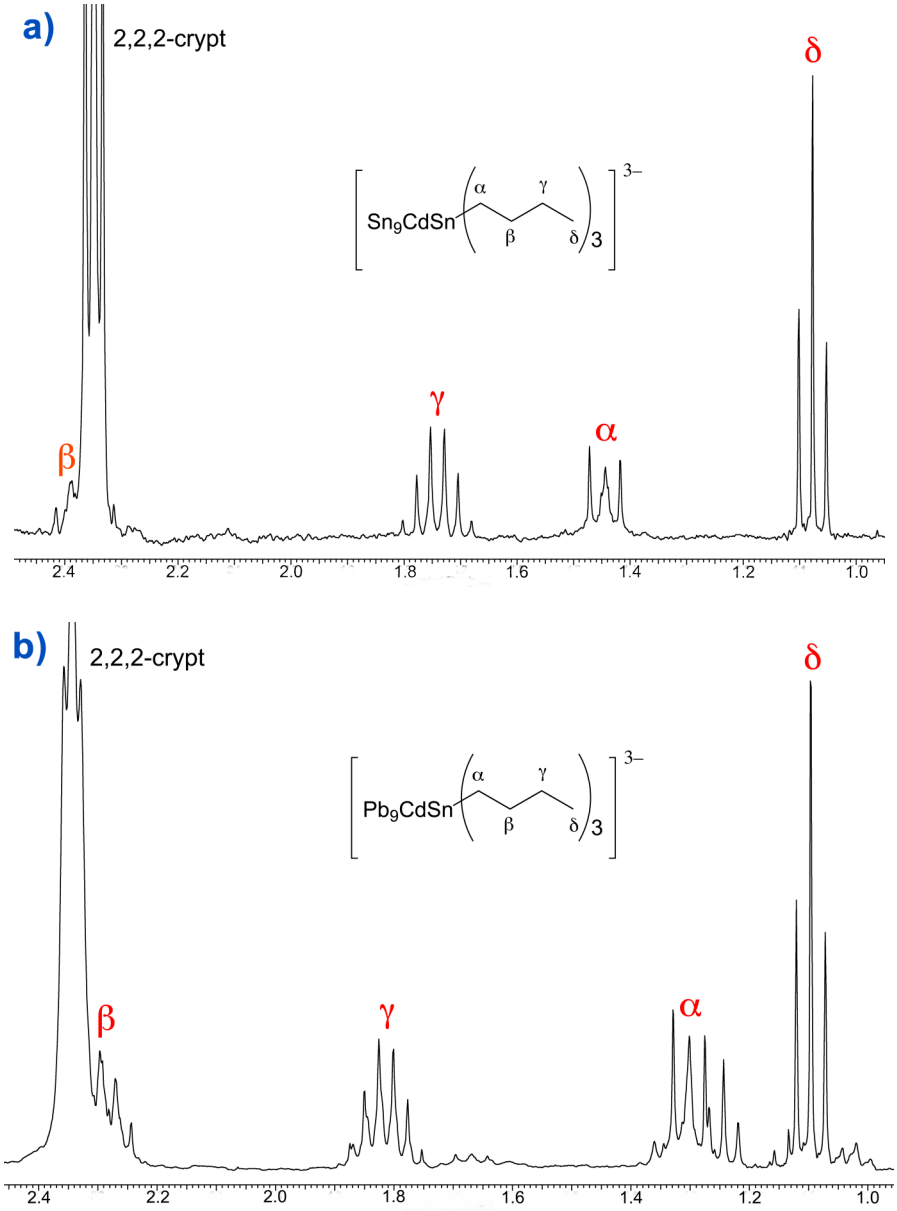

Figure 2.20 Aliphatic regions of ^{1}H NMR spectra for a) $[Sn_9CdSn(^{n}Bu)_3]^{3-}$ (**13**) and b) $[Pb_9CdSn(^{n}Bu)_3]^{3-}$ (**14**) collected in d_5-pyridine. Data were collected at 298 K at 300.17 MHz.

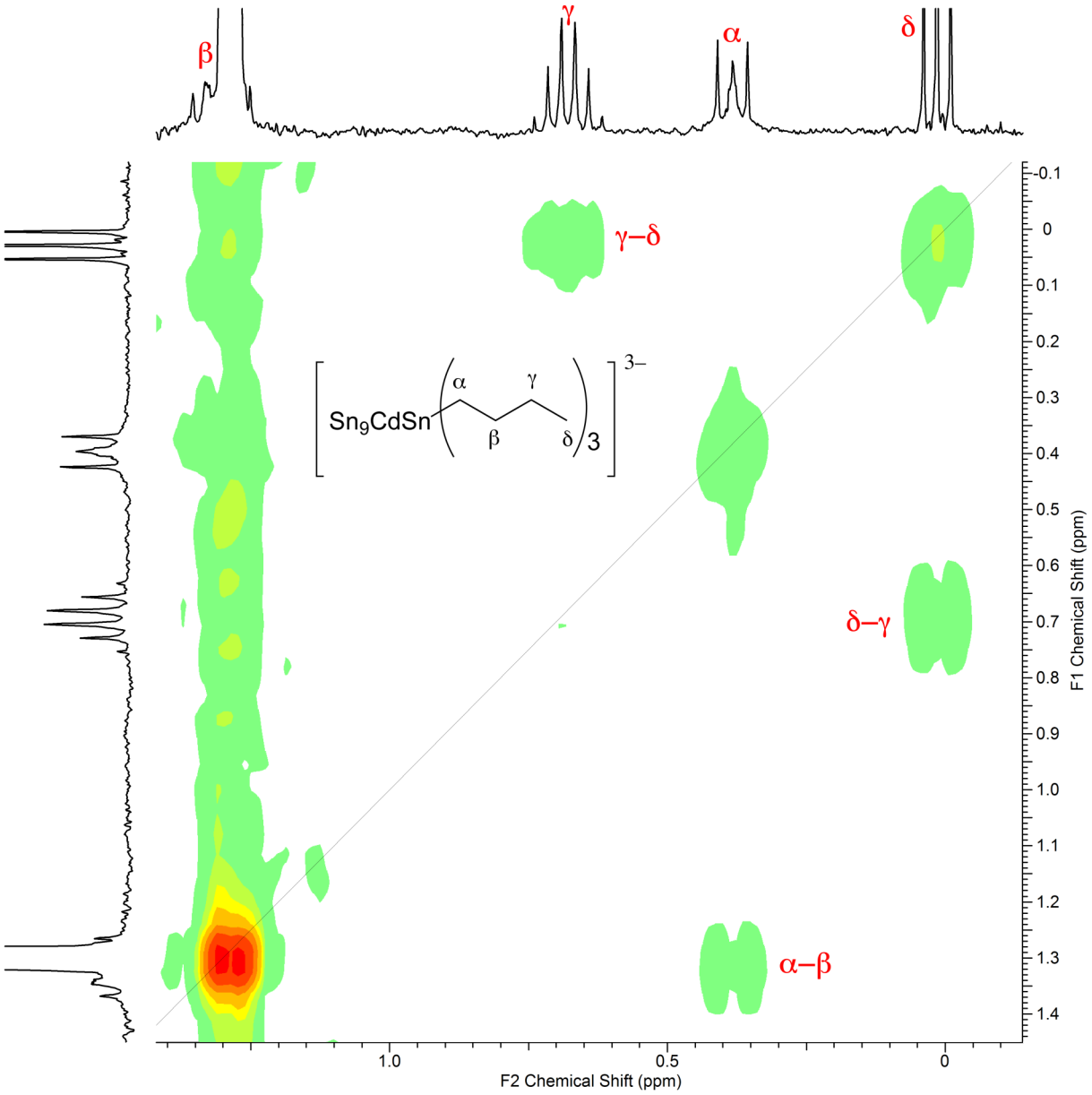

Figure 2.21 Aliphatic region of the ^{1}H COSY NMR spectrum of [K(2,2,2-crypt)]$_6$[**13**]$_2$•6tol•py in d$_5$-pyridine. Data were recorded at 298 K at 300.17 MHz.

2.3 Conclusions

Following the success in isolation and characterisation of $[E_9ZnPh]^{3-}$ (E = Si, Ge, Sn, Pb) by the Sevov group, more examples of organozinc functionalised Zintl clusters have been

synthesised and characterised both in the solid state and also in solution. The results show that in going from phenyl to mesityl and finally to isopropyl groups, the difference in electronic and steric properties of the organozinc fragments does not seem to alter the coordination mode to the clusters. These borderline metals behave more like transition metals in their reactions with the Zintl clusters and coordinate to the nine-atom cages at the open square base.

The aforementioned results also detail an accessible route to organocadmium functionalised Zintl ions, the first examples of such species isolated to date and close relatives of analogous zinc counterparts $[E_9ZnPh]^{3-}$ (E = Si, Ge, Sn, Pb). It is found that the organocadmium fragments coordinate to the clusters in the same fashion as the analogous zinc counterparts: the electrophilic attack takes place at the open square face of the deltahedral ions and the Zintl cluster acts as a six-electron donor ligand.

Furthermore the presence and stability of these functionalised clusters in ethylenediamine, pyridine and DMF solutions has been confirmed by NMR spectroscopic measurements and electrospray mass spectrometry, which opens up the potential for further solution reactivity studies such as substitution at Cd and Zn centres by breaking the remaining M–C bond.

The synthesis of the metal-bridged dimers $[Ge_9CdGe_9]^{6-}$ and $[Pb_9CdCdPb_9]^{6-}$ has expanded the coordination chemistry of group 14 Zintl clusters. In the case of the Cd–Cd bridged dimer $[Pb_9CdCdPb_9]^{6-}$ the electronic properties of the highly reduced clusters are used to stabilise an unsupported metal–metal bond. This shows that the negatively charged clusters can be used as six-electron donors to stabilise otherwise weak bonds.

Attempting to actively target the synthesis of metal–metal bonded Zintl cluster species by reacting the intermediate $[E_9MR]^{3-}$ with various different reducing agents has proven to be unsuccessful. Despite this, studies on the solution reactivity of $[E_9CdPh]^{3-}$ (E = Sn, Pb) towards tributyltin hydride have yielded the novel *closo*-clusters $[E_9CdSn(^nBu)_3]^{3-}$, the first examples of such a coupling reaction involving functionalised Zintl ions. Furthermore they represent a rare example of structurally characterised molecular complexes exhibiting Sn–Cd bonds, of which only one other species has been previously reported in the literature.

2.4 Reference

1. Ugrinov, A.; Sevov, S. C., *J. Am. Chem. Soc.* **2003**, *125*, 14059.
2. Ugrinov, A.; Sevov, S. C., *J. Am. Chem. Soc.* **2002**, *124*, 2442.
3. Ugrinov, A.; Sevov, S. C., *Chem. Eur. J.* **2004**, *10*, 3727.
4. Ugrinov, A.; Sevov, S. C., *J. Am. Chem. Soc.* **2002**, *124*, 10990.
5. Gillett-Kunnath, M. M.; Oliver, A. G.; Sevov, S. C., *J. Am. Chem. Soc.* **2011**, *133*, 6560.
6. Goicoechea, J. M.; Sevov, S. C., *Organometallics* **2006**, *25*, 4530.
7. Eichhorn, B. W.; Haushalter, R. C.; Pennington, W. T., *J. Am. Chem. Soc.* **1988**, *110*, 8704.
8. Yong, L.; Hoffmann, S. D.; Fassler, T. F., *Z. Krist. New Cryst. St.* **2005**, *220*, 53.
9. Kesanli, B.; Fettinger, J.; Eichhorn, B., *Chem. Eur. J.* **2001**, *7*, 5277.
10. Campbell, J.; Mercier, H. P. A.; Franke, H.; Santry, D. P.; Dixon, D. A.; Schrobilgen, G. J., *Inorg. Chem.* **2002**, *41*, 86.
11. Yong, L.; Hoffmann, S. D.; Fassler, T. F., *Eur. J. Inorg. Chem.* **2005**, 3663.

12. Denning, M. S.; Goicoechea, J. M., *Dalton Trans.* **2008**, 5882.

13. Nienhaus, A.; Hauptmann, R.; Fassler, T. F., *Angew. Chem. Int. Ed.* **2002**, *41*, 3213.

14. Boeddinghaus, M. B.; Hoffmann, S. D.; Faessler, T. F., *Z. Anorg. Allg. Chem.* **2007**, *633*, 2338.

15. Fischer, B.; Wijkens, P.; Boersma, J.; Vankoten, G.; Smeets, W. J. J.; Spek, A. L.; Budzelaar, P. H. M., *J. Organomet. Chem.* **1989**, *376*, 223.

16. Pyykko, P.; Atsumi, M., *Chem. Eur. J.* **2009**, *15*, 186.

17. Zhu, Z.; Brynda, M.; Wright, R. J.; Fischer, R. C.; Merrill, W. A.; Rivard, E.; Wolf, R. R.; Fettinger, J. C.; Olmstead, M. M.; Power, P. P., *J. Am. Chem. Soc.* **2007**, *129*, 10847.

18. Zhu, Z. L.; Wright, R. J.; Olmstead, M. M.; Rivard, E.; Brynda, M.; Power, P. P., *Angew. Chem. Int. Ed.* **2006**, *45*, 5807.

19. Resa, I.; Carmona, E.; Gutierrez-Puebla, E.; Monge, A., *Science* **2004**, *305*, 1136.

20. Wang, Y. Z.; Quillian, B.; Wei, P. R.; Wang, H. Y.; Yang, X. J.; Xie, Y. M.; King, R. B.; Schleyer, P. V.; Schaefer, H. F.; Robinson, G. H., *J. Am. Chem. Soc.* **2005**, *127*, 11944.

21. Grirrane, A.; Resa, I.; Rodriguez, A.; Carmona, E.; Alvarez, E.; Gutierrez-Puebla, E.; Monge, A.; Galindo, A.; del Rio, D.; Andersen, R. A., *J. Am. Chem. Soc.* **2007**, *129*, 693.

22. Schulz, S.; Schuchmann, D.; Westphal, U.; Bolte, M., *Organometallics* **2009**, *28*, 1590.

23. Burkey, T. J.; Majewski, M.; Griller, D., *J. Am. Chem. Soc.* **1986**, *108*, 2218.

24. Neumann, W. P., *Synthesis-Stuttgart* **1987**, 665.

25. Reed, D.; Stalke, D.; Wright, D. S., *Angew. Chem. Int. Ed.* **1991**, *30*, 1459.

26. Paver, M. A.; Russell, C. A.; Wright, D. S., *Angew. Chem. Int. Ed.* **1995**, *34*, 1545.

27. Lutz, M.; Findeis, B.; Haukka, M.; Graff, R.; Pakkanen, T. A.; Gade, L. H., *Chem. Eur. J.* **2002**, *8*, 3269.

Chapter 3 – Reactivity of the $[Ge_9]^{4-}$ Zintl anion towards $Fe(COT)(CO)_3$

3.1 Introduction

The solution reactivity of group 14 Zintl clusters towards mid-row transition metal tricarbonyl reagents was first studied by Eichhorn and Haushalter, resulting in the isolation and characterisation of several metalated complexes. Examples of the structurally characterised functionalised clusters include $[(\eta^4\text{-}E_9)M(CO)_3]^{4-}$ (E = Sn, Pb; M = Cr, Mo, W), $[(\eta^5\text{-}Sn_9)W(CO)_3]^{4-}$ and $[(\eta^5\text{-}Pb_9)Mo(CO)_3]^{4-}$.[1-6] They can be synthesised by reacting nine-atom Zintl cluster anions with organometallic reagents $LM(CO)_3$, where L represents a labile organic ligand such as mesitylene, cycloheptatriene or toluene. Analogously functionalised clusters are also available using $[M(CO)_3(CH_3CN)_3]$ as a reagent.

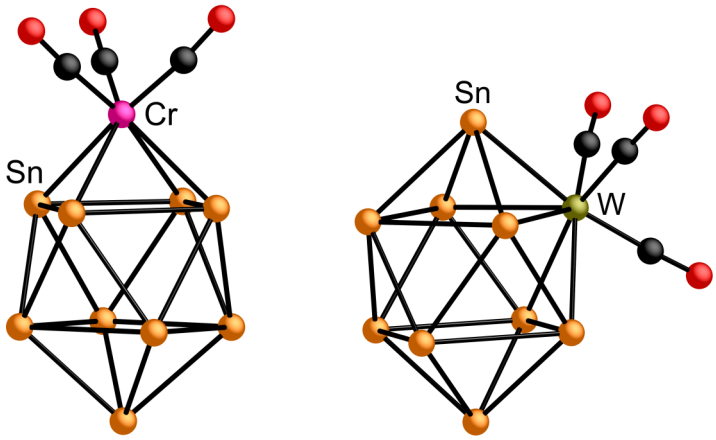

Figure 3.1 Structures of the functionalised cluster anions $[(\eta^4\text{-}Sn_9)Cr(CO)_3]^{4-}$ and $[(\eta^5\text{-}Sn_9)W(CO)_3]^{4-}$ as determined by single crystal X-ray diffraction.

Single crystal X-ray structural analysis of these metalated Zintl ions shows that both the η^4 and η^5 isomers exhibit bicapped square antiprismatic geometries. In the η^4 coordination mode,

the metal tricarbonyl moiety occupies one of the capping positions of the 10-atom deltahedral cluster. However, in the η^5 coordination mode, the transition metal centre is inserted into one of the square planes of the polyhedral cage, occupying a waist position. In both cases, the neutral $[M(CO)_3]$ fragment does not contribute any electrons to cluster bonding, leading to a total of $(2 \times 9) + 4 = 22$ skeletal electrons. The observed crystal structures are in accordance with the Wade-Mingos rules for a *closo*-cluster that possesses (2n + 2) cluster bonding electrons.

The *closo*-$[(\eta^4\text{-}Sn_9)M(CO)_3]^{4-}$ (M = Cr, Mo, W) anions have been studied comprehensively in liquid ammonia solutions using ^{119}Sn and ^{117}Sn NMR spectroscopy.[4] Both the ^{119}Sn and ^{117}Sn NMR spectra of these complexes show three resonances in a 1:4:4 intensity ratio, indicating the functionalised clusters are rigid and retain their η^4 coordination mode in solution. This is in contrast with the parent *nido*-$[Sn_9]^{4-}$ anion, which shows only a single resonance in its ^{119}Sn NMR spectrum, implying a rapid fluxionality of all nine vertices.[7] All the ^{119}Sn resonances of the $[(\eta^4\text{-}Sn_9)M(CO)_3]^{4-}$ anions are shifted downfield relative to the $[Sn_9]^{4-}$ precursor, suggesting electron transfer from the negatively charged nonastannide cage to the transition metal fragment. The ^{119}Sn and ^{117}Sn resonances with the most downfield chemical shifts correspond to the apical Sn atom, whereas the most upfield ones correspond to the vertices in the square plane capped by the apical tin atom.

The charge distribution in the $[(\eta^4\text{-}E_9)M(CO)_3]^{4-}$ (E = Sn, Pb; M = Cr, Mo, W) anions has been calculated using computational methods, revealing that the $[E_9]^{4-}$ clusters act as π donors to the $[M(CO)_3]$ fragments.[4] Around 90% of the transferred charge arises from the basal

square plane that is capped by the transition metal centers. The apical E atoms and the middle planes donate comparable amounts of charge to the π-accepting $[M(CO)_3]$ moieties. This also explains why the resonance of the tin atoms in the basal plane is more downfield than that of the middle ring in the ^{119}Sn and ^{117}Sn NMR spectra.

Infrared (IR) spectra were recorded for the $[(\eta^4\text{-}E_9)M(CO)_3]^{4-}$ (E = Sn, Pb; M = Cr, Mo, W) anions.[4] With the exception of the $[(\eta^4\text{-}Sn_9)Cr(CO)_3]^{4-}$ cluster anion, three vibrational bands corresponding to the in-phase and out-of-phase C–O vibrational stretching modes are observed. These three bands arise due to the fact that coordination of an $[M(CO)_3]$ fragment to an $[E_9]^{4-}$ cage breaks the three-fold rotational symmetry of the $[M(CO)_3]$ moieties. The vibrational frequencies of the carbonyl groups are all shifted to lower frequencies with respect to those of the organometallic precursors. This is a result of the electron transfer from the negatively charged nine-atom cluster to the transition metal centers. The buildup of the negative charge on M enhances the metal d orbital to CO π^* orbital back-donation, weakening the carbonyl bonds and lowering their vibrational frequencies. The IR spectra of these metal tricarbonyl functionalised clusters are very useful in determining the purity of the solid sample and distinguishing between the η^4 and η^5 isomers. In the η^5 isomers, the transition metal atom has a higher coordination number, resulting in more negative charge on M and hence lower ν(C–O) band frequencies than those in the IR spectra of the η^4 isomers.[3, 6]

All of the transition metal tricarbonyl functionalised clusters structurally characterised to date are polystannide and polyplumbide complexes. There have been no reports of analogous $[Ge_9M(CO)_3]^{4-}$ cluster anions in the literature. In addition, the reactivity towards transition

metal tricarbonyl reagents has only been studied for the group 6 elements: Cr, Mo and W, and the $[M(CO)_3]$ fragments all donate zero electrons to cluster bonding. Therefore we set out to study the reaction of K_4Ge_9 with $Fe(COT)(CO)_3$ (COT = 1,3,5,7-cyclooctatetraene) in ethylenediamine, which results in the formation of $[K(2,2,2\text{-crypt})]_3[Ge_8Fe(CO)_3]$.

3.2 Results and discussion

3.2.1 General synthetic methods

In a glovebox, an ethylenediamine solution of K_4Ge_9 and 2,2,2-crypt was mixed with a toluene solution of $Fe(COT)(CO)_3$ and then stirred for one hour. After filtration, the dark red filtrate was layered with toluene to yield dark orange, plate-like crystals of $[K(2,2,2\text{-crypt})]_3K_{0.22}[Ge_8Fe(CO)_3]\bullet 2en\bullet(COT)_{0.11}$. The crystalline phase is highly disordered and contains 0.11 equivalents of a COT moiety in the lattice. It is known that cyclooctatetraene can be reduced to give the radical anion and dianion, which makes it challenging to unambiguously assign the charge on the $[Ge_8Fe(CO)_3]$ cluster.[8-10]

A modified synthetic method was employed to eliminate the organic COT contaminant in the crystal structure. After stirring the reaction mixture for an hour, it was dried *in vacuo* and washed with a small amount of tetrahydrofuran. The orange THF solution was filtered and layered with hexane to give orange, rod-like crystals of $[K(2,2,2\text{-crypt})][Fe(\eta^3\text{-}C_8H_8)(CO)_3]$ as a side-product of the reaction. The remaining solid was reduced to dryness under a dynamic vacuum and redissolved in ethylenediamine. After filtration, the brown filtrate was layered with toluene to yield thin orange plates of $[K(2,2,2\text{-crypt})]_3[Ge_8Fe(CO)_3]$. Both of these crystalline phases have been characterised by single crystal X-ray diffraction, IR spectroscopy

and electrospray mass spectrometry. The metalated cluster salt $[K(2,2,2\text{-crypt})]_3[Ge_8Fe(CO)_3]$ has also been studied by EPR spectroscopy and DFT methods.

3.2.2 Characterisation of $[K(2,2,2\text{-crypt})]_3[Ge_8Fe(CO)_3]$

3.2.2.1 Single crystal X-ray structural analysis

The crystalline phase contains three $[K(2,2,2\text{-crypt})]^+$ cations and a single $[Ge_8Fe(CO)_3]^{3-}$ (**15**) cluster anion in the asymmetric unit cell. The metalated nine-atom deltahedral cage has the geometry of a slightly distorted monocapped square antiprism, with the $[Fe(CO)_3]$ fragment occupying one of the vertices of the basal square face. The transition metal tricarbonyl moiety replaces a vertex of the parent *nido*-$[Ge_9]^{4-}$ cluster ion, making this functionalised Zintl anion a stark contrast to the other previously reported ten-atom *closo*-$[E_9M(CO)_3]^{4-}$ (E = Sn, Pb; M = Cr, Mo, W) complexes.[1-6]

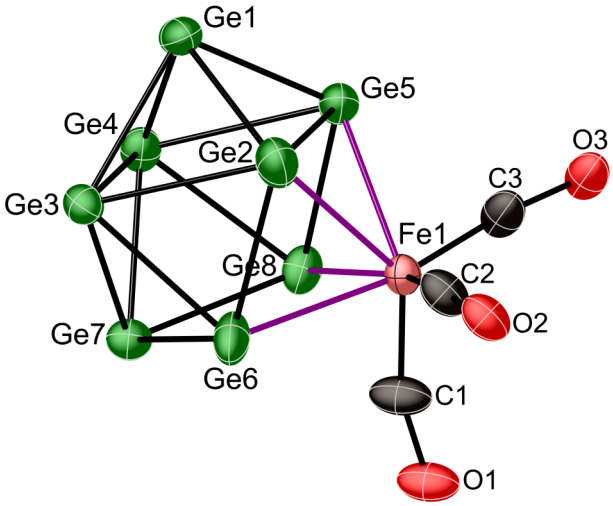

Figure 3.2 Thermal ellipsoid plot of $[Ge_8Fe(CO)_3]^{3-}$ (**15**) cluster anion as determined by single crystal X-ray diffraction. Anisotropic displacement ellipsoids are pictured at the 50% probability level.

The Ge–Ge bond lengths in the $[Ge_8Fe(CO)_3]^{3-}$ (**15**) cluster lie in the range 2.491(1) – 2.913(1) Å, and are comparable with the bond metric values in the previously reported naked $[Ge_9]^{n-}$ (n = 2, 3, 4) Zintl anions.[11-13] The longest Ge–Ge bond in the deltahedral cage is Ge2–Ge5 (2.913(1) Å), which is in the square plane that contains the $[Fe(CO)_3]$ fragment. It is approximately 0.2 Å longer than the Ge3–Ge4 bond (2.712(1) Å) in the upper square plane, suggesting that the η^4 coordinated organometallic moiety has caused some degree of distortion in the monocapped square antiprism. The diagonal interatomic distance in the open square face (Ge6–Ge8) is 3.342(1) Å, which is non-bonding and substantially longer than all the other Ge–Ge distances. The Fe–Ge bond lengths fall within the range 2.510(1) to 2.711(1) Å, longer than other reported Fe–Ge single bond lengths in compounds such as $(C_5H_5CoCO)_2(GeCl_2)_2Fe(CO)_4$ (2.433(8) Å) and $Cl_2Ge[C_5H_5Fe(CO)_2]_2$ (2.357(4) Å).[14, 15] This implies that the interaction between the Fe and Ge atoms in the $[Ge_8Fe(CO)_3]^{3-}$ cluster anion is delocalised in nature. The Fe–C and C–O bonds vary between 1.666(6) – 1.728(6) Å and 1.227(7) – 1.248(7) Å, respectively. Overall the $[Fe(CO)_3]$ moiety is incorporated into the delocalised skeletal bonding, giving rise to a nine-atom monocapped square antiprism.

3.2.2.2 Electronic structure

Applying the isolobal analogy, the $[Fe(CO)_3]$ fragment is isoelectronic with a Ge atom, donating three orbitals and two electrons to the cluster bonding.[16] Taking into account the eight germanium atoms and the overall negative charge, there are (2 × 8) + 2 + 3 = 21 skeletal electrons. According to the Wade-Mingos rules, a cluster with (2n + 3) bonding electrons is predicted to have a structure somewhere between a *closo*- (tricapped trigonal prism, 20 skeletal electrons) and *nido*- (monocapped square antiprism, 22 skeletal electrons) geometry.

The experimentally observed shape of the $[Ge_8Fe(CO)_3]^{3-}$ cluster anion is a slightly distorted monocapped antiprism, which is reasonable considering the flexible framework of these Zintl clusters.[7, 17, 18] In addition, it is conceivable that crystal packing effects may also affect the structure adopted by the anionic cage. The $[Ge_8Fe(CO)_3]^{3-}$ cluster anion is isoelectronic with the known paramagnetic parent cluster $[Ge_9]^{3-}$.[12]

DFT level computational studies show that the bond lengths and angles of the optimized geometry of the $[Ge_8Fe(CO)_3]^{3-}$ cluster are largely comparable to those determined by single crystal X-ray crystallography. However the computed structure more closely resembles a tricapped trigonal prism, rather than the observed monocapped square antiprism. For example, the calculated interatomic distance Ge6–Ge8 is 3.0093 Å, which is shorter than that observed crystallographically. This minor inconsistency can probably be explained by the small energy gap between the two geometries (the difference in bonding energy is calculated to be 28.5 kJ mol^{-1}) and crystal packing effects. In fact the closely related, isostructural and isoelectronic species $[Ge_9]^{3-}$ have been found to adopt different geometries depending on the number of solvent molecules present in the crystal lattice.[12]

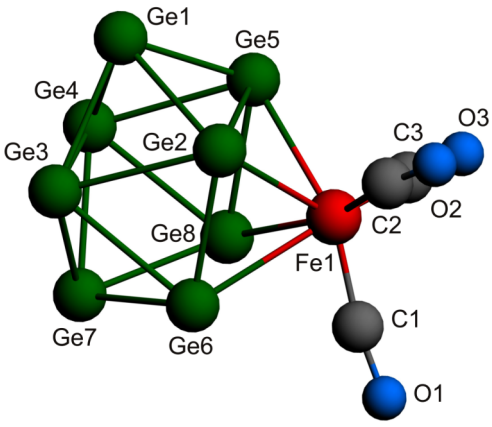

Figure 3.3 Optimized geometry for the unrestricted $[Ge_8Fe(CO)_3]^{3-}$ cluster anion.

Interatomic distances	15	15_{calc}
Ge1-Ge2	2.536(1)	2.660
Ge1-Ge3	2.606(1)	2.593
Ge1-Ge4	2.576(1)	2.688
Ge1-Ge5	2.591(1)	2.588
Ge2-Ge3	2.773(1)	2.810
Ge2-Ge5	2.913(1)	2.952
Ge2-Ge6	2.524(1)	2.616
Ge3-Ge4	2.712(1)	2.788
Ge3-Ge6	2.636(1)	2.786
Ge3-Ge7	2.700(1)	2.600
Ge4-Ge5	2.782(1)	2.771
Ge4-Ge7	2.576(1)	2.705
Ge4-Ge8	2.684(1)	2.747
Ge5-Ge8	2.540(1)	2.711
Ge6-Ge7	2.491(1)	2.658
Ge6-Ge8	3.342(1)	3.036
Ge7-Ge8	2.643(1)	2.581
Fe1-Ge2	2.690(1)	2.725
Fe1-Ge5	2.677(1)	2.630
Fe1-Ge6	2.510(1)	2.719
Fe1-Ge8	2.711(1)	2.622
Fe1-C1	1.728(6)	1.744
Fe1-C2	1.666(6)	1.749
Fe1-C3	1.691(6)	1.738
C1-O1	1.227(7)	1.187
C2-O2	1.248(7)	1.187
C3-O3	1.241(8)	1.184

Table 3.1 Comparison of bond distances for the cluster anion $[Ge_8Fe(CO)_3]^{3-}$ in **15** and for the calculated ground state optimized geometry $\mathbf{15_{calc}}$.

The highest occupied molecular orbital for $[Ge_8Fe(CO)_3]^{3-}$ is mainly cluster-based and very similar to that of the related species $[Ge_9]^{3-}$. It is predominantly composed of the p orbitals of the germanium atoms in the two triangular faces of the tricapped trigonal prism. The interaction within each triangular face is π-bonding, whereas the one between two bases is σ-antibonding. As mentioned previously, the two related cluster anions are isostructural and isoelectronic.

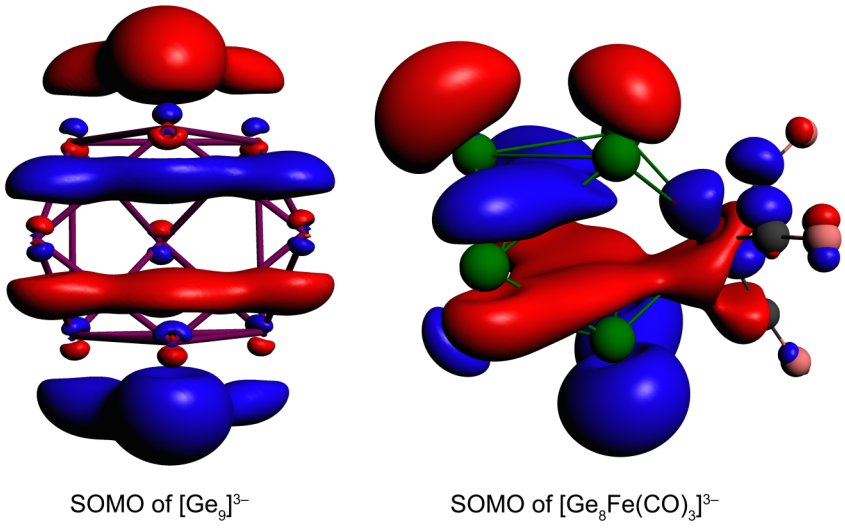

Figure 3.4 The computed singly-occupied molecular orbitals of two closely related species $[Ge_9]^{3-}$ and $[Ge_8Fe(CO)_3]^{3-}$ (**15**).

3.2.2.3 EPR spectroscopy

The highest occupied molecular orbital of the cluster anion $[Ge_8Fe(CO)_3]^{3-}$ (**15**) is singly-occupied and as a result the paramagnetism of $[K(2,2,2\text{-crypt})]_3[Ge_8Fe(CO)_3]$ was examined by solid state EPR spectroscopy. Data were recorded on approximately 2 mg of a solid sample in a flame-sealed quartz capillary. The room temperature measurement reveals an extremely weak, broadened resonance. Upon cooling to 20 K, the resonance splits and sharpens to reveal

a complex pattern, which we were able to simulate for the $[Ge_8Fe(CO)_3]^{3-}$ (**15**) anion. ^{73}Ge (7.73%, I = 9/2) is the only spin-active naturally occurring isotope of germanium. The simulated spectrum was obtained by combining the results for the three most abundant anions: $[Ge_8Fe(CO)_3]^{3-}$, $[Ge_7{}^{73}GeFe(CO)_3]^{3-}$ and $[Ge_6{}^{73}Ge_2Fe(CO)_3]^{3-}$ (unlabelled Ge represents all the other zero-spin nuclei). The EPR spectrum confirms the paramagnetic character of the metalated Zintl cluster with the peak centered at around g = 2.0200.

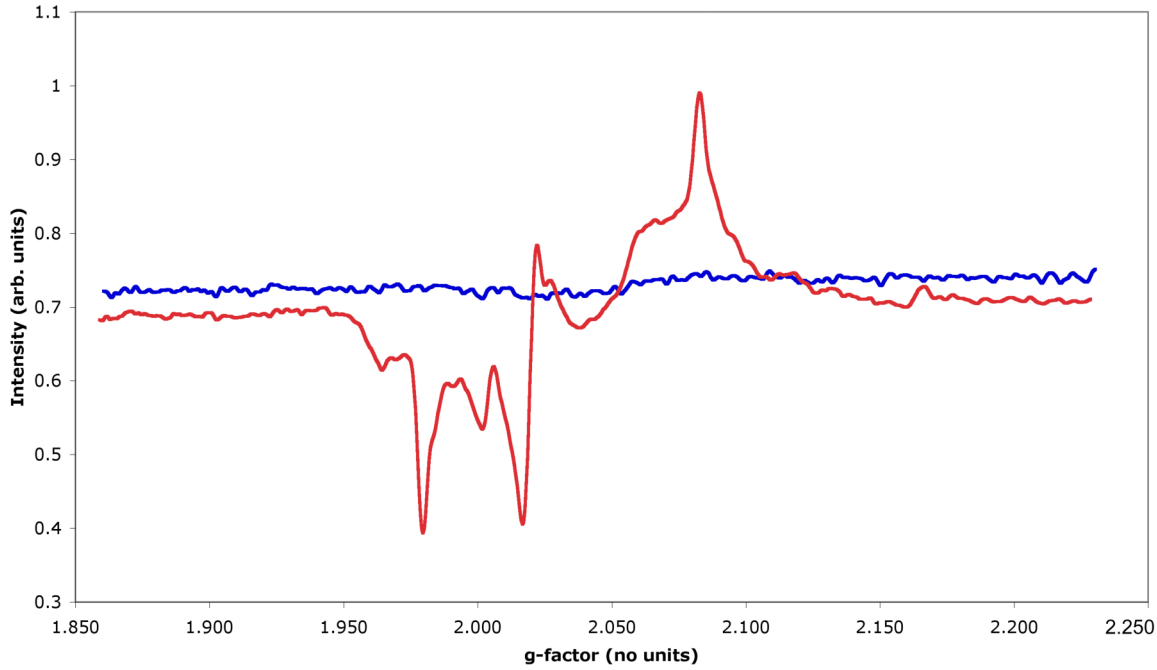

Figure 3.5 X-band (9.3896 GHz) CW EPR spectrum of a solid sample of $[K(2,2,2\text{-crypt})]_3[Ge_8Fe(CO)_3]$ collected at 20 K. The sample resonance data (red) has not been corrected for the resonator background noise (blue).

3.2.2.4 Infrared spectroscopy

The solid state IR spectrum of a crystalline sample of $[K(2,2,2\text{-crypt})]_3[Ge_8Fe(CO)_3]$ was recorded, revealing two bands at ν = 1884 and 1820 cm^{-1}. These correspond to the characteristic in-phase and out-of-phase C–O stretching vibrational modes, and are

significantly red-shifted relative to those of the precursor $Fe(COT)(CO)_3$ at ν = 2058 and 1992 cm^{-1}. As with the previously reported metalated clusters $[E_9M(CO)_3]^{4-}$ (E = Sn, Pb; M = Cr, Mo, W; η^4 and η^5 coordination modes), the carbonyl stretching bands all appear at lower wavenumbers with regard to the starting material $LM(CO)_3$ (L = labile organic ligand).[1-6] This can be explained by the buildup of negative charge on the transition metal centre M as a result of the electron transfer from the group 14 Zintl cluster. Subsequently the charge in the metal d orbital is back donated to the π^* orbital of the carbonyl groups, weakening the bonds and lowering the vibrational frequencies.

3.2.2.5 Electrospray mass spectrometry

Crystals of $[K(2,2,2\text{-crypt})]_3[Ge_8Fe(CO)_3]$ were found to be soluble in DMF and the negative ion mode electrospray mass spectra of such solutions were recorded. The metalated complex $[Ge_8Fe(CO)_3]^-$ (*m/z* 721.0) has a similar mass to that of the commonly observed species $[Ge_{10}]^-$ (*m/z* 726.4) or $[Ge_9(DMF)]^-$ (*m/z* 726.8) in the mass spectra of DMF solutions of germanium Zintl clusters. Therefore the mass envelope at *m/z* 726.8 in the negative ion mode is probably a result of the overlapping of the isotopic distributions of the parent compound $[Ge_8Fe(CO)_3]^-$ and $[Ge_{10}]^-$ and/or $[Ge_9(DMF)]^-$. Despite this ambiguity, the mass envelopes corresponding to both $[Ge_8Fe(CO)_2]^-$ and $[Ge_8Fe(CO)]^-$, due to the sequential loss of carbonyl groups, can be clearly observed at *m/z* values of 693.7 and 665.4, respectively.

3.2.3 Characterisation of $[Fe(\eta^3\text{-}C_8H_8)(CO)_3]^-$

The THF soluble fraction of the reaction, which yielded **15**, was found to give crystals of $[K(2,2,2\text{-crypt})][Fe(\eta^3\text{-}C_8H_8)(CO)_3]$ upon layering with hexane. This side-product of the

reaction results from a single electron reduction of the $Fe(COT)(CO)_3$ organometallic precursor, and has been characterised by single crystal X-ray diffraction, EPR spectroscopy and electrospray mass spectrometry.

It is well known that the COT ligand can be reduced to give a radical anion or dianion. The cyclooctatetradienide $[COT]^{2-}$ dianion is aromatic and exhibits a planar geometry in compounds such as $U(COT)_2$.[19] The radical anionic ligand $[COT]^{-}$ observed in species such as $Ni(R_2PC_2H_4PR_2)(COT)$ (R = ^{i}Pr, ^{t}Bu) also exhibits a planar geometry.[20] The $[Fe(\eta^3\text{-}C_8H_8)(CO)_3]^{-}$ anion (**16**) can either be regarded as a neutral COT ligand coordinated to an iron (–I) centre, or an iron (0) complex with a radical anionic ligand $[COT]^{-}$. The crystallographic data shows that the η^3 coordinated organic ligand adopts a non-planar boat-like configuration.

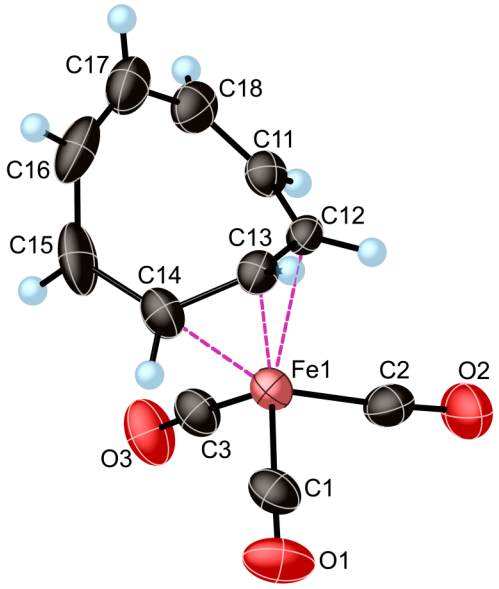

Figure 3.6 Thermal ellipsoid plot of the $[Fe(\eta^3\text{-}C_8H_8)(CO)_3]^{-}$ (**16**) anion as determined by single crystal X-ray diffraction. Anisotropic displacement ellipsoids of non-hydrogen atoms are pictured at the 50% probability level.

Structural analysis by single crystal X-ray diffraction reveals that the C–C interatomic distances in the cyclooctatetraene moiety fall within four ranges: a) 1.275(5) and 1.335(4) Å, formal double bonds (C16–C17 and C11–C18); b) 1.410(4) and 1.417(4) Å, bonds with some allylic character (C12–C13 and C13–C14); c) 1.431(5) to 1.515(6) Å, single bonds with some degree of sp^2 character (C11–C12, C15–C16 and C17–C18); d) 1.562(5) Å, a single bond with a great degree of sp^3 character (C14–C15). The Fe–C distances to the COT moiety vary between 2.013(3) and 2.145(3) Å, which are comparable to those found in other related organometallic complexes, such as [FeMo{μ-σ,η-C(C_6H_4Me-4)=CH_2}(μ-CH_2)$(CO)_5$(η-C_5H_5)] (2.055(2) and 2.127(3) Å between Fe and the sp^2 carbon atoms).[21-23] The Fe–C distances to the carbonyl groups lie in the range between 1.757(3) and 1.762(3) Å, which are substantially longer than those in the previously discussed cluster anion $[Ge_8Fe(CO)_3]^{3-}$ (**15**) and this indicates a much lesser degree of π backbonding from the metal to the carbonyl ligands. The alternating C–C bond lengths in the η^3-cyclooctatetraene unit and the Fe–C distances give some indication about the charge distribution in the ligand, as well as the degree of electron transfer to the π* orbitals of both the COT and CO substituents.

Crystals of [K(2,2,2-crypt)][Fe(η^3-C_8H_8)$(CO)_3$] were additionally characterised in the solid state by IR and EPR spectroscopy. Two bands corresponding to the carbonyl vibrational stretching modes at ν = 1928 and 1828 cm^{-1} have been observed in the IR spectra. They are also redshifted with regard to the bands of the neutral precursor Fe(COT)$(CO)_3$ at ν = 2058 and 1992 cm^{-1}. Again this reflects the degree of electron back donation from the transition metal centre to the CO π-antibonding orbitals. The paramagnetic character of the [Fe(η^3-C_8H_8)$(CO)_3$]$^-$ anion (**16**) was confirmed by solid state EPR spectroscopy.

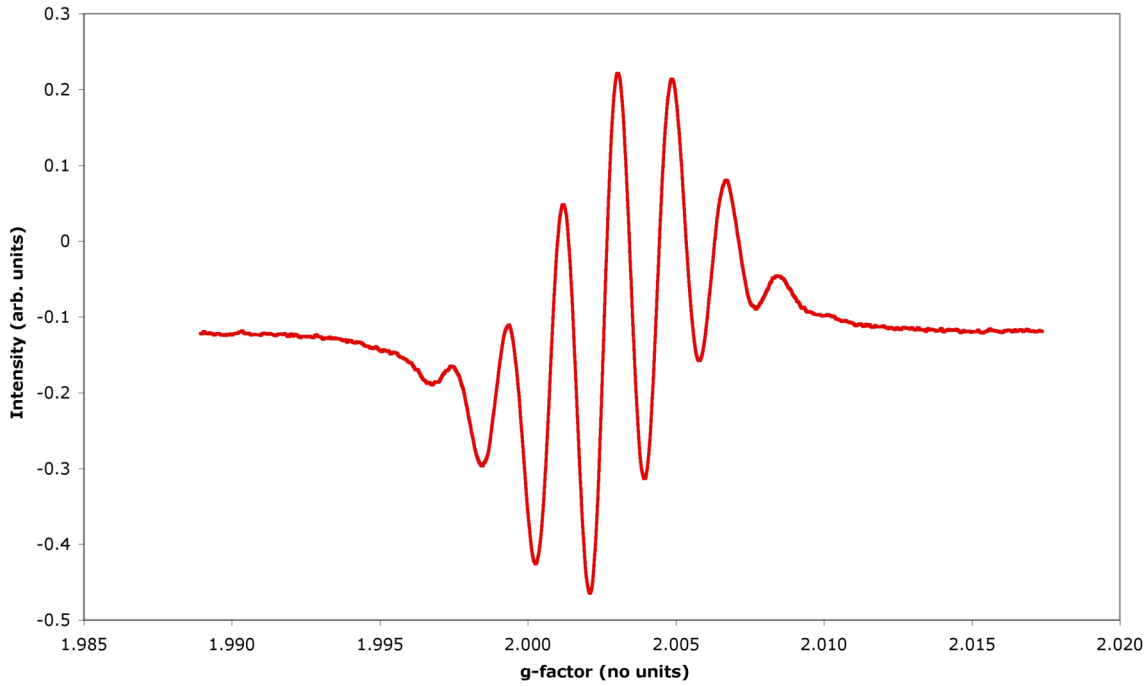

Figure 3.7 X-band (9.3896 GHz) CW EPR spectrum of a solid sample of [K(2,2,2-crypt)][Fe(η^3-C_8H_8)$(CO)_3$] collected at room temperature. The red line corresponds to the uncorrected sample data without subtracting the resonator background resonance.

3.2.4 Synthesis and characterisation of $[Fe_2(\eta^3,\eta'^3\text{-}C_{16}H_{16})(CO)_6]^{2-}$

The formation of the side-product [Fe(η^3-C_8H_8)$(CO)_3$]$^-$ (**16**) presumably occurs *via* a single electron reduction of the starting material Fe(COT)$(CO)_3$. To test this hypothesis, the neutral precursor was reduced using one equivalent of potassium metal in DMF in the presence of the cation sequestering agent 2,2,2-crypt. Layering the reaction mixture with Et_2O, however, afforded dark yellow block-like crystals of [K(2,2,2-crypt)]$_2$[$Fe_2(\eta^3,\eta'^3$-$C_{16}H_{16})(CO)_6$]. This species was characterised by single crystal X-ray diffraction, multielement NMR spectroscopy, IR spectroscopy and electrospray mass spectrometry.

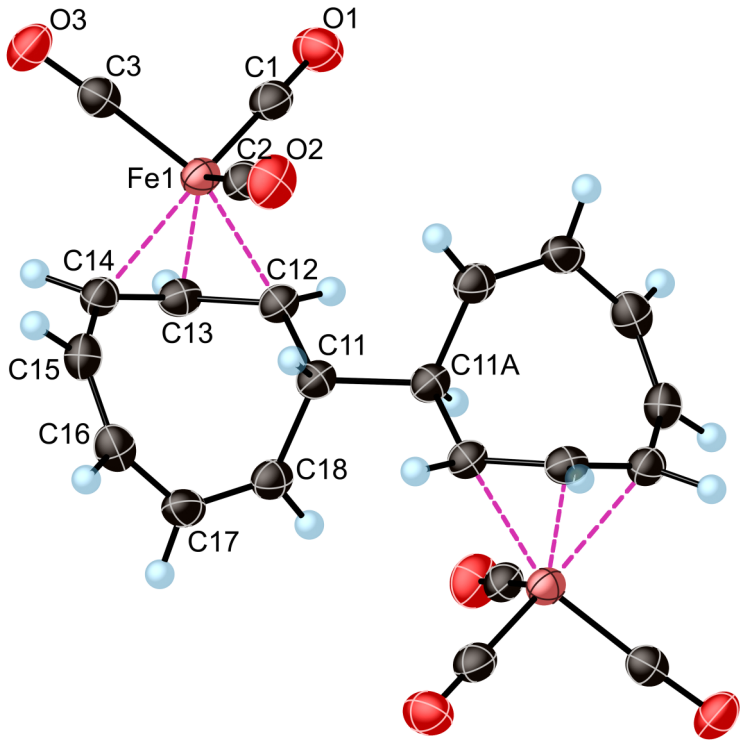

Figure 3.8 Thermal ellipsoid plot of the $[Fe_2(\eta^3,\eta'^3\text{-}C_{16}H_{16})(CO)_6]^{2-}$ (**17**) anion as determined by single crystal X-ray diffraction. Anisotropic displacement ellipsoids of non-hydrogen atoms are pictured at the 50% probability level.

The asymmetric unit contains half of the $[Fe_2(\eta^3,\eta'^3\text{-}C_{16}H_{16})(CO)_6]^{2-}$ moiety and one $[K(2,2,2\text{-crypt})]^+$ cation. There is an inversion centre at the mid-point of the inter-ring C–C bond, and as a result the dianion possesses C_i symmetry. Bond metric data show that there is a similar interatomic distance distribution to that in the $[Fe(\eta^3\text{-}C_8H_8)(CO)_3]^-$ radical anion (**16**): a) 1.341(3) and 1.334(3) Å, formal double bonds (C15–C16 and C17–C18); b) 1.429(2) and 1.417(3) Å, bonds with some allylic character (C12–C13 and C13–C14); c) 1.463(3) to 1.532(2) Å, single bonds with some degree of sp^2 character (C11–C12, C11–C18, C14–C15 and C16–C17); d) 1.544(3) Å, a single bond with a great degree of sp^3 character (C11–C11A).

The Fe–C distances to the [$C_{16}H_{16}$] moiety vary between 2.016(2) and 2.137(2) Å, and the Fe–C distances to the carbonyl groups lie in the range between 1.754(2) and 1.763(2) Å, which are almost identical to those found in the radical anion [Fe(η^3-C_8H_8)$(CO)_3]^-$ (**16**). Hence the same charge distribution in the ligand, as well as the degree of electron transfer to the π* orbitals of both the [$C_{16}H_{16}$] and CO substituents, are also present in the dimeric species. The reaction presumably proceeds via the initial formation of the monomeric radical anion, followed by the coupling of two such species to yield the dianion.

This organometallic complex was further studied using multielement NMR spectroscopy by dissolving crystals of [K(2,2,2-crypt)]$_2$[Fe_2(η^3,η'^3-$C_{16}H_{16}$)$(CO)_6$] in d_7-DMF. There is an inversion centre in the molecule, leading to eight unique proton and carbon environments in the ^{1}H and $^{13}C\{^1H\}$ NMR spectra. Seven resonances at 6.50, 6.23, 5.59, 5.02, 3.78, 3.02 and 2.46 ppm were observed in the ^{1}H NMR. The missing resonance was masked by a resonance corresponding to the protons in the sequestering agent 2,2,2-crypt, as revealed by the COSY spectra. The $^{13}C\{^1H\}$ NMR spectrum shows a carbonyl carbon resonance at 226.93 ppm, and eight singlets corresponding to the COT ligand at 145.34, 140.57, 123.36, 114.28, 71.04, 68.02, 59.07 and 56.02 ppm. All the observed resonances have been fully assigned using COSY and gHMQC correlation experiments. The off-diagonal cross-peaks in the COSY spectrum directly correlate the coupling between protons that are three bonds apart. The cross-peaks in gHMQC provide correlation between a proton and the carbon atom, to which it is bonded to. The solution NMR spectra confirm that the coordination mode in the molecule in the crystal lattice is retained in solution.

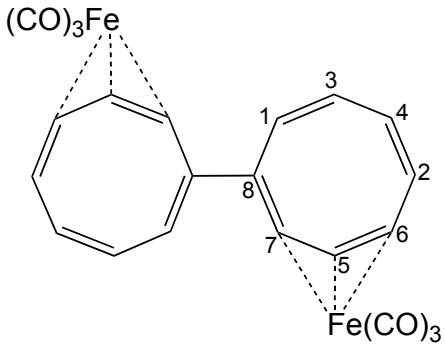

Figure 3.9 Numbering scheme for $[Fe_2(\eta^3,\eta'^3\text{-}C_{16}H_{16})(CO)_6]^{2-}$ (**17**).

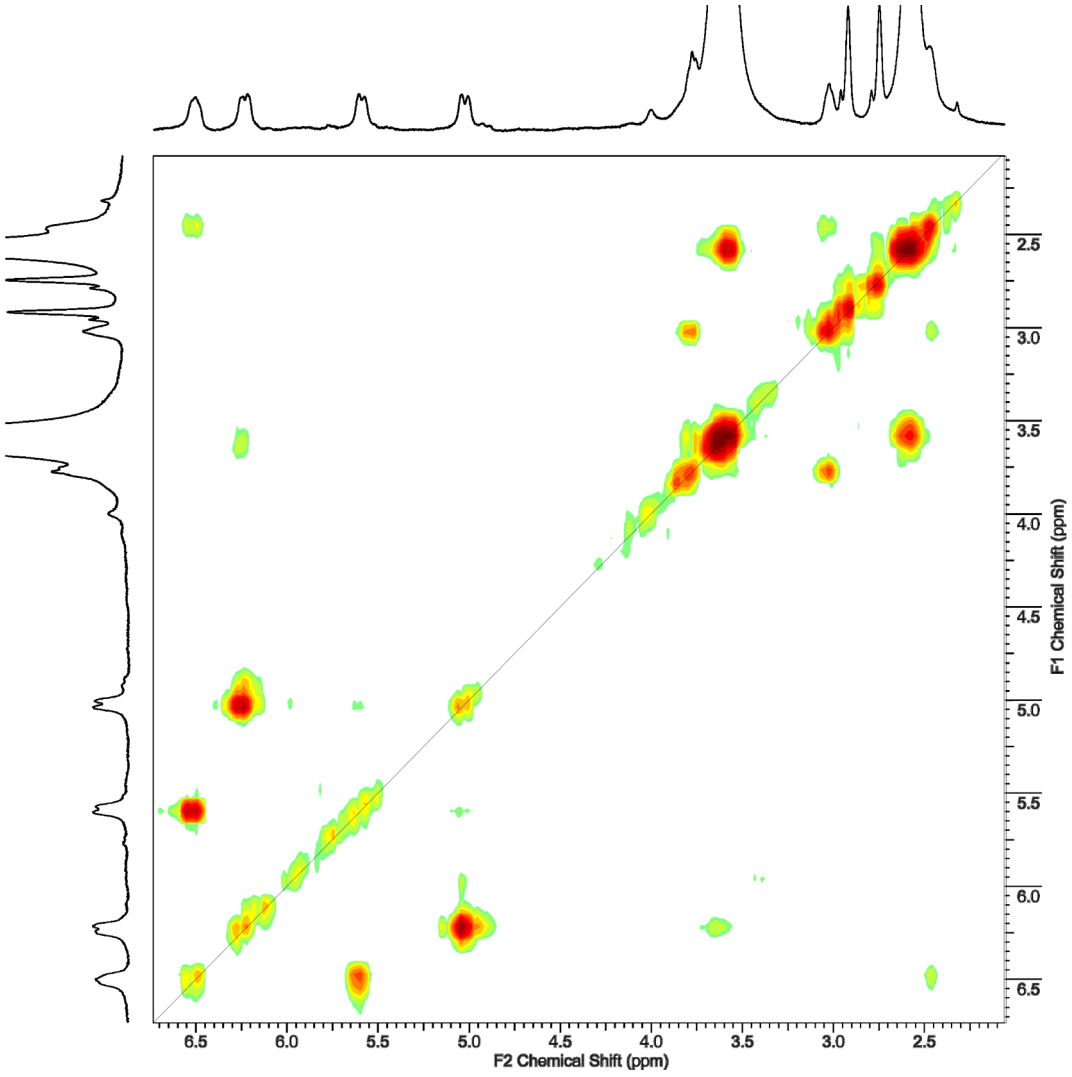

Figure 3.10 COSY spectrum of $[K(2,2,2\text{-crypt})]_2[Fe_2(\eta^3,\eta'^3\text{-}C_{16}H_{16})(CO)_6]$ in d_7-DMF.

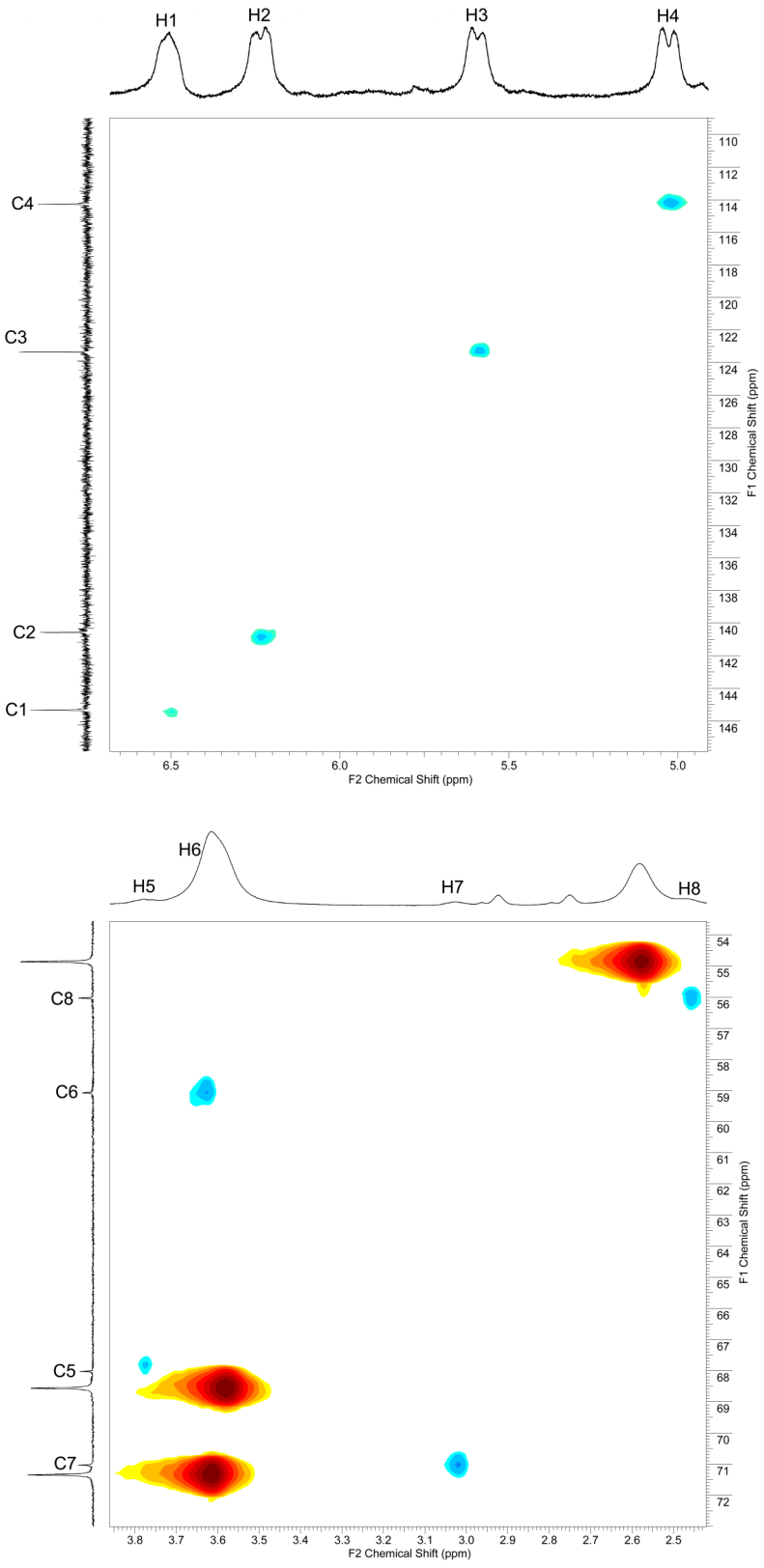

Figure 3.11 HMQC spectrum of $[K(2,2,2\text{-crypt})]_2[Fe_2(\eta^3,\eta'^3\text{-}C_{16}H_{16})(CO)_6]$ in d_7-DMF.

The dianionic species $[Fe_2(\eta^3,\eta'^3\text{-}C_{16}H_{16})(CO)_6]^{2-}$ (C_i symmetry) was additionally characterised in the solid state by infrared spectroscopy. Three bands corresponding to carbonyl vibrational stretching modes at ν = 1922, 1828 and 1725 cm^{-1} have been observed in the IR spectrum. They have been redshifted with regard to the starting material $Fe(COT)(CO)_3$ (ν = 2058 and 1992 cm^{-1}). Analogous to the radical anion $[Fe(\eta^3\text{-}C_8H_8)(CO)_3]^-$ (**16**), this observation reflects the amount of back donation from the iron centre to the CO π-antibonding orbitals.

3.3 Conclusion

The reaction of K_4Ge_9 with $Fe(COT)(CO)_3$ in the presence of 2,2,2-crypt was investigated, yielding a metalated nine-atom anionic species $[Ge_8Fe(CO)_3]^{3-}$. It is entirely unique to all the previously reported transition metal tricarbonyl functionalised group 14 Zintl clusters because the nuclearity of the parent cluster is altered upon coordination of the $[Fe(CO)_3]$ moiety. The organometallic fragment replaces one of the vertices in the open square face of the nonagermanide cage, donating the same number of orbitals and electrons to cluster bonding as a germanium atom. This makes the $[Ge_8Fe(CO)_3]^{3-}$ ion isostructural and isoelectronic with the closely related species *nido*-$[Ge_9]^{3-}$.

During the course of these studies, the radical anion $[Fe(\eta^3\text{-}C_8H_8)(CO)_3]^-$ has been isolated and characterised as a side product of the above reaction. Attempting to reduce the precursor $Fe(COT)(CO)_3$ with potassium metal yields a dianionic species $[Fe_2(\eta^3,\eta'^3\text{-}C_{16}H_{16})(CO)_6]^{2-}$.

3.4 References

1. Eichhorn, B. W.; Haushalter, R. C.; Pennington, W. T., *J. Am. Chem. Soc.* **1988**, *110*, 8704.
2. Yong, L.; Hoffmann, S. D.; Fassler, T. F., *Z. Krist. New Cryst. St.* **2005**, *220*, 53.
3. Kesanli, B.; Fettinger, J.; Eichhorn, B., *Chem. Eur. J.* **2001**, *7*, 5277.
4. Campbell, J.; Mercier, H. P. A.; Franke, H.; Santry, D. P.; Dixon, D. A.; Schrobilgen, G. J., *Inorg. Chem.* **2002**, *41*, 86.
5. Eichhorn, B. W.; Haushalter, R. C., *J. Chem. Soc. Chem. Commun.* **1990**, 937.
6. Yong, L.; Hoffmann, S. D.; Fassler, T. F., *Eur. J. Inorg. Chem.* **2005**, 3663.
7. Rudolph, R. W.; Wilson, W. L.; Parker, F.; Taylor, R. C.; Young, D. C., *J. Am. Chem. Soc.* **1978**, *100*, 4629.
8. Katz, T., *J. Am. Chem. Soc.* **1960**, *82*, 3784.
9. Katz, T.; Strauss, H., *J. Chem. Phys.* **1960**, *32*, 1873.
10. Strauss, H.; Fraenkel, G.; Katz, T., *J. Am. Chem. Soc.* **1963**, *85*, 2360.
11. Belin, C. H. E.; Corbett, J. D.; Cisar, A., *J. Am. Chem. Soc.* **1977**, *99*, 7163.
12. Fassler, T. F.; Schutz, U., *Inorg. Chem.* **1999**, *38*, 1866.
13. Somer, M.; Carrillo-Cabrera, W.; Peters, E. M.; Peters, K.; von Schnering, H. G., *Z. Anorg. Allg. Chem.* **1998**, *624*, 1915.
14. Bennett, M.; Brooks, W.; Elder, M.; Graham, W.; Hall, D.; Kummer, R., *J. Am. Chem. Soc.* **1970**, *92*, 208.
15. Bush, M.; Woodward, P., *J. Chem. Soc. A* **1967**, 1833.
16. Hoffmann, R., *Angew. Chem. Int. Ed.* **1982**, *21*, 711.
17. Rudolph, R. W.; Wilson, W. L.; Taylor, R. C., *J. Am. Chem. Soc.* **1981**, *103*, 2480.

18. Wilson, W. L.; Rudolph, R. W.; Lohr, L. L.; Taylor, R. C.; Pyykko, P., *Inorg. Chem.* **1986**, *25*, 1535.

19. Zalkin, A.; Raymond, K., *J. Am. Chem. Soc.* **1969**, *91*, 5667.

20. Bach, I.; Porschke, K. R.; Proft, B.; Goddard, R.; Kopiske, C.; Kruger, C.; Rufinska, A.; Seevogel, K., *J. Am. Chem. Soc.* **1997**, *119*, 3773.

21. Ros, J.; Solans, X.; Fontaltaba, M.; Mathieu, R., *Organometallics* **1984**, *3*, 1014.

22. Garcia, M.; Jeffery, J.; Sherwood, P.; Stone, F., *J. Chem. Soc. Chem. Commun.* **1986**, 802.

23. Rumin, R.; Petillon, F.; Manojlovicmuir, L.; Muir, K., *Organometallics* **1990**, *9*, 944.

Chapter 4 – Reactivity of $[E_9]^{4-}$ (E = Ge, Sn, Pb) cluster anions towards homoleptic mid-row transition metal organometallic reagents

4.1 Introduction

In solution, transition metal organometallic reagents with labile ligands can react with group 14 Zintl precursors to yield ligand-free anionic metal-centred deltahedral clusters. These reactions are thought to proceed *via* extensive cluster fragmentation and rearrangement, which results in the formation of endohedral cages exhibiting nuclearities different to those of the parent clusters. This is in contrast with the reactions between $[E_9]^{4-}$ (E = Ge, Sn, Pb) and main group reagents or group 12 organometallics, in which the nuclearity of the nine-atom clusters is generally retained and there is no encapsulation of guest atoms.

The nine-vertex endohedral clusters $[Cu@E_9]^{3-}$ (E = Sn, Pb) have been synthesised by the reaction of K_4E_9 with mesitylcopper(II) in DMF.[1] Crystallographic studies of the anionic clusters revealed that the nine-atom cages have a distorted tricapped trigonal prismatic geometry. All the interatomic distances between the encapsulated Cu atom and the surrounding E atoms fall within a very narrow range, resulting in an almost perfect spherical coordination environment for the central metal atom. This is reflected in the solution state ^{119}Sn NMR spectrum of $[K(2,2,2\text{-crypt})]_3[Cu@Sn_9]$•2DMF, which displays a 1:1:1:1 quartet at δ = –1440 ppm. The observation of one single resonance confirms that all nine Sn atoms are equivalent on the spectral NMR time scale. The splitting pattern results from the coupling with the interstitial quadrupolar Cu nuclei (69% ^{63}Cu and 31% ^{65}Cu, both I = 3/2). Coupling between ^{119}Sn and ^{117}Sn (8.58% ^{119}Sn and 7.61% ^{117}Sn, both I = 1/2) was also visible as

satellites adjacent to each resonance. Another consequence of the highly symmetrical cluster around the Cu atom was the observation of one sharp resonance at $\delta = -330$ ppm in the ^{65}Cu NMR spectrum. Similar endohedral species $[Ni@E_9]^{3-}$ (E = Ge, Sn) were formed by reaction of $[E_9]^{4-}$ with $Ni(COD)_2$ (COD = 1,5-cyclooctadiene).[2] Both the Ni-centered and empty clusters display the same reactivity towards TlCp (Cp = cyclopentadienyl), yielding the deltahedral cluster anions $[Ni@E_9Tl]^{3-}$ and $[E_9Tl]^{3-}$ (E = Ge, Sn).[3] From the point of view of electron counting, these endohedral cluster anions can be treated as $[(Cu^{+})(E_9^{4-})]^{3-}$, $[(Ni^{0})E_9]^{3-}$ and $[(Ni^{0})E_9Tl]^{3-}$. The central transition metal atoms achieve a closed-shell d^{10} configuration, contributing no electrons to cluster bonding.

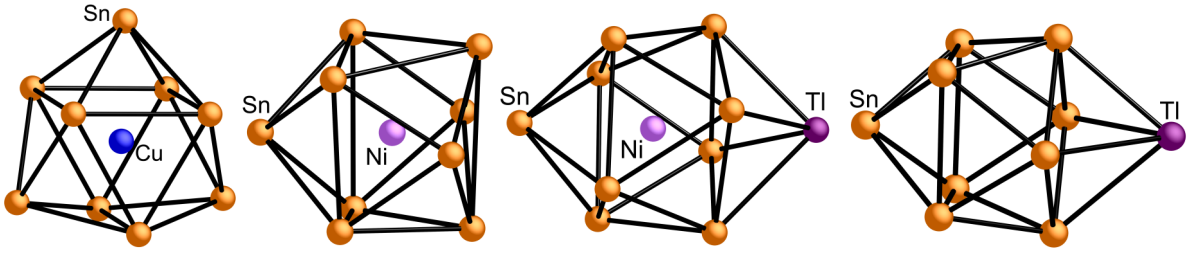

Figure 4.1 Structures of the cluster anions $[Cu@Sn_9]^{3-}$, $[Ni@Sn_9]^{3-}$, $[Ni@Sn_9Tl]^{3-}$ and $[Sn_9Tl]^{3-}$ as determined by single crystal X-ray diffraction.

Analogous reactions between the heavier counterpart $[Pb_9]^{4-}$ and $Ni(COD)_2$ result in the formation of the ten-vertex endohedral anion $[Ni@Pb_{10}]^{2-}$ (primary product) accompanied by the twelve-vertex endohedral anion $[Ni@Pb_{12}]^{2-}$ (< 10%).[4, 5] The ten-atom $[Ni@Pb_{10}]^{2-}$ ion contains a bicapped square antiprismatic *closo*-$[Pb_{10}]^{2-}$ moiety with D_{4d} symmetry, which encapsulates a Ni atom. The Ni–Pb contacts fall within two categories: long Ni–Pb bonds (to the axial Pb atoms; av. 3.210 Å) and shorter Ni–Pb bonds (to the "waist" of the cluster; av. 2.722 Å). The crystallographic data for the interatomic distances are close to the theoretical

values in the neutral binary cluster [$NiPb_{10}$], of which the most stable isomer is predicted to have the same point symmetry.[6]

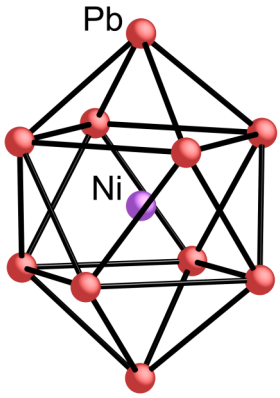

Figure 4.2 Structure of the bicapped square antiprismatic cluster anion $[Ni@Pb_{10}]^{2-}$ as determined by single crystal X-ray diffraction.

The central Ni atom donates zero electrons to cluster bonding, giving rise to a total number of $2 \times 10 + 2 = 2n + 2$ skeletal electrons. According to the Wade-Mingos rules for electron counting, this ten-atom cage is predicted to have a *closo* bicapped square antiprismatic geometry, which is consistent with the experimentally observed structure. Variable-temperature ^{207}Pb NMR spectra for solutions of $[K(2,2,2\text{-crypt})]_2[Ni@Pb_{10}]$ in DMF were recorded at temperatures between 25 and –45 °C. The solid-state single crystal structure reveals two distinct Pb environments, and as a result two resonances would be expected in the NMR spectra. However, a single, broad resonance with a line width that increases as the temperature decreases was observed at $\delta = -996$ ppm. This finding can probably be explained by the rapid intramolecular exchange of both Pb environments that slows down up cooling.

As mentioned previously, the reaction between $[Pb_9]^{4-}$ and $Ni(COD)_2$ yields a minor product containing the twelve-vertex endohedral anion $[Ni@Pb_{12}]^{2-}$.[5] Similarly, the heavier analogues $[M@Pb_{12}]^{2-}$ (M = Pd, Pt) can also be obtained by reacting the group 14 Zintl precursors with the metal reagents $M(PPh_3)_4$ in solution.[5, 7] Another example of such an endohedral cluster ion is $[Ir@Sn_{12}]^{3-}$, produced by oxidation of $[Sn_9Ir(COD)]^{3-}$ (section **1.3.3.2**) with triphenylphosphine or dppe (dppe = $Ph_2PCH_2CH_2PPh_2$) at 80 °C.[8, 9] The step-wise synthesis of the cluster $[Ir@Sn_{12}]^{3-}$ from the intermediate $[Sn_9Ir(COD)]^{3-}$ sheds new light on the probable reaction mechanism of the formation of these ligand-free endohedral species.

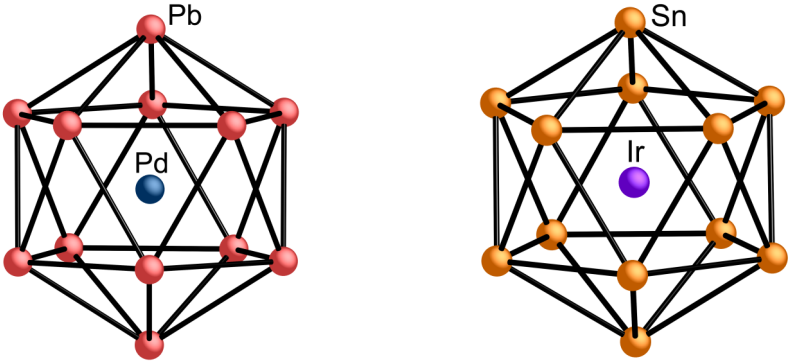

Figure 4.3 Structures of the cluster anions $[Pd@Pb_{12}]^{2-}$ and $[Ir@Sn_{12}]^{3-}$ as determined by single crystal X-ray diffraction.

The crystallographic data for the $[K(2,2,2\text{-crypt})]^{+}$ salts of the cluster anions show that they are all isostructural, containing a regular metal-centered icosahedral cluster moiety with near perfect I_h point group symmetry. From the point of view of electron counting, they are treated as $[(M^0)Pb_{12}]^{2-}$ (M = Ni, Pd, Pt) and $[(Ir^-)(Sn_{12}^{2-})]^{3-}$. The central transition metal atoms have closed-shell d^{10} configurations, contributing no electrons to cluster bonding. According to Wade-Mingos rules, a twelve-atom cluster with $2 \times 12 + 2 = 2n + 2$ skeletal electrons is predicted to have a *closo* icosahedral geometry.

DFT calculations have been performed on the empty ions $[Pb_{12}]^{2-}$ and $[Pb_{10}]^{2-}$, as well as the endohedral clusters $[M@Pb_{10}]^{2-}$ (M = Ni, Pd, Pt) and $[Ir@Sn_{12}]^{3-}$.[5, 9] The calculated structural parameters of the $[Pb_{10}]^{2-}$ ion are very close to both the calculated and observed bond metric data for $[Ni@Pb_{10}]^{2-}$. This probably explains why the Ni-centered species can be isolated, but there has been no evidence for the heavier analogues $[M@Pb_{10}]^{2-}$ (M = Pd, Pt). In contrast, the optimally sized interstitial atom for the twelve-atom cage $[Pb_{12}]^{2-}$ is Pt, which agrees with the observation of the endohedral cluster anion $[Pt@Pb_{12}]^{2-}$. The ground-state geometry of the optimised cluster anion $[Ir@Sn_{12}]^{3-}$ is icosahedral, consistent with the crystallographic data. In addition, the Ir centre is calculated to carry a natural charge of –1.07, supporting the previous assumption of the charge allocation $[(Ir^{-})(Sn_{12}^{2-})]^{3-}$.

Endohedral clusters with higher nuclearities such as $[Ni_2Sn_{17}]^{4-}$, $[(Ni@Ge_9)Ni(Ni@Ge_9)]^{4-}$, $[Pt_2@Sn_{17}]^{4-}$, $[Pd_2@Ge_{18}]^{4-}$ and $[Pd_2@Sn_{18}]^{4-}$ have also been synthesised.[10-15]

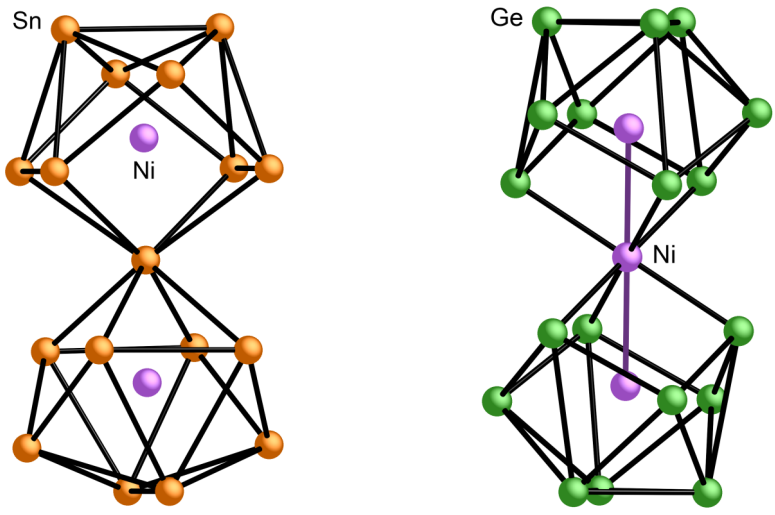

Figure 4.4 Structures of the cluster anions $[Ni_2Sn_{17}]^{4-}$ and $[(Ni@Ge_9)Ni(Ni@Ge_9)]^{4-}$ as determined by single crystal X-ray diffraction.

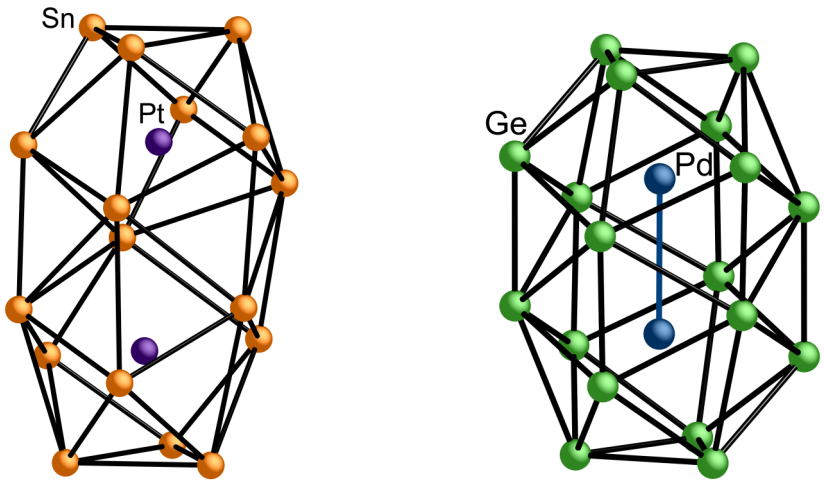

Figure 4.5 Structures of the cluster anions $[Pt_2@Sn_{17}]^{4-}$ and $[Pd_2@Ge_{18}]^{4-}$ as determined by single crystal X-ray diffraction. The endohedral cage $[Pd_2@Sn_{18}]^{4-}$ is isoelectronic and isostructural with $[Pd_2@Ge_{18}]^{4-}$.

All of the ligand-free endohedral group 14 Zintl clusters reviewed so far are deltahedral, and contain transition metals of group 9, 10 and 11 with closed-shell d^{10} configurations. We thus set out to study the reactions between $[E_9]^{4-}$ (E = Ge, Sn, Pb) and homoleptic organometallic reagents of group 7 and 8 elements such as Fe and Mn. This has resulted in the isolation and characterisation of three new metal-centered "naked" Zintl ions: the first non-deltahedral endohedral cluster $[Fe@Ge_{10}]^{3-}$ (**18**), the isoelectronic deltahedral analogue $[Fe@Sn_{10}]^{3-}$ (**19**) and the first example of a highly distorted open-shell cage $[Mn@Pb_{12}]^{3-}$ (**22**). In addition to their solution and solid-state characterisation, they have also been investigated in depth by DFT calculations to explore the electronic origin of their varied structures.

4.2 Results and discussion: ten-vertex endohedral clusters $[Fe@Ge_{10}]^{3-}$ and $[Fe@Sn_{10}]^{3-}$

4.2.1 Isolation of the pentagonal prismatic cluster anion $[Fe@Ge_{10}]^{3-}$ (18)

4.2.1.1 Synthetic method

K_4Ge_9, $FeAr_2$ (Ar = 2,6-$mes_2C_6H_3$) and 2,2,2-crypt were reacted in the molar ratio of 2:1:3.5 in ethylenediamine with the addition of trace amounts of THF (THF = tetrahydrofuran). After stirring for 1 h, the dark brown reaction mixture was filtered and layered with toluene for crystallisation. Small greenish black rods of $[K(2,2,2\text{-crypt})]_3[Fe@Ge_{10}]$•2en were obtained after a few days. The reaction is non-stoichiometric, and crystals of the $[K(2,2,2\text{-crypt})]^+$ salts of $[Ge_9]^{3-}$ and $[Ge_9–Ge_9]^{6-}$ were often observed alongside the desired product. It is worth noting that the synthesis of $[Fe@Ge_{10}]^{3-}$ is strongly dependent on the nature of the organometallic reagent employed. The analogous reaction between K_4Ge_9, $Fe_2(mes)_4$ and 2,2,2-crypt was performed using similar conditions, but this yielded the *exo*-functionalised cluster $[Ge_9(mes)]^{3-}$ (**19**) rather than the endohedral cage $[Fe@Ge_{10}]^{3-}$.

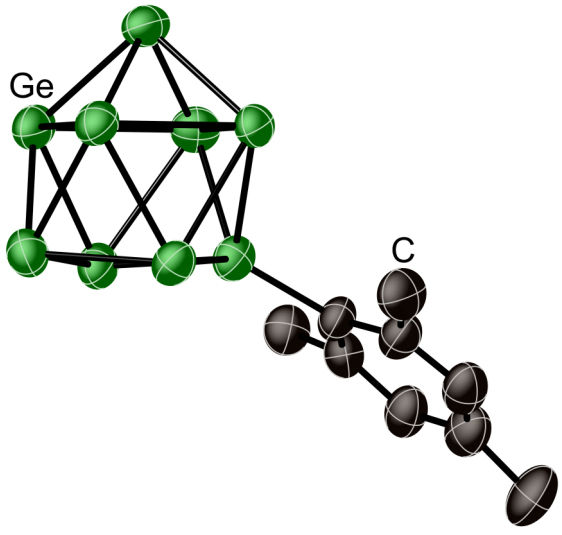

Figure 4.6 Thermal ellipsoid plot of $[Ge_9(mes)]^{3-}$ (**19**) cluster anion as determined by single crystal X-ray diffraction. Anisotropic displacement ellipsoids pictured at the 50% probability level. Hydrogen atoms have been omitted for clarity.

The reaction between $FeAr_2$ and K_4Ge_9 is presumed to proceed *via* the reductive cleavage of both Fe–C bonds of the two-coordinate, monomeric organometallic reagent $FeAr_2$.[16] It has been established that the free solvated electrons resulting from the dissolution of the group 14 Zintl precursors K_4E_9 can activate metal-carbon bonds of compounds such as $ZnPh_2$.[17] In this case the reductive activation reaction produces an organic anion Ar^-, which can readily abstract a proton from the solvent to yield ArH and an amide. Following the cleavage of both Ar groups, the resulting "naked" Fe atom is inserted into the 10-atom cage accompanied by some degree of cluster decomposition and redistribution.

At the time of publication of our findings, independent research by the Fässler group resulted in the isolation of a pentagonal prismatic endohedral cluster $[Co@Ge_{10}]^{3-}$.[18] Crystals of the salt $[K(2,2,2\text{-crypt})]_4[Co@Ge_{10}][Co(C_8H_{12})_2]$•tol were obtained by reacting K_4Ge_9 with $Co(C_8H_{12})(C_8H_{13})$ in the presence of 2,2,2-crypt in ethylenediamine.

4.2.1.2 Characterisation of $[K(2,2,2\text{-crypt})]_3[Fe@Ge_{10}]$•2en

4.2.1.2.1 Single crystal X-ray structural analysis

The endohedral cluster $[Fe@Ge_{10}]^{3-}$ (**18**) is composed of a pentagonal prismatic $[Ge_{10}]$ cage encapsulating an iron atom at the centre. It possesses a pseudo D_{5h} symmetry, which makes it unique amongst all of the previously reported ligand-free endohedral Zintl clusters. All the examples discussed in section **4.1** are deltahedral and therefore follow Wade-Mingos rules for electron counting. The Co analogue $[Co@Ge_{10}]^{3-}$ is isostructural with the cluster **18** and also carries a 3-fold negative charge.

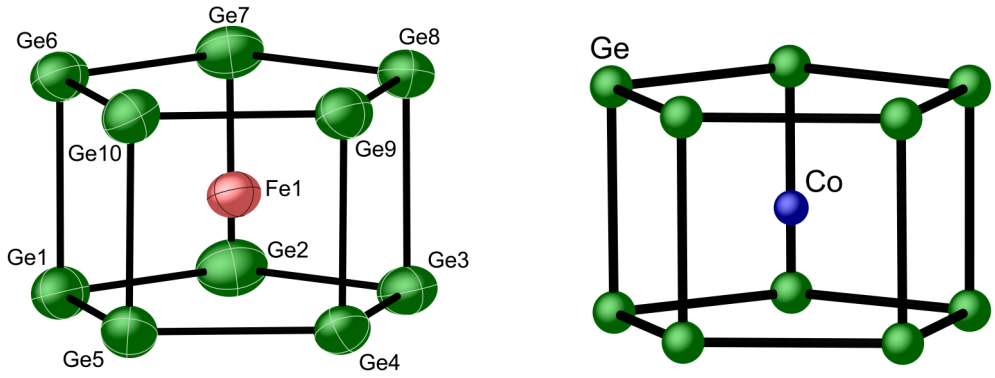

Figure 4.7 Thermal ellipsoid plot of $[Fe@Ge_{10}]^{3-}$ (**18**) and a ball & stick model of the analogous $[Co@Ge_{10}]^{3-}$ cluster anions as determined by single crystal X-ray diffraction. Anisotropic displacement ellipsoids pictured at the 50% probability level.

The Ge–Ge interatomic distances in cluster **18** fall within two ranges: 2.6049(7) – 2.6222(6) Å for the bonds between the two pentagons, and 2.5259(7) – 2.5462(7) Å for those within the pentagons. The Ge–Ge bonds linking the two five-membered rings are slightly longer than those in the pentagonal faces. Compared to the Co-centered cluster anion, the bond lengths between the pentagons are almost identical. However, the Ge–Ge distances in the pentagons of cluster **18** are longer than those in $[Co@Ge_{10}]^{3-}$ by approx. 0.2 Å. The Fe–Ge contacts vary between 2.5087(7) and 2.5353(7) Å, which are greater than the longest Fe–Ge bond reported to date (2.497(1) Å) in $[CpFe(CO)_2]_2Ge(N^tBu)_2SiMe_2$.[19] This implies weak interactions between the central transition metal atom and the surrounding germanium atoms. The bond angles in the five side faces of the pentagonal prism **18** fall in the range between 88.90(2)° and 91.04(2)° and those in the cluster $[Co@Ge_{10}]^{3-}$ are 90 ± 0.7°.

4.2.1.2.2 Electronic structure

The unique D_{5h} symmetry exhibited by **18** is different from other reported deltahedral Zintl clusters, indicating that conventional electron counting rules may not apply. The overall cluster charge suggests it should be paramagnetic, and hence magnetic measurements would give insight into the electronic structure of the cluster. However, crystals of paramagnetic species such as $[Ge_9]^{3-}$ were always present alongside [K(2,2,2-crypt)]$_3$[**18**]•2en, which made it difficult to isolate a compositionally pure sample for further studies. DFT calculations on the analogous $[Co@Ge_{10}]^{3-}$ by the Fässler group indicates that the interstitial transition metal carries a natural charge of –1.05, suggesting a closed-shell d^{10} configuration of the Co atom. It is interesting to note that while $[Fe@Ge_{10}]^{3-}$ and $[Co@Ge_{10}]^{3-}$ are isostructural, the Co-centered system has an additional e^- available for cluster bonding. The electronic structures of these cluster anions will be discussed in depth in section 4.2.3.

4.2.1.2.3 Electrospray mass spectrometry

DMF solutions of the crystalline solid isolated from the reaction of K_4Ge_9 with $FeAr_2$ were studied by electrospray mass spectrometry in both the positive and negative ion modes. The negative ion mode mass spectrum reveals mass envelopes corresponding to $[Fe@Ge_{10}]^-$ (*m/z* = 781.2), $\{K[Fe@Ge_{10}]\}^-$ (*m/z* = 822.2) and $\{[K(2,2,2\text{-crypt})][Fe@Ge_{10}]\}^-$ (*m/z* = 1198.7). The positive ion mode mass spectrum contains a peak with an isotopic distribution corresponding to $\{[K(2,2,2\text{-crypt})]_4[Fe@Ge_{10}]\}^+$ (*m/z* = 2443.9). Peaks corresponding to unreacted nonagermanide species were also visible in both ion modes.

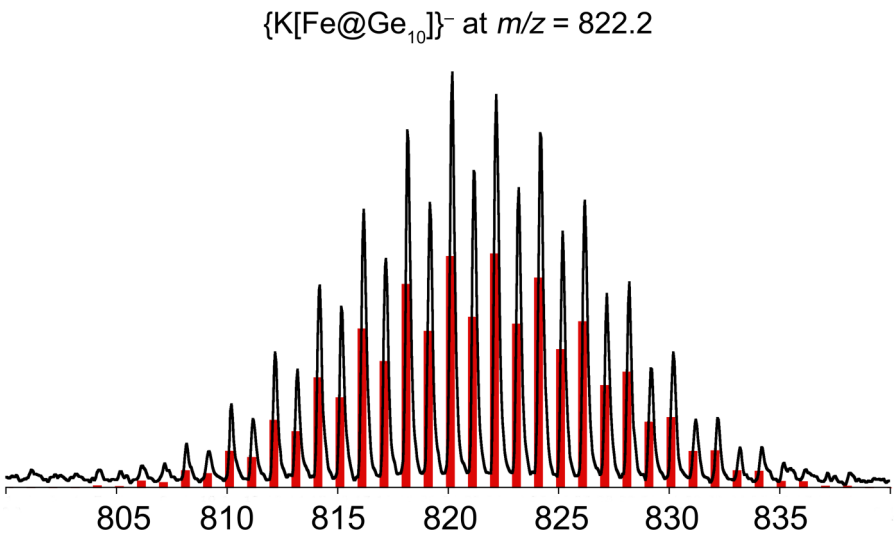

Figure 4.8a Electrospray mass-envelope corresponding to $\{K[Fe@Ge_{10}]\}^-$. Experimental data are drawn in black with calculated isotopic distributions in red.

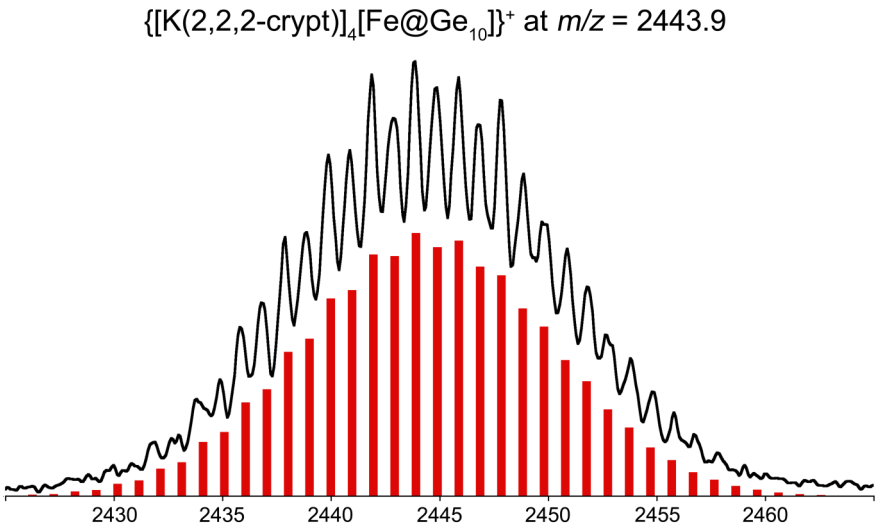

Figure 4.8b Electrospray mass-envelope corresponding to $\{[K(2,2,2\text{-crypt})]_4[Fe@Ge_{10}]\}^+$. Experimental data are drawn in black with calculated isotopic distributions in red.

4.2.2 Isolation of the deltahedral cluster anion $[Fe@Sn_{10}]^{3-}$ (20)

4.2.2.1 Synthetic methods

Prompted by the synthesis and isolation of $[Fe@Ge_{10}]^{3-}$ (**18**), a similar reaction between K_4Sn_9 and $Fe_2(mes)_4$ in the presence of 2,2,2-crypt was explored in solution. A THF solution of $Fe_2(mes)_4$ was added dropwise to an ethylenediamine solution of K_4Sn_9 and 2,2,2-crypt. After stirring for 1 h, the reaction mixture was filtered and the filtrate dried under vacuum. The solid was then redissolved in pyridine and the filtrate layered with toluene for crystallisation. After several days, black crystalline rods of $[K(2,2,2\text{-crypt})]_3[Fe@Sn_{10}]\bullet 4py$ were obtained in low crystalline yield. The reaction is again assumed to proceed *via* the reductive cleavage of all the Fe–C bonds of the organometallic reagent $Fe_2(mes)_4$ by the solvated electrons in the reaction mixture.

4.2.2.2 Characterisation of $[K(2,2,2\text{-crypt})]_3[Fe@Sn_{10}]\bullet 4py$

4.2.2.2.1 Single crystal X-ray structural analysis

Single crystal X-ray diffraction reveals that the endohedral cluster anion $[Fe@Sn_{10}]^{3-}$ (**20**) is approximately spherical. There is some rotational disorder at the cluster site with the two components (60% to 40%) exhibiting similar geometries and hence only the major component will be discussed in detail in the following section.

The Sn–Sn bond lengths lie in the range between 2.585(6) and 3.273(7) Å, and the interatomic distances for Fe–Sn contacts vary between 2.495(5) and 2.831(2) Å. The 10-vertex metal-centered cluster $[Fe@Sn_{10}]^{3-}$ (**20**) exhibits approximate C_s symmetry with the reflection plane defined by Sn8, Sn9 and Fe1. However it does not deviate far from the higher order D_{4d}

geometry, in which the axis passing through Sn3, Fe1 and Sn6 would define the 4-fold rotational axis. As discussed in section 4.1, the related endohedral Zintl cluster $[Ni@Pb_{10}]^{2-}$ can be described as a bicapped square antiprism with an interstitial Ni atom, possessing virtual D_{4d} point symmetry. In contrast, the isoelectronic counterpart $[Fe@Ge_{10}]^{3-}$ (**18**) discussed in section 4.2.1.2.1 is non-deltahedral, featuring an iron-centered pentagonal prismatic structure.

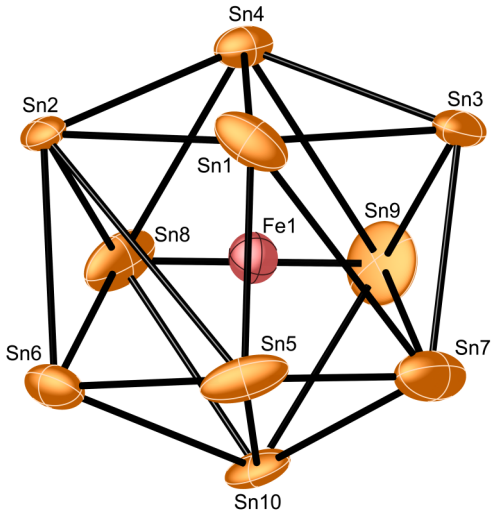

Figure 4.9 Thermal ellipsoid plot of the major component of $[Fe@Sn_{10}]^{3-}$ (**20**) cluster anion as determined by single crystal X-ray diffraction. Anisotropic displacement ellipsoids pictured at the 30% probability level.

4.2.2.2.2 Electrospray mass spectrometry

DMF solutions of the solid isolated from the reactions of K_4Sn_9 with $Fe_2(mes)_4$ were studied by electrospray mass spectrometry in both positive and negative ion modes. The negative ion mode mass spectrum reveals mass envelopes corresponding to $[Fe@Sn_{10}]^-$ (*m/z* = 1242.8), $\{[K(2,2,2\text{-crypt})][Fe@Sn_{10}]\}^-$ (*m/z* = 1659.1) and $\{[K(2,2,2\text{-crypt})]_2[Fe@Sn_{10}]\}^-$ (*m/z* = 2075.4). The positive ion mode mass spectrum contains a peak with an isotopic distribution corresponding to $\{[K(2,2,2\text{-crypt})]_4[Fe@Sn_{10}]\}^+$ (*m/z* = 2904.9). Mass envelopes

corresponding to empty cages were also visible in both ion modes, such as $[Sn_{10}]^-$ (*m/z* = 1187.0), $\{[K(2,2,2\text{-crypt})][Sn_{10}]\}^-$ (*m/z* = 1602.3), $\{[K(2,2,2\text{-crypt})]_2[Sn_{10}]\}^-$ (*m/z* = 2019.5) and $\{[K(2,2,2\text{-crypt})]_3[Sn_{10}]\}^+$ (*m/z* = 2433.8). These species probably arise from some degree of cluster decomposition during the ionisation process.

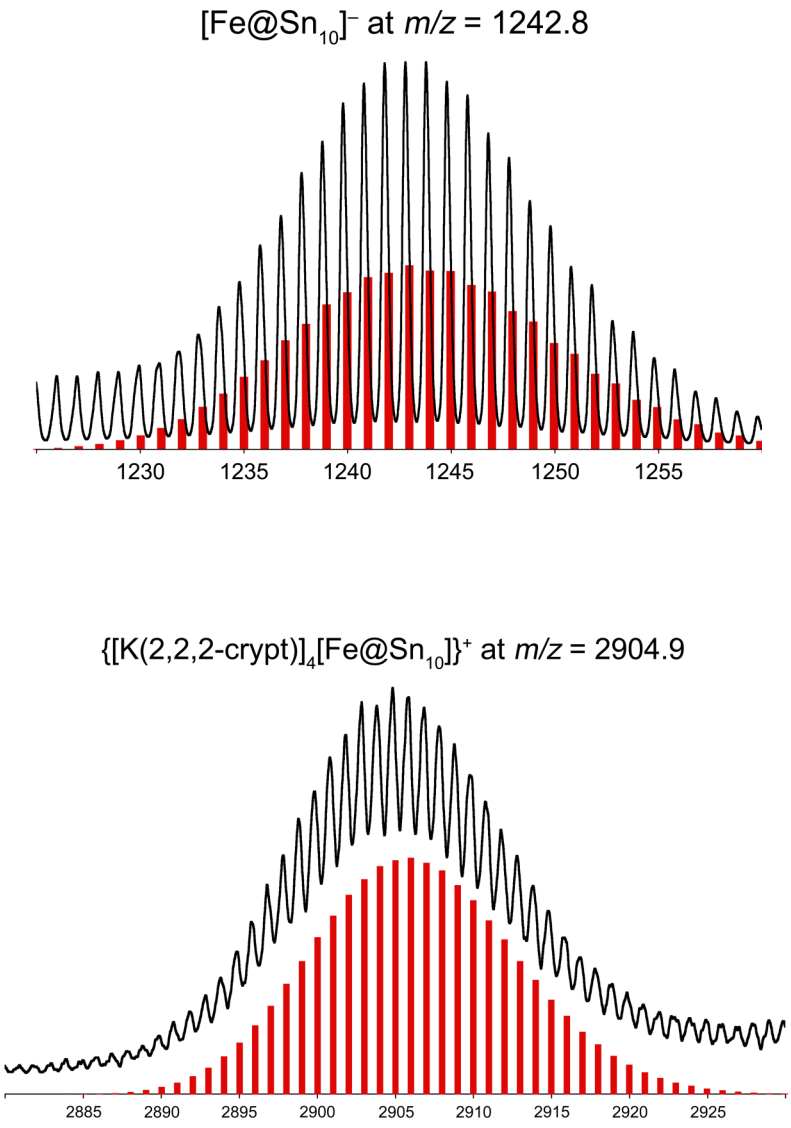

Figure 4.10 Electrospray mass-envelopes corresponding to $[Fe@Sn_{10}]^-$ (top) and $\{[K(2,2,2\text{-crypt})]_4[Fe@Sn_{10}]\}^+$ (bottom). Experimental data are drawn in black with calculated isotopic distributions in red.

4.2.2.2.3 EPR spectroscopy

The total valence electron count of the cluster anion $[Fe@Sn_{10}]^{3-}$ (**20**) is 4 × 10 + 8 + 3 = 51, so it should be paramagnetic. Its paramagnetic nature was investigated by solid-state EPR spectroscopy both at room temperature and at 15 K. The room temperature EPR spectrum of a crystalline sample of $[K(2,2,2\text{-crypt})]_3[Fe@Sn_{10}]$•4py contains a weak and broad resonance centered at a *g* factor of 2.0229. Upon cooling to 15 K this resonance sharpens and intensifies at the *g* factor of 2.0297. The temperature dependence of the EPR resonance may be explained by spin-orbit coupling and/or fast relaxation effects at higher temperature.[20]

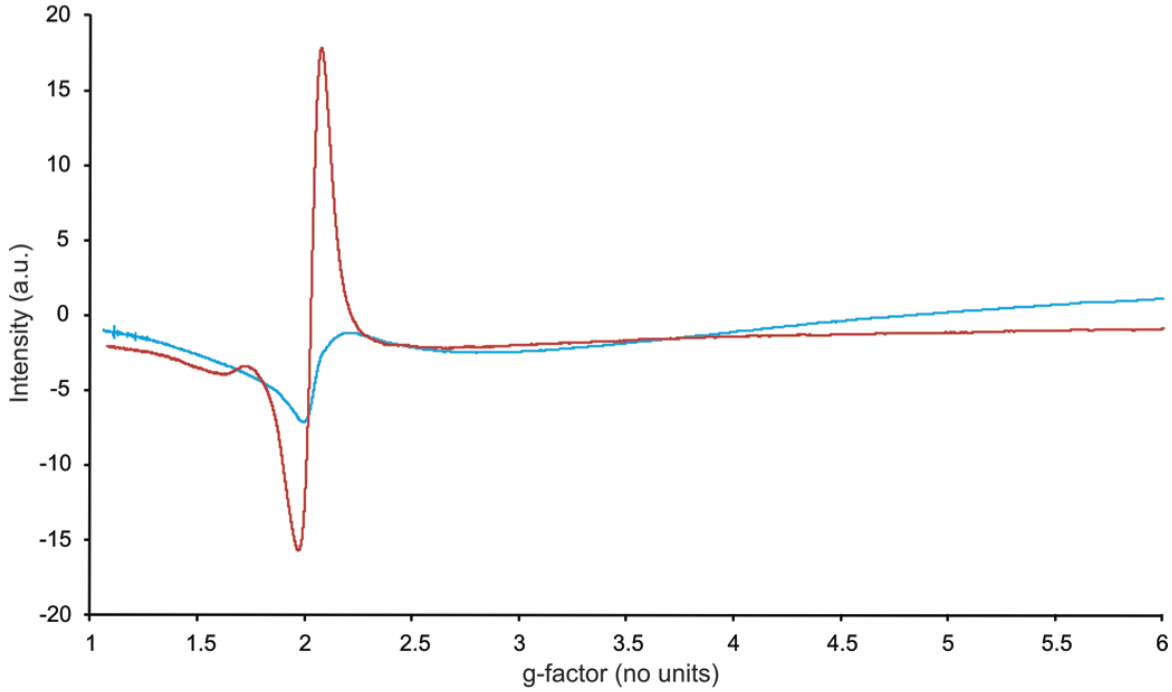

Figure 4.11 X-band (9.3896 GHz) CW EPR spectrum of a solid sample of $[K(2,2,2\text{-crypt})]_3[Fe@Sn_{10}]$•4py collected at room temperature (blue) and at 15 K (red).

4.2.3 Computational analysis and comparison of $[Fe@Ge_{10}]^{3-}$ and $[Fe@Sn_{10}]^{3-}$

The isoelectronic species $[Fe@Ge_{10}]^{3-}$ and $[Fe@Sn_{10}]^{3-}$ exhibit remarkably different geometries and the origin of this difference was explored by an in depth computational investigation of their electronic structures by our collaborators Tobias Krämer and John McGrady (Oxford).

A number of computational analyses on similar systems have been reported in the literature. For example $[Ni@Pb_{10}]^{2-}$ was found to have a D_{4d} stable minimum, which is consistent with the observed crystal structure.[4, 5, 21] Similarly, the isoelectronic cluster $[Ni@Ge_{10}]^{2-}$ was also calculated to have a stable D_{4d} symmetric minimum.[22] However the heavier congeners $[Pd@Ge_{10}]^{2-}$ and $[Pt@Ge_{10}]^{2-}$ prefer a non-deltahedral D_{5h} symmetric structure. This has been rationalised by the size difference of the cavity for the two different cages, and hence the larger D_{5h} cluster can better accommodate bigger central atoms. The isoelectronic species $[Co@Ge_{10}]^{3-}$ was computed to have a D_{5h} global minimum, which agrees with the experimental observation. The deltahedral D_{4d} symmetric species is at a stationary point lying 0.58 eV above D_{5h}.[18]

The same steric arguments can also be applied to the cluster anions $[Fe@Ge_{10}]^{3-}$ and $[Fe@Sn_{10}]^{3-}$. Ge is smaller than Sn and therefore the larger D_{5h} cage is more suitable to accommodate the central Fe atom. However there is one more significant factor, which needs to be addressed. The differing degrees of electron density transfer from the central metal atom to the cluster cage may play a significant role in determining the cluster geometry. This concept will be explained in the following section.

Exploring the potential energy surface of the anion $[Fe@Ge_{10}]^{3-}$ reveals a global minimum with D_{5h} symmetry. The calculated bond metric data are consistent with the experimental values determined from single crystal X-ray diffraction. The C_{2v}-symmetric form is a stationary point, which is 0.26 eV higher in energy than the global minimum. Two almost iso-energetic states D_{4d} and C_{3v} are second order transition points linking two C_{2v} states. The same study was performed on the cluster $[Fe@Sn_{10}]^{3-}$, which reveals two almost iso-energetic low-lying states C_2 and D_{4d}. The C_2 symmetry is the global minimum and agrees well with the observed crystallographic data. D_{5h} is a stationary point lying 0.33 eV above the global minimum. These results show that the DFT calculations can reproduce the observed crystal structures of the cluster anions $[Fe@Ge_{10}]^{3-}$ and $[Fe@Sn_{10}]^{3-}$.

To investigate the electronic origins of the structural differences, the spin density distribution was computed for the cluster anion $[Fe@Ge_{10}]^{3-}$ (D_{5h}). The results ρ(Fe) = + 1.45 and $\rho(Ge_{10})$ = – 0.45 suggest an accumulation of spin-α density on the central metal ion, and a transfer of spin-β density onto the cluster cage. In theory there are three limiting models for the charge distribution between the central metal and the surrounding cage for $[Fe@E_{10}]^{3-}$ (E = Ge and Sn): 1) $[Fe(–I)@E_{10}^{2-}]^{3-}$, a *closo*-cage; 2) $[Fe(–II)@E_{10}^{-}]^{3-}$, a closed-shell d^{10} configuration for Fe; 3) $[Fe(III)@E_{10}^{6-}]^{3-}$, a half-filled d^5 configuration for Fe. The calculated values indicate that the true situation is closer to the *closo*-cage, but with a significant tendency to donate electron density to the cage.

The transfer of charge density from Fe to the $[Ge_{10}]$ cluster gives rise to the observed structural distortion. When transforming the deltahedral D_{4d} symmetry to the non-deltahedral

D_{5h} geometry, four empty cluster-based orbitals can overlap with high-lying metal d orbitals. This stabilises these unoccupied orbitals and transfers some β spin density onto the cage.

In summary, there are three factors governing the geometry of these endohedral clusters. For a given cluster element, the deltahedral structure is intrinsically more stable than the non-deltahedral structure. However, the non-deltahedral cage is larger than the deltahedral one and can accommodate a larger central atom. The number of metal d orbitals that can overlap with empty cluster-based orbitals can determine the preferred structural distortion. In the case of the anion $[Fe@Ge_{10}]^{3-}$ both steric factors and the charge transfer favour a non-deltahedral D_{5h} symmetry. In contrast, for the isoelectronic species $[Fe@Sn_{10}]^{3-}$ the deltahedral form is large enough to encapsulate the Fe atom. Despite having the same charge transfer from the central Fe to the $[Sn_{10}]$ cluster, a distorted D_{4d} geometry is still favourable.

4.2.4 Isolation and characterisation of reaction side products

In the process of synthesising the compound $[K(2,2,2\text{-crypt})]_3[Fe@Sn_{10}]\bullet 4py$, crystalline phases of two side products $[K(2,2,2\text{-crypt})]_3[Sn_9(mes)]\bullet 2py$ and $[K(2,2,2\text{-crypt})]_3[Sn_9Fe(mes)]$ were occasionally isolated. They may arise from the reactions between the cluster anions $[Sn_9]^{4-}$ and the organic and organometallic fragments, which are generated in the formation of $[Fe@Sn_{10}]^{3-}$. Another possibility is that the functionalized cluster $[Sn_9Fe(mes)]^{3-}$ (**22**) is the intermediate of the reaction, which then undergo partial fragmentation to give the endohedral compound $[Fe@Sn_{10}]^{3-}$ or to $[Sn_9(mes)]^{3-}$ (**21**).

The structure of the salt $[K(2,2,2\text{-crypt})]_3[Sn_9(mes)]\bullet 2py$ was examined in the solid state by single crystal X-ray diffraction. The *exo*-functionalised cluster anion $[Sn_9(mes)]^{3-}$ (**21**) is geometrically similar to other previously reported alkylated nonastannide species, such as $[Sn_9–{}^t\text{Bu}]^{3-}$. It is a distorted monocapped square antiprism with the organic group bonded to the Sn atom of the shorter diagonal in the open square base. The C1–Sn9–Sn7 bond angle is 154.1º, which is smaller than the value in analogous clusters (160.8(2)º in $[Sn_9–{}^t\text{Bu}]^{3-}$ and 164.2(1) in $[Sn_9–CH{=}CH_2]^{3-}$). The Sn–Sn bond distances vary between 2.8667(7) and 3.2352(7) Å, comparable to those in other alkylated nonastannide clusters. The length of the *exo* C1–Sn9 bond is 2.219(7) Å, which is similar to those found for analogous compounds such as $[Sn_9–{}^t\text{Bu}]^{3-}$ (2.265(7) Å).

Electronically, the substituted Sn vertex donates one more electron to cluster bonding than the other Sn atoms, because only one electron is used for the *exo* Sn–C bond. As a result there are $2 \times 8 + 3 + 3 = 22 = 2n + 4$ skeletal electrons, suggesting a *nido* structure according to Wade-Mingos rules.

DMF solutions of the crystalline sample $[K(2,2,2\text{-crypt})]_3[Sn_9(mes)]\bullet 2py$ were studied by electrospray mass spectrometry in both the positive and negative ion modes. The negative ion mode mass spectrum reveals mass envelopes corresponding to $[Sn_9(mes)]^-$ (*m/z* = 1188.2) and $\{[K(2,2,2\text{-crypt})][Sn_9(mes)]\}^-$ (*m/z* = 1602.0). The positive ion mode mass spectrum contains a mass envelope corresponding to the cation paired species $\{[K(2,2,2\text{-crypt})]_3[Sn_9(mes)]\}^+$ (*m/z* = 2432.8).

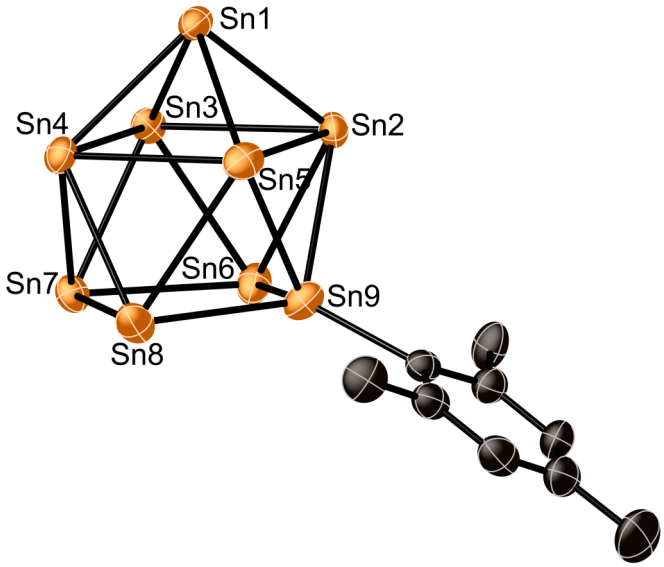

Figure 4.12 Thermal ellipsoid plot of the cluster anion $[Sn_9(mes)]^{3-}$ (**21**) as determined by single crystal X-ray diffraction. Anisotropic displacement ellipsoids pictured at the 50% probability level. Hydrogen atoms have been omitted for clarity.

Crystals of $[K(2,2,2\text{-crypt})]_3[Sn_9Fe(mes)]$ were not of sufficient quality for a suitable X-ray structure to be obtained and hence the bond metric data cannot be discussed. That being said, the data obtained were of sufficient quality to determine cluster connectivity and composition. The negative ion-mode electrospray mass spectra of the compound reveal isotopic distributions corresponding to $[Sn_9Fe]^-$ (*m/z* = 1125.2), $[Sn_9(mes)]^-$ (*m/z* = 1188.2), $[Sn_9Fe(mes)]^-$ (*m/z* = 1244.0), $\{[K(2,2,2\text{-crypt})][Sn_9(mes)]\}^-$ (*m/z* = 1602.2) and $\{[K(2,2,2\text{-crypt})][Sn_9Fe(mes)]\}^-$ (*m/z* = 1658.0). The positive ion-mode spectra show mass envelopes corresponding to $\{[K(2,2,2\text{-crypt})]_4[Sn_9(mes)]\}^+$ (*m/z* = 2852.1) and $\{[K(2,2,2\text{-crypt})]_4[Sn_9Fe(mes)]\}^+$ (*m/z* = 2906.1).

4.3 Results and discussion: the twelve-vertex endohedral cluster $[Mn@Pb_{12}]^{3-}$ (23)

4.3.1 Synthetic method

A THF solution of $Mn_3(mes)_6$ was added dropwise to an ethylenediamine solution of K_4Pb_9 and 2,2,2-crypt. After being stirred for 1 h, the reaction mixture was filtered and layered with Et_2O for crystallisation. After a few days, thin black plate-like crystals of $[K(2,2,2\text{-crypt})]_3[Mn@Pb_{12}]\bullet 1.5en$ were obtained in low crystalline yield, accompanied by some degree of metallic decomposition. Once again, the reaction is thought to proceed *via* the reductive cleavage of all the Mn–C bonds of the organometallic reagent $Mn_3(mes)_6$ by solvated electrons.

4.3.2 Characterisation of $[K(2,2,2\text{-crypt})]_3[Mn@Pb_{12}]\bullet 1.5en$

4.3.2.1 Single crystal X-ray structural analysis

It proved problematic to collect high-quality single crystal X-ray data for the product $[K(2,2,2\text{-crypt})]_3[Mn@Pb_{12}]\bullet 1.5en$. The crystals were very small, thin, black plates that decomposed rapidly even under Paratone-N oil, making it challenging to select a suitable crystal. The heavy cluster anions in the crystalline lattice scattered very strongly, which saturated the detector at low angles and imposed pseudosymmetry on the system. Attempts to synthesise the product using alternative solvent mixtures and cation sequestering agents under different reaction conditions did not prove fruitful. Despite these challenges, a final structural solution of the product of reasonable quality was obtained. The accuracy and precision of the bond metric parameters for the lighter atoms in the 2,2,2-crypt portion of the structure may be limited, however the geometric and electronic features of the endohedral clusters are unequivocal.

There are three crystallographically independent $[Mn@Pb_{12}]^{3-}$ (**23**) clusters in the crystal lattice. The central Mn atoms of two of the anions sit on inversion centres whereas the remaining cluster is entirely crystallographically unique. The cage that is not constrained by inversion symmetry exhibits D_{2h} geometry, which deviates away from the icosahedral structure of the other reported 12-vertex metal-centered Zintl clusters, such as $[M@Pb_{12}]^{2-}$ (M = Ni, Pd, Pt) and $[Ir@Sn_{12}]^{3-}$. The $[Mn@Pb_{12}]^{3-}$ anions that sit on crystallographic inversion centres display C_{2h} symmetry.

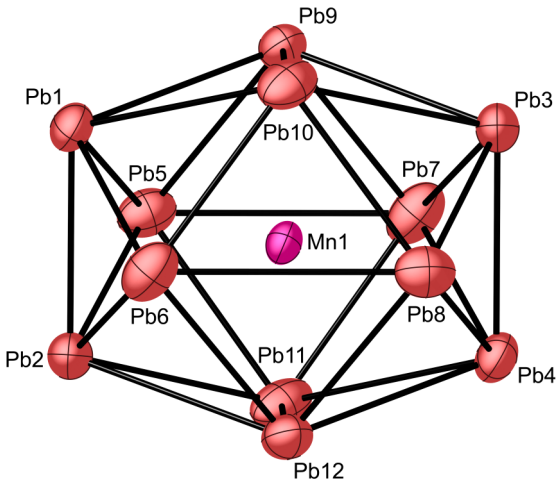

Figure 4.13 Thermal ellipsoid plot of the crystallographically unconstrained $[Mn@Pb_{12}]^{3-}$ (**23**) cluster anion as determined by single crystal X-ray diffraction. Anisotropic displacement ellipsoids pictured at the 50% probability level.

For the highly symmetrical closed-shell analogues $[M@Pb_{12}]^{2-}$ (M = Ni, Pd, Pt) and $[Ir@Sn_{12}]^{3-}$, the interatomic M–E and E–E distances fall within narrow ranges. In the case of the highly distorted open-shell cluster anion $[Mn@Pb_{12}]^{3-}$ (**23**) with D_{2h} symmetry, the Mn–Pb contacts lie in three ranges: 2.869(3) – 2.891(3) Å (Mn–Pb9, Pb10, Pb11, Pb12), 3.080(4)

– 3.112(4) Å (Mn–Pb5, Pb6, Pb7, Pb8) and 3.272(4) – 3.308(4) Å (Mn–Pb1, Pb2, Pb3, Pb4). The Pb–Pb bond lengths vary between 3.100(2) and 3.748(3) Å.

4.3.2.2 Electrospray mass spectrometry

DMF solutions of $[K(2,2,2\text{-crypt})]_3[Mn@Pb_{12}]\bullet 1.5en$ were studied by electrospray mass spectrometry in both the positive and negative ion modes. The negative ion mode mass spectrum reveals mass envelopes corresponding to $[Mn@Pb_{12}]^-$ (*m/z* = 2541.4) and $\{[K(2,2,2\text{-crypt})][Mn@Pb_{12}]\}^-$ (*m/z* = 2957.5). The positive ion mode mass spectrum contains a mass envelope with an isotopic distribution corresponding to $\{[K(2,2,2\text{-crypt})]_3[Mn@Pb_{12}]\}^+$ (*m/z* = 3788.1). Mass envelopes corresponding to empty cages were also visible in both ion modes, such as $[Pb_5]^-$ (*m/z* = 1035.7), $[Pb_{10}]^-$ (*m/z* = 2072.6), $[Pb_{12}]^-$ (*m/z* = 2487.8) and $\{[K(2,2,2\text{-crypt})]_3[Pb_{12}]\}^+$ (*m/z* = 3733.0). These species presumably arise from some degree of cluster decomposition during the ionisation process.

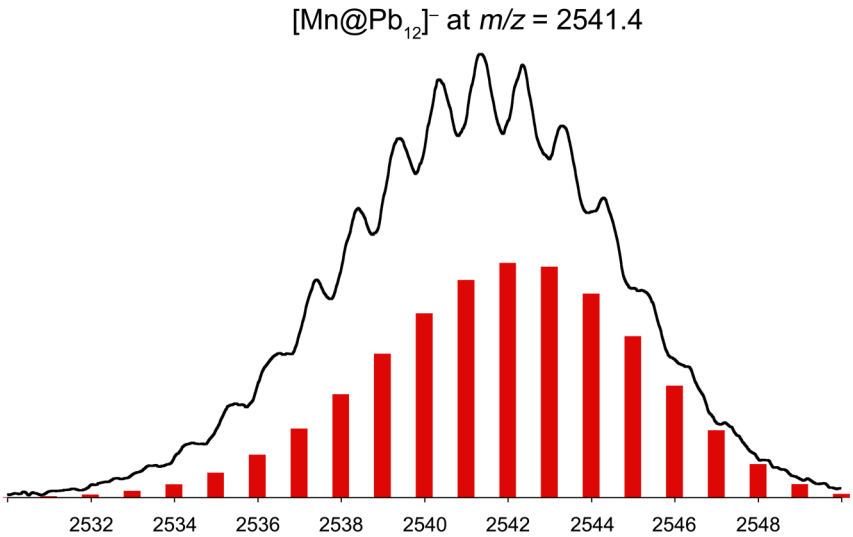

Figure 4.14a Electrospray mass-envelope corresponding to $[Mn@Pb_{12}]^-$. Experimental data are drawn in black with calculated isotopic distributions in red.

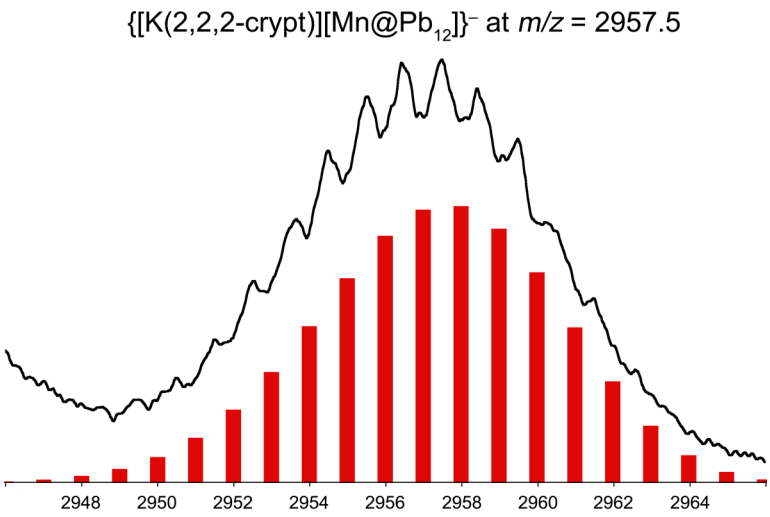

Figure 4.14b Electrospray mass-envelope corresponding to $\{[K(2,2,2\text{-crypt})][Mn@Pb_{12}]\}^-$. Experimental data are drawn in black with calculated isotopic distributions in red.

4.3.2.3 EPR spectroscopy

The paramagnetic character of the $[Mn@Pb_{12}]^{3-}$ cluster anion was studied by solid-state EPR spectroscopy at room temperature. A very broad resonance centered at a *g* factor of 2.0095 was observed. The broad nature of the spectrum resonance is probably an indication of fast relaxation effects owing to the spin-orbit coupling.[20] No solution-phase spectra were recorded due to the low stability of the sample at high dilution.

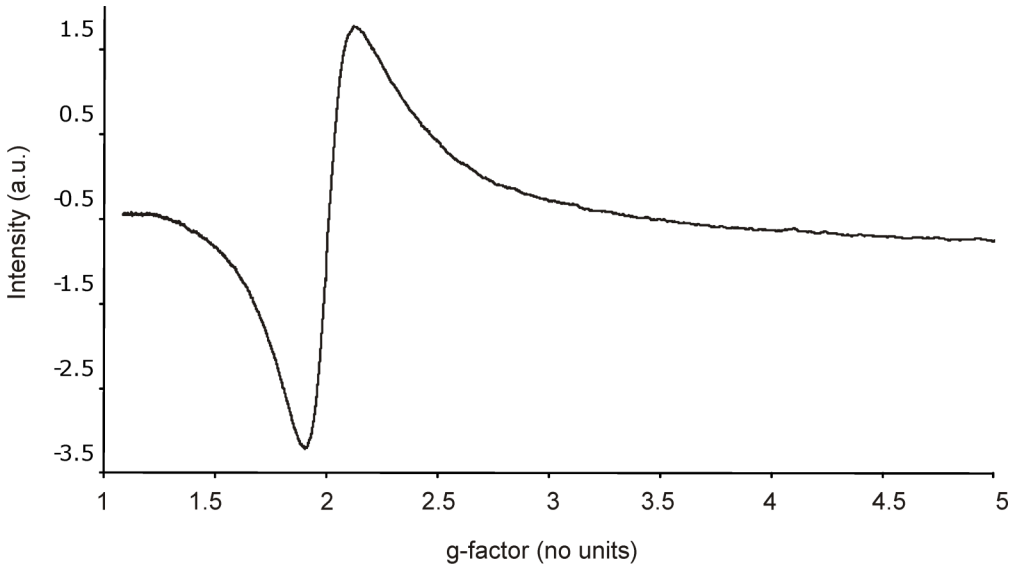

Figure 4.15 X-band (9.3896 GHz) CW EPR spectrum of a solid sample of $[K(2,2,2\text{-crypt})]_3[Mn@Pb_{12}]\bullet 1.5en$ collected at room temperature.

4.3.2.4 Computational analysis of $[Mn@Pb_{12}]^{3-}$

The electronic structure of the endohedral cluster $[Mn@Pb_{12}]^{3-}$ has been studied using Density Functional Theory (DFT) by our collaborator Tobias Krämer of the McGrady group (University of Oxford).[23] Exploring the potential energy surface of $[Mn@Pb_{12}]^{3-}$ reveals a global minimum with D_{3d} symmetry. There is a D_{2h} stationary point lying just 0.02 eV above it, which can be described as a transition state linking two D_{3d}-symmetric points. Both of these stationary points are triplet states ($S = 1$) and show strongly prolate distortions from the highly symmetric icosahedral structure. In particular, the bond metric data for the D_{2h} symmetric point are very similar to those of the experimental values determined by single crystal X-ray diffraction of $[K(2,2,2\text{-crypt})]_3[Mn@Pb_{12}]\bullet 1.5en$. However the structural differences between the two almost iso-energetic states D_{3d} and D_{2h} are very small. The idealised I_h stationary point sits 0.46 eV above the global minimum D_{3d}, which further supports the observed distortions

from icosahedral in the solid-state structure of the cluster. Hence DFT calculations prove to successfully reproduce the geometric features of the endohedral anion $[Mn@Pb_{12}]^{3-}$.

The molecular orbitals of $[Mn@Pb_{12}]^{3-}$ have been studied by employing the perfectly icosahedral $[Ni@Pb_{12}]^{2-}$ cluster anion as the reference point. This is because upon removing two electrons, the resulting neutral $[Ni@Pb_{12}]$ cluster is isoelectronic with $[Mn@Pb_{12}]^{3-}$.

The Kohn-Sham orbitals of the closed-shell icosahedral species $[Ni@Pb_{12}]^{2-}$ reveal that the LUMO ($1g_g$) is mainly a linear combination of tangential Pb 6*p* orbitals, whereas the LUMO+1 ($3h_g$) contains both radial (dominant) and tangential Pb 6*p* orbitals. A Jahn-Teller distortion from the I_h symmetry is expected if two electrons are removed from the 5-fold degenerate HOMO ($2h_g$) orbitals. However, the electron density distribution and structural properties are very different for the two isoelectronic endohedral clusters $[Ni@Pb_{12}]$ and $[Mn@Pb_{12}]^{3-}$. For the neutral cluster $[Ni@Pb_{12}]$ the majority of the spin density is delocalised over the 12-atom cluster cage, with only a small amount on the central Ni atom. The D_{2h} symmetry is only very slightly more stable than I_h and the impact of the structural distortion on the spin density distribution is not significant. In the case of the anion $[Mn@Pb_{12}]^{3-}$, a greater amount of the spin-β density is transferred from the central Mn centre (ρ(Mn) = + 3.21), leaving an opposite spin distributed over the Pb_{12} cluster ($\rho(Pb_{12}) = -1.21$). If there was no spin transfer to the cage, then the endohedral cluster anion would be expressed as $[Mn(-I)Pb_{12}^{2-}]^{3-}$ (ρ(Mn) = + 2.0, $\rho(Pb_{12}) = 0.0$). If all three spin-β electrons were transferred to the Pb_{12} cage, then the formula would be $[Mn(II)Pb_{12}^{5-}]^{3-}$ (ρ(Mn) = + 5.0, $\rho(Pb_{12}) = -3.0$), where the Mn centre achieves a half-filled d^5 configuration. The actual spin density distribution

between the central Mn and the surrounding Pb_{12} cluster is halfway between these two limiting situations. As described previously, the symmetric forms D_{3d} and D_{2h} for $[Mn@Pb_{12}]^{3-}$ are low-lying stationary points and I_h is 0.46 eV above the global minimum D_{3d}.

The electronic origin of the different geometries and spin density distributions can be explained by the Kohn-Sham orbitals of the cluster anions $[Ni@Pb_{12}]$ and $[Mn@Pb_{12}]^{3-}$. The HOMO ($2h_g$) of the I_h-symmetric $[Mn@Pb_{12}]^{3-}$ anion has more contribution from the Mn 3*d* orbitals than the Pb 6*p*, implying the unpaired electron density is localised on the central Mn atom. It is also higher in energy than the HOMO of $[Ni@Pb_{12}]$ under the same symmetry, which allows the spin-β component to mix with the Pb_{12} based low-lying vacant orbitals. As a result some of the β spin density of Mn can be transferred to the 12-atom cage. Under the I_h symmetry, the Mn 3*d* orbitals can only interact with LUMO+1 ($2h_g$), which consists mainly of radial Pb 6*p* orbitals. When distorted to the D_{2h} symmetric form, the metal 3*d* orbitals can interact with both LUMO+1 ($2h_g$) and LUMO ($1g_g$), which has dominant tangential Pb 6*p* orbitals. This strongly prolate distortion stabilises three of the spin-β components of the HOMO of $[Mn@Pb_{12}]^{3-}$ and introduces tangential Pb–Pb antibonding character to it. In summary the formation of half-filled *d* shells is the strong driving force of prolate distortions.

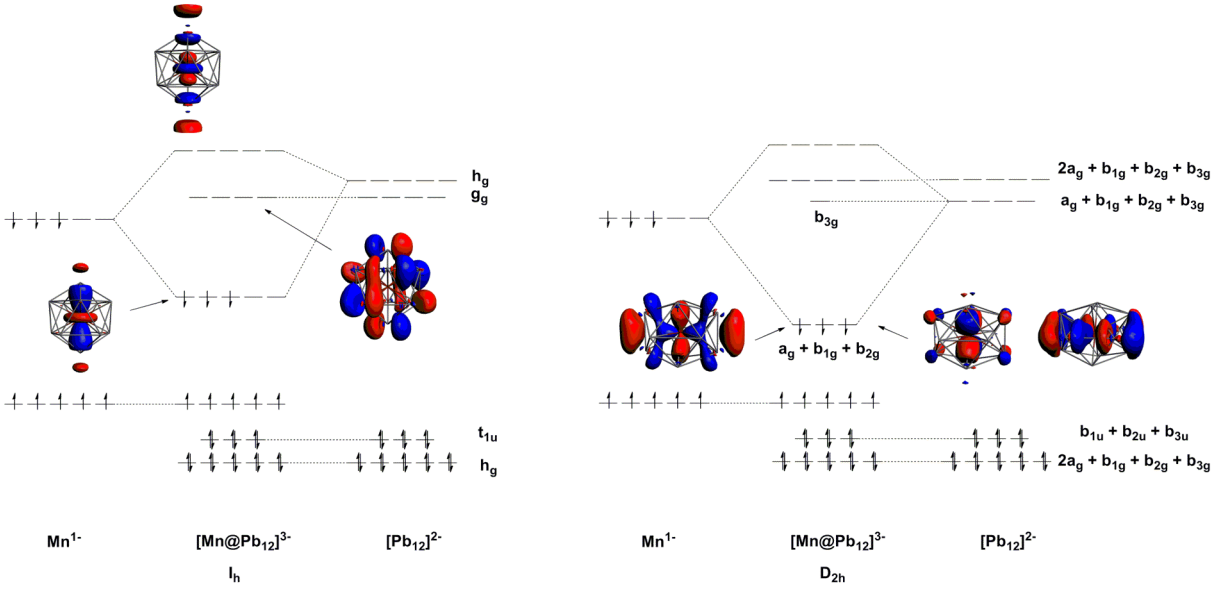

Figure 4.16 Schematic molecular orbital diagrams for $[Mn@Pb_{12}]^{3-}$ in a) I_h and b) D_{2h} symmetries.

4.3.3 Functionalisation of group 14 Zintl clusters $[Ge_9]^{4-}$ and $[Sn_9]^{4-}$

Analogous reactions were carried out for both $[Ge_9]^{4-}$ and $[Sn_9]^{4-}$ with the organometallic reagent $Mn_3(mes)_6$. These yielded dark red plate-like crystals of $[K(2,2,2\text{-crypt})]_3[Ge_9(mes)]_{0.62}[Ge_9Mn(mes)]_{0.38}$ and black block-shaped crystals of $[K(2,2,2\text{-crypt})]_3[Sn_9Mn(mes)]\bullet py$.

$[K(2,2,2\text{-crypt})]_3[Ge_9(mes)]_{0.62}[Ge_9Mn(mes)]_{0.38}$ was characterized by single crystal X-ray diffraction. It had the same unit cell parameters as those for $[K(2,2,2\text{-crypt})]_3[Ge_9(mes)]$, and was solved to contain both $[Ge_9(mes)]^{3-}$ and $[Ge_9Mn(mes)]^{3-}$ with different partial occupancies. Presumably both species were present in the reaction mixture and due to carrying the same charge and possessing a very similar volume, allowed them to co-crystallize in a form of "solid solution".

The *exo*-functionalised cluster anion $[Ge_9(mes)]^{3-}$ is a distorted monocapped square antiprism, with the organic group bonded to the shorter diagonal of the open square face. This cluster anion is the germanium analogue of **21** discussed in section **4.2.4**. The Ge–Ge bond lengths lie in the range between 2.503(2) and 2.898(6) Å and the *exo*-bond C1–Ge5 is 2.024(5) Å. They are comparable with the interatomic distances in similar nonagermanide clusters with organic ligands, such as $[^t Bu–Ge_9–Ge_9–^t Bu]^{4-}$.

$[Ge_9(mes)]^{3-}$ is isostructural and isoelectronic with the functionalized cluster anion $[Sn_9(mes)]^{3-}$ (**21**). The substituted Ge5 vertex donates one more electron to cluster bonding than the other Ge atoms, because only one electron is used for the *exo* Ge–C bond. As a result there are $2 \times 8 + 3 + 3 = 22 = 2n + 4$ skeletal electrons, suggesting a *nido* structure according to Wade-Mingos rules.

The other component $[Ge_9Mn(mes)]^{3-}$ has a rather different coordination mode: the Mn(mes) organometallic fragment is bonded to the open square face of the monocapped square antiprism in a η^4 fashion. The same coordination mode has been observed in other functionalised Zintl clusters with transition metal organometallic groups, such as the previously discussed $[E_9ZnPh]^{3-}$ (E = Si, Ge, Sn and Pb), $[E_9M(CO)_3]^{4-}$ (E = Sn, Pb; M = Cr, Mo, W) and $[E_9Ir(COD)]^{3-}$ (E = Sn, Pb).

The Ge–Ge distances fall within the range of 2.503(12) – 2.866(2) Å and the Ge–Mn bond length is 2.668(3) Å. Electronically the Mn(mes) fragment donates one electron to cluster bonding, resulting in $2 \times 9 + 1 + 3 = 22 = 2n + 2$ skeletal electrons.

DMF solutions of the crystalline sample $[K(2,2,2\text{-crypt})]_3[Ge_9(mes)]_{0.62}[Ge_9Mn(mes)]_{0.38}$ were studied by electrospray mass spectrometry in both the positive and negative ion modes. The negative ion mode mass spectrum reveals mass envelopes corresponding to $[Ge_9(mes)]^-$ (*m/z* = 772.8), $[Ge_9Mn(mes)]^-$ (m/z = 827.8), $\{[K(2,2,2\text{-crypt})][Ge_9(mes)]\}^-$ (*m/z* = 1188.8), $\{[K(2,2,2\text{-crypt})][Ge_9Mn(mes)]\}^-$ (*m/z* = 1244.6) and $\{[K(2,2,2\text{-crypt})]_2[Ge_9Mn(mes)]\}^-$ (*m/z* = 1658.6). The positive ion mode mass spectrum contains isotopic distribution corresponding to the cation paired species $\{[K(2,2,2\text{-crypt})]_3[Ge_9(mes)]\}^+$ (*m/z* = 2022.9), $\{[K(2,2,2\text{-crypt})]_3[Ge_9Mn(mes)]\}^+$ (*m/z* = 2078.0), $\{[K(2,2,2\text{-crypt})]_4[Ge_9(mes)]\}^+$ (*m/z* = 2437.4) and $\{[K(2,2,2\text{-crypt})]_4[Ge_9Mn(mes)]\}^+$ (*m/z* = 2492.4). In addition mass envelopes corresponding to the starting material $[Ge_9]$, alongside $[Ge_{10}]$ and related cation paired species were also observed in both ion modes.

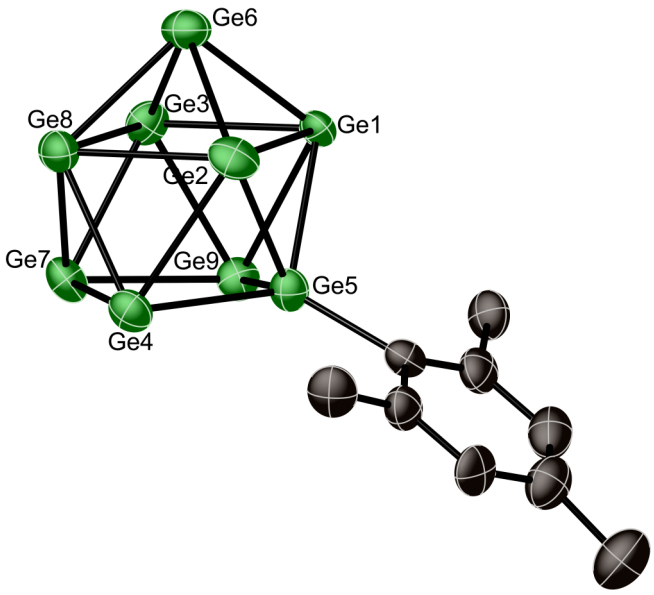

Figure 4.17 Thermal ellipsoid plot of the cluster anion $[Ge_9(mes)]^{3-}$ (**24**) in $[K(2,2,2\text{-crypt})]_3[Ge_9(mes)]_{0.62}[Ge_9Mn(mes)]_{0.38}$ as determined by single crystal X-ray diffraction. Anisotropic displacement ellipsoids pictured at the 50% probability level. Hydrogen atoms have been omitted for clarity.

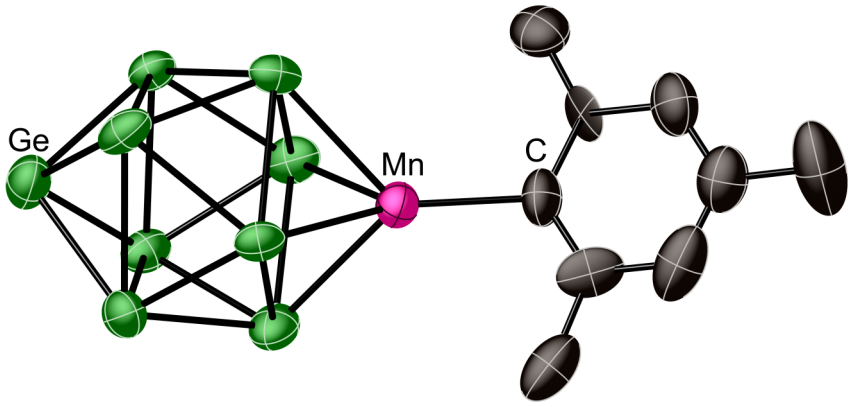

Figure 4.16 Thermal ellipsoid plot of the cluster anion $[Ge_9Mn(mes)]^{3-}$ (**25**) in $[K(2,2,2\text{-crypt})]_3[Ge_9(mes)]_{0.62}[Ge_9Mn(mes)]_{0.38}$ as determined by single crystal X-ray diffraction. Anisotropic displacement ellipsoids pictured at the 50% probability level. Hydrogen atoms have been omitted for clarity.

The single crystal X-ray diffraction data of $[K(2,2,2\text{-crypt})]_3[Sn_9Mn(mes)]\bullet py$ were not of sufficient quality for the discussion of the bond metric data, but suitable for the determination of the composition and connectivity in the cluster. The negative ion-mode electrospray mass spectra reveal isotopic distributions corresponding to the anion $[Sn_9Mn(mes)]^-$ (*m/z* = 1242.92), the cation paired species $\{[K(2,2,2\text{-crypt})][Sn_9Mn(mes)]\}^-$ (*m/z* = 1658.02) and $\{[K(2,2,2\text{-crypt})]_2[Sn_9Mn(mes)]\}^-$ (*m/z* = 2073.18). The positive ion-mode spectra show mass envelopes corresponding to $\{[K(2,2,2\text{-crypt})]_4[Sn_9Mn(mes)]\}^+$ (*m/z* = 2902.57).

4.4 Conclusions

The solution reactions between nonatetrelide group 14 Zintl clusters $[E_9]^{4-}$ (E = Ge, Sn, Pb) and the homoleptic mid-row transition metal reagents $Fe_2(mes)_4$, $FeAr_2$ (Ar = 2,6-$mes_2C_6H_3$) and $Mn_3(mes)_6$ have been studied. They have yielded three metal-centered cluster anions

$[Fe@Ge_{10}]^{3-}$, $[Fe@Sn_{10}]^{3-}$ and $[Mn@Pb_{12}]^{3-}$. The cluster nuclearities are greater than nine, suggesting the reactions proceed *via* decomposition and reassembly of the Zintl cages. The organometallic reagents can lose their aryl ligands by reductive cleavage of the M–C bonds, and the resulting 'naked' transition metal atoms may template the formation of endohedral species.

The cluster anions $[Fe@Ge_{10}]^{3-}$, $[Fe@Sn_{10}]^{3-}$ and $[Mn@Pb_{12}]^{3-}$ exhibit interesting structural features. $[Fe@Ge_{10}]^{3-}$ and $[Fe@Sn_{10}]^{3-}$ are isoelectronic, yet the former shows a non-deltahedral D_{5h} symmetry, whereas the latter is a distorted deltahedral D_{4d}. The anionic species $[Mn@Pb_{12}]^{3-}$ is a highly distorted open-shell endohedral cluster, the first fully characterised example of a 'magnetic superatom'.

The electronic origin of the geometries adopted by these endohedral cluster anions has been explored with DFT calculations. The results show that the structural distortions lead to overlapping of some metal *d* orbitals with the empty cluster-based orbitals. Metal to cluster charge transfer stabilises some spin-β electron density of the central metal atom, which is the driving force for the observed geometries. Effectively the cluster is more reduced than the corresponding empty *closo*-cage. As a result the *d* electrons of the transition metal play an important role in determining the unique geometric features of these endohedral clusters.

4.5 References

1. Scharfe, S.; Fassler, T. F.; Stegmaier, S.; Hoffmann, S. D.; Ruhland, K., *Chem. Eur. J.* **2008**, *14*, 4479.

2. Rios, D.; Gillett-Kunnath, M. M.; Taylor, J. D.; Oliver, A. G.; Sevov, S. C., *Inorg. Chem.* **2011**, *50*, 2373.

3. Burns, R.; Corbett, J., *J. Am. Chem. Soc.* **1982**, *104*, 2804.

4. Esenturk, E. N.; Fettinger, J.; Eichhorn, B., *Chem. Commun.* **2005**, 247.

5. Esenturk, E. N.; Fettinger, J.; Eichhorn, B., *J. Am. Chem. Soc.* **2006**, *128*, 9178.

6. Schrodt, C.; Weigend, F.; Ahlrichs, R., *Z. Anorg. Allg. Chem.* **2002**, *628*, 2478.

7. Esenturk, E. N.; Fettinger, J.; Lam, Y. F.; Eichhorn, B., *Angew. Chem. Int. Ed.* **2004**, *43*, 2132.

8. Downing, D. O.; Zavalij, P.; Eichhorn, B. W., *Eur. J. Inorg. Chem.* **2010**, 890.

9. Wang, J.-Q.; Stegmaier, S.; Wahl, B.; Faessler, T. F., *Chem. Eur. J.* **2010**, *16*, 1793.

10. Esenturk, E. N.; Fettinger, J. C.; Eichhorn, B. W., *J. Am. Chem. Soc.* **2006**, *128*, 12.

11. Goicoechea, J. M.; Sevov, S. C., *Angew. Chem. Int. Ed.* **2005**, *44*, 4026.

12. Kesanli, B.; Halsig, J. E.; Zavalij, P.; Fettinger, J. C.; Lam, Y. F.; Eichhorn, B. W., *J. Am. Chem. Soc.* **2007**, *129*, 4567.

13. Goicoechea, J. M.; Sevov, S. C., *J. Am. Chem. Soc.* **2005**, *127*, 7676.

14. Kocak, F. S.; Zavalij, P.; Lam, Y.-F.; Eichhorn, B. W., *Inorg. Chem.* **2008**, *47*, 3515.

15. Sun, Z.-M.; Xiao, H.; Li, J.; Wang, L.-S., *J. Am. Chem. Soc.* **2007**, *129*, 9560.

16. Kays, D.; Cowley, A., *Chem. Commun.* **2007**, 1053.

17. Goicoechea, J. M.; Sevov, S. C., *Organometallics* **2006**, *25*, 4530.

18. Wang, J. Q.; Stegmaier, S.; Fassler, T. F., *Angew. Chem. Int. Ed.* **2009**, *48*, 1998.

19. Veith, M.; Stahl, L.; Huch, V., *Organometallics* **1993**, *12*, 1914.

20. Hiney, R. M.; Chaplin, A. B.; Harmer, J.; Green, J. C.; Weller, A. S., *Dalton Trans.* **2010**, *39*, 1726.

21. Chen, Z. F.; Neukermans, S.; Wang, X.; Janssens, E.; Zhou, Z.; Silverans, R. E.; King, R. B.; Schleyer, P. V.; Lievens, P., *J. Am. Chem. Soc.* **2006**, *128*, 12829.

22. King, R. B.; Silaghi-Dumitrescu, I.; Uta, A. M., *J. Phys. Chem. A* **2009**, *113*, 527.

23. Zhou, B.; Kramer, T.; Thompson, A.; McGrady, J.; Goicoechea, J., *Inorg. Chem.* **2011**, *50*, 8028.

Chapter 5 – Experimental

5.1 General synthetic methods

Due to the high air- and moisture-sensitivity of reagents and products, all syntheses and manipulations were carried out under an inert atmosphere of argon or dinitrogen using standard Schlenk-line or glovebox techniques (MBraun UNIlab glovebox maintained at < 0.1 ppm H_2O and O_2). In addition, for reactions involving organocadmium reagents, Schlenk tubes and crystallisation ampoules were wrapped in aluminium foil due to the light sensitivity of these compounds.

The intermetallic precursors, K_4E_9 (E = Ge, Sn, Pb), were synthesised according to previously reported synthetic procedures from stoichiometric mixtures of the elements (K 99.95%, Aldrich; Ge 99.999%, Strem; Sn 99.8%, Strem; Pb 99.99%, Alfa-Aesar) heated to 900 °C for 72 h in sealed niobium tubes.[1-3] The niobium vessels were jacketed in flame-sealed silica ampoules under vacuum prior to heating in order to avoid metal oxidation at the high reaction temperatures.

Ethylenediamine (99%, Alfa Aesar) and diethyl ether (99%, Fisher) were distilled over sodium metal, pyridine (99.9%, Rathburn Chemicals Ltd.) was distilled over CaH_2, and tetrahydrofuran (99.9%, Rathburn Chemicals Ltd.) was distilled over Na/Ph_2CO. Toluene, *N*,*N*-dimethylformamide (dmf), and hexane (all 99.9%, Rathburn Chemicals Ltd.) were used after purification by passage through an MBraun MB SPS-800 solvent system. d_5-pyridine (99.5%, Cambridge Isotope Laboratories, Inc.) and d_7-dmf (99.5%, Cambridge Isotope

Laboratories, Inc.) were dried over CaH_2 and vacuum distilled. All solvents were stored in gas-tight ampoules under argon. In addition, diethyl ether, toluene and hexane were stored over activated 3 Å molecular sieves (Acros).

2,2,2-crypt (4,7,13,16,21,24-hexaoxa-1,10-diazabicyclo[8.8.8]-hexacosane; ≥ 99%, Merck), 18-crown-6 (1,4,7,10,13,16-hexaoxacyclooctadecane; 99%, Alfa-Aesar) and cyclooctatetraene iron tricarbonyl ([$Fe(COT)(CO)_3$], 98%, Strem) were used as received after careful drying under vacuum. Tributyltinhydride ($HSn(^nBu)_3$, 97%, Aldrich) was used as received and stored in a glovebox under a nitrogen atmosphere.

Dimesitylzinc, $Zn(mes)_2$ (mes = 2,4,6-$Me_3C_6H_2$), diisopropylzinc, $Zn(^iPr)_2$ (^iPr = $(CH_3)_2CH$), diphenylcadmium, $CdPh_2$ (Ph = C_6H_5), dimesitylcadmium, $Cd(mes)_2$, trimeric bis(mesityl)manganese, $Mn_3(mes)_6$, dimeric bis(mesityl)iron, $Fe_2(mes)_4$ were synthesised using either previously reported methods or modified literature procedures.[4-10] $FeAr_2$ (Ar = 2,6-$Mes_2C_6H_3$) was kindly donated by Dr. Deborah Kays (University of Nottingham). Most of these reagents were dried thoroughly under vacuum before storing them in a glovebox at room temperature. Diisopropylzinc was stored under an inert atmosphere at −20 °C. Sample vials containing the organocadmium reagents were wrapped in aluminium foil and stored in darkness in the glovebox due to the light sensitivity of these compounds.

5.2 Experimental details

$[E_9Zn(mes)]^{3-}$ (E = Ge (1), Sn (2), Pb (3))

$[K(2,2,2\text{-crypt})]_3[Ge_9Zn(mes)]$

K_4Ge_9 (62 mg, 0.076 mmol), 2,2,2-crypt (103 mg, 0.275 mmol) and $Zn(mes)_2$ (35 mg, 0.114 mmol) were dissolved in 2 mL of ethylenediamine and the reaction mixture stirred for 1 h, after which the resulting dark red-orange solution was filtered and the filtrate layered with toluene. Large dark red-orange rod-shaped crystals suitable for single-crystal X-ray diffraction were obtained after 2 days (76 mg, 48% crystalline yield). Anal. Calcd for $C_{63}H_{119}Ge_9K_3N_6O_{18}Zn$: C 36.27, H 5.75, N 4.03. Found: C 36.18, H 5.81, N 4.09. ^{1}H NMR (299.86 MHz, d_5-pyridine): δ (ppm) 6.95 (s, 2H, *m*-C_9H_{11}), 3.78 (s, 6H, *o*-CH_3), 3.42 (s, 36H, 2,2,2-crypt), 3.35 (t, $^3J_{H-H}$ = 6 Hz, 36H, 2,2,2-crypt), 2.32 (t, 36H, 2,2,2-crypt), 2.19 (s, 3H, *p*-CH_3). $^{13}C\{^1H\}$ NMR (75.49 MHz, d_5-pyridine): δ (ppm) 172.3 (*i*-C_9H_{11}), 144.9 (*o*-C_9H_{11}), 132.1 (*m*-C_9H_{11}), 126.6 (*p*-C_9H_{11}), 70.9 (2,2,2-crypt), 68.1 (2,2,2-crypt), 54.3 (2,2,2-crypt), 31.0 (*o*-CH_3), 22.2 (*p*-CH_3). ES-MS (ES–): *m/z* 838.5 $\{[Ge_9Zn(mes)]\}^-$, 1253.8 {[K(2,2,2-crypt)][Ge9Zn(mes)]}$^-$, 1669.0 $\{[K(2,2,2\text{-crypt})]_2[Ge_9Zn(mes)]\}^-$. ES-MS (ES+): *m/z* 2500.0 $\{[K(2,2,2\text{-crypt})]_4[Ge_9Zn(mes)]\}^+$.

$[K(2,2,2\text{-crypt})]_3[Sn_9Zn(mes)]$•tol

K_4Sn_9 (80 mg, 0.066 mmol), 2,2,2-crypt (103 mg, 0.273 mmol) and $Zn(mes)_2$ (30 mg, 0.099 mmol) were dissolved in 2 mL of ethylenediamine and the reaction mixture was stirred for 1 h, after which the resulting dark yellow-brown solution was filtered and the filtrate layered with toluene. Small dark brown-black brick-shaped crystals suitable for single-crystal X-ray diffraction were obtained after 2 days (39 mg, 23%, crystalline yield). Anal. Calcd for

$C_{70}H_{127}K_3N_6O_{18}Sn_9Zn$: C 32.42, H 4.94, N 3.24. Found: C 30.09, H 4.72, N 3.26. ^{1}H NMR (299.87 MHz, d_5-pyridine): δ (ppm) 6.99 (s, 2H, *m*-C_9H_{11}), 3.85 (s, 6H, *o*-C*H*$_3$), 3.32 (s, 36H, 2,2,2-crypt), 3.26 (broad, 36H, 2,2,2-crypt), 2.29 (broad, 36H, 2,2,2-crypt), 2.19 (s, 3H, *p*-C*H*$_3$). ^{13}C{^{1}H} NMR (75.49 MHz, d_5-pyridine): δ (ppm) 142.1 (*o*-C_9H_{11}), 130.8 (*m*-C_9H_{11}), 126.2 (*p*-C_9H_{11}), 70.2 (2,2,2-crypt), 69.3 (2,2,2-crypt), 55.7 (2,2,2-crypt), 31.4 (*o*-*C*H$_3$), 21.0 (*p*-*C*H$_3$). ES-MS (ES–): *m/z* 1251.9 {[Sn_9Zn(mes)]}$^-$, 1667.2 {[K(2,2,2-crypt)][Sn_9Zn(mes)]}$^-$, 2083.4 {[K(2,2,2-crypt)]$_2$[Sn_9Zn(mes)]}$^-$. ES-MS (ES+): *m/z* 2917.0 {[K(2,2,2-crypt)]$_4$[Sn_9Zn(mes)]}$^+$.

[K(2,2,2-crypt)]$_3$[Pb_9Zn(mes)]

K_4Pb_9 (159 mg, 0.079 mmol), 2,2,2-crypt (101 mg, 0.268 mmol) and $Zn(mes)_2$ (27 mg, 0.088 mol) were dissolved in 2 mL of ethylenediamine and the reaction mixture was stirred for 1 h, after which the resulting dark brown-black solution was filtered and the filtrate layered with toluene to allow for crystallisation (81 mg, 31% crystalline yield). Anal. Calcd for $C_{63}H_{119}K_3N_6O_{18}Pb_9Zn$: C 22.94, H 3.64, N 2.55. Found: C 22.85, H 3.70, N 2.52. ^{1}H NMR (300.17 MHz, d_5-pyridine): δ (ppm) 7.28 (s, 2H, *m*-C_9H_{11}), 3.86 (s, 6H, *o*-C*H*$_3$), 3.42 (s, 36H, 2,2,2-crypt), 3.35 (t, 36H, $^3J_{H–H}$ = 5 Hz, 2,2,2-crypt), 2.34 (t, 36H, 2,2,2-crypt), 2.18 (s, 3H, *p*-C*H*$_3$). ^{13}C {^{1}H} NMR (75.49 MHz, d_5-pyridine): δ (ppm) 177.4 (*i*-C_9H_{11}), 142.5 (*o*-C_9H_{11}), 134.2 (*m*-C_9H_{11}), 131.4 (*p*-C_9H_{11}), 71.4 (2,2,2-crypt), 68.6 (2,2,2-crypt), 54.7 (2,2,2-crypt), 29.9 (*o*-*C*H$_3$), 23.3 (*p*-*C*H$_3$). ES-MS (ES–): *m/z* 2050.0 {[Pb_9Zn(mes)]}$^-$, 2465.1 {[K(2,2,2-crypt)][Pb_9Zn(mes)]}$^-$, 2882.2 {[K(2,2,2-crypt)]$_2$[Pb_9Zn(mes)]}$^-$.

$[E_9Zn(^iPr)]^{3-}$ (E = Ge (4), Sn (5), Pb (6))

$[K(2,2,2\text{-crypt})]_3[Ge_9Zn(^iPr)]$•2tol•en

K_4Ge_9 (61 mg, 0.074 mmol) and 2,2,2-crypt (101 mg, 0.267 mmol) were dissolved in 2 mL of ethylenediamine. After 5 min of stirring, $Zn(^iPr)_2$ (24 mL, 0.158 mmol) was added with a microsyringe. The reaction mixture was stirred for 1 h, after which the resulting dark red-orange solution was filtered and the filtrate layered with toluene. Long clear orange-yellow crystals suitable for single-crystal X-ray diffraction were obtained after 2 days (97 mg, 58% crystalline yield). Anal. Calcd for $C_{73}H_{139}Ge_9K_3N_8O_{18}Zn$: C 38.89, H 6.22, N 4.97. Found: C 38.83, H 6.08, N 5.04. ^{1}H NMR (300.17 MHz, d_5-pyridine): δ (ppm) 3.48 (s, 36H, 2,2,2-crypt), 3.37 (t, $^3J_{H-H}$ = 5 Hz, 36H, 2,2,2-crypt), 2.35 (d, $^3J_{H-H}$ = 8 Hz, 6H, $CH(CH_3)_2$), 2.34 (t, 36H, 2,2,2-crypt), 1.36 (sep, 1H, $CH(CH_3)_2$). $^{13}C\{^1H\}$ NMR (75.49 MHz, d_5-pyridine): δ (ppm) 71.0 (2,2,2-crypt), 68.2 (2,2,2-crypt), 54.4 (2,2,2-crypt), 36.8 ($CH(CH_3)_2$), 27.5 ($CH(CH_3)_2$). ES-MS (ES–): *m/z* 762.2 $\{[Ge_9Zn(^iPr)]\}^-$, 1177.4 $\{[K(2,2,2\text{-crypt})][Ge_9Zn(^iPr)]\}^-$, 1592.5 $\{[K(2,2,2\text{-crypt})]_2[Ge_9Zn(^iPr)]\}^-$. ES-MS (ES+): *m/z* 2428.0 $\{[K(2,2,2\text{-crypt})]_4[Ge_9Zn(^iPr)]\}^+$.

$[K(2,2,2\text{-crypt})]_3[Sn_9Zn(^iPr)]$•0.5en

K_4Sn_9 (84 mg, 0.069 mmol) and 2,2,2-crypt (106 mg, 0.2804 mmol) were dissolved in 2 mL of ethylenediamine giving rise to a dark red-brown solution. After stirring for 5 min, $Zn(^iPr)_2$ (19 mL, 0.125 mmol) was added using a microsyringe. The reaction mixture was stirred for 1 h, after which the resulting dark brown-yellow solution was filtered and the filtrate layered with toluene. Large dark orange-yellow plate-like crystals suitable for single crystal X-ray diffraction were obtained after 2 days (46 mg, 27% crystalline yield). Anal. Calcd for $C_{58}H_{119}K_3N_7O_{18}Sn_9Zn$: C 28.37, H 4.89, N 4.00. Found: C 28.34, H 4.90, N 3.95. ^{1}H NMR

(300.17 MHz, d_5-pyridine): δ (ppm) 3.43 (s, 36H, 2,2,2-crypt), 3.36 (t, $^3J_{H–H}$ = 5 Hz, 36H, 2,2,2-crypt), 2.51 (d, $^3J_{H–H}$ = 8 Hz, 6H, CH(CH_3)$_2$), 2.35 (t, 36H, 2,2,2-crypt), 1.09 (sep, 1H, CH(CH$_3$)$_2$). ^{13}C{^{1}H} NMR (75.49 MHz, d_5-pyridine): δ (ppm) 71.2 (2,2,2-crypt), 68.3 (2,2,2-crypt), 60.1 (*C*H(CH$_3$)$_2$), 54.5 (2,2,2-crypt), 25.3 (CH(*C*H$_3$)$_2$). ES-MS (ES–): *m/z* 1175.7 {[Sn$_9$Zn(^{i}Pr)]}$^-$, 1590.8 {[K(2,2,2-crypt)][Sn$_9$Zn(^{i}Pr)]}$^-$, 2006.8 {[K(2,2,2-crypt)]$_2$[Sn$_9$Zn(^{i}Pr)]}$^-$. ES-MS (ES+): *m/z* 2839.0 {[K(2,2,2-crypt)]$_4$[Sn$_9$Zn(^{i}Pr)]}$^+$.

[K(2,2,2-crypt)]$_6$[Pb$_9$Zn(^{i}Pr)]$_2$•en

K_4Pb_9 (158 mg, 0.079 mmol) and 2,2,2-crypt (107 mg, 0.284 mmol) were dissolved in 2 mL of ethylenediamine. After stirring for approximately 5 min, Zn(^{i}Pr)$_2$ (20 mL, 0.132 mmol) was added with a microsyringe. The reaction mixture was stirred for 2–3 h, after which the resulting dark black-brown solution was filtered and the filtrate layered with toluene to allow for crystallisation. Large black plate-like crystals suitable for single-crystal X-ray diffraction were obtained after 2 days (69 mg, 27% crystalline yield). Anal. Calcd for $C_{116}H_{238}K_6N_{14}O_{36}Pb_{18}Zn_2$: C 21.42, H 3.69, N 3.02. Found: C 21.51, H 3.59, N 2.92. ^{1}H NMR (300.17 MHz, d_5-pyridine): δ (ppm) 3.42 (s, 36H, 2,2,2-crypt), 3.35 (t, $^3J_{H–H}$ = 5 Hz, 36H, 2,2,2-crypt), 2.83 (d, $^3J_{H–H}$ = 7 Hz, 6H, CH(CH_3)$_2$), 2.35 (t, 36H, 2,2,2-crypt), 0.03 (sep, 1H, CH(CH$_3$)$_2$). ^{13}C{^{1}H} NMR (75.49 MHz, d_5-pyridine): δ (ppm) 71.1 (2,2,2-crypt), 70.4 (*C*H(CH$_3$)$_2$), 68.6 (2,2,2-crypt), 54.7 (2,2,2-crypt), 17.5 (CH(*C*H$_3$)$_2$). ES-MS (ES–): *m/z* 1974.2 {[Pb$_9$Zn(^{i}Pr)]}$^-$, 2389.1 {[K(2,2,2-crypt)][Pb$_9$Zn(^{i}Pr)]}$^-$.

$[E_9CdPh]^{3-}$ (E = Sn (7), Pb (8))

$[K(2,2,2\text{-crypt})]_3[Sn_9CdPh]_{0.8}[Sn_9]_{0.2}$•en

K_4Sn_9 (200 mg, 0.163 mmol), 2,2,2-crypt (221 mg, 0.587 mmol) and $CdPh_2$ (44 mg, 0.165 mmol) were dissolved in 2 mL of dry ethylenediamine yielding a dark reddish-brown solution. The reaction mixture was then allowed to stir for 1 h, after which the resulting intensely coloured dark red solution was filtered and layered with dry toluene. Thin dark brown plate-like crystals suitable for single crystal X-ray diffraction were obtained after several days (225 mg, 55% crystalline yield). Anal. Calcd for $C_{62}H_{121}CdK_3N_8O_{18}Sn_9$: C, 29.02; H, 4.76; N, 4.37. Found: C, 29.00; H, 4.83; N, 4.32. ^{1}H NMR (300.17 MHz, d_5-pyridine): δ (ppm) 8.86 (dd, $^3J_{ortho-meta}$ = 7.5 Hz, $^4J_{ortho-para}$ = 1.4 Hz, $^3J_{Cd-H}$ = 36 Hz, 2H, *o*-C_6H_5), 7.55 (dd, $^3J_{meta-para}$ = 7.5 Hz, $^4J_{Cd-H}$ = 6 Hz, 2H, *m*-C_6H_5), 7.15 (tt, 1H, *p*-C_6H_5), 3.40 (s, 36H, 2,2,2-crypt), 3.33 (t, $^3J_{H-H}$ = 6 Hz, 36H, 2,2,2-crypt), 2.32 (t, 36H, 2,2,2-crypt). ^{13}C {^{1}H} NMR (75.49 MHz, d_5-pyridine): δ (ppm) 137.9 (*o*-C_6H_5), 127.5 (*m*-C_6H_5), 123.1 (*p*-C_6H5), 73.2 (2,2,2-crypt), 70.0 (2,2,2-crypt), 55.63 (2,2,2-crypt). ES-MS (ES–): *m*/*z* 1258.0 $\{[Sn_9CdPh]\}^-$, 1673.2 $\{[K(2,2,2\text{-crypt})][Sn_9CdPh]\}^-$, 2089.4 $\{[K(2,2,2\text{-crypt})]_2[Sn_9CdPh]\}^-$.

$[K(2,2,2\text{-crypt})]_6[Pb_9CdPh]_2$•2en•tol

K_4Pb_9 (300 mg, 0.148 mmol), 2,2,2-crypt (200 mg, 0.531 mmol) and $CdPh_2$ (40 mg, 0.150 mmol) were dissolved in 2 mL of ethylenediamine. The reaction mixture was allowed to stir for 1 h, after which the resulting dark brown solution was filtered and the filtrate layered with toluene. Large black rod-like crystals suitable for single-crystal X-ray diffraction were obtained after 3 days (230 mg, 47% crystalline yield). Anal. Calcd for $C_{131}H_{250}Cd_2K_6N_{16}O_{36}Pb_{18}$: C, 23.07; H, 3.70; N, 3.29. Found: C, 22.95; H, 3.67; N, 3.28. ^{1}H

NMR (300.17 MHz, d_5-pyridine): δ (ppm) 9.38 (dd, $^3J_{ortho–meta}$ = 7.5 Hz, $^4J_{ortho–para}$ = 1.8 Hz, $^3J_{Cd–H}$ = 33 Hz, 2H, *o*-C_6H_5), 7.98 (dd, $^3J_{meta–para}$ = 7.5 Hz, $^4J_{Cd–H}$ = 5 Hz, 2H, *m*-C_6H_5), 7.36 (tt, 1H, *p*-C_6H_5), 3.41 (s, 36H, 2,2,2-crypt), 3.34 (t, $^3J_{H–H}$ = 5 Hz, 36H, 2,2,2-crypt), 2.34 (t, 36H, 2,2,2-crypt). ^{13}C {^1H} NMR (75.49 MHz, d_5-pyridine): δ (ppm) 134.6 (*o*-C_6H_5), 129.7 (*m*-C_6H_5), 122.7 (*p*-C_6H_5), 71.56 (2,2,2-crypt), 68.70 (2,2,2-crypt), 54.80 (2,2,2-crypt). ES-MS (ES–): *m*/*z* 2054.4 $[Pb_9CdPh]^-$, 2470.3 {[K(2,2,2-crypt)][Pb_9CdPh]}$^-$.

$[Ge_9CdGe_9]^{6-}$ (9)

K_4Ge_9 (74 mg, 0.09 mmol), $CdPh_2$ (24 mg, 0.09 mmol) and 18-crown-6 (90 mg, 0.34 mmol) were dissolved in 2 mL of ethylenediamine under an inert atmosphere and allowed to stir for one hour, after which the resulting red-brown solution was filtered and the filtrate layered with toluene. Yellow/light brown plate-like hexagonal crystals of a highly disordered crystalline phase of $[Ge_9CdGe_9]^{6-}$ were obtained alongside elemental decomposition after 4 days. A similar reaction was attempted by using 2,2,2-crypt as the cation sequestering agent rather than 18-crown-6 no crystalline material was produced. ES-MS(ES–): *m*/*z* 1802.3 {[K(18-crown-6)]K_2[Ge_9CdGe_9] }$^-$, 2066.4 {[K(18-crown-6)]$_2$K[Ge_9CdGe_9]}$^-$.

$[E_9Cd(mes)]^{3-}$ (E = Sn (10), Pb (11))

[K(2,2,2-crypt)]$_3$[$Sn_9Cd(mes)$]•en

K_4Sn_9 (182 mg, 0.149 mmol), $Cd(mes)_2$ (52 mg, 0.148 mmol) and 2,2,2-crypt (200 mg, 0.531 mmol) were dissolved in ethylenediamine (2 mL) and allowed to stir for 1 h, after which the resulting reddish-brown solution was filtered and the filtrate layered with toluene. Large red hexagonal plate-like crystals suitable for single-crystal X-ray diffraction were obtained after 4

days (14 mg, 4% crystalline yield). Anal. Calcd for $C_{65}H_{127}CdK_3N_8O_{18}Sn_9$: C, 29.93; H, 4.91; N, 4.30. Found: C, 29.87; H, 4.85; N, 4.17. ^{1}H NMR (300.17 MHz, ethylenediamine, C_6D_6 capillary): δ (ppm) 6.98 (s, 3H, aromatic protons), 3.83 (s, 12H, 2,2,2-crypt), 3.78 (t, $^3J_{H–H}$ = 5 Hz, 12H, 2,2,2-crypt), the resonances corresponding to the rest of the protons of 2,2,2-crypt and the methyl protons of the mesitylene were obscured by one of the proton resonances of ethylenediamine in the solution. ^{13}C NMR (75.49 MHz, ethylenediamine, C_6D_6 capillary): δ (ppm) 138.00 (CH_3-*C* of mesitylene), 110.62 (*C*H of mesitylene), 71.09 (2,2,2-crypt), 68.20 (2,2,2-crypt), 54.45 (2,2,2-crypt), 21.39 (*C*H_3 of mesitylene). ES-MS (ES–): *m*/*z* 1300.2 $[Sn_9Cd(mes)]^-$, 1715.5 $\{[K(2,2,2\text{-crypt})][Sn_9Cd(mes)]\}^-$, 2131.6 $\{[K(2,2,2\text{-crypt})]_2[Sn_9Cd(mes)]\}^-$.

$[K(2,2,2\text{-crypt})]_{12}[Pb_9Cd(mes)]_4$•tol•py

K_4Pb_9 (300 mg, 0.148 mmol), $Cd(mes)_2$ (52 mg, 0.148 mmol) and 2,2,2-crypt (200 mg, 0.531 mmol) were dissolved in ethylenediamine (2 mL) and allowed to stir for 1 h, after which the resulting dark brown reaction mixture was filtered. The dark brown filtrate was layered with toluene, which yielded no crystals. The original reaction vessel showed a significant amount of black solid residue. Some of the solid residue (200 mg) was redissolved in pyridine (1 mL) and layered with toluene. Small black block-like crystals suitable for single-crystal X-ray diffraction were obtained after a few days alongside metal decomposition. Anal. Calcd for $C_{264}H_{489}Cd_4K_{12}N_{25}O_{72}Pb_{36}$: C, 23.40; H, 3.64; N, 2.59. Found: C, 23.30; H, 3.60; N, 2.65. ^{1}H NMR (300.17 MHz, d_5-pyridine): δ (ppm) 7.24 (s, 2H, C*H*), 3.55 (m, 6H, *o*-CH_3), 3.38 (s, 36H, 2,2,2-crypt), 3.31 (t, $^3J_{H–H}$ = 5 Hz, 36H, 2,2,2-crypt), 2.31 (t, 36H, 2,2,2-crypt), 2.70 (m, 3H, *p*-CH_3). ^{13}C NMR (75.49 MHz, d_5-pyridine): δ (ppm) 144.43 (*o*-*C*), 134.27 (*m*-*C*H),

131.29 (*p*-*C*), 71.34 (2,2,2-crypt), 68.51 (2,2,2-crypt), 54.63 (2,2,2-crypt), 46.01 (*o*-*C*H_3), 25.74 (*p*-*C*H_3).

[$Pb_9CdCdPb_9$]$^{6-}$ (12)

[K(2,2,2-crypt)]$_6$[$Pb_9CdCdPb_9$]•2en

K_4Pb_9 (150 mg, 0.07 mmol), $Cd(mes)_2$ (25 mg, 0.07 mmol) and 2,2,2-crypt (100 mg, 0.27 mmol) were dissolved in 2 mL of ethylenediamine under an inert atmosphere and allowed to stir for 1 h, after which the resulting dark brown solution was filtered and the filtrate layered with toluene. Trace amounts of extremely air- and moisture-sensitive purple/black plate-like crystals of [K(2,2,2-crypt)]$_6$[$Pb_9CdCdPb_9$]•2en and considerable amounts of metallic lead precipitate were isolated from the crystallisation ampoule after several days. Anal. Calcd for $C_{112}H_{232}Cd_2K_6N_{16}O_{36}Pb_{18}$: C, 20.47; H, 3.56; N, 3.41. Found: C, 20.38; H, 3.46; N, 3.28.

[$Sn_9CdSn(^nBu)_3$]$^{3-}$ (13)

[K(2,2,2-crypt)]$_6$[$Sn_9CdSn(^nBu)_3$]$_2$•6tol•py

Crystals of [K(2,2,2-crypt)]$_3$[Sn_9CdPh]•en (70 mg, 0.027 mmol) were dissolved in d_5-pyridine (1 mL) into a NMR tube equipped with a J. Young's air-tight valve yielding a reddish brown solution, to which $HSn(^nBu)_3$ (7 μL, 0.026 mmol) was added. The reaction mixture was shaken and left to stand for 1 h. After the reaction had come to completion as manifested by ^{1}H NMR spectra, the solution was reduced to dryness in *vacuo* and redissolved in pyridine yielding a yellowish brown solution. The solution was filtered and layered with toluene. Orange-brown, plate-like rectangular crystals suitable for single-crystal X-ray diffraction were obtained after 1 day (30 mg, 48% crystalline yield). Anal. Calcd for $C_{179}H_{323}Cd_2K_6N_{13}O_{36}Sn_{20}$:

C, 35.42; H, 5.37; N, 3.00. Found: C, 35.44; H, 5.26; N, 3.16. ^{1}H NMR (300.17 MHz, d_5-pyridine): δ (ppm) 3.43 (s, 12H, 2,2,2-crypt), 3.36 (t, $^{3}J_{H–H}$ = 6 Hz, 12H, 2,2,2-crypt), 2.37 (m, 2H, H_{β}), 2.35 (t, 12H, 2,2,2-crypt), 1.74 (tq, $^{3}J_{\beta\text{-}\gamma}$ = 7.5 Hz, $3J_{\gamma–\delta}$ = 7.5 Hz, 2H, H_{γ}), 1.44 (m, $^{3}J_{\alpha–\beta}$ = 7.5 Hz, 2H, H_{α}), 1.08 (t, 3H, H_{δ}). ^{13}C {^{1}H} NMR (75.49 MHz, d_5-pyridine): δ (ppm) 71.0 (2,2,2-crypt), 68.2 (2,2,2-crypt), 54.5 (2,2,2-crypt), 32.9 (^{n}Bu), 29.5 (^{n}Bu), 17.7 (^{n}Bu), 15.1 (^{n}Bu). ES-MS (ES–): *m*/*z* 1358.2 $[Sn_9CdSn(^{n}Bu)H]^{-}$. ES-MS (ES+): *m*/*z* 3131.0 $\{[K(2,2,2\text{-crypt})]_4[Sn_9CdSn(^{n}Bu)_3]\}^{+}$.

$[Pb_9CdSn(^{n}Bu)_3]^{3-}$ (14)

$[K(2,2,2\text{-crypt})]_6[Pb_9Cd(C_6H_5)]_2$•2en•tol (105 mg, 0.031 mmol) was dissolved in d_5-pyridine (1 mL) into a NMR tube equipped with a J. Young's air-tight valve to give a dark brown solution, to which $HSn(^{n}Bu)_3$ (8 μL, 0.030 mmol) was added. The reaction mixture was shaken and left to stand for 3 days, after which the resulting dark brown solution was filtered and the filtrate layered with toluene. The product was highly air- and moisture- sensitive and not very stable in pyridine, which prevented crystallographic characterisation. The ^{1}H and ^{13}C {^{1}H} NMR spectra of the crude reaction mixture both revealed four multiplet resonances corresponding to the tributyltin fragment, which were very similar to those of the analogous $[Sn_9CdSn(^{n}Bu)_3]^{3-}$ cluster. ^{1}H NMR (300.17 MHz, d_5-pyridine): δ (ppm) 3.41 (s, 12H, 2,2,2-crypt), 3.35 (t, $^{3}J_{H–H}$ = 6 Hz, 12H, 2,2,2-crypt), 2.34 (t, 12H, 2,2,2-crypt), 2.30 (m, 2H, H_{β}), 1.82 (tq, $^{3}J_{\beta\text{-}\gamma}$ = 7.5 Hz, $3J_{\gamma–\delta}$ = 7.5 Hz, 2H, H_{γ}), 1.30 (m, $^{3}J_{\alpha–\beta}$ = 7.5 Hz, 2H, H_{α}), 1.10 (t, 3H,

H_δ). ^{13}C NMR (75.49 MHz, d_5-pyridine): δ (ppm) 71.07 (2,2,2-crypt), 68.32 (2,2,2-crypt), 54.54 (2,2,2-crypt), 35.02 (^{n}Bu), 30.25 (^{n}Bu), 19.24 (^{n}Bu), 15.15 (^{n}Bu).

$[Ge_8Fe(CO)_3]^{3-}$ (15), $[Fe(\eta^3\text{-}C_8H_8)(CO)_3]^-$ (16)

$[K(2,2,2\text{-crypt})]_3[Ge_8Fe(CO)_3]$ and *$[K(2,2,2\text{-crypt})][Fe(\eta^3\text{-}C_8H_8)(CO)_3]$*

K_4Ge_9 (82 mg, 0.101 mmol) and 2,2,2-crypt (114 mg, 0.303 mmol) were dissolved in 4 mL of ethylenediamine in a sample vial in the glovebox yielding a dark-orange solution. In a separate vial, $[Fe(COT)(CO)_3]$ (COT = cyclooctatetraene) (25 mg, 0.103 mmol) was dissolved in 2 mL of toluene producing a bright red solution. The toluene solution was added dropwise to the ethylenediamine solution, and the reaction mixture was stirred for 1 h, yielding a dark-brown mixture. All the volatiles were removed in *vacuo* and the solid residue was extracted with thf (4 mL). The mixture was stirred for 20 min giving rise to an orange solution, which was subsequently filtered and the filtrate layered with hexane to allow for crystallisation (this mixture yielded crystals of $[K(2,2,2\text{-crypt})][Fe(\eta^3\text{-}C_8H_8)(CO)_3]$). The solid residue was dried under a dynamic vacuum and redissolved in 4 mL of ethylenediamine. The mixture was stirred for 20 min to give a dark-brown solution, which was then filtered and layered with toluene to allow for crystallisation of $[K(2,2,2\text{-crypt})]_3[Ge_8Fe(CO)_3]$. After several days, orange rod-like crystals of [K(2,2,2-crypt)][**16**] suitable for single-crystal X-ray diffraction were obtained from the thf/hexane mixture (14 mg, 21% crystalline yield based on $[Fe(COT)(CO)_3]$) and thin orange plates of $[K(2,2,2\text{-crypt})]_3$[**15**] were isolated from the en/toluene mixture (81 mg, 40% crystalline yield based on $[Fe(COT)(CO)_3]$). $[K(2,2,2\text{-crypt})]_3$[**15**]: IR (nujol mull): ν =1884, 1820 cm^{-1}. ES-MS (ES–): *m/z* 581.9 $[Ge_8]^-$, 665.4 $[Ge_8Fe(CO)]^-$, 693.7 $[Ge_8Fe(CO)_2]^-$, 725.9 $[Ge_{10}]^-/[Ge_8Fe(CO)_3]^-$, 1141.6 {[K(2,2,2-

crypt)][Ge_{10}]}$^{-}$. ES-MS (ES+): *m/z* 1972.3 {[K(2,2,2-crypt)]$_3$[Ge_{10}]}$^{+}$. An EPR resonance centered at g = 2.0200 was observed for a solid crystalline sample at 20 K. [K(2,2,2-crypt)][**16**]: IR (nujol mull): ν = 1928, 1828 cm^{-1}. ES-MS (ES–): *m/z* 376.3 [$Fe_2(C_8H_8)_2(CO)_2$]$^{-}$, 404.3 [$Fe_2(C_8H_8)_2(CO)_3$]$^{-}$, 432.3 [$Fe_2(C_8H_8)_2(CO)_4$]$^{-}$, 471.3 {K[$Fe_2(C_8H_8)_2(CO)_4$]}$^{-}$, 499.3 {K[$Fe_2(C_8H_8)_2(CO)_5$]}$^{-}$, 527.3 {K[$Fe_2(C_8H_8)_2(CO)_6$]}$^{-}$. ES-MS (ES+): *m/z* 1075.8 {[K(2,2,2-crypt)]$_2$[$Fe(C_8H_8)(CO)_3$]}$^{+}$, 1734.2 {[K(2,2,2-crypt)]$_3$[$Fe_2(C_8H_8)_2(CO)_6$]}$^{+}$. Anal. Calcd for $C_{29}H_{44}FeKN_2O_9$: C 52.79, H 6.73, N 4.25; found: C 52.83, H 6.65, N 4.18.

[$Fe_2(\eta^3,\eta'^3$-$C_{16}H_{16})(CO)_6$]$^{2-}$ (17)

[K(2,2,2-crypt)]$_2$[$Fe_2(\eta^3,\eta'^3$-$C_{16}H_{16})(CO)_6$]

K (16 mg, 0.410 mmol), Fe(COT)(CO)$_3$ (100 mg, 0.410 mmol) and 2,2,2-crypt (155 mg, 0.412 mmol) were dissolved in 8 mL of dmf in a sample vial in the glovebox and stirred for 12 h to give a red/orange suspension, which was then filtered and layered with Et_2O. Orange block-like crystals of [K(2,2,2-crypt)]$_2$[$Fe_2(\eta^3,\eta'^3$-$C_{16}H_{16})(CO)_6$] suitable for single crystal X-ray diffraction were obtained after a few days (18.7 mg, 7% crystalline yield). Anal. Calcd for $C_{58}H_{88}Fe_2K_2N_4O_{18}$: C 52.79, H 6.73, N 4.25; found: C 52.71, H 6.64, N 4.33. IR (nujol mull): ν = 1922, 1828, 1725 cm^{-1}. ^{1}H NMR (300.27 MHz, d$_7$-dmf): δ (ppm) 6.50 (m, 1H, H1), 6.23 (m, 1H, H2), 5.59 (m, 1H, H3), 5.02 (m, 1H, H4), 3.78 (m, 1H, H5), 3.61 (broad s, 24H, 2,2,2-crypt, H6 of the product is masked by this peak, confirmed by COSY), 3.02 (m, 1H, H7), 2.58 (broad s, 12H, 2,2,2-crypt), 2.46 (m, 1H, H8). Assignment of the proton resonances was confirmed by a ^{1}H COSY experiment. ^{13}C NMR (75.41 MHz, d$_7$-dmf): δ (ppm) 226.93 (CO), 145.34 (s, C1), 140.57 (s, C2), 123.36 (s, C3), 114.28 (s, C4), 71.35 (s, 2,2,2-crypt), 71.04 (s,

C7), 68.56 (s, 2,2,2-crypt), 68.02 (s, C5), 59.07 (s, C6), 56.02 (s, C8), 54.86 (s, 2,2,2-crypt). Assignment of the carbon resonances was confirmed by a $^{1}H–^{13}C$ HMQC experiment. The labelling scheme for protons and carbons is as follows: H1 is bonded to C1, H2 is bonded to C2, etc. ES-MS (ES–): *m/z* 376.1 $[Fe_2(C_8H_8)_2(CO)_2]^-$, 404.1 $[Fe_2(C_8H_8)_2(CO)_3]^-$, 433.1 $[Fe_2(C_8H_8)_2(CO)_4]^-$, 471.1 $\{K[Fe_2(C_8H_8)_2(CO)_4]\}^-$, 499.1 $\{K[Fe_2(C_8H_8)_2(CO)_5]\}^-$, 527.1 $\{K[Fe_2(C_8H_8)_2(CO)_6]\}^-$. ES-MS (ES+): *m/z* 1734.1 $\{[K(2,2,2\text{-crypt})]_3[Fe_2(C_8H_8)_2(CO)_6]\}^+$.

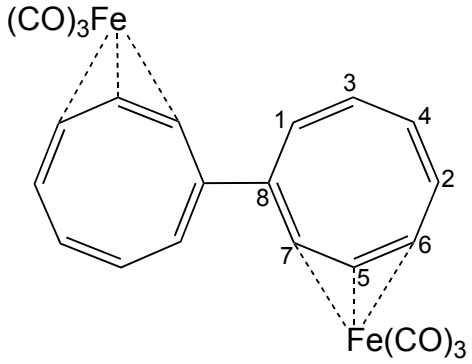

Figure 5.1 Numbering scheme for $[Fe_2(\eta^3,\eta'^3\text{-}C_{16}H_{16})(CO)_6]^{2-}$ (**17**).

$[Fe@Ge_{10}]^{3-}$ (18)

$[K(2,2,2\text{-crypt})]_3[Fe@Ge_{10}]$•2en

K_4Ge_9 (62 mg, 0.077 mmol), $FeAr_2$ (Ar = 2,6-$Mes_2C_6H_3$) (26 mg, 0.038 mmol, kindly donated by Dr. Deborah Kays, University of Nottingham), and 2,2,2-crypt (50 mg, 0.133 mmol) were dissolved in 2 mL of ethylenediamine and a few drops of thf were added to aid the dissolution of $FeAr_2$. The reaction mixture was allowed to stir for one hour, yielding a dark brown solution, which was subsequently filtered and layered with toluene. Small greenish black rod like crystals of $[K(2,2,2\text{-crypt})]_3[Fe@Ge_{10}]$•2en suitable for single-crystal X-ray diffraction were obtained after 3 days alongside crystals of other known $[Ge_9]^{n-}$ clusters. ES-MS (ES–):

m/z 781.2 $[Fe@Ge_{10}]^-$, 822.2 $\{K[Fe@Ge_{10}]\}^-$, 1198.7 $\{[K(2,2,2\text{-crypt})][Fe@Ge_{10}]\}^-$. ES-MS (ES+): *m/z* 2443.9 $\{[K(2,2,2\text{-crypt})]_4[Fe@Ge_{10}]\}^+$.

$[Ge_9(mes)]^{3-}$ (19)

$[K(2,2,2\text{-crypt})]_3[Ge_9(mes)]$

Analogous reactions between K_4Ge_9, $Fe_2(mes)_4$ and 2,2,2-crypt were carried out under similar conditions, but occasionally yielded an *exo*-functionalised cluster $[Ge_9(mes)]^{3-}$ rather than the endohedral cage $[Fe@Ge_{10}]^{3-}$ (**18**). The yield and crystal quality of the product were not sufficiently good for further characterisations to be carried out.

$[Fe@Sn_{10}]^{3-}$ (20)

$[K(2,2,2\text{-crypt})]_3[Fe@Sn_{10}]$•4py

K_4Sn_9 (90 mg, 0.073 mmol) and 2,2,2-crypt (100 mg, 0.266 mmol) were dissolved in ethylenediamine (2 mL) to give a dark brown solution. $Fe_2(mes)_4$ (22 mg, 0.037 mmol) was dissolved in thf (2 mL) to give a brown solution. The thf solution was added dropwise to the stirred ethylenediamine solution. The reaction mixture was stirred for 1 h, after which the resulting brown solution was filtered and the filtrate layered with toluene. After a few days, the black solid in the crystallisation ampoule was isolated, dried and redissolved in pyridine (2 mL) to give a dark brown solution. The solution was then filtered into another crystallisation ampoule and layered with toluene. After several days, black rod-like crystals of $[K(2,2,2\text{-crypt})]_3[Fe@Sn_{10}]$•4py suitable for single crystal X-ray diffraction were obtained along with some metallic decomposition. Due to the low crystalline yield, a slightly modified bulk synthesis of $[K(2,2,2\text{-crypt})]_3[Fe@Sn_{10}]$•4py was explored. K_4Sn_9 (203 mg, 0.166 mmol) and

2,2,2-crypt (250 mg, 0.664 mmol) were dissolved in ethylenediamine (4 mL) to give a dark brown solution. It was allowed to stir for 1 h and then toluene (80 mL) was added to give a black precipitate. The mixture was stirred for 30 mins and left to stand for 30 mins. The colourless solution was filtered off and the solid precipitate dried under *vacuo* for 30 mins. Dark red/black powder (360 mg, 79% yield) was isolated in the glovebox. Assuming the product had the formula of $[K(2,2,2\text{-crypt})]_4[Sn_9]$, some of the dark red/black powder (180 mg, 0.066 mmol) was redissolved in pyridine (2 mL) to give a dark brown solution. $Fe_2(mes)_4$ (29 mg, 0.049 mmol) was dissolved in thf (2 mL) to give a brown solution. The thf solution was added dropwise to the stirred pyridine solution. The reaction mixture was stirred for 1 h and toluene (80 mL) was added to give a black precipitate. The mixture was then stirred for 30 mins and left to stand for 30 mins. The pale yellow solution was filtered off and the solid precipitate dried under vacuo for 30 mins. Black powder (140 mg, 68% yield) was isolated in the glovebox. Anal. Calcd for $C_{74}H_{128}FeK_3N_{10}O_{18}Sn_{10}$: C 31.66, H 4.60, N 4.99. Found: C 31.49, H 4.48, N 4.81. ES-MS (ES–): *m/z* 1066.7 $[Sn_9]^-$, 1187.0 $[Sn_{10}]^-$, 1242.8 $[Fe@Sn_{10}]^-$, 1602.3 $\{[K(2,2,2\text{-crypt})][Sn_{10}]\}^-$, 1659.1 $\{[K(2,2,2\text{-crypt})][Fe@Sn_{10}]\}^-$, 2019.5 $\{[K(2,2,2\text{-crypt})]_2[Sn_{10}]\}^-$, 2075.4 $\{[K(2,2,2\text{-crypt})]_2[Fe@Sn_{10}]\}^-$. ES-MS (ES+): *m/z* 2315.0 $\{[K(2,2,2\text{-crypt})]_3[Sn_9]\}^+$, 2433.8 $\{[K(2,2,2\text{-crypt})]_3[Sn_{10}]\}^+$, 2850.1 $\{[K(2,2,2\text{-crypt})]_4[Sn_{10}]\}^+$, 2904.9 $\{[K(2,2,2\text{-crypt})]_4[Fe@Sn_{10}]\}^+$. An EPR resonance centered at $g = 2.0297$ was observed for a solid crystalline sample at 15 K.

$[Sn_9(mes)]^{3-}$ (21)

$[K(2,2,2\text{-crypt})]_3[Sn_9(mes)]\bullet 2py$

Black rod-like crystals of $[K(2,2,2\text{-crypt})]_3[Sn_9(mes)]\bullet 2py$ suitable for single crystal X-ray diffraction were occasionally obtained as side products in the synthesis of $[K(2,2,2\text{-crypt})]_4[Fe@Sn_{10}]\bullet 4py$. ES-MS (ES–): *m/z* 1188.2 $[Sn_9(mes)]^-$, 1602.0 $\{[K(2,2,2\text{-crypt})][Sn_9(mes)]\}^-$. ES-MS (ES+): *m/z* 2432.8 $\{[K(2,2,2\text{-crypt})]_3[Sn_9(mes)]\}^+$.

$[Sn_9Fe(mes)]^{3-}$ (22)

In the process of attempting to synthesise more of the compound $[Fe@Sn_{10}]^{3-}$, occasionally crystals of $[K(2,2,2\text{-crypt})]_3[Sn_9Fe(mes)]$ were isolated. ES-MS (ES–): *m/z* 1070.4 $[Sn_9]^-$, 1125.2 $[Sn_9Fe]^-$, 1188.2 $[Sn_9(mes)]^-$, 1244.0 $[Sn_9Fe(mes)]^-$, 1602.2 $\{[K(2,2,2\text{-crypt})][Sn_9(mes)]\}^-$, 1658.0 $\{[K(2,2,2\text{-crypt})][Sn_9Fe(mes)]\}^-$, 1713.7 $\{[K(2,2,2\text{-crypt})][Sn_9Fe_2(mes)]\}^-$. ES-MS (ES+): *m/z* 2852.1 $\{[K(2,2,2\text{-crypt})]_4[Sn_9(mes)]\}^+$, 2906.1 $\{[K(2,2,2\text{-crypt})]_4[Sn_9Fe(mes)]\}^+$.

$[Mn@Pb_{12}]^{3-}$ (23)

$[K(2,2,2\text{-crypt})]_3[Mn@Pb_{12}]\bullet 1.5en$

K_4Pb_9 (150 mg, 0.074 mmol) and 2,2,2-crypt (85 mg, 0.226 mmol) were dissolved in 2 mL of ethylenediamine to give a dark green solution. $Mn_3(mes)_6$ (22 mg, 0.025 mmol) was dissolved in thf (1.5 mL) to give a pale yellow solution, which was then added dropwise to the stirred en solution. The reaction mixture changed from dark green to dark brown and was allowed to stir for 1 h, after which the solution was filtered and the filtrate layered with Et_2O. Thin black diamond-shaped crystals of $[K(2,2,2\text{-crypt})]_3[Mn@Pb_{12}]\bullet 1.5en$ suitable for single crystal X-

ray diffraction were obtained after a few days (86 mg, 30% crystalline yield based on $Mn_3(mes)_6$). Anal. Calcd for $C_{56}H_{116}K_3Mn_1N_8O_{16}Pb_{12}$: C, 17.47; H, 3.04; N, 2.91. Found: C, 17.47; H, 2.99; N, 2.93. ES-MS (ES–): *m/z* 1035.7 $[Pb_5]^-$, 1074.7 $\{K[Pb_5]\}^-$, 1452.1 $\{[K(2,2,2\text{-crypt})][Pb_5]\}^-$, 2072.6 $[Pb_{10}]^-$, 2487.8 $[Pb_{12}]^-$, 2541.4 $[Mn@Pb_{12}]^-$, 2902.7 $\{[K(2,2,2\text{-crypt})][Pb_{12}]\}^-$, 2957.5 $\{[K(2,2,2\text{-crypt})][Mn@Pb_{12}]\}^-$. ES-MS (ES+): *m/z* 2283.3 $\{[K(2,2,2\text{-crypt})]_3[Pb_5]\}^+$, 3318.1 $\{[K(2,2,2\text{-crypt})]_3[Pb_{10}]\}^+$, 3733.0 $\{[K(2,2,2\text{-crypt})]_3[Pb_{12}]\}^+$, 3788.1 $\{[K(2,2,2\text{-crypt})]_3[Mn@Pb_{12}]\}^+$. An EPR resonance centered at g = 2.0095 was observed for a solid crystalline sample at room temperature.

$[Ge_9(mes)]^{3-}$ (24) & $[Ge_9Mn(mes)]^{3-}$ (25)

$[K(2,2,2\text{-crypt})]_3[Ge_9(mes)]_{0.62}[Ge_9Mn(mes)]_{0.38}$

K_4Ge_9 (108 mg, 0.133 mmol) and 2,2,2-crypt (200 mg, 0.532 mmol) were dissolved in ethylenediamine (4 mL) to give a dark orange-yellow solution. The reaction mixture was stirred for 1 h and then toluene (80 mL) was added to give an orange precipitate. It was stirred for a further 30 mins and left to stand for 30 mins. The colourless solution was filtered off and the solid precipitate dried under *vacuo* for 30 mins. The orange powder (224 mg) was isolated in the glovebox. Assuming the powder had the formula of $[K(2,2,2\text{-crypt})]_4[Ge_9]$, a portion of the dark orange powder (110 mg, 0.048 mmol) was redissolved in pyridine (2 mL) to give a dark yellow-brown solution. $Mn_3(mes)_6$ (17 mg, 0.019 mmol) was dissolved in thf (2 mL) to give a colourless solution. The thf solution was added dropwise to the pyridine solution with stirring. The reaction mixture was stirred for 1 h, filtered and the filtrate layered with toluene for crystallisation. After a few days dark red plate-like crystals (92 mg, 30% crystalline yield based on $Mn_3(mes)_6$) suitable for single crystal X-ray diffraction were obtained. Anal. Calcd

for $C_{63}H_{119}Mn_{0.38}K_3N_6O_{18}Ge_9$: C 37.08, H 5.88, N 4.12. Found: C 37.03, H 5.76, N 4.12. ES-MS (ES–): *m/z* 653.6 $[Ge_9]^-$, 772.9 $[Ge_9(mes)]^-$, 827.8 $[Ge_9Mn(mes)]^-$, 1068.9 {[K(2,2,2-crypt)][Ge_9]}$^-$, 1142.7 {[K(2,2,2-crypt)][Ge_{10}]}$^-$, 1188.8 {[K(2,2,2-crypt)][Ge_9(mes)]}$^-$, 1244.6 {[K(2,2,2-crypt)][Ge_9Mn(mes)]}$^-$, 1658.6 {[K(2,2,2-crypt)]$_2$[Ge_9Mn(mes)]}$^-$. ES-MS (ES+): *m/z* 1902.7 {[K(2,2,2-crypt)]$_3$[Ge_9]}$^+$, 1974.7 {[K(2,2,2-crypt)]$_3$[Ge_{10}]}$^+$, 2022.9 {[K(2,2,2-crypt)]$_3$[Ge_9(mes)]}$^+$, 2078.0 {[K(2,2,2-crypt)]$_3$[Ge_9Mn(mes)]}$^+$, 2437.4 {[K(2,2,2-crypt)]$_4$[Ge_9(mes)]}$^+$, 2492.4 {[K(2,2,2-crypt)]$_4$[Ge_9Mn(mes)]}$^+$.

$[Sn_9Mn(mes)]^{3-}$ (26)

[K(2,2,2-crypt)]$_3$[Sn_9Mn(mes)]•py

K_4Sn_9 (100 mg, 0.082 mmol) and 2,2,2-crypt (123 mg, 0.327 mmol) were dissolved in 3 mL of pyridine to give a dark brown solution. $Mn_3(mes)_6$ (22 mg, 0.025 mmol) was dissolved in thf (1.5 mL) to give a pale yellow solution, which was then added dropwise to the stirred pyridine solution. The reaction mixture was then allowed to stir for 1 h, after which the solution was filtered and the filtrate layered with toluene. Black block-shaped crystals of [K(2,2,2-crypt)]$_3$[Sn_9Mn(mes)]•py suitable for single crystal X-ray diffraction were obtained after a few days (53 mg, 28% crystalline yield based on $Mn_3(mes)_6$). ES-MS (ES–): *m/z* 1242.9 $[Sn_9Mn(mes)]^-$, 1658.0 {[K(2,2,2-crypt)][Sn_9Mn(mes)]}$^-$, 2073.2 {[K(2,2,2-crypt)]$_2$[Sn_9Mn(mes)]}$^-$. ES-MS (ES+): *m/z* 2902.6 {[K(2,2,2-crypt)]$_4$[Sn_9Mn(mes)]}$^+$.

5.3 Structure determination

Single crystal X-ray diffraction data were collected on an Enraf-Nonius Kappa CCD diffractometer and a 95 mm CCD area detector equipped with an Oxford Cryosystems low-

temperature device. The crystals were selected under Paratone-N oil, mounted on micro-mount loops and positioned in the cold stream of the diffractometer. Data were collected at 150 K using graphite monochromated Mo Kα radiation (λ = 0.71073 Å); equivalent reflections were merged, and the images were processed with the DENZO and SCALEPACK programs.[11] Corrections for Lorentz-polarization effects and absorption were performed, and the structures were solved by direct methods and refined on F^2 using the SHELX-97 package.[12, 13] Because of the large number of unique non-hydrogen atoms present in the asymmetric units of $[K(2,2,2\text{-crypt})]_6[Pb_9CdPh]_2$•2en•tol and $[K(2,2,2\text{-crypt})]_6[Sn_9CdSn(^nBu)_3]_2$•6tol•py, these species were refined on F^2 using SHELXH, a special version of SHELXL for the refinement of very large structures. Single crystal X-ray diffraction data for $[K(2,2,2\text{-crypt})]_3[Mn@Pb_{12}]$•1.5en were collected on an Enraf-Nonius Kappa CCD diffractometer and using synchrotron radiation on a CrystalLogic Kappa (3 circle) diffractometer at beamline I19 (EH1) at the Diamond Light Source, Didcot. The synchrotron data were collected at the zirconium edge (λ = 0.6889 Å) and were processed using CrystalClear-SM Expert 2.0 r4. The synchrotron data was solved by refinement of the structure determined from the laboratory data.

5.4 NMR

$^{13}C\{^1H\}$ and ^1H NMR spectra were recorded at room temperature in either d_5-pyridine or d_7-dmf using a Varian Mercury VX300 spectrometer (^1H 300 MHz). They were referenced to the most upfield of residual solvent resonances: 1) d_5-pyridine, δ_H = 7.22 ppm and δ_C = 123.87 ppm; 2) d_7-dmf, δ_H = 2.75 ppm and δ_C = 29.76 ppm. For compounds $[E_9CdSn(^nBu)_3]^{3-}$ (E = Sn, Pb) and $\{[Fe(COT)(CO)_3]_2\}^{2-}$ the COSY and HMQC two-dimensional correlation

experiments were used to analyse and determine the coupling relationship between protons that are two or three bonds apart and directly bonded H–C, respectively.

5.5 Electrospray mass-spectrometry

Positive and negative ion mode electrospray mass spectra were recorded from dmf solutions (10–20 μM) on a Micromass LCT Time of Flight mass spectrometer with a Z-spray source (150 °C source temperature, 200 °C desolvation temperature, 2.2 kV capillary voltage, and 20 V cone voltage).

5.6 Infra Red Measurements

IR data were recorded on solid samples in Nujol mulls. The mulls were made up inside an inert atmosphere glovebox and the NaCl plates placed in a gas-tight sample holder prior to data collection. Spectra were recorded on a Nicolet Magna-IR 560 spectrometer in absorbance mode (Happ-Genzel FT apodization) with a Ge/CsI beam splitter and liquid nitrogen cooled Mercury Cadmium Telluride (MCT) detector.

5.7 EPR

Continuous-wave electron paramagnetic resonance (CW-EPR) experiments were performed using an X-band Bruker BioSpin GmbH EMX spectrometer equipped with a high sensitivity Bruker probehead and a low-temperature Oxford Instruments CF935 helium-flow cryostat. Experiments were conducted with 2–10 mW microwave power, 0.1 mT modulation amplitude, and a modulation frequency of 100 kHz. The magnetic field was calibrated at room temperature with an external 2,2-diphenyl-1-picrylhydrazyl standard (g = 2.0036).

5.8 Electronic structure determination

5.8.1 $[Pb_9CdCdPb_9]^{6-}$ (12)

DFT calculations were performed using the Amsterdam Density Functional package (ADF2007.01) by Prof. John McGrady (University of Oxford).[14] A triple-ζ Slater-type basis set, extended with a single polarization function, was used to describe Cd and Pb. Electrons in orbitals up to and including 3*d* {Cd} and 4*d* {Pb} were considered part of the core and treated in accordance with the frozen core approximation. The local density approximation was employed for the optimizations,[15] along with the local exchange-correlation potential of Vosko, Wilk and Nusair[16] and gradient corrections to exchange and correlation proposed by Becke and Perdew (BP86).[17, 18] Relativistic effects were incorporated using the Zeroth Order Relativistic Approximation (ZORA).[19-21] The presence of cations in the crystal lattice was modelled by surrounding the anion with a continuum dielectric using COSMO.[22] The chosen dielectric constant ε = 16.9 corresponds to that of ammonia, although structural parameters are not strongly dependent on this choice. All structures were optimized using the gradient algorithm of Versluis and Ziegler.[23]

5.8.2 $[Fe@Ge_{10}]^{3-}$ (18), $[Fe@Sn_{10}]^{3-}$ (20) and $[Mn@Pb_{12}]^{3-}$ (23)

All calculations were performed with the Amsterdam Density Functional package (ADF2010.02) by Tobias Krämer and Prof. John McGrady (University of Oxford).[14] The TZ2P Slater-type basis set of triple-ζ quality, extended with two polarisation functions, was used to describe the 1st row transition metals (M = Fe, Co, Ni, Cu, Zn) as well as the Group 14 elements (E = Ge, Sn). Electrons in orbitals up to and including 2*p* for the transition metals as well as 3*p* and 4*p* Ge and Sn, respectively, were considered part of the core and treated in

accordance with the frozen core approximation (M.2p, Ge.3p and Sn.4p). All calculations employed the Local Density Approximation (LDA) to the exchange potential,[15] along with the local exchange-correlation potential of Vosko, Wilk and Nusair (VWN)[16] and gradient corrections to non-local exchange and correlation proposed by Becke and Perdew (BP86).[17, 18] All calculations were unrestricted. Relativistic effects were incorporated using the Zeroth Order Relativistic Approximation (ZORA).[19-21] The confining effect of cations in the crystal lattice was modelled by surrounding the clusters with a continuum dielectric model (COSMO).[22] The chosen dielectric constant $\varepsilon = 78.4$ corresponds to that of water although structural parameters are not strongly dependent on this choice. All structures were optimized using the gradient algorithm of Versluis and Ziegler.[23] In order to explore the potential energy landscape of the clusters, the nine-atom polyhedra with 3-, 4- and 5-fold symmetry were used as starting point for the optimizations. During the initial geometry optimisation the symmetries were kept fixed. When imaginary frequencies were present in the converged structure further optimisation using structures distorted along the imaginary modes lead to the nearest local minimum.

5.9 Elemental analysis

Elemental analyses were carried out by Stephen Boyer of the London Metropolitan University. Samples (approx. 5 mg) were submitted in Pyrex ampoules sealed under vacuum.

5.9 References

1. von Schnering, H. G.; Baitinger, M.; Bolle, U.; Carrillo Cabrera, W.; Curda, J.; Grin, Y.; Heinemann, F.; Llanos, J.; Peters, K.; Schmeding, A.; Somer, M., *Z. Anorg. Allg. Chem.* **1997**, *623*, 1037.
2. Queneau, V.; Sevov, S. C., *Inorg. Chem.* **1998**, *37*, 1358.
3. Hoch, C.; Wendorff, M.; Rohr, C., *Acta Crystallogr. Sect. C-Cryst. Struct. Commun.* **2002**, *58*, I45.
4. Seidel, W.; Burger, I., *Z. Anorg. Allg. Chem.* **1981**, *473*, 166.
5. Boudier, A.; Darcel, C.; Flachsmann, F.; Micouin, L.; Oestreich, M.; Knochel, P., *Chem. Eur. J.* **2000**, *6*, 2748.
6. Tang, H.; Richey, H. G., *Organometallics* **2001**, *20*, 1569.
7. Kays, D.; Cowley, A., *Chem. Commun.* **2007**, 1053.
8. Gambarotta, S.; Floriani, C.; Chiesivilla, A.; Guastini, C., *J. Chem. Soc. Chem. Commun.* **1983**, 1128.
9. Solari, E.; Musso, F.; Gallo, E.; Floriani, C.; Re, N.; Chiesivilla, A.; Rizzoli, C., *Organometallics* **1995**, *14*, 2265.
10. Klose, A.; Solari, E.; Floriani, C.; Chiesivilla, A.; Rizzoli, C.; Re, N., *J. Am. Chem. Soc.* **1994**, *116*, 9123.
11. Otwinowski, Z.; Minor, W., *Macromolecular Crystallography, Pt A* **1997**, *276*, 307.
12. Sheldrick, G. M., *Acta Crystallogr. Sect. A* **1990**, *46*, 467.
13. Sheldrick, G. M., *SHELX97 - Programs for Crystal Structure Analysis, Release 97-2*. Institüt für Anorganische Chemie der Universität, Tammanstrasse 4, D-3400 Göttingen, Germany, 1998.

14. (a) te Velde, G.; Bickelhaupt, F. M.; Baerends, E. J.; Fonseca Guerra, C.; van Gisbergen, S. J. A.; Snijders, J. G.; Ziegler, T., *J. Comput. Chem.* **2001**, *22*, 931. (b) C. Fonseca Guerra, J. G. Snijders, G. te Velde and E. J. Baerends, *Theor. Chem. Acc*., **1998**, *99*, 391. (c) ADF 2008.01, SCM, Theoretical Chemistry, Vrije Universiteit, Amsterdam, The Netherlands, http://www.scm.com.

15. Parr, R. G.; Yang, W., *Density Functional Theory of Atoms and Molecules*. Oxford University Press, Oxford, 1989.

16. Vosko, S. H.; Wilk, L.; Nusair, M., *Can. J. Phys.* **1980**, *58*, 1200.

17. Becke, A. D., *Phys. Rev. A* **1988**, *38*, 3098.

18. Perdew, J. P., *Phys. Rev. B* **1986**, *33*, 8822.

19. van Lenthe, E.; Ehlers, A.; Baerends, E. J., *J. Chem. Phys.* **1999**, *110*, 8943.

20. van lenthe, E.; Baerends, E. J.; Snijders, J. G., *J. Chem. Phys.* **1993**, *99*, 4597.

21. van lenthe, E.; Baerends, E. J.; Snijders, J. G., *J. Chem. Phys.* **1994**, *101*, 9783.

22. Klamt, A., *J. Phys. Chem.* **1995**, *99*, 2224.

23. Versluis, L.; Ziegler, T., *J. Chem. Phys.* **1988**, *88*, 322.

Appendix One. Selected X-ray data collection and refinement parameters.

Compound	[K(2,2,2-crypt)]$_3$[**1**]	[K(2,2,2-crypt)]$_3$[**2**]·tol	[K(2,2,2-crypt)]$_3$[**4**]·en·2tol
Formula	$C_{63}H_{119}Ge_9K_3N_6O_{18}Zn_1$	$C_{70}H_{127}K_3N_6O_{18}Sn_9Zn_1$	$C_{73}H_{139}Ge_9K_3N_8O_{18}\ Zn_1$
Fw [g mol^{-1}]	2084.62	2590.84	2252.90
crystal system	Monoclinic	Monoclinic	Triclinic
space group	$P2_1/c$	$P2_1/c$	$P\bar{1}$
a (Å)	17.3897(1)	14.7470(1)	13.8650(1)
b (Å)	22.4685(2)	24.6645(2)	15.1706(1)
c (Å)	22.0943(2)	27.0957(2)	26.0077(2)
α (°)	90.00	90.00	75.4570(10)
β (°)	98.0425(3)	101.4626(3)	85.3940(10)
γ (°)	90.00	90.00	69.1790(10)
V (Å^3)	8547.79(12)	9658.86(12)	4949.15(6)
Z	4	4	2
radiation, λ (Å)	Mo K_α, 0.71073	Mo K_α, 0.71073	Mo K_α, 0.71073
T (K)	150(2)	150(2)	150(2)
ρ_{calc} (g cm^{-3})	1.620	1.782	1.512
μ (mm^{-1})	3.600	2.716	3.116
reflections collected	29330	31887	43107
independent reflections	14916	16791	22374
parameters	901	993	987
R(int)	0.0285	0.0220	0.0261
R1/wR2,[a] $I \geq 2\sigma_I$ (%)	5.61 / 14.21	7.62 / 17.39	3.55 / 7.91
R1/wR2,[a] all data (%)	7.58 / 15.10	9.64 / 18.35	4.83 / 8.38
GOF	1.042	1.018	1.027

[a] $R1 = [\sum||F_o| - |F_c||]/\sum|F_o|$; $wR2 = \{[\sum w[(F_o)^2 - (F_c)^2]^2]/[\sum w(F_o^2)^2]\}^{1/2}$; $w = [\sigma^2(F_o)^2 + (AP)^2 + BP]^{-1}$, where $P = [(F_o)^2 + 2(F_c)^2]/3$ and the A and B values are 0.0698 and 34.71 for [K(2,2,2-crypt)]$_3$**1**, 0.0579 and 97.35 for [K(2,2,2-crypt)]$_3$**2**·tol and 0.0280 and 7.93 for [K(2,2,2-crypt)]$_3$**4**·en·2tol.

Compound	$[K(2,2,2\text{-crypt})]_3[\mathbf{5}]\cdot 0.5en$	$[K(2,2,2\text{-crypt})]_6[\mathbf{6}]_2\cdot en$	$[K(2,2,2\text{-crypt})]_3[\mathbf{7}]_{0.8}[Sn_9]_{0.2}\cdot en$
Formula	$C_{58}H_{115}K_3N_7O_{18}Sn_9Zn_1$	$C_{116}H_{238}K_6N_{14}O_{36}Pb_{18}Zn_2$	$C_{61}H_{120}Cd_1K_3N_8O_{18}Sn_9$
Fw [g mol^{-1}]	2453.48	6498.28	2551.56
crystal system	Triclinic	Triclinic	Triclinic
space group	$P\bar{1}$	$P\bar{1}$	$P\bar{1}$
a (Å)	14.0006(1)	14.0881(1)	15.2071(1)
b (Å)	14.5855(1)	25.5722(2)	15.4662(1)
c (Å)	21.8839(2)	27.1348(2)	21.4652(2)
α (°)	86.8242(4)	112.1484(3)	91.0976(4)
β (°)	86.3706(5)	100.0104(3)	95.6698(4)
γ (°)	79.6696(4)	92.2170(3)	113.5806(4)
V (Å^3)	4383.15(6)	8858.10(12)	4594.79(6)
Z	2	2	2
radiation, λ (Å)	Mo K_α, 0.71073	Mo K_α, 0.71073	Mo K_α, 0.71073
T (K)	150(2)	100(2)	150(2)
ρ_{calc} (g cm^{-3})	1.859	2.436	1.844
μ (mm^{-1})	2.987	17.501	2.822
reflections collected	36870	54321	31323
independent reflections	19739	30777	16029
parameters	776	1729	969
R(int)	0.0294	0.0536	0.0241
R1/wR2,[a] $I \geq 2\sigma_I$ (%)	5.47 / 13.95	4.86 / 11.99	3.31 / 7.30
R1/wR2,[a] all data (%)	7.32 / 14.67	7.08 / 12.87	4.53 / 7.64
GOF	1.129	1.009	1.039

[a] $R1 = [\sum||F_o| - |F_c||]/\sum|F_o|$; $wR2 = \{[\sum w[(F_o)^2 - (F_c)^2]^2]/[\sum w(F_o^2)^2]\}^{1/2}$; $w = [\sigma^2(F_o)^2 + (AP)^2 + BP]^{-1}$, where $P = [(F_o)^2 + 2(F_c)^2]/3$ and the A and B values are 0.0273 and 75.48 for $[K(2,2,2\text{-crypt})]_3\mathbf{5}\cdot 0.5en$, 0.0779 and 0.00 for $[K(2,2,2\text{-crypt})]_6\mathbf{6}_2\cdot en$ and 0.0234 and 13.83 for $[K(2,2,2\text{-crypt})]_3\mathbf{7}_{0.8}[Sn_9]_{0.2}\cdot en$.

Compound	[K(2,2,2-crypt)]$_6$[**8**]$_2$·2en·tol	[K(2,2,2-crypt)]$_6$[**12**]·2en	[K(2,2,2-crypt)]$_6$[**13**]$_2$·6tol·py
Formula	$C_{131}H_{250}Cd_2K_6N_{16}O_{36}Pb_{18}$	$C_{168}H_{348}Cd_3K_9N_{24}O_{54}Pb_{27}$	$C_{179}H_{323}Cd_2K_6N_{13}O_{36}Sn_{20}$
Fw [g mol^{-1}]	6814.29	9851.93	6066.70
crystal system	Triclinic	Monoclinic	Triclinic
space group	$P\bar{1}$	$P2_1/c$	$P\bar{1}$
a (Å)	15.8896(1)	23.4485(1)	15.5506(1)
b (Å)	22.6342(1)	26.7397(1)	28.2557(2)
c (Å)	27.7421(2)	43.1335(2)	28.9528(2)
α (°)	88.0220(3)	90.00	78.8039(2)
β (°)	74.9160(2)	103.3206(1)	75.0316(2)
γ (°)	89.5042(2)	90.00	76.5925(3)
V (Å^3)	9627.90(10)	26317.29(19)	11832.37(14)
Z	2	4	2
radiation, λ (Å)	Mo K_α, 0.71073	Mo K_α, 0.71073	Mo K_α, 0.71073
T (K)	150(2)	150(2)	150(2)
ρ_{calc} (g cm^{-3})	2.351	2.487	1.703
μ (mm^{-1})	16.078	17.641	2.409
reflections collected	62371	78794	100829
independent reflections	33535	43674	53966
parameters	1873	2566	2106
R(int)	0.0485	0.0515	0.0540
R1/wR2,[a] $I \geq 2\sigma_I$ (%)	4.56 / 11.74	4.89 / 9.44	5.23 / 12.78
R1/wR2,[a] all data (%)	6.60 / 12.48	9.64 / 10.36	10.01 / 15.19
GOF	1.025	1.025	1.030

[a] $R1 = [\sum||F_o| - |F_c||]/\sum|F_o|$; $wR2 = \{[\sum w[(F_o)^2 - (F_c)^2]^2]/[\sum w(F_o^2)^2]\}^{1/2}$; $w = [\sigma^2(F_o)^2 + (AP)^2 + BP]^{-1}$, where $P = [(F_o)^2 + 2(F_c)^2]/3$ and the A and B values are 0.0784 and 0.00 for [K(2,2,2-crypt)]$_6$**8**$_2$·2en·tol, 0.0460 and 0.00 for [K(2,2,2-crypt)]$_6$**12**·2en and 0.0648 and 13.55 for [K(2,2,2-crypt)]$_6$**13**$_2$·6tol·py.

Compound	[K(2,2,2-crypt)]$_3$[**15**]	[K(2,2,2-crypt)][**16**]	[K(2,2,2-crypt)]$_2$[**17**]
Formula	$C_{57}H_{108}Fe_1Ge_8K_3N_6O_{21}$	$C_{29}H_{44}Fe_1K_1N_2O_9$	$C_{29}H_{44}Fe_1K_1N_2O_9$
Fw [g mol^{-1}]	1967.36	659.61	659.26
crystal system	Monoclinic	Monoclinic	Monoclinic
space group	$P2_1/c$	$P2_1/c$	$P2_1/c$
a (Å)	14.4556(1)	10.7868(2)	15.7708(2)
b (Å)	18.7806(1)	12.1806(2)	12.0839(2)
c (Å)	30.9698(4)	24.3535(4)	21.1602(3)
α (°)	90.00	90.00	90.00
β (°)	106.8930(10)	92.8870(10)	128.6920(10)
γ (°)	90.00	90.00	90.00
V (Å^3)	8045.02(13)	3195.74(9)	3147.48(8)
Z	4	4	4
radiation, λ (Å)	Mo K_α, 0.71073	Mo K_α, 0.71073	Mo K_α, 0.71073
T (K)	150(2)	150(2)	150(2)
ρ_{calc} (g cm^{-3})	1.624	1.371	1.391
μ (mm^{-1})	3.341	0.655	0.665
reflections collected	26657	13226	13981
independent reflections	14029	7271	7169
parameters	847	379	403
R(int)	0.0342	0.0437	0.0337
R1/wR2,[a] $I \geq 2\sigma_I$ (%)	5.63 / 14.92	4.99 / 12.03	3.75 / 8.69
R1/wR2,[a] all data (%)	7.14 / 15.73	8.94 / 14.03	6.13 / 9.71
GOF	1.033	0.973	1.028

[a] $R1 = [\sum||F_o| - |F_c||]/\sum|F_o|$; $wR2 = \{[\sum w[(F_o)^2 - (F_c)^2]^2]/[\sum w(F_o^2)^2]\}^{1/2}$; $w = [\sigma^2(F_o)^2 + (AP)^2 + BP]^{-1}$, where $P = [(F_o)^2 + 2(F_c)^2]/3$ and the A and B values are 0.0825 and 34.99 for [K(2,2,2-crypt)]$_3$**15**, 0.0698 and 1.55 for [K(2,2,2-crypt)]**16** and 0.0460 and 0.54 for [K(2,2,2-crypt)]$_2$**17**.

Compound	[K(2,2,2-crypt)]$_3$[**18**]·2en	[K(2,2,2-crypt)]$_3$[**19**]	[K(2,2,2-crypt)]$_3$[**20**]·4py
Formula	$C_{58}H_{124}Fe_1Ge_{10}K_3N_{10}O_{18}$	$C_{63}H_{119}Ge_9K_3N_6O_{18}$	$C_{74}H_{128}Fe_1K_3N_{10}O_{18}Sn_{10}$
Fw [g mol^{-1}]	2148.72	2019.25	2805.91
crystal system	Triclinic	Monoclinic	Monoclinic
space group	$P\bar{1}$	$P2_1/c$	$P2_1$
a (Å)	14.4014(1)	17.5546(3)	14.2743(1)
b (Å)	15.7227(1)	22.4830(3)	25.9819(2)
c (Å)	21.6608(2)	21.3616(4)	14.5250(1)
α (°)	93.2587(3)	90.00	90.00
β (°)	100.4043(3)	96.7790(10)	108.088(3)
γ (°)	107.2794(4)	90.00	90.00
V (Å^3)	4574.29(6)	8372.1(2)	5120.72(11)
Z	2	4	2
radiation, λ (Å)	Mo K_α, 0.71073	Mo K_α, 0.71073	Mo K_α, 0.71073
T (K)	150(2)	150(2)	150(2)
ρ_{calc} (g cm^{-3})	1.560	1.602	1.820
μ (mm^{-1})	3.584	3.396	2.713
reflections collected	30663	28550	98869
independent reflections	15928	14598	17070
parameters	1136	892	1136
R(int)	0.0298	0.0493	0.050
R1/wR2,[a] $I \geq 2\sigma_I$ (%)	4.38 / 11.88	6.50 / 16.04	5.68 / 15.22
R1/wR2,[a] all data (%)	5.72 / 12.56	10.19 / 17.37	6.48 / 15.85
GOF	1.047	1.033	1.020

[a] $R1 = [\sum||F_o| - |F_c||]/\sum|F_o|$; $wR2 = \{[\sum w[(F_o)^2 - (F_c)^2]^2]/[\sum w(F_o^2)^2]\}^{1/2}$; $w = [\sigma^2(F_o)^2 + (AP)^2 + BP]^{-1}$, where $P = [(F_o)^2 + 2(F_c)^2]/3$ and the A and B values are 0.0612 and 5.44 for [K(2,2,2-crypt)]$_3$**18**·2en, 0.0759 and 24.39 for [K(2,2,2-crypt)]$_3$**19**,0.1019 and 15.51 for [K(2,2,2-crypt)]$_3$**20**·4py.

Compound	[K(2,2,2-crypt)]$_3$[**21**]·2py	[K(2,2,2-crypt)]$_3$[**23**]•1.5en	[K(2,2,2-crypt)]$_3$[**23**]•1.5en
Formula	$C_{73}H_{129}K_3N_8O_{18}Sn_9$	$C_{57}H_{120}K_3Mn_1N_9O_{18}$ Pb_{12}	$C_{57}H_{120}K_3Mn_1N_9O_{18}Pb_{12}$
Fw [g mol^{-1}]	2592.35	3878.14	3878.14
crystal system	Triclinic	Monoclinic	Monoclinic
space group	$P\bar{1}$	$P2_1/c$	$P2_1/c$
a (Å)	14.3352(1)	17.4420(1)	17.373(3)
b (Å)	14.4887(1)	23.2970(2)	23.275(5)
c (Å)	24.5941(2)	50.4120(4)	50.436(12)
α (°)	76.3870(10)	90.00	90.00
β (°)	88.1220(10)	110.2300(10)	109.82(3)
γ (°)	79.1000(10)	90.00	90.00
V (Å^3)	4874.72(6)	19221.1(3)	19186(7)
Z	2	8	8
radiation, λ (Å)	Mo K_α, 0.71073	Mo K_α, 0.71073	Synchrotron, 0.68890
T (K)	150(2)	150(2)	150(2)
ρ_{calc} (g cm^{-3})	1.766	2.680	2.685
μ (mm^{-1})	2.454	21.246	21.285
reflections collected	37427	41527	105799
independent reflections	21768	32162	34956
parameters	1000	2007	1905
R(int)	0.0215	0.0843	0.1212
R1/wR2,[a] $I \geq 2\sigma_I$ (%)	5.72 / 14.54	7.83 / 12.77	7.32 / 19.29
R1/wR2,[a] all data (%)	7.30 / 15.65	12.20 / 13.80	9.00 / 21.75
GOF	1.014	1.146	1.055

[a] $R1 = [\sum||F_o| - |F_c||]/\sum|F_o|$; $wR2 = \{[\sum w[(F_o)^2 - (F_c)^2]^2]/[\sum w(F_o^2)^2]\}^{1/2}$; $w = [\sigma^2(F_o)^2 + (AP)^2 + BP]^{-1}$, where $P = [(F_o)^2 + 2(F_c)^2]/3$ and the A and B values are 0.0690 and 45.99 for [K(2,2,2-crypt)]$_3$**21**·2py, 0.00 and 885.01 for [K(2,2,2-crypt)]$_3$[**23**]•1.5en (Mo K_α), 0.1113 and 25.90 for [K(2,2,2-crypt)]$_3$[**23**]•1.5en (Synchrotron).

Compound	$[K(2,2,2\text{-crypt})]_3[\mathbf{24}]_{0.62}[\mathbf{25}]_{0.38}$
Formula	$C_{63}H_{119}Ge_9K_3Mn_{0.50}N_6O_{18}$
Fw [g mol^{-1}]	2046.72
crystal system	Monoclinic
space group	$P2_1/c$
a (Å)	17.5120(1)
b (Å)	22.4720(1)
c (Å)	21.6467(1)
α (°)	90.00
β (°)	97.4150(10)
γ (°)	90.00
V (Å^3)	8447.38(7)
Z	4
radiation, λ (Å)	Mo K_α, 0.71073
T (K)	150(2)
ρ_{calc} (g cm^{-3})	1.609
μ (mm^{-1})	3.437
reflections collected	37272
independent reflections	19259
parameters	1039
R(int)	0.0344
R1/wR2,[a] $I \geq 2\sigma_I$ (%)	5.06 / 11.11
R1/wR2,[a] all data (%)	8.42 / 12.68
GOF	1.014

[a] $R1 = [\sum||F_o| - |F_c||]/\sum|F_o|$; $wR2 = \{[\sum w[(F_o)^2 - (F_c)^2]^2]/[\sum w(F_o^2)^2]\}^{1/2}$; $w = [\sigma^2(F_o)^2 + (AP)^2 + BP]^{-1}$, where $P = [(F_o)^2 + 2(F_c)^2]/3$ and the A and B values are 0.0440 and 17.31 for $[K(2,2,2\text{-crypt})]_3[\mathbf{24}]_{0.62}[\mathbf{25}]_{0.38}$.

Appendix Two. List of publications.

1. "Synthesis and Isolation of $[Fe@Ge_{10}]^{3-}$: A Pentagonal Prismatic Zintl Ion Cage Encapsulating an Interstitial Iron Atom". **Zhou, B.**; Denning, M. S.; Kays, D. L.; Goicoechea, J. M. *J. Am. Chem. Soc.* **2009**, *131*, 2802.

2. "$[Pb_9CdCdPb_9]^{6-}$: A Zintl cluster anion with an unsupported cadmium-cadmium bond". **Zhou, B.**; Denning, M. S.; Chapman, T. A. D.; McGrady, J. E.; Goicoechea, J. M. *Chem. Commun.* **2009**, 7221.

3. "Studies on the reactivity of $[Ge_9]^{4-}$ towards $Fe(COT)(CO)_3$: Synthesis and characterization of $[Ge_8Fe(CO)_3]^{3-}$ and of the anionic organometallic species $[Fe(COT)(CO)_3]^{-}$". **Zhou, B.**; Goicoechea, J. M. *Chem. -Eur. J.* **2010**, *16*, 11145.

4. "Coupling Reactions of Functionalized Zintl Ions $[E_9Cd(C_6H_5)]^{3-}$ (E = Sn, Pb) with Tributyltinhydride: Synthesis and Isolation of $\{Sn_9CdSn[(CH_2)_3CH_3]_3\}^{3-}$". **Zhou, B.**; Denning, M. S.; Chapman, T. A. D.; Goicoechea, J. M. *Inorg. Chem.* **2009**, *48*, 2899.

5. "Reductive cleavage of Zn–C bonds by group 14 Zintl anions: Synthesis and characterisation of $[E_9ZnR]^{3-}$ (E = Ge, Sn, Pb; R = Mes, ^{i}Pr)". **Zhou, B.**; Denning, M. S.; Jones, C.; Goicoechea, J. M. *Dalton Trans.* **2009**, 1571.

6. “Reactivity Studies of group 15 Zintl ions towards homoleptic post-transition metal organometallics: a 'bottom-up' approach to bimetallic molecular clusters”. Knapp, C.; **Zhou, B.**; Denning, M. S.; Rees, N. H.; Goicoechea, J. M. *Dalton Trans.* **2010**, *39*, 426.

7. “A Highly Distorted Open-Shell Endohedral Zintl Cluster: $[Mn@Pb_{12}]^{3-}$”. **Zhou, B.**; Krämer, T.; Thompson, A. L.; McGrady, J. E.; Goicoechea, J. M. *Inorg. Chem.* **2011**, *50*, 8028-8037.

8. “Structural and electronic differences between iron-centred endohedral ten-vertex Zintl clusters of the group 14 elements”, **Zhou, B.**; Krämer, T.; McGrady, J. E.; Goicoechea, J. M. *J. Am. Chem. Soc.* Submitted for publication.